

DTIC FILE COPY

AD-A213 896

**RADC -TR-89-8, Vol II (of two)
Final Technical Report
April 1989**



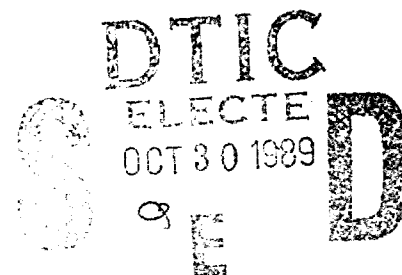
SCANNABLE MILLIMETER WAVE ARRAYS

Polytechnic University

Arthur A. Oliner

APPROVED FOR PUBLIC RELEASE; DISTRIBUTION UNLIMITED.

**THIS DOCUMENT CONTAINED
BLANK PAGES THAT HAVE
BEEN DELETED**



**ROME AIR DEVELOPMENT CENTER
Air Force Systems Command
Griffiss Air Force Base, NY 13441-5700**

**REPRODUCED FROM
BEST AVAILABLE COPY**

89 10 30 117

This report has been reviewed by the RADC Public Affairs Division (PA) and is releasable to the National Technical Information Service (NTIS). At NTIS it will be releasable to the general public, including foreign nations.

RADC-TR-89-8, Vol II (of two) has been reviewed and is approved for publication.

APPROVED:



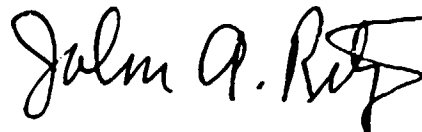
HANS P. STEYSKAL
Project Engineer

APPROVED:



JOHN K. SCHINDLER
Director of Electromagnetics

FOR THE COMMANDER:



JOHN A. RITZ
Directorate of Plans & Programs

If your address has changed or if you wish to be removed from the RADC mailing list, or if the addressee is no longer employed by your organization, please notify RADC (EEAA) Hanscom AFB MA 01731-5000. This will assist us in maintaining a current mailing list.

Do not return copies of this report unless contractual obligations or notices on a specific document require that it be returned.

UNCLASSIFIED

SECURITY CLASSIFICATION OF THIS PAGE

REPORT DOCUMENTATION PAGE				Form Approved OMB No. 0704-0188	
1a. REPORT SECURITY CLASSIFICATION UNCLASSIFIED			1b. RESTRICTIVE MARKINGS N/A		
2a. SECURITY CLASSIFICATION AUTHORITY N/A			3. DISTRIBUTION/AVAILABILITY OF REPORT Approved for public release; distribution unlimited.		
2b. DECLASSIFICATION/DOWNGRADING SCHEDULE N/A					
4. PERFORMING ORGANIZATION REPORT NUMBER(S) POLY-WRI-1543-88			5. MONITORING ORGANIZATION REPORT NUMBER(S) RADC-TR-89-8, Vol II (of two)		
6a. NAME OF PERFORMING ORGANIZATION Polytechnic University		6b. OFFICE SYMBOL (if applicable)	7a. NAME OF MONITORING ORGANIZATION Rome Air Development Center (EEAA)		
6c. ADDRESS (City, State, and ZIP Code) Weber Research Institute 333 Jay Street Brooklyn NY 11201			7b. ADDRESS (City, State, and ZIP Code) Hanscom AFB MA 01731-5000		
8a. NAME OF FUNDING/SPONSORING ORGANIZATION Rome Air Development Center		8b. OFFICE SYMBOL (if applicable) EEAA	9. PROCUREMENT INSTRUMENT IDENTIFICATION NUMBER F19628-84-K-0025		
8c. ADDRESS (City, State, and ZIP Code) Hanscom AFB MA 01731-5000			10. SOURCE OF FUNDING NUMBERS		
			PROGRAM ELEMENT NO. 61102F	PROJECT NO. 2305	TASK NO. J3
11. TITLE (Include Security Classification) SCANNABLE MILLIMETER WAVE ARRAYS					
12. PERSONAL AUTHOR(S) Arthur A. Oliner					
13a. TYPE OF REPORT Final		13b. TIME COVERED FROM Apr 84 to Jan 87		14. DATE OF REPORT (Year, Month, Day) April 1989	
15. PAGE COUNT 250					
16. SUPPLEMENTARY NOTATION					
17. COSATI CODES			18. SUBJECT TERMS (Continue on reverse if necessary and identify by block number) Millimeter waves, antennas, leaky waves, scanning arrays, printed circuit arrays, nonradiative dielectric (NRD) guide, groove guide, microstrip line.		
FIELD	GROUP	SUB-GROUP			
09	05				
09	01				
19. ABSTRACT (Continue on reverse if necessary and identify by block number) The complexity usually associated with scanning arrays at millimeter wavelengths produces fabrication difficulties, so that alternative methods are needed that employ simpler structures. This Final Report describes such an alternative scanning approach, and presents a group of new and simpler radiating structures suitable for millimeter-wave applications. The new class of scanning arrays described here achieves scanning in two dimensions by creating a one dimensional array of leaky-wave line-source antennas. The individual line sources are fed from one end and are scanned in elevation by electronic means or by varying the frequency. Scanning in the cross plane, and therefore in azimuth, is produced by phase shifters arranged in the feed structure of the one-dimensional array of line sources. Within the sector of space over which the arrays can be scanned, the radiation has negligible cross polarization, no blind spots and no grating lobes. These are significant, and also (Cont'd)					
20. DISTRIBUTION/AVAILABILITY OF ABSTRACT <input checked="" type="checkbox"/> UNCLASSIFIED/UNLIMITED <input type="checkbox"/> SAME AS RPT. <input type="checkbox"/> DTIC USERS			21. ABSTRACT SECURITY CLASSIFICATION UNCLASSIFIED		
22a. NAME OF RESPONSIBLE INDIVIDUAL HANS STEYSKAL			22b. TELEPHONE (Include Area Code) (617) 377-2052		22c. OFFICE SYMBOL RADC/EEAA

DD Form 1473, JUN 86

Previous editions are obsolete.

SECURITY CLASSIFICATION OF THIS PAGE

UNCLASSIFIED

UNCLASSIFIED

Block 19 (Cont'd)

unusual advantages. The novel features in the study reported here relate mainly to the new structures employed for the individual leaky-wave line sources and their combination into arrays, but also to analyses of the interactive effects produced when scanning occurs in both planes simultaneously.

The analyses of the various antenna structures are believed to be accurate, and for most of the antennas they are notable for resulting in transverse equivalent networks in which all the elements are in closed form, so that the dispersion relations for the propagation properties of the leaky-wave structures are also in closed form. It should be added that for all the array structures the analyses take all mutual coupling effects into account.

Although these studies are predominantly theoretical in nature, sets of careful measurements were made for two of the novel leaky-wave line-source antennas: the foreshortened NRD guide structure and the offset-groove-guide antenna. The agreement with the theoretical calculations was excellent in both cases.

In the Final Report, seven different novel antennas are described, of which four are leaky-wave line sources that scan in elevation, and three are arrays that scan in two dimensions. They represent examples of the new class of scannable antennas that are simple in configuration and suitable for millimeter wavelengths.

This Final Report is composed of 12 Chapters, of which the first is an introduction and summary, the second discusses some general features of our approach to the analysis of arrays, and the twelfth contains the list of references. Chapters III through XI discuss in detail our comprehensive studies on the various specific antennas; the material is presented under three broad categories: NRD guide antennas, groove guide antennas, and printed-circuit antennas. Because of the binding problems created by the size of this report, it is being printed in a two-volume format.

Accession For	
NTIS GRA&I	<input checked="checked" type="checkbox"/>
DTIC TAB	<input type="checkbox"/>
Unannounced	<input type="checkbox"/>
Justification	
By	
Distribution/	
Availability Codes	
Dist	Avail and/or Special
A-1	



UNCLASSIFIED

PRINTED-CIRCUIT ANTENNAS

IX.	MICROSTRIP LINE LEAKY-WAVE STRIP ANTENNAS	289
A.	BACKGROUND AND MOTIVATION	289
B.	THE NATURE OF THE LEAKAGE FROM HIGHER MODES ON MICROSTRIP LINE	292
	1. The Radiation Region and Leaky Modes	292
	2. The Two Forms of Leakage	294
	3. The Ratio of Powers in the Surface Wave and the Space Wave	296
C.	ANALYSIS AND PROPERTIES OF THE LEAKY MODES	304
	1. Derivation of Accurate Expression for the Propagation Characteristics	304
	2. Numerical Comparisons with the Literature	310
D.	STEEPEST-DESCENT PLANE FORMULATIONS	315
	1. Motivation	315
	2. Review of Some Properties of the Steepest-Descent Representation	316
	3. Steepest-Descent Plane Plots for Microstrip Line Higher Modes	324
	a. Microstrip Line with Open Top Using the Cross-Section Dimensions of Boukamp and Jansen	325
	b. The Boukamp-Jansen Structure with a Covered Top	334
	c. The Menzel Antenna Structure	336
E.	INVESTIGATIONS RELATING TO MENZEL'S ANTENNA	341
	1. Description of Menzel's Antenna	341
	2. Analysis of Menzel's Antenna in Leaky Mode Terms	343
	3. Parametric Dependences for Antenna Design	350
	4. Performance When Properly Designed as a Leaky-Wave Antenna	355

IX. MICROSTRIP LINE LEAKY-WAVE STRIP ANTENNAS

(With: Dr. K. S. Lee, former Ph.D. student,
now at Texas Instruments, Dallas.)

A. BACKGROUND AND MOTIVATION

During the late 1970's, a paper presented by H. Ermert at the European Microwave Conference stimulated instant controversy. That paper and a subsequent publication [25] presented a thorough mode-matching analysis of modes on microstrip line, treating numerically the dominant mode and the first two higher modes. A principal conclusion was that a "radiation" region exists close to the cutoff of the higher modes, although no mention was made of the characteristics of this "radiation" region or of the nature of the radiation. Because the description of this region, made in that talk and in published papers [25,26], was incomplete and therefore unclear to many, confusion persisted and certain practical consequences remained hidden.

Also in this general period, a paper by W. Menzel [27] presented a new traveling-wave antenna on microstrip line fed in its first higher mode and operated near to the cutoff of that mode. Menzel proposed his structure as a competitor to a microstrip patch antenna, and he therefore made his antenna short in terms of wavelength. He also assumed that the propagation wavenumber of the first higher mode was real in the very region where Ermert said no such solutions exist; since his guided wave, with a real wavenumber, was fast in that frequency range, Menzel presumed that it should radiate. His approximate analysis and his physical reasoning were therefore also incomplete, but his proposed antenna was valid and his measurements demonstrated reasonably successful performance.

The first feature of interest or challenge here thus involves the clarification of the confusion or contradictions implicit in the paragraphs above. The second feature of interest relates to the stark *simplicity* of Menzel's antenna; it consists simply of a *length of uniform microstrip line fed in its first higher mode*. Menzel's antenna is incompletely understood; for example, it seems to be too short since a large back lobe was found experimentally, but it is puzzling why the antenna should radiate so well in traveling wave fashion even though it is so short ($2.23\lambda_0$). Thus, an accurate analysis of that structure should explain the questions about its behavior, and indeed tell us how to improve its performance features. In view of the structural simplicity, one is stimulated to perform such an analysis in case it may result in a practical new antenna type.

The apparent contradictions are resolved when it is realized that *leaky modes* are present in this "radiation" region, and particularly so if the region can be characterized by only a *single* leaky mode. Not all leaky modes are physically significant, and more than one leaky mode may be present at the same time; each case must be examined separately for the physical significance of the role of leaky waves in any given "radiation" region. We conduct such an examination in Sec. D of this chapter, making use of the *steepest descent plane*, and we show that Ermert's "radiation" region is characterized in a highly convergent manner by essentially a single leaky mode.

Once we recognize the relevance of leaky modes to the "radiation" region of microstrip line higher modes, the application to leaky-wave antennas becomes evident. In particular, it is clear that Menzel's traveling-wave patch antenna is a leaky-wave antenna in principle, even though he did not recognize this fact and did not discuss the antenna's design or behavior in those terms. A leaky-wave analysis is necessary to answer the questions raised above, and to learn how to improve the antenna performance in a controlled way.

The existing literature does not contain any solutions relevant directly to this problem. Neither Ermert's [25,26] nor Menzel's [27] papers contain any complex solutions for the propagation constant. The only complex solutions for microstrip higher modes are given by J. Boukamp and R.H. Jansen [28] as part of a larger paper, but those solutions hold for a line with a top cover such that only the surface-wave mode can leak away.

None of these papers discusses the nature of the leakage produced. It turns out that the leakage is composed of two types, a surface wave and a space wave, and that each occurs at different onset conditions. These interesting features, and the ratio of the powers radiated into each type, are discussed in Sec. B.

Motivated by the reasons above, we have conducted studies along the following lines:

(a) Examination of the nature of the leakage: the types, onset conditions, and proportion of power into each type (Sec. B).

(b) Derivation of an accurate solution and computation of numerical values for the properties of microstrip line higher modes in their leakage range when there is no top cover, corresponding to the case of an antenna (Sec. C).

(c) Employment of the steepest descent plane to assess the validity of the intuitive presumption that the "radiation" region is characterized essentially by only a single leaky mode (Sec. D).

(d) Analysis of Menzel's antenna, and numerical comparisons with his experimental and theoretical results, together with an evaluation of his antenna (Sec. E).

(e) Presentation of performance characteristics of properly designed leaky-wave antennas of the Menzel type (Sec. E).

Some of the contents of Secs. B, C and E have been presented at symposia and appear in their Digests [29-31].*

* After the writing of this chapter was completed, some of the material that was presented at an URSI Symposium [31] was included in a short paper that appeared in Radio Science [32]. One of the reviewers of that paper indicated that some Russian publications contained material that overlapped some parts of Secs. B and C of this chapter. Those references, and how their contents relate to those of Secs. B and C of this chapter, are given in [32].

B. THE NATURE OF THE LEAKAGE FROM HIGHER MODES ON MICROSTRIP LINE

The dominant mode on open microstrip line is always purely bound, but the higher modes can leak power away when the frequency goes below some critical value. When the open microstrip line is operated in its first higher mode, the electric field lines are roughly those shown sketched in Fig. 9.1. We see, therefore, that radiation can be expected to occur directly above the strip and with horizontal electric field polarization. Power can also be leaked away in the horizontal direction in the form of a surface wave.

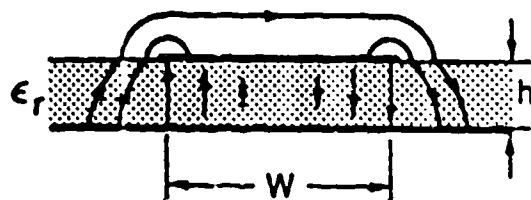


Fig. 9.1 Rough sketch of electric field lines for open microstrip line operated in its first higher mode.

The complex wavenumber k_z of the guided leaky mode is in the form

$$k_z = \beta - j\alpha \quad (9.1)$$

where β is the phase constant and α is the attenuation constant, which represents loss due both to leakage and to metal and dielectric losses. We assume here, however, that the metal and dielectric losses are negligible, so that α may be viewed directly as a leakage constant.

1. The Radiation Region and Leaky Modes

One of the figures presented by Ermert [25,26] is reproduced here, with modifications, as Fig. 9.2. His curves are the solid ones shown, for the lowest mode and the first two higher modes of microstrip line. All of his wavenumber values are real, meaning that the modes are purely bound in those ranges. He states, however, that in the region shown lined no real solutions exist, and he called this region the "radiation region." We have added the *dashed lines* appearing in this region in Fig. 9.2,

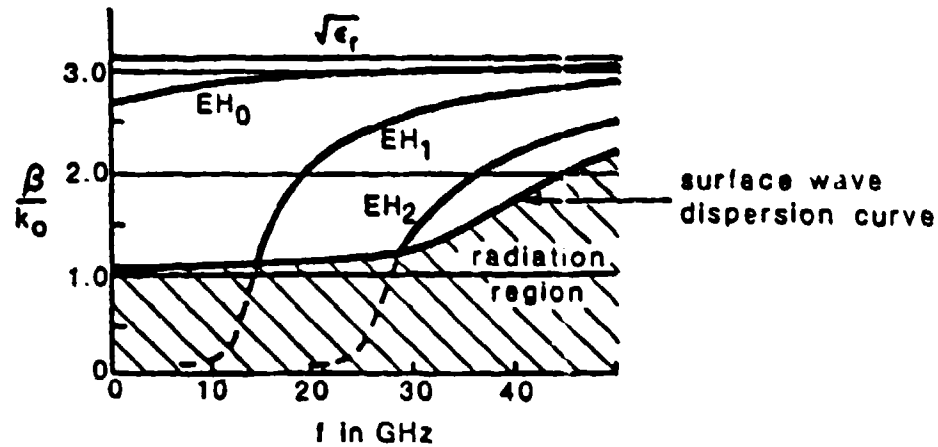


Fig. 9.2

Dispersion curves for the lowest mode and the first two higher modes in microstrip line with a top cover. The normalized phase constant β/k_0 is plotted against frequency. The solid lines (given by Eismert [25,26]) represent real wavenumbers, whereas the dashed lines correspond to the real parts of the leaky mode (complex) solutions in the "radiation region." The microstrip line dimensions are: strip width = 3.00 mm; dielectric layer thickness = 0.635 mm, $\epsilon_r = 9.80$, and the height of the top cover is five times the dielectric layer thickness.

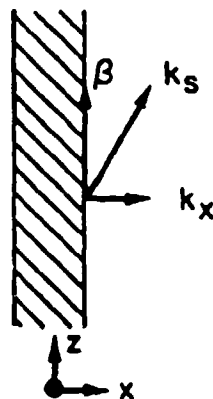


Fig. 9.3

Top view of the strip of microstrip line and the dielectric region around it. Wavenumbers β and k_s correspond, respectively, to the phase constant of the leaky mode guided by the strip and the wavenumber of the surface wave that propagates away at some angle during the leakage process.

which corresponds to complex solutions, and where, of course, only the real part is plotted. Physically, these complex solutions signify that this mode has become *leaky* in this region.

Ermert selects a *spectral* description for the modes of microstrip, and in his second paper [26] he rejects any inclusion of leaky modes since they are non-spectral (true). He then concludes that these leaky modes are "no longer of importance" in his analysis (false). His rejection of leaky modes not only caused much initial confusion, but it prevents one from understanding certain practical consequences. Not all leaky modes are physically significant, but we show in Sec. D, by reference to steepest-descent plots, that for this problem the continuous spectrum in Ermert's region is characterized in a highly convergent manner by essentially a single leaky mode. The physical importance of leaky modes despite their non-spectral nature is quite an old story, but it must be shown in each case that a particular leaky mode is physically valid; in this case, we have shown that it is, in agreement with obvious physical intuition.

2. The Two Forms of Leakage

The leakage can occur in two forms: a surface wave and a space wave. Furthermore, the onset of leakage for each form is given by simple conditions.

A top view of the strip and the dielectric region around it is shown in Fig. 9.3. With this figure, we examine the case of leakage away from the strip in the form of a *surface wave* on the dielectric layer outside of the strip region. When there is leakage into the surface wave, the modal field propagates axially (in the z direction) with phase constant β , and the surface wave propagates away (on both sides) at some angle with phase constant k_s , as shown in Fig. 9.3. The surface-wave wavenumber k_s has components k_z and k_x in the z and x directions, respectively, where k_z must be equal to β , since all field constituents are part of the same leaky modal field. We may therefore write:

$$k_x^2 = k_s^2 - \beta^2 \quad (9.2)$$

For actual leakage, k_x must be real, so that the condition for leakage is $k_x^2 > 0$. (When there is no leakage, i.e., the mode is purely bound, the modal field decays transversely and k_x is imaginary.) Applying this condition to (9.2), we find that, for leakage,

$$\beta < k_s \quad (9.3)$$

Relation (9.3) defines the lined region in Fig. 9.2; the upper boundary of that region is actually the dispersion curve for the surface wave, of wavenumber k_s , that can be supported by the dielectric layer on a ground plane, if the microstrip line is open above, or by the dielectric layer between parallel plates, if there is a metal top cover. At the onset of the surface wave, it emerges essentially parallel to the strip axis, consistent with the condition $\beta = k_s$.

As β (by lowering the frequency) is decreased below the value k_s , power leaks away in the form of a surface wave, as discussed above. As β is decreased further, power is then *also* leaked away in another form, the *space wave*. If the microstrip line is *open above*, this wave actually corresponds to radiation at some angle in the yz plane, the value of this angle changing with the frequency. At the onset of this space wave, the wave emerges essentially parallel to the strip axis, so that $\beta = k_o$, then, where $k_o (= 2\pi/\lambda_o)$ is the free-space wavenumber. This boundary corresponds to the horizontal line $\beta/k_o = 1$ in Fig. 9.2. For values of $\beta/k_o < 1$ or

$$\beta < k_o \quad (9.4)$$

power will leak into a space wave in addition to the surface wave. Condition (9.4) corresponds to the statement that the mode will radiate when its velocity is fast relative to that for free space, in conformity with standard antenna thinking.

What happens when the microstrip line has a *top cover*, of height H ? If $H < \lambda_o/2$, approximately, such that only the surface wave can propagate in the dielectric-loaded parallel-plate region, then all the other modes are below cutoff, and power can leak away *only* in surface wave form. If the plate spacing is increased, then some of the non-surface-wave modes are above cutoff, and these modes can also carry away power. The "space wave" then corresponds to the sum of those modes.

At what value of β do these "space wave" modes begin to contribute to the leakage? The value depends on the height H of the top cover. In most microstrip lines, the dielectric layer is only about a tenth of a wavelength thick. If the top layer is two wavelengths high, for example, the dielectric layer occupies a very small portion of the cross-section, and it affects only slightly the properties of the *non-surface-wave* modes. As a good approximation for such modes, therefore, let us neglect the dielectric layer in computing the mode propagation constants so that we can obtain a simple condition for the onset of that form of leakage. The first above-cutoff parallel-plate mode will then have the wavenumber

$$k_{pp} \approx \sqrt{k_o^2 - (\pi/H)^2}$$

and the condition for the leakage into that mode, following the reasoning used previously, is

$$\beta < k_{pp} \quad (9.5)$$

or

$$\frac{\beta}{k_o} < \left[1 - \left(\frac{\lambda_o}{2H} \right)^2 \right]^{1/2} \quad (9.6)$$

For H large with respect to wavelength, the critical value of β/k_o is almost unity, which is the value corresponding to the open microstrip line. As examples, for $H/\lambda_o = 5, 2$, and 1 , respectively, β/k_o is $0.995, 0.97$, and 0.87 .

3. The Ratio of Powers in the Surface Wave and the Space Wave

The last consideration in this section relates to the *ratio* of power leaked into the surface wave to that into the "space wave" in either the open or covered cases. As one extreme, when the height of the top cover causes all of the non-surface-wave modes to be below cutoff, all leaked power must be in surface wave form. As the height of the top cover is increased, so that both forms of leakage may be present simultaneously, this ratio will decrease. To determine this ratio quantitatively, we set up a *mode-matching analysis* that permitted us to know how much power leaks into each of the above-cutoff modes, including the surface-wave mode. The mode matching was established at the vertical plane corresponding to the side (or edge) of the strip, and the computer program for the procedure was furnished through the courtesy of Prof. S.T. Peng of the New York Institute of Technology.

We define R as the ratio of the power radiated into the surface wave to the total radiated power. The structure into which the radiation occurs is a parallel-plate waveguide of height H , in which we vary the height H of the top cover to determine how the ratio R changes with height H . We achieve the open microstrip line in the limit as $H \rightarrow \infty$. Curves of ratio R as a function of height H were obtained for a specific set of microstrip line dimensions, for three different frequencies. The line parameters are (see Fig. 9.1) $w = 15.00$ mm, $h = 0.794$ mm and $\epsilon_r = 2.32$, and the three frequencies are 8.20 GHz, 8.00 GHz and 6.70 GHz. These cross-section

dimensions are those used by Menzel [27] for his antenna; his operating frequency was 6.70 GHz. In order to simplify the calculation, since $h/\lambda_0 \ll 1$ and $H \gg h$, we assume that the dielectric material does not extend outside of the strip region, so that the region outside is a pure parallel-plate region. The resulting geometry is shown in the insets in Figs. 9.4 to 9.6. The error introduced is believed to be very small, but the calculation procedure is simplified substantially.

To summarize the objective here, we take the microstrip line to be operating in the leakage range of the first higher mode. When there is a top cover present, of height H , the power that leaks goes into parallel-plate modes. As the frequency is lowered into the leakage range, the power at first leaks only into the $n=0$ parallel-plate mode (a TEM mode, which corresponds to the surface-wave mode that would be present if the thin dielectric layer of height h continued into the parallel-plate region). As the frequency is lowered further, or as the top cover is raised, additional parallel-plate modes carry power. We wish to know, for the antenna application later, the proportion of power going into the surface wave (here the TEM mode) to the total power radiated. We thus define the ratio R as

$$R = \frac{P_o}{P_o + \sum_n P_n' + \sum_n P_n''} \quad (9.7)$$

where P_o is the power in the TEM ($n=0$) mode, and P_n' and P_n'' are the powers carried by the n th TE and TM modes, respectively, where these various modes propagate at various angles in the parallel-plate region, the angles changing as the frequency or the plate height H changes.

The variations of ratio R with normalized plate height H/λ_0 for three different frequencies are presented in Figs. 9.4 to 9.6. The frequency of 8.2 GHz for Fig. 9.4 is the one closest to the onset of leakage. We note that for small values of H/λ_0 the ratio $R=1$, indicating that only the TEM mode is above cutoff. As H/λ_0 increases, we observe first a very sharp drop and then a recovery to a much smaller value since now the $n=1$ modes share the total power. This behavior continues in characteristic fashion as H/λ_0 increases further. For the curves in Figs. 9.5 and 9.6, corresponding to lower values of frequency, we see that the range over which only the TEM mode is present becomes greatly reduced, and that the value of the ratio R becomes very small when H/λ_0 becomes large. The latter feature is especially pronounced in Fig. 9.6, where a dashed line is introduced to represent the average behavior of the curve since

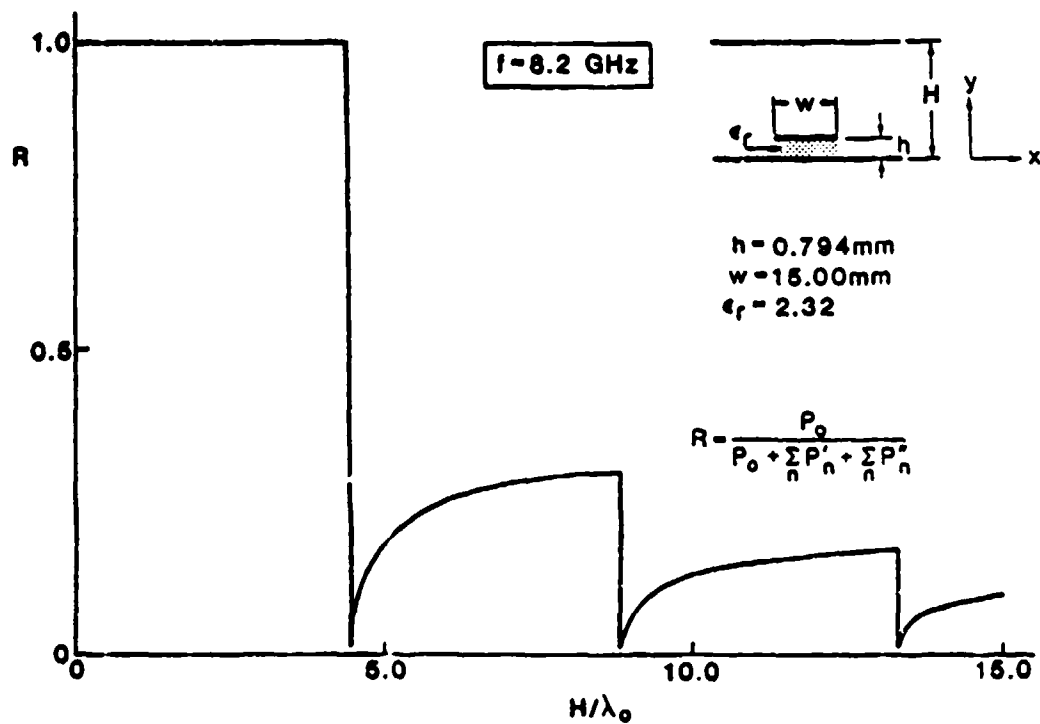


Fig. 9.4

The ratio R of the power radiated into the lowest mode to the total power radiated into all the propagating modes in the external parallel plate guide as a function of the height H of the metal top cover (see inset). For frequency $f = 8.20 \text{ GHz}$, near to the onset of leakage.

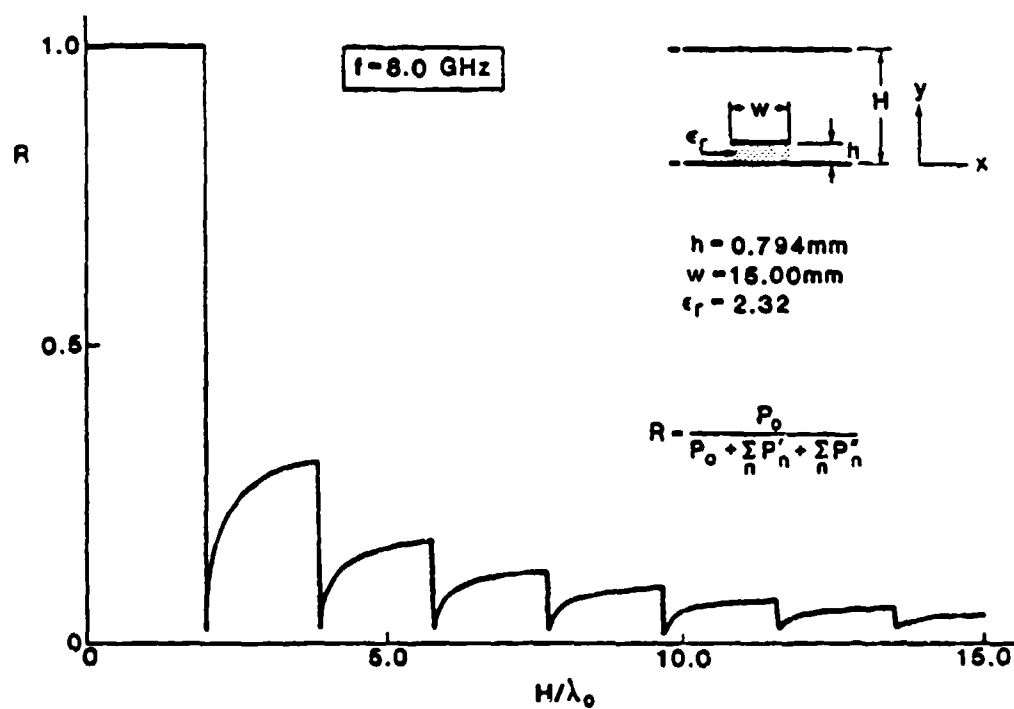


Fig. 9.5 Same as Fig. 9.4 except that frequency $f = 8.00$ GHz.

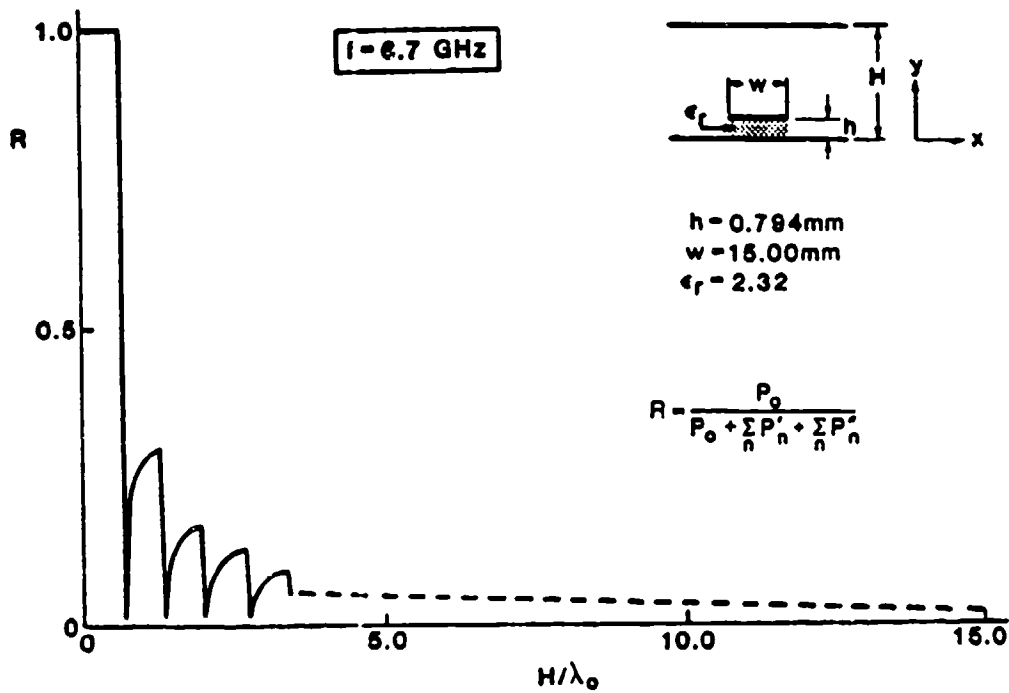


Fig. 9.6

Same as Fig. 9.4 except that frequency $f = 6.70$ GHz, the operating frequency that Menzel [27] employed for his antenna. The dimensions in the inset correspond to those of his antenna.

the sharp variations then become individually small and very close together. At a value of H/λ_o of 15 or so, for this case, we see that the ratio R is only about 0.02, signifying that *very little* of the radiated power actually ends up in the lowest mode when the top cover height is electrically large. This result is very encouraging for antenna applications, where one wants as much power as possible to go into the space wave.

The *extremely sharp dip* that is seen in Figs. 9.4 to 9.6 at the value of H/λ_o at which the next higher mode begins to propagate deserves further examination. Since $P_n = Y_n |V_n|^2$ for any given mode, we may rewrite (9.7) in these terms. The mode voltages V_n are excited by the electric field in the vertical plane defined by the side of the strip region, and are different for each mode. The characteristic admittances Y_n could be phrased either in terms of TE and TM modes propagating at an angle or as H-type and E-type modes propagating in the x direction. It is more direct to use the H-type (LSE) and E-type (LSM) modes, for which ([33] or [14])

$$Y_n' = \frac{(k_{ppn}')^2}{\omega \mu_o k_{xn}'} \quad (9.8)$$

$$Y_n'' = \frac{\omega \epsilon_o k_{xn}''}{(k_{ppn}'')^2} \quad (9.9)$$

where k_{ppn} is the propagation wavenumber of the n th parallel-plate mode in some direction θ_n , and k_{xn} is the component of that mode in the x direction, perpendicular to the strip axial direction.

Relation (9.7) for R is then rewritten as

$$R = \frac{Y_o |V_o|^2}{Y_o |V_o|^2 + \sum_n Y_n' |V_n'|^2 + \sum_n Y_n'' |V_n''|^2} \quad (9.10)$$

or

$$R = \frac{1}{1 + \sum_i \frac{Y_n'}{Y_o} \left| \frac{V_n'}{V_o} \right|^2 + \sum_n \frac{Y_n''}{Y_o} \left| \frac{V_n''}{V_o} \right|^2} \quad (9.11)$$

The forms of Y_n' and Y_n'' are given by (9.8) and (9.9); we see from (9.8), for H-type (LSE) modes, that when $k_{xn}' \rightarrow 0$, $Y_n' \rightarrow \infty$, corresponding to the condition for cutoff of that mode. Thus, as that mode just begins to propagate, the term corresponding to it in the denominator of (9.11) then greatly exceeds all the others, and $R \rightarrow 0$ as a result. The effect should be very sharp, and it should therefore result in a strong deformation of a curve of R vs. H/λ_o . The question as to whether R actually goes to zero at that point is still open, however, since V_n may simultaneously go to zero. One cannot be sure from the numerical solutions, and we have not checked this point analytically.

Finally, we wish to find at what values of H/λ_o the ratio R approaches zero. For any given mode, the sum-of-squares relation becomes

$$1 = \left(\frac{k_{xn}}{k_o} \right)^2 + \left(\frac{k_{yn}}{k_o} \right)^2 + \left(\frac{\beta}{k_o} \right)^2 \quad (9.12)$$

where

$$\frac{k_{yn}}{k_o} = \frac{n}{2H/\lambda_o} \quad (9.13)$$

and $\beta_n = \beta$ for all the parallel-plate modes since the whole guided mode moves in the z direction with phase constant β . Relation (9.12) thus becomes

$$1 = \left(\frac{k_{xn}}{k_o} \right)^2 + \left(\frac{n}{2H/\lambda_o} \right)^2 + \left(\frac{\beta}{k_o} \right)^2 \quad (9.14)$$

For Y_n' to become infinite, we must set $k_{xn}'/k_o = 0$, so that (9.14) yields

$$\frac{H}{\lambda_o} = \frac{n/2}{[1 - (\beta/k_o)^2]^{1/2}} \quad (9.15)$$

The sharp dips in the curves in Figs. 9.4 to 9.6 are found to occur exactly in accord with condition (9.15).

C. ANALYSIS AND PROPERTIES OF THE LEAKY MODES

1. Derivation of Accurate Expression for the Propagation Characteristics

H. Ermert [25] has performed a careful mode-matching analysis for the propagation characteristics of higher modes on microstrip line, but two limitations exist with respect to his solution. The first is that he obtains only *real* solutions, so that he provides no information with respect to the leaky wave range, which requires complex solutions. The second is that his microstrip line structure has a *top cover* with a height only five or so times the substrate thickness, so that even if he had furnished leaky mode numerical values they would not be directly applicable to antenna problems.

J. Boukamp and R.H. Jansen [28] do present *complex* solutions valid for the leaky wave region of the first higher mode, but their structure also has a top cover that permits *only the surface wave* to propagate in the region away from the strip. Their radiated power therefore occurs *only* in surface wave form, whereas we showed in the previous section that in an antenna application very little of the radiated power appears in that form since almost all of it goes into the space wave. Since the Boukamp-Jansen results are not directly applicable, we felt it was necessary to derive a reasonably accurate result for such leaky waves when there is *no top cover* present. We present such a derivation below in this section, but a little later we compare numerical values obtained from it with the values given by Boukamp and Jansen, and we note the differences that arise when a top cover is present or absent.

The cross section of microstrip line is shown again in Fig. 9.7, where the mid-plane is seen to be an electric wall, or short circuit, in agreement with the electric field lines indicated in Fig. 9.1. We also draw attention to the vertical plane T, located at the side (or edge) of the metal strip. The width w of the strip is also much wider than typical values for dominant mode use. Below the cross section in Fig. 9.7, we have a transverse equivalent network, representing the bisected structure, consisting of a transmission line of length equal to $w/2$, the half-width of the strip, with a short circuit on one side corresponding to the electric wall mid-plane, and a terminating admittance on the other. The transmission line represents the dielectric-filled parallel-plane region under the metal strip; the only mode that can propagate there is the TEM mode at an angle. The only element still needing characterization is the admittance element Y_t evaluated at reference plane T. A transverse resonance of this network would then yield the transverse wavenumber k_{xe} , which is related to the desired longitudinal propagation wavenumber $k_z = \beta - j\alpha$ by

$$k_z^2 = k_o^2 \epsilon_r - k_x^2 \quad (9.16)$$

The propagation of the guided first higher microstrip mode can, of course, be viewed in terms of this TEM mode under the strip bouncing back and forth at an angle between the two sides of the strip. In the frequency range corresponding to *real* values of k_z (see Fig. 9.2), total reflection occurs at each bounce, and the reflection coefficient Γ at the strip side has magnitude unity. As the frequency is reduced, the angle of the bounce gets closer to the normal. In the *leaky wave* region (the lined region in Fig. 9.2), this angle is no longer beyond the total reflection value, and $|\Gamma| < 1$, where Γ is the reflection coefficient at T for the TEM wave incident at an angle on the strip side, the geometry for which is shown in Fig. 9.3.

We therefore need an expression for either the output admittance Y_l or the reflection coefficient Γ at the strip side (they are simply related, of course). It turns out that a rigorous solution for Γ for the structure in Fig. 9.8 has been provided by D.C. Chang and E.F. Kuester [34]. Their solution is based on a Wiener-Hopf approach, but unfortunately it is difficult to extract a useful analytical form from this paper. In a later paper, however, E.F. Kuester, R.T. Johnk and D.C. Chang [35] present a simpler formulation valid for electrically thin substrates ($k_o h \sqrt{\epsilon_r} < 1$), which corresponds to our needs. They give numerical comparisons for several cases between their approximate simpler solution and their rigorous one, and they show that their approximate expression is very good under the thin-substrate condition. We therefore employ their approximate formulation, which they phrase in the form

$$\Gamma = e^{j\chi} \quad (9.17)$$

which is most directly useful when total reflection occurs, since χ is then real. When $|\Gamma| < 1$, corresponding to the leakage range, χ becomes complex.

The expression for χ under the thin-substrate approximation is given in reference [35] as Eqs. (13) to (16), together with Eqs. (7) and (9). Their notation is quite different from ours, and the following correspondences apply:

$$n = \sqrt{\epsilon_r}, \alpha = k_z/k_o, d = h, [n^2 - \alpha^2]^{1/2} = k_{xs}/k_o \quad (9.18)$$

$$[1 - \alpha^2]^{1/2} = k_x/k_o, [\alpha^2 - 1]^{1/2} = jk_x/k_o \quad (9.19)$$

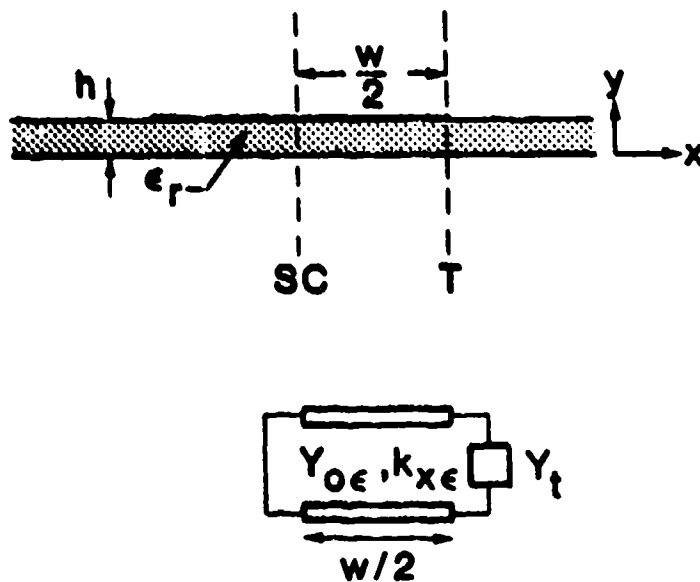


Fig. 9.7 Cross-section of microstrip line operated in its first higher mode, so that the strip is wider than usual and the mid-plane has short-circuit symmetry. Below it we have the transverse equivalent network for the structure, where terminating admittance Y_t is located at reference plane T .

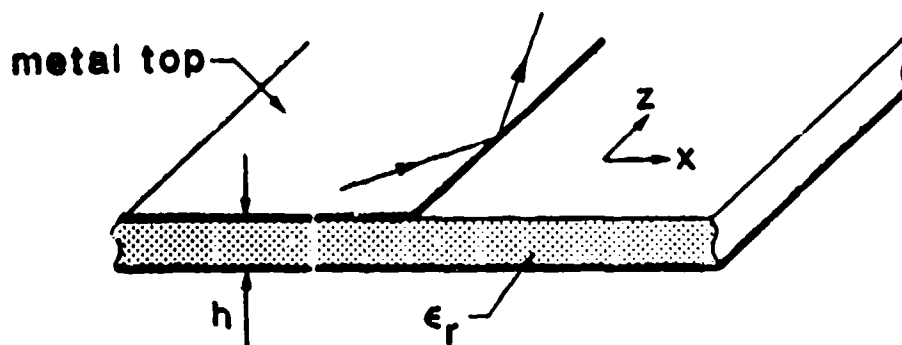


Fig. 9.8 Geometry of side of strip in microstrip line when isolated from the other side. This is the structure for which Γ is derived in reference [35], but the notation and coordinate system used in our equations are those indicated here.

For total reflection, $k_x = -j |k_x|$, so that then

$$[\alpha^2 - 1]^{1/2} = |k_x| / k_o \quad (9.20)$$

When our notation is employed in their equations, the expression for χ actually looks a bit simpler, and becomes

$$\chi = 2 \tan^{-1} \left[\frac{k_z}{k_{x\epsilon}} \tanh \Delta \right] - f_\epsilon(-k_{x\epsilon}/k_o) \quad (9.21)$$

with

$$\Delta = \frac{k_z h}{\pi} \left\{ \left(\frac{1}{\epsilon_r} - 1 \right) \left[\ln(jk_x h) + \gamma - 1 \right] + 2Q_o(-\delta_\epsilon) - 2Q_o(\delta_\mu) \right\} \quad (9.22)$$

$$f_\epsilon(-k_{x\epsilon}/k_o) = -\frac{2k_{x\epsilon} h}{\pi} \left\{ \frac{1}{\epsilon_r} \left[\ln(jk_x h) + \gamma - 1 \right] - 2Q_o(-\delta_\epsilon) - \ln 2\pi \right\} \quad (9.23)$$

where

$$\delta_\epsilon = \frac{\epsilon_r - 1}{\epsilon_r + 1}, \quad \delta_\mu = \frac{\mu_r - 1}{\mu_r + 1} = 0 \quad (9.24)$$

$$Q_o(z) = \sum_{m=1}^{\infty} z^m \ln m, \quad |z| < 1 \quad (9.25)$$

$$Q_o(0) = 0, \quad \gamma = 0.5772$$

We find that for $\epsilon_r = 9.70$, $Q_o = 0.175$, while for $\epsilon_r = 2.32$, $Q_o = 0.064$.

Expressions (9.17) and (9.21) through (9.25) provide only the reflection coefficient at the side of the strip; this reflection coefficient is simply an element in the transverse

equivalent network shown in Fig. 9.7, and it must be utilized in the transverse resonance condition. If we wish to employ the admittance form of this condition, we recall that

$$\frac{Y_t}{Y_{os}} = \frac{1 - \Gamma}{1 + \Gamma} = -j \tan \frac{\chi}{2} \quad (9.26)$$

using (9.17). For the short-circuit bisection of the structure shown in Fig. 9.7, corresponding to the first higher mode and other odd-numbered higher modes of microstrip line, the transverse resonance condition

$$\bar{Y}(T) + \bar{Y}(T) = 0 \quad (9.27)$$

in admittance form yields

$$\cot k_{xs} \frac{w}{2} + \tan \frac{\chi}{2} = 0 \quad (9.28)$$

For the even-numbered modes, for which the mid-plane is a magnetic wall or open circuit, relation (9.27) yields

$$\tan k_{xs} \frac{w}{2} - \tan \frac{\chi}{2} = 0 \quad (9.29)$$

The complex phase term χ is of course given by (9.21) and the equations following it; the final desired longitudinal wavenumber $k_z (= \beta - j\alpha)$ is obtained by using (9.28) or (9.29) together with (9.16).

Although expressions (9.28) and (9.29) are simple enough, even simpler transverse resonance relations are obtained by using the reflection coefficient form of the transverse resonance condition

$$\bar{\Gamma}(T) \bar{\Gamma}(T) = 1 \quad (9.30)$$

When the mid-plane is a short circuit, Γ at the mid-plane is -1, and

$$\bar{\Gamma}(T) = -e^{-j2k_{xs} w/2} \quad (9.31)$$

Since $\tilde{\Gamma}(T)$ is given by (9.17), we find on use of (9.30) that

$$e^{j(\chi - k_{xe}w)} = -1 = e^{\pm jn\pi}, \quad n \text{ odd} \quad (9.32)$$

or

$$\chi - k_{xe}w = \pm n\pi, \quad n \text{ odd} \quad (9.33)$$

When the mid-plane is an open circuit, Γ at the mid-plane becomes unity, and the relation corresponding to (9.33) is

$$\chi - k_{xe}w = \pm 2m\pi, \quad m \text{ integer} \quad (9.34)$$

Of course, (9.33) and (9.34) can be combined as

$$\chi - k_{xe}w = \pm n\pi, \quad n = 0, 1, 2, \dots \quad (9.35)$$

where $n=0$ yields the dominant (quasi-TEM) mode, $n=1$ produces the first higher mode, which is our primary interest, and the higher even and odd values of n correspond to higher modes with open-circuit and short-circuit mid-planes, respectively.

Some additional considerations are required before computations can progress for complex values of k_z . The quantities k_{xe} and k_x occurring in (9.21) to (9.23) and in (9.35) involve square roots in their relation to k_z , as seen in (9.18) and (9.19). It is necessary to select the proper signs of these square roots so that our solutions appear on the proper sides of the branch cuts associated with these square roots. In reference [35] the authors considered all wavenumber quantities to be either real or imaginary, so that the considerations mentioned above were simpler. Here, the wavenumbers in the leaky wave region are all complex.

The square roots involved are those indicated in (9.18) and (9.19) (it is seen that the last equation in (9.18) is the same as that in (9.16)). The sign of each square root must be taken consistent with the requirement that the guided mode field decay in the z (longitudinal) direction, and therefore increase transversely in the x direction, such that

$$k_z = \beta - j\alpha, \quad k_{xe} = k_{x\sigma} + jk_{xi}, \quad k_x = k_{x\sigma} + jk_{xi} \quad (9.36)$$

where all constituent quantities are positive real. The signs to be taken are already indicated in (9.18) and (9.19).

Lastly, we should appreciate that two types of *approximation* are present in this analysis of higher modes on microstrip line. The first one has already been mentioned; it is that expression (9.21) for χ is valid only for thin substrates, and is a simplification [35] of a rigorous (Wiener-Hopf) solution derived earlier [34]. The error introduced should be small, since our microstrip dielectric thicknesses h all satisfy the thin substrate condition.

The second type of approximation may be expressed as the neglect of interaction between opposite sides of the microstrip line. Our transverse equivalent network (Fig. 9.7) recognizes the symmetry present, and accurately represents it. The representation for the strip side, however, comes from a solution, (9.21), that corresponds to an isolated strip side, as shown in Fig. 9.8, with the other side infinitely far away. There can exist some field interaction between the two sides that is not taken into account in our analysis, but such interaction should be very small when the strip is reasonably wide, as it is for all the cases we consider.

It is believed that the analysis presented is accurate for the structures and the conditions considered here, and such belief is vindicated by the comparisons shown next with special cases in the literature where the results have been derived by different approaches.

2. Numerical Comparisons with the Literature

In order to check the accuracy of the analysis presented above, we have made numerical comparisons with two cases in the literature, the first for purely real solutions for the propagation wavenumber and the second for complex values. These two cases have already been mentioned at the beginning of subsection 1.

The case for which all the numerical values of the propagation wavenumber are *real* is the one by Ermert [25]. He computes numerical results for three modes: the dominant mode ($n=0$), and the first two higher modes ($n=1$ and 2), but only in the range for which the modes are purely bound. His analysis involves a mode-matching procedure in the horizontal direction, and it is therefore completely different from the one presented here. Furthermore, his structure is somewhat different; it has a metallic top cover whereas ours is completely open above.

A comparison between the wavenumber values computed by Ermert [25] and by us is presented in Fig. 9.9, where the solid lines represent our numerical values and the dashed lines those of Ermert. It is seen that the agreement between the two solutions is excellent for all three modes over most of the frequency range. A small discrepancy between the two solutions appears for each mode near the low frequency end for each of the modes. Such a discrepancy is to be expected since in those regions the vertical decay rate of the field is less, so that the effect of the top cover is more pronounced. We may therefore conclude that the difference between the two solutions is due to the presence of the top cover in Ermert's structure, and that the accuracies of both solutions are quite good.

The second comparison is made with the results presented by Boukamp and Jansen [28], which apply to the leakage range, where the wavenumbers are *complex*. They present results only for the first higher mode; their method of analysis is completely different from ours, being based on a spectral domain approach taken in the vertical direction; and their structure differs from ours in that they employ a metallic top cover, as does Ermert. We should therefore expect certain differences in our comparison, and indeed we find some.

The dispersion data are presented by Boukamp and Jansen in a different sort of plot, reproduced here as Fig. 9.10.

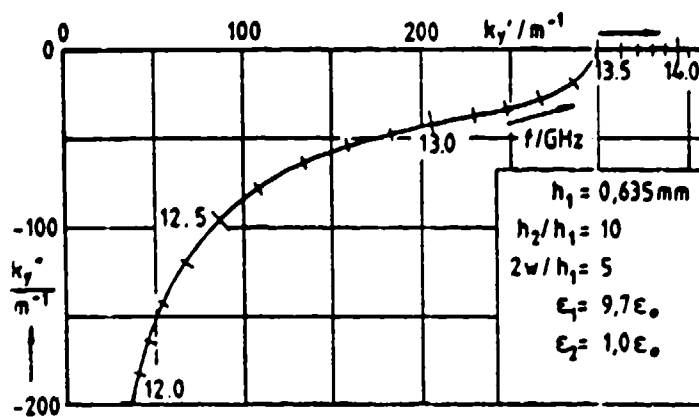


Fig. 9.10

Dispersion data computed by Boukamp and Jansen [28] for a covered microstrip line for the first higher mode in the range of *complex* values. The notation is different from ours; in particular k_y' and k_y'' are our β and $-\alpha$, respectively.

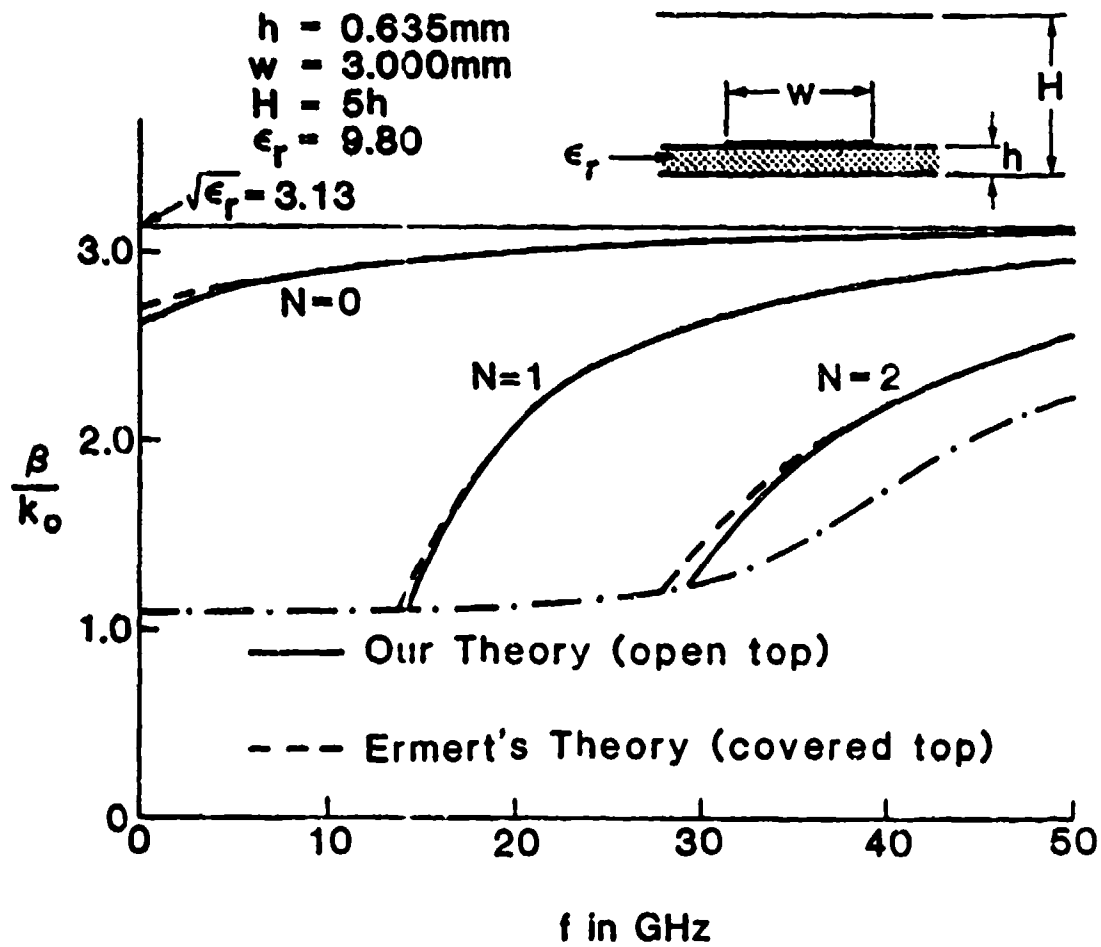


Fig. 9.9

Comparisons between *real* values of β/k_0 computed by us and by Ermer [25] for the lowest three modes of microstrip line. Ermer's structure has a metal covered top whereas ours is completely open above.

The wavenumber components k_y' and k_y'' are our β and $-\alpha$, respectively, their $2w$ is our strip width w , h_1 is our dielectric thickness h , and h_2 is the height of the top cover measured from the strip. The frequency is indicated as a parameter along the curve of k_y'' vs. k_y' . We have obtained their values of α and β as a function of frequency by interpolation from this plot.

Since k_z is now complex, comparisons are made for both α/k_o and β/k_o , and these comparisons appear in Fig. 9.11(a) and (b). The effect of a top cover is obviously more pronounced in the leakage range since the nature of the space wave is seriously modified by it. In fact, for the dimensions of the structure in Fig. 9.11, the top cover permits the presence of the surface wave only, whereas the leakage from our open-topped structure is due almost completely to a space wave, as shown in Sec. B.3. We should therefore expect significant differences between our solution (solid curves) and those of Boukamp and Jansen [28] (dashed curves).

We observe from Fig. 9.11(b) that in the neighborhood of the onset of leakage the values of β/k_o for the structure with a top cover are slightly higher than those for the completely open structure. That same behavior is seen in Fig. 9.9 for Ermert's structure as one approaches the onset of leakage. Also shown in Fig. 9.11(b) are the very slightly curved solid and dashed lines corresponding to $\beta/k_o = k_s/k_o$ for the open structure and for the one with the top cover, where k_s is the wavenumber of the surface wave in the outside region in each case. Those values are different for the two structures because the top cover increases the value of k_s . As explained in the discussion surrounding (9.3) in Sec. B.2, the leakage begins in the form of a surface wave when the β/k_o curve crosses the k_s/k_o dispersion curve corresponding to it. We may note that the onsets of leakage in Fig. 9.11(a) correspond to those crossings in Fig. 9.11(b), as they should. The space wave contribution to the leakage from the open structure begins at the frequency at which the β/k_o curve crosses the $\beta/k_o = 1$ line.

It is interesting to observe that despite the structural differences and the differences in the nature of the leakage, the basic curve shapes are very similar, and the onsets of leakage occur at almost the same frequency. Regarding the performance differences, some points have been noted above; another feature is that the top cover seems to enhance the leakage rate. It should also be observed that for both cases the leakage rate becomes large rather rapidly as the frequency is lowered.

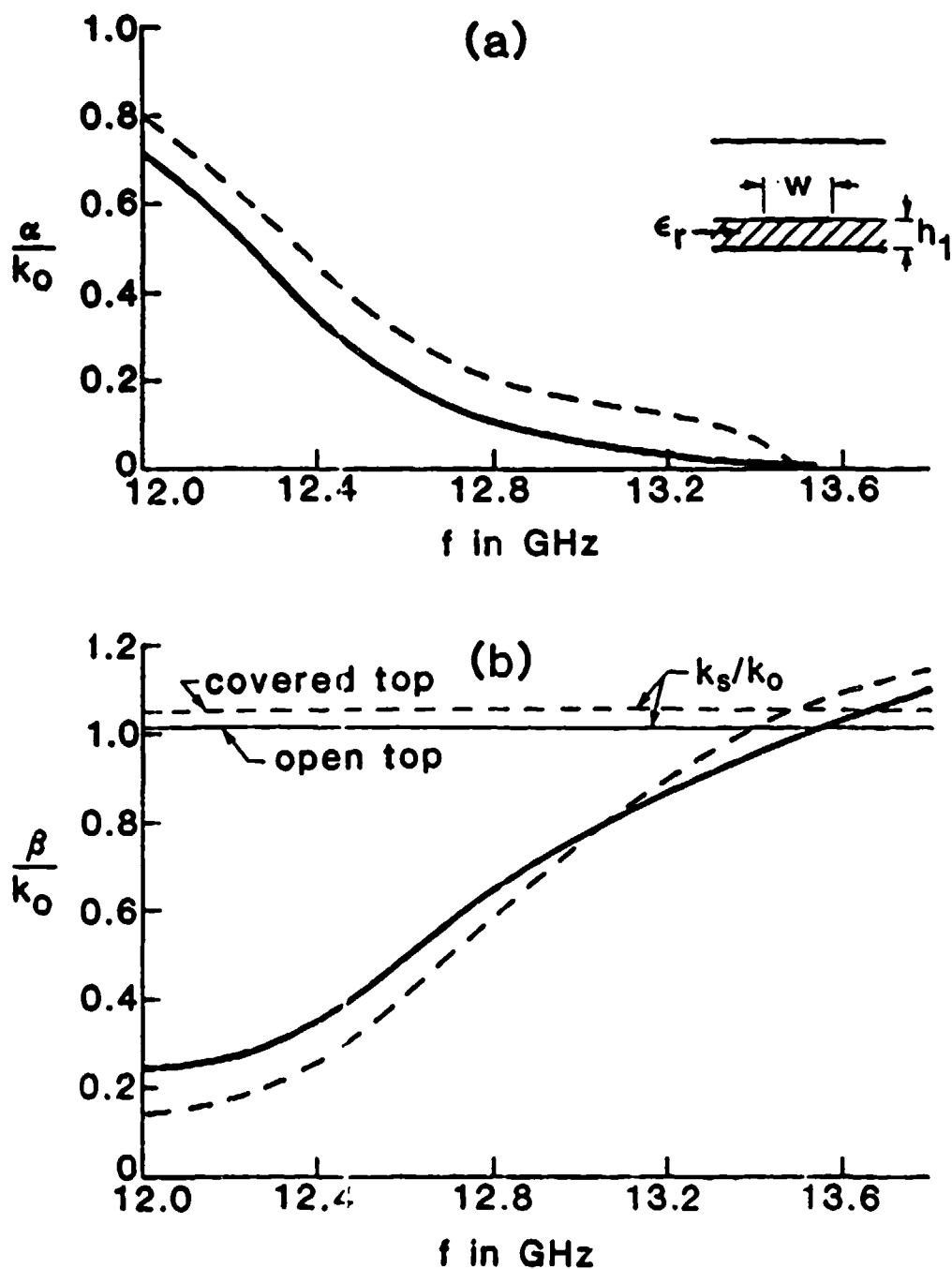


Fig. 9.11

Variation of leakage constant α/k_0 (figure (a)) and phase constant β/k_0 (figure (b)) with frequency for the first higher microstrip mode in its leakage range. The solid lines in both (a) and (b) represent our solution for an open microstrip line, and the dashed lines are the numbers presented by Boukamp and Jansen [28] for a line with a top cover of small height. The microstrip line dimensions are those given in reference [28]: dielectric layer thickness $h_1 = 0.635$ mm, strip width $= 5 h_1$, $\epsilon_r = 9.70$, and for the covered case, the height of the top cover $= 10 h_1$.

D. STEEPEST-DESCENT PLANE FORMULATIONS

1. Motivation

The two related reasons for undertaking an alternative representation of the field in terms of the steepest-descent plane are:

- (a) to assess whether or not the complex (leaky mode) solutions for microstrip line higher modes are physically realizable; and
- (b) to determine whether or not more than one such leaky mode can contribute physically to the field at the same time.

Solutions to the dispersion relation for a given structure may or may not be physically meaningful. We must examine whether or not that solution will contribute to the field of an arbitrary source placed in the neighborhood of that structure. Even a solution that satisfies all boundary conditions in addition to the field equations need not contribute directly to the actual field, and may therefore not be actually physically realizable. A well-known example is the Zenneck wave, which can at best contribute weakly to the total field only as a correction term, in the mathematical sense of a pole located close to a saddle point with the pole itself not contributing.

When the solution is a *leaky mode*, a further doubt is introduced because the leaky mode does not satisfy the boundary conditions at infinity in the cross-section. The solution thus implies that the field increases transversely away from the structure and diverges at infinity. This non-physical feature of the leaky wave solution disqualifies it from inclusion in a "proper" or "spectral" field representation, but the leaky wave can itself be physical because it exists only in a *restricted region of space* and never reaches infinity. These subtle features have historically been the subject of much confusion and speculation, but they have been explained in quite simple terms many years ago in various contexts [for example, 36-38]. The fact that leaky waves can indeed be physical and can indeed represent a physically realizable and practical portion of an antenna's near field is a well-known old story, but in each case one's intuition must be supplemented by a determination as to whether or not a particular leaky wave actually contributes to the field.

The usual field representations are the "proper" or "spectral" representations, consisting of all the discrete modes plus the continuous spectrum of an open structure. All of these modes are proper in the sense that, suitably defined, they satisfy all boundary conditions, including those at infinity for an open structure. Since leaky waves do not satisfy the boundary conditions at infinity, they are "improper" modes

and they are not included in a spectral representation.

On the other hand, leaky waves are included in a hidden way within the continuous spectrum of proper modes, and may in fact in many cases be viewed as a *highly convergent rephrasing* of this continuous spectrum. The continuous spectrum has rarely been found to be useful directly in practical problems, whereas leaky waves have been shown to be enormously practical both in the design of leaky-wave antennas and in the explanation of many physical phenomena, including Wood's anomalies on optical gratings [39], Cerenkov and Smith-Purcell radiation [40,41], radiation from plasma-sheathed reentry vehicles [42,43], blind spots in phased-array antennas [44], optical prism and grating couplers [45], and so on. Ermert [26] realized that leaky waves were included in the continuous spectrum description of his "radiation" region of microstrip higher modes, but he chose to describe that region only in spectral terms, and he rejected any further consideration of leaky modes, thereby neglecting the only practical way to evaluate explicitly the properties of the "radiation" field.

We stated above that leaky modes are contained within the continuous spectrum, but a rephrasing of the continuous spectrum in terms of leaky modes is most practical if the field in the "radiation" region can be represented essentially by only a *single* leaky mode. Although we may believe intuitively that this should be the case, the purpose of this section is to assess quantitatively the validity of this supposition.

In order to determine whether or not the leaky mode corresponding to the first higher mode on microstrip line contributed to the "radiation" region field, and also if other leaky modes may contribute at the same time, it is necessary to use a representation that is *not spectral*. The customary alternative representation for this purpose is the *steepest-descent representation*. It is simple in formulation, and it possesses many virtues. For example, the representation automatically has a polar form, with a saddle point given directly by the observation angle θ . Before we make use of the steepest-descent representation, we review some of its properties in the next subsection.

2. Review of Some Properties of the Steepest-Descent Representation

We are concerned with evaluating the field in the vertical plane above the center of the strip; that plane is the xz plane in Fig. 9.12, and it bisects the cross section. The field E at and above the interface ($y \geq 0$) is then given as

$$E(y, z) = \frac{1}{2\pi} \int_{-\infty}^{\infty} f(k_y) e^{ik_y y} e^{ik_z z} dk_z \quad (9.37)$$

when we adopt the time dependence $\exp(-i\omega t)$. This time dependence was selected in this section so that the more customary form for the steepest-descent plane can be employed; however, all relations here can be made consistent with the usual engineering choice ($\exp(j\omega t)$) for the time dependence, used everywhere else in this report, by simply replacing i by $-j$ wherever it appears.

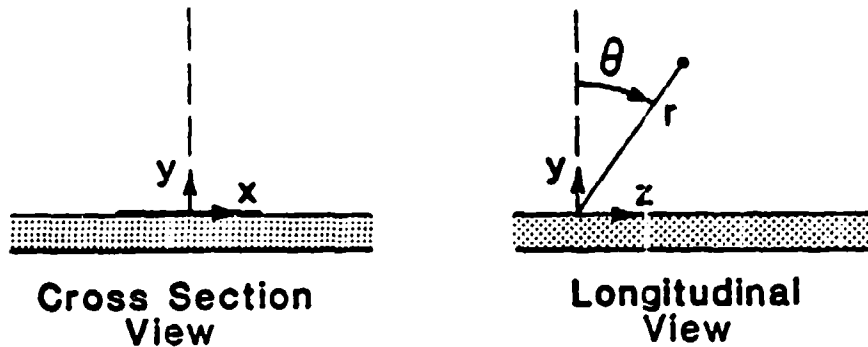


Fig. 9.12 Cross-section and longitudinal views of microstrip line, showing the coordinate system used.

The wavenumber variables k_y and k_z in (9.37) are evidently related to each other by

$$k_z = \pm (k_o^2 - k_y^2)^{1/2} \quad (9.38)$$

where k_o is the free-space wavenumber. The term $f(k_y)$ depends on the structure and the manner of excitation. Relation (9.37) expresses the field as a Fourier transform with respect to k_z , the integration being carried out along the real axis of the complex k_z plane. Physically, this representation is phrased in terms of *transmission* in the *transverse* (y) direction, with modes of the form $\exp(ik_z z)$. Thus,

this representation consists of a continuous spectrum with purely real eigenvalues varying between positive and negative infinity. Lastly, because of the open nature of the structure we must impose a radiation condition at infinity in the y direction as

$$\text{Im}(k_y) = k_{yi} > 0 \quad (9.39)$$

where Im means the "imaginary part of;" condition (9.39) thus implies that the waves are decaying properly in the cross section as $y \rightarrow \infty$.

Because of the square root in (9.38), the k_z plane contains two branch points and therefore consists of two Riemann sheets. It is convenient to choose the branch cuts so that those solutions satisfying (9.39) lie on the upper of the two Riemann sheets; the appropriate branch cuts are shown in Fig. 9.13, which presents the upper (or top) sheet of the k_z plane. The cuts, corresponding to $k_{yi} = 0$, and the locations of the branch points above and below the real k_z axis, are consistent with the consideration that the medium in space possesses infinitesimal losses, that is,

$$0 < \text{Im } k^2 \ll |k|^2 \quad (9.40)$$

The integration in (9.37) can then be carried out along the entire real k_z axis in the top sheet of the two-sheeted k_z plane.

The usual first approach to evaluating this integral is to deform the original path P of integration into the path P' along the semicircle at infinity, as shown in Fig. 9.13 for positive z ; for negative z , the semicircle would be in the lower half of the top sheet of the k_z plane. The semicircle at infinity contributes nothing to the integral; hence, by Cauchy's theorem for complex integration, the representation in (9.37) may be written as

$$E(y, z) = \frac{1}{2\pi} \left[\int_{-\infty}^{\infty} \left(f(k_y) e^{ik_y y} e^{ik_z z} \frac{dk_z}{dk_y} \right) dk_y + 2\pi i \sum \text{Residues} \right] \quad (9.41)$$

The integration in (9.41) is carried out along the entire real k_y axis, and it corresponds to a path around the branch cut in Fig. 9.13. The residue contributions may be present because of possible pole singularities which occur in the top sheet of the k_z plane.

The alternative representation effected by the path deformation and indicated in (9.41) corresponds to *transmission longitudinally* along the z direction, with modes defined in the plane transverse to z . The representation in (9.37) involved a

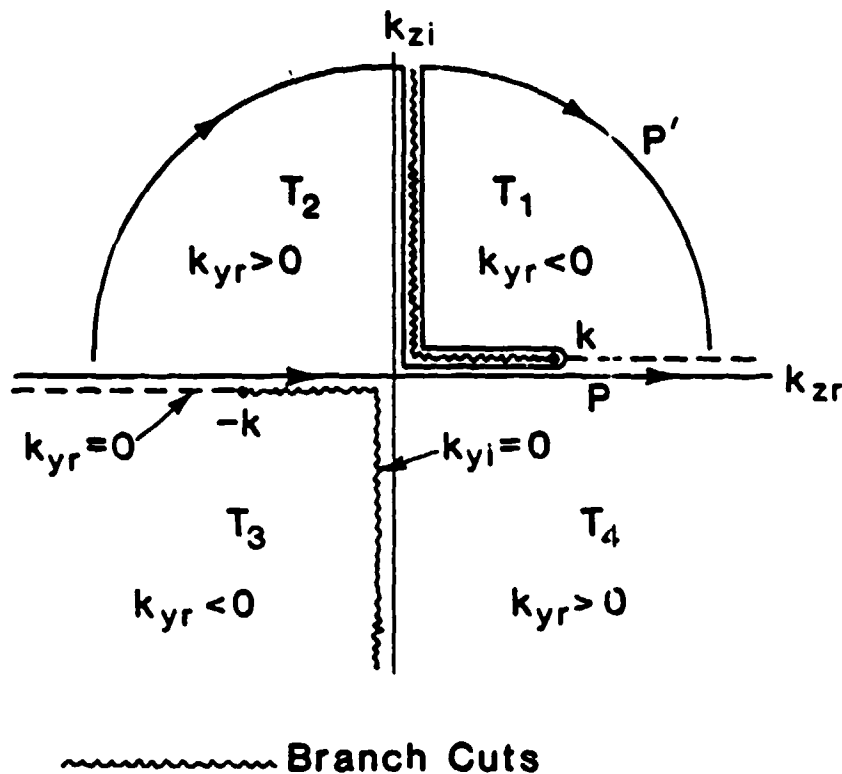


Fig. 9.13 Top Riemann sheet of the complex k_z plane, showing branch cuts and paths of integration.

continuous spectrum only, but the one in (9.41) is seen to comprise both a continuous spectrum and discrete modes, corresponding to the pole residues. These poles are classified as "proper" or "spectral" poles since their fields comply with radiation condition (9.39) and therefore decay at infinity. Such poles correspond to surface waves or proper complex waves. On the other hand, leaky-wave poles are located on the *bottom* sheet of the k_z plane and are never captured by the deformed path P' ; they therefore never contribute to a spectral representation, and are classified as improper, or non-spectral.

The continuous spectrum in (9.41) corresponds precisely to the continuous spectrum representation of Ermert [26] in his "radiation" region. Unfortunately, the

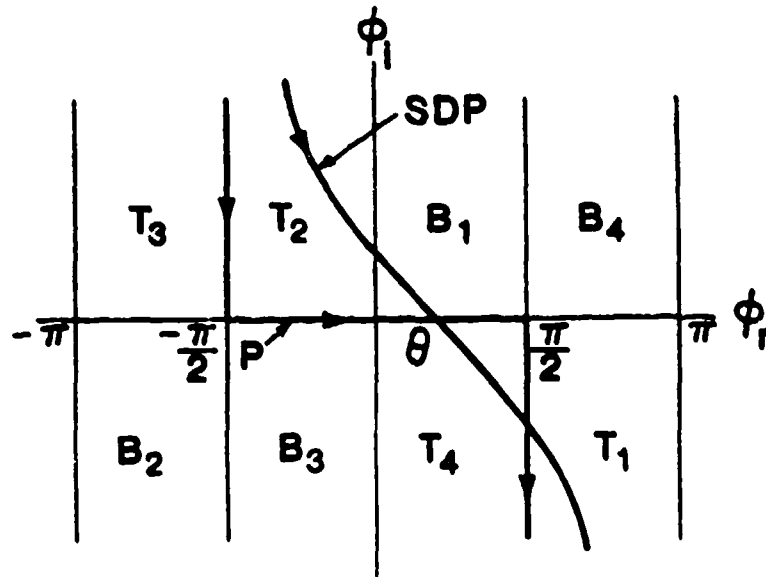


Fig. 9.14 The steepest-descent plane, showing the original path P and the steepest-descent path SDP. The semi-infinite strips marked T_1 through T_4 correspond to quadrants similarly labeled on the top surface of the k_z plane in Fig. 9.13; the ones marked B correspond to quadrants on the bottom Riemann sheet of the k_z plane.

integral in (9.41), corresponding to this continuous spectrum, is still very difficult to evaluate, and another method is often used. This other method employs a transformation to the *steepest-descent representation*.

For the steepest-descent representation, a transformation

$$k_x = k_0 \sin \phi, \quad k_y = k_0 \cos \phi \quad (9.42)$$

is employed, where $\phi = \phi_r + i\phi_i$ is the complex plane in which the steepest-descent integration is carried out. The transformations in (9.42) plot the entire two-sheeted k_z plane into a strip 2π wide in the ϕ plane, as shown in Fig. 9.14. It is noted that each of the eight quadrants in the k_z plane transforms into a semi-infinite strip in the ϕ plane identified as T (top) or B (bottom) and the quadrant number. The original path P, also shown in Fig. 9.14, is deformed into the steepest-descent path SDP which passes through the saddle point at $\phi = \theta$ and is defined by

$$\cos(\phi_r - \theta) \cosh \phi_i = 1 \quad (9.43)$$

The saddle point integration is straight-forward since simple recipes are available for it. We need not consider that integration procedure here except to point out some features concerning it. The result of that integration yields the asymptotic far field, valid only when r is large, in a direct polar form with the observation point represented by (r, θ) rather than (y, z) . Also, the saddle point is given directly by the angle of observation θ (As seen from Fig. 9.12, r and θ are respectively the radius vector and the polar angle of the field point in space.)

The saddle point integration is only a partial solution of the integral in (9.37), and it represents a contribution to the field that is called the "space wave." Additional discrete contributions may be present because of poles located between the original path P and the deformed path SDP in the ϕ plane. As seen from Fig. 9.14, these poles between the two paths will be captured independently of whether they lie on a strip marked T or B ; in other words, the poles will contribute to the field whether or not the poles are proper. Improper poles, such as leaky waves, which lie on the bottom sheet of the two-sheeted k_z plane, will contribute just as surely as proper poles, such as surface waves, as long as they are captured during the deformation between the two paths.

Whether or not a pole will be captured also depends on the angle of observation θ . As one scans the field from broadside to endfire as a function of θ , the steepest-descent path (SDP) moves parallel to itself from its intersection with $\phi_r = 0$ to its intersection with $\phi_r = \pi/2$. Thus, if one wishes to be sure that all possible poles will be captured, the SDP curve should intersect the ϕ_r line at $\pi/2$. Let us label that SDP curve as SDP^+ , and note from (9.43) that for $\theta = \pi/2$ the SDP^+ curve is defined by

$$\sin \phi_r \cosh \phi_i = 1 \quad (9.44)$$

Since our primary interest is in the *leaky wave poles*, the relevant steepest-descent plane is shown in Fig. 9.15, where a typical improper pole of this type is illustrated. The pole is seen to be located on strip $B1$, which corresponds to the "wrong" Riemann sheet of the k_z plane as regards the spectral solution. When the pole is located as shown, between the furthest steepest-descent path (SDP^+) and the original path (P), it is clearly captured, and it will contribute to the field. The condition for the leaky-wave pole to be captured is thus

$$\sin \phi_r \cosh \phi_i < 1 \quad (9.45)$$

making use of (9.44).

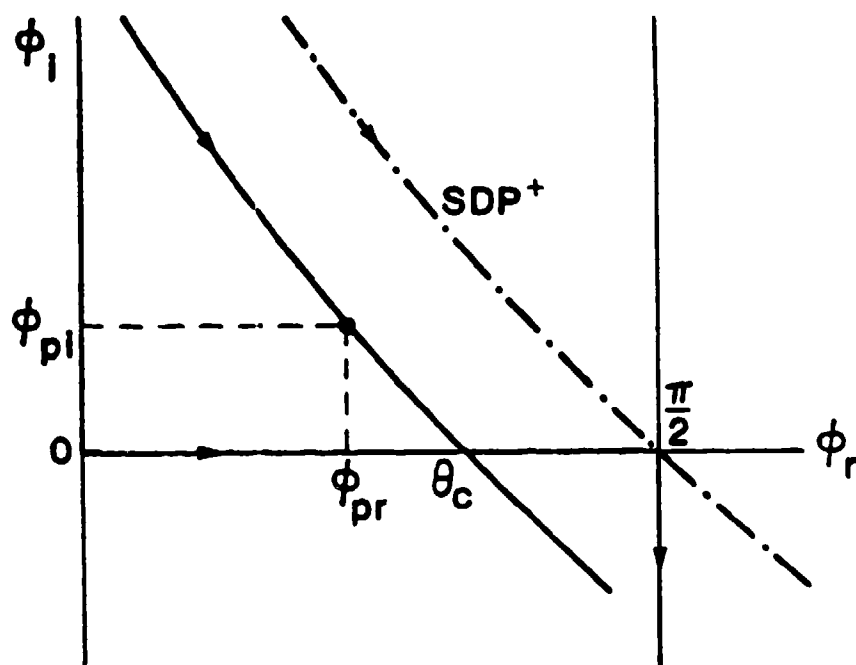


Fig. 9.15 Leaky-wave pole located on strip corresponding to improper solutions; also shown are the observation angle θ_c , and the furthest steepest-descent path, SDP^+ , indicating pole capture.

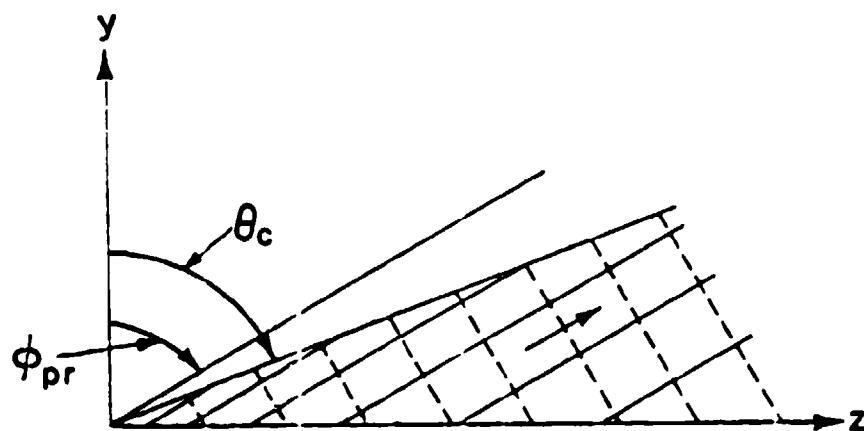


Fig. 9.16 Near field contours of a leaky-wave pole, where θ_c is the observation angle and ϕ_{pr} is the real part of the leaky-wave pole location. Within the wedge-shaped domain of validity, the solid lines represent equi-amplitude contours and the dashed lines signify equi-phase contours. The arrow represents the direction of power flow and increasing phase.

When the observation angle is θ_c , the SDP_c will go through the pole, as seen in Fig. 9.15. We note, however, that angle θ_c is always greater than the angle corresponding to ϕ_{pr} . This fact has important physical significance, as illustrated in Fig. 9.16, which presents some field characteristics associated with the leaky wave. The pole at ϕ_p contributes to the field when $\theta > \theta_c$, but is not included in the field for $\theta < \theta_c$. The region for which $\theta > \theta_c$ thus defines the *domain of validity* for the leaky wave; it is physically significant only in that region. As seen in Fig. 9.16, the field amplitude decays along z and is constant in the ϕ_{pr} direction, so that the amplitude must *decay in all directions* inside the domain of validity. Hence, the leaky wave field exists only in the *near field*, and it cannot contribute directly to the far field. The direction of power flow is also shown to occur in the ϕ_{pr} direction, however, so that the power in the leaky wave field continually moves out of the valid domain as the field amplitude decays, thereby transferring its power to the space wave in steady fashion.

Having discussed the physical meaning of the leaky wave, let us return to how one can locate the leaky-wave pole in the steepest-descent plane. Writing $k_z = \beta - j\alpha = \beta + i\alpha$, and $\phi = \phi_r + i\phi_i$, the first of the two relations in (9.42) becomes

$$\beta/k_o = \sin \phi_r \cosh \phi_i \quad (9.46)$$

$$\alpha/k_o = \cos \phi_r \sinh \phi_i \quad (9.47)$$

We thus can readily find α and β from the pole location, but an expression for the reverse is not easy to locate in the literature. After inverting (9.46) and (9.47), however, we can obtain ϕ_i and ϕ_r in terms of α/k_o and β/k_o by means of the following expressions:

$$\cosh^2 \phi_i = \gamma + \left[\gamma^2 - (\beta/k_o)^2 \right]^{1/2} \quad (9.48)$$

$$\sin^2 \phi_i = \gamma - \left[\gamma^2 - (\beta/k_o)^2 \right]^{1/2} \quad (9.49)$$

where γ is defined as

$$2\gamma = 1 + (\alpha/k_o)^2 + (\beta/k_o)^2 \quad (9.50)$$

These expressions were employed to obtain the various leaky-wave pole plots described in the next subsection.

The field at the interface (in our case, the field at the top surface of the strip, constituting an "aperture" field) due to a pole at $\phi_p = \phi_{pr} + i\phi_{pi}$ is of the form

$$e^{i\beta z} e^{-\alpha z}, \text{ for } z > 0 \quad (9.51)$$

where α and β are found from ϕ_p using (9.46) and (9.47). The terms β and α are respectively the phase and the leakage constants along the interface. For low decay rates, it is clear from (9.47) that either $\cos \phi_r$ or $\sinh \phi_i$ must be small; the corresponding poles must therefore be located close to either the $\phi_r = \pi/2$ axis or the $\phi_i = 0$ axis. If we set $k_o z = 1$ in the $\exp(-\alpha z)$ factor, we see that if

$$\left| \alpha/k_o \right| = \left| \cos \phi_{pr} \sinh \phi_{pi} \right| \geq 1 \quad (9.52)$$

the wave is very strongly attenuated, since the amplitude then decays by $1/e$ ($e = 2.718$) in a travel of approximately one-sixth of a wavelength. In Fig. 9.17, the region defined by (9.52) is shown *unlined*; if poles exist in this region, their contribution to the total field can usually be disregarded since these waves may be significant only within a very small region. Conversely, poles located in the *lined* region of Fig. 9.17 yield fields that are more slowly damped and therefore extend out for a larger distance. Contributions to the total field from these poles outside of the lined region are generally negligible compared to contributions from poles within the lined region.

3. Steepest-Descent Plane Plots for Microstrip Line Higher Modes

Using the steepest-descent plane, we next determine the locations of the microstrip-line higher-mode leaky-wave poles in this plane, to find out, first, whether or not these poles are captured and therefore contribute to the total field, and second, if more than one higher-mode pole may contribute at the same time. Before that, however, we must obtain the values of α/k_o and β/k_o over a much larger range of frequencies than we did in Sec. C. In that section, we computed the values for the first higher mode ($N=1$) only; here, we present results for the $N=2$ and $N=3$ higher modes as well.

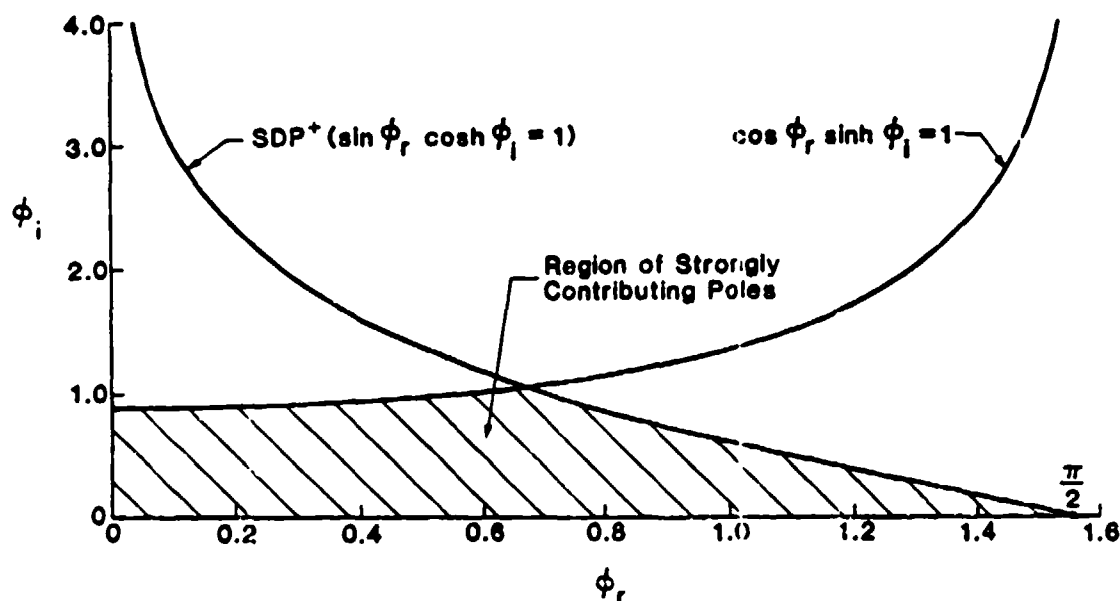


Fig. 9.17 Steepest-descent plane, showing the lined region within which leaky-wave poles contribute strongly to the aperture field.

Numerical results are presented below for three structures: (a) a microstrip line having the cross-section dimensions used by Boukamp and Jansen [28] but with an open top, (b) the actual Boukamp and Jansen structure with a covered top, and (c) the antenna structure described by Menzel [27], which of course has an open top. For cases (a) and (c), we have results for the first three higher modes; for case (b), only the first higher mode is treated, and the numerical values used for α/k_0 and β/k_0 are those computed by Boukamp and Jansen [28].

a. Microstrip Line with Open Top Using the Cross-Section Dimensions of Boukamp and Jansen

The microstrip line structure treated in this subsection has the cross-section dimensions of the line considered by Boukamp and Jansen [28], except for their top cover. We have removed their top cover so that the line is completely open above; as

a result, space wave radiation occurs when the frequency is lowered enough to cause β/k_0 to become less than unity (see Sec. B,2). The cross-section dimensions (see Fig. 9.1) are $h = 0.635$ mm, $w = 3.175$ mm, $\epsilon_r = 9.70$. The numerical values of α/k_0 and β/k_0 were computed using the theory described in Sec. C,1; in particular, condition (9.35) was employed together with (9.21) and its corollary relations.

In Sec. C,2 numerical values for α/k_0 and β/k_0 were presented for the first higher mode only, and also for a restricted frequency range, only that corresponding to small values of α/k_0 . Here we must consider a much wider frequency range, and we also present calculations for other higher modes. The first higher mode, which we label as the $N=1$ mode, possesses field symmetry corresponding to an electric wall at the vertical bisection plane ($x=0$). The next higher mode, designated the $N=2$ mode, has a magnetic wall at the bisection plane, as does the dominant mode, whereas the $N=3$ mode is the next higher mode with electric wall symmetry.

In Fig. 9.18, the values of α/k_0 are given as a function of frequency for the $N=2$ and $N=3$ higher modes. The onset of leakage for these modes occurs at much higher frequencies, of course, but one notes that the values of α/k_0 continue to increase monotonically as the frequency is lowered. The corresponding values of β/k_0 as a function of frequency are presented in Fig. 9.19. The behavior for frequencies just below the onset of leakage is similar to that found in Fig. 9.11(b) for the first higher ($N=1$) mode; i.e., the values of β/k_0 decrease as the frequency is lowered. When the frequency is reduced further, however, an interesting effect occurs: the values of β/k_0 reach a minimum and then slowly increase. For significantly lower frequencies, the β/k_0 values actually exceed unity, but it is to be noted that for those frequencies the values of α/k_0 are substantially larger than those of β/k_0 . The concept of "cutoff" for these higher modes requires some modification in the light of this behavior.

Figures 9.20 and 9.21 show how these values of α/k_0 and β/k_0 for higher modes $N=2$ and $N=3$ compare with those for the first higher mode ($N=1$) in the frequency range in which the $N=1$ mode is most important. One sees that the behavior for the $N=1$ mode is qualitatively similar to that for the other modes in Fig. 9.18 and 9.19, and that, although the values for the $N=2$ and $N=3$ modes are considerably higher than those for the $N=1$ mode, these other higher modes are still around and may therefore contribute to the total field.

The ways in which these higher modes may contribute to the total field are more clearly revealed by the use of the *steepest-descent plane*. Using the values of α/k_0 and

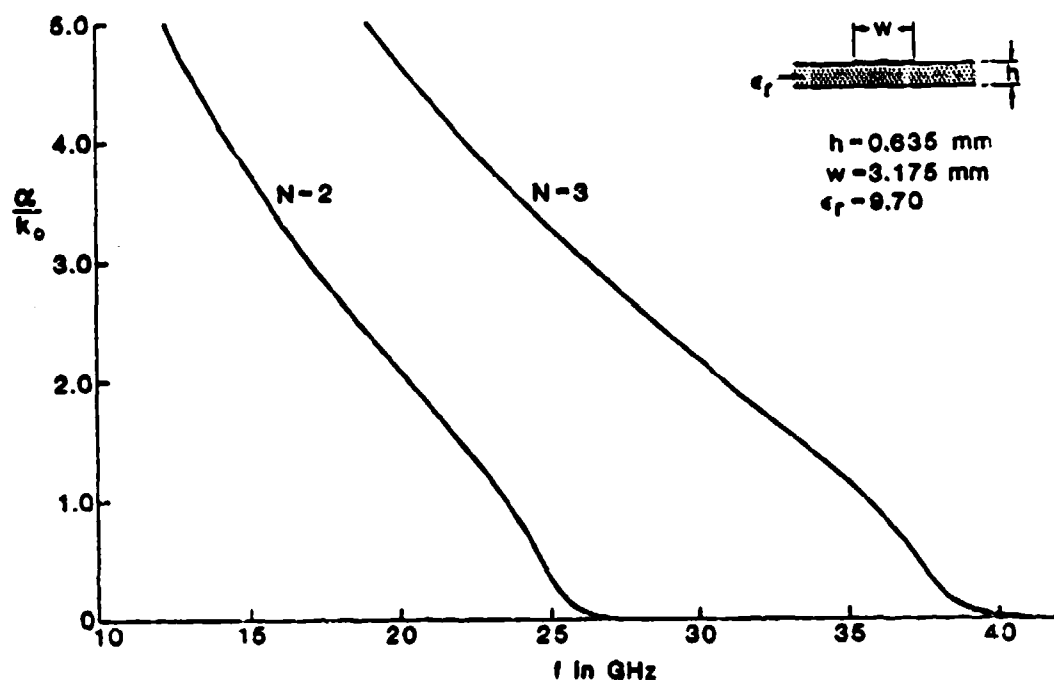


Fig. 9.18 The leakage constant α/k_0 for the $N = 2$ and $N = 3$ higher modes of open microstrip line as a function of frequency over a very wide frequency range.

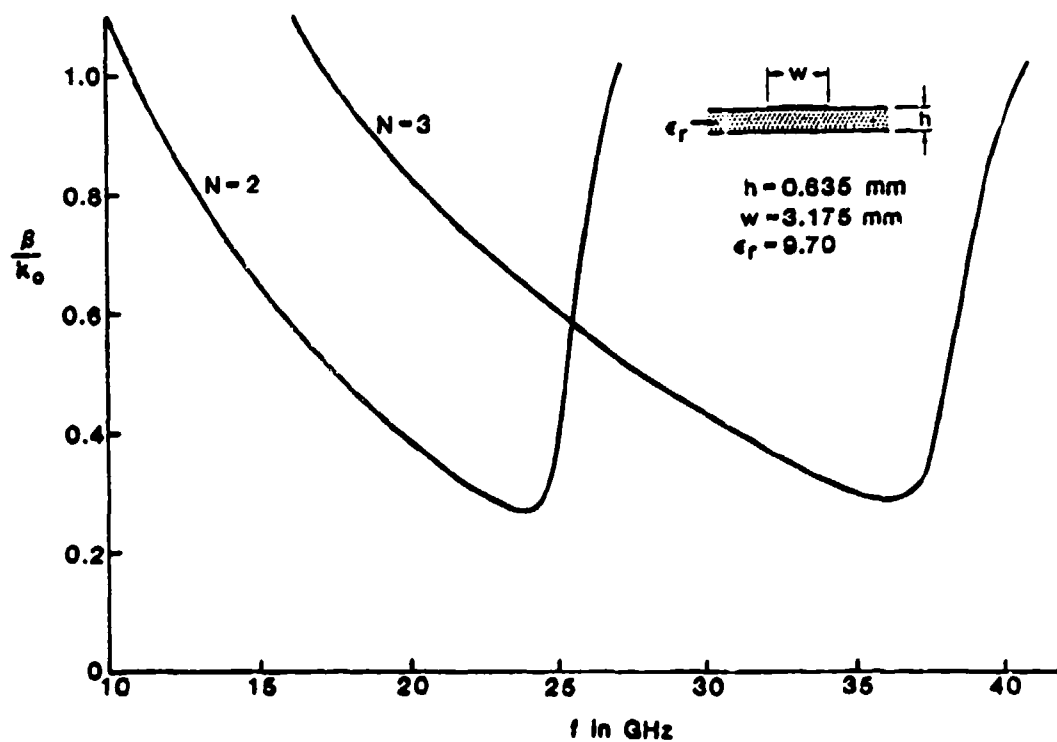


Fig. 9.19 The normalized phase constant β/k_0 for the $N = 2$ and $N = 3$ higher modes of open microstrip line as a function of frequency over a very wide frequency range.

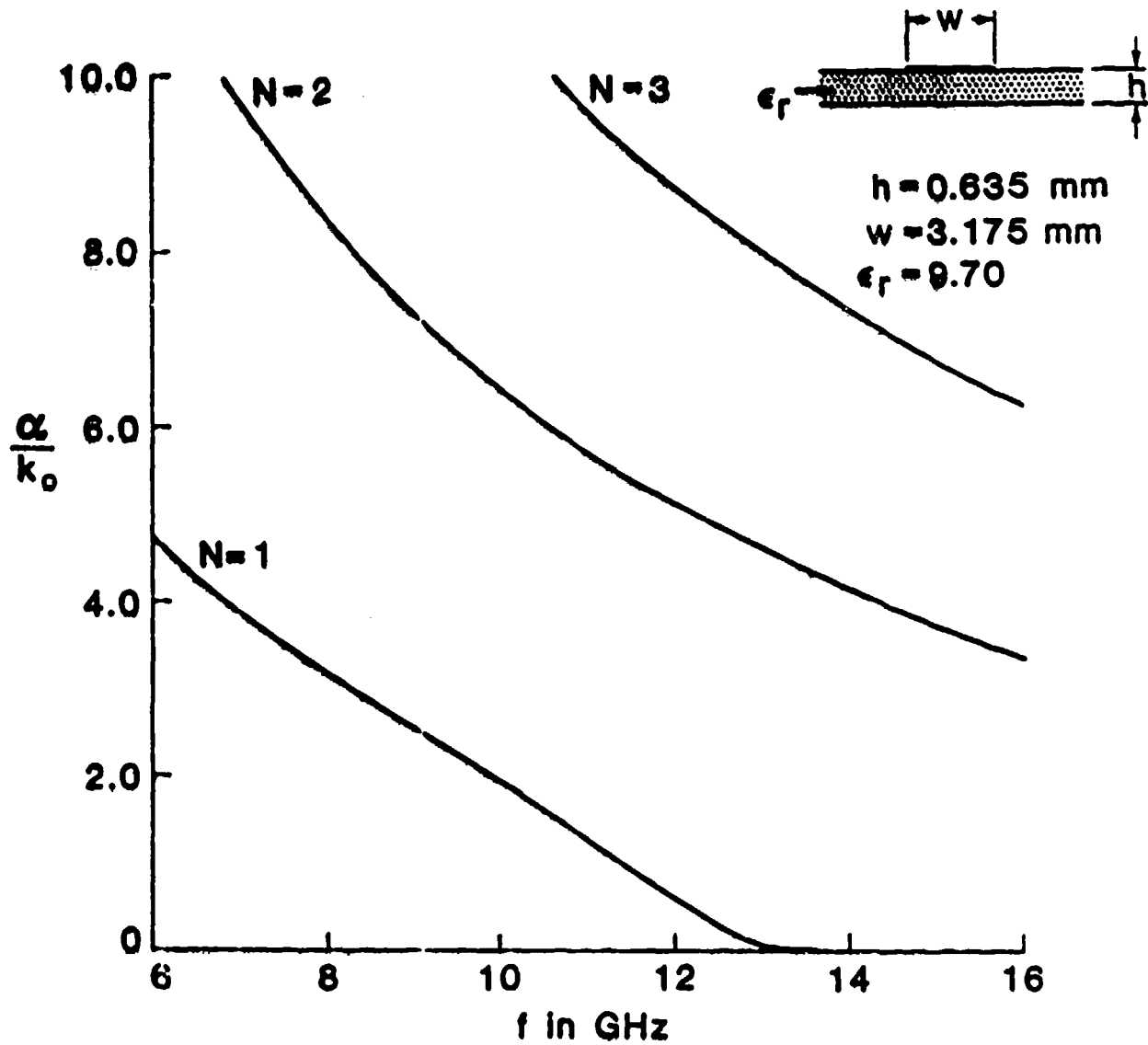


Fig. 9.20 Values of α/k_0 for the first three higher modes of open microstrip line in the frequency range over which the leaky $N = 1$ mode is most important.

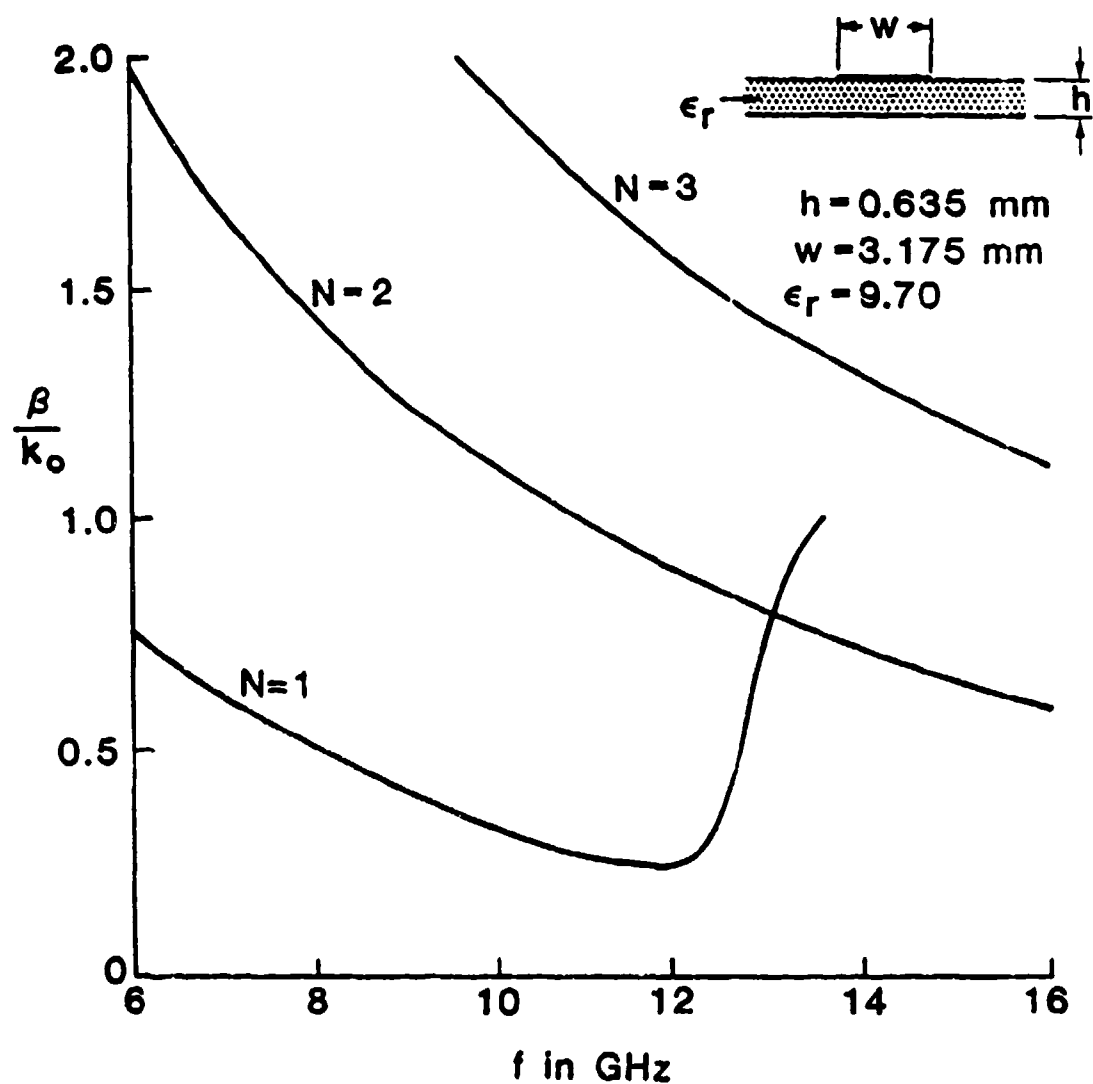


Fig. 9.21 Values of β/k_0 for the first three higher modes of open microstrip line in the frequency range over which the leaky $N = 1$ mode is most important.

β/k_o in Figs. 9.20 and 9.21, the pole locations ϕ_p for various frequencies were obtained on use of relations (9.48) through (9.50). The results for the *first* higher mode ($N=1$) are presented in Fig. 9.22. The pole locations are shown corresponding to a very wide frequency range, from 13.5 GHz down to 1.0 GHz, where the points are numbered to permit identification with the corresponding frequencies. We first note that most of the pole locations lie between the furthest steepest-descent path (SDP^+) and the original path P (see Fig. 9.15), so that those poles *are* captured. This plot therefore proves that when the higher modes possess complex wavenumbers those solutions correspond to leaky modes that are indeed *physically realizable* and that *do* contribute to the field.

We further see from Fig. 9.22 that for the lower frequencies the trajectory of pole locations rises steeply and becomes essentially vertical; this behavior is a consequence of α/k_o becoming much greater than β/k_o . For sufficiently low frequencies (here for $f < 5.0$ GHz), the poles lie on the other side of the SDP^+ curve, so that they are no longer captured and therefore cannot contribute to the field. Finally, by comparison with Fig. 9.17, we observe that for frequencies between about 11.5 GHz and 5.0 GHz, the pole locations lie outside of the lined region in Fig. 9.17. The leaky mode for this frequency range does contribute to the field, but corresponds to a very rapidly decaying wave (decaying by at least $1/e$ in a travel of about a sixth of a wavelength). As explained in subsection 2 above, contributions from these poles are generally negligible compared to those from the poles lying in the lined region of Fig. 9.17, which in Fig. 9.22 corresponds to the frequency range from about 11.5 GHz to about 13.5 GHz, near the onset of leakage for this mode.

We next consider the $N=2$ and $N=3$ *higher modes* to determine if they contribute in a significant manner to the field in the frequency range for which the $N=1$ higher mode is complex and important. The behaviors in the steepest-descent plane for those modes are presented in Figs. 9.23 and 9.24. Their pole locations are plotted for the same range of frequencies as that appearing in Fig. 9.22 for the $N=1$ mode, namely, from $f=13.5$ GHz down to 1.0 GHz. The first feature to note is that the poles already lie on an essentially vertical line in both plots, because the values of α/k_o (see Fig. 9.20) are all so high in this frequency range. The second principal feature is that for the $N=2$ higher mode *most* of the pole locations lie *above* the SDP^+ curve, and that for the $N=3$ higher mode *all* of them do. We therefore see that the $N=3$ *higher mode*, which is the next higher mode of the same symmetry as the first higher mode ($N=1$), *does not contribute at all to the field* in this frequency range.

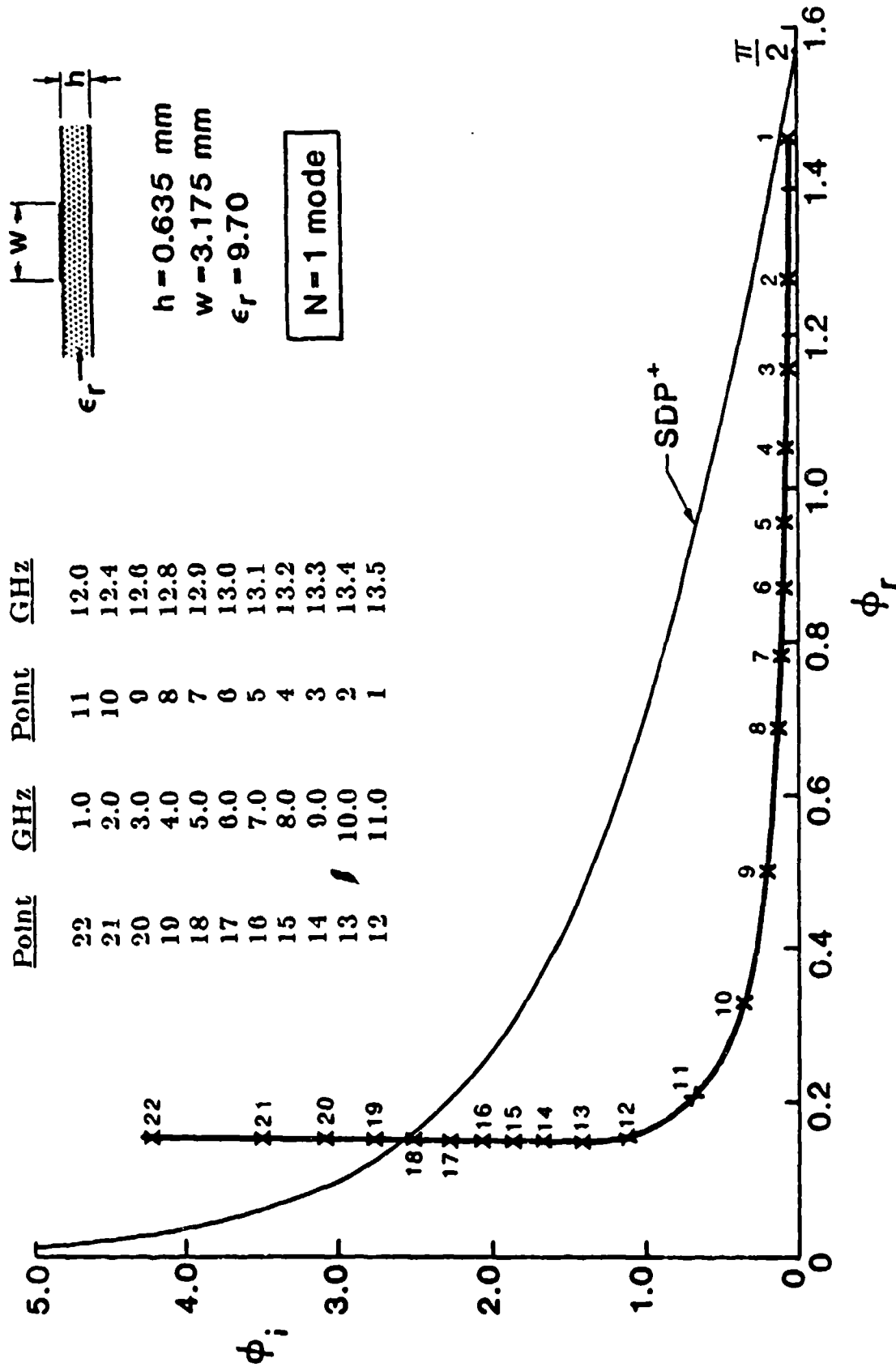


Fig. 9.22 Leaky-wave pole locations on the steepest-descent plane for the first higher mode ($N = 1$) over a very wide frequency range. Numbered points indicate the locations corresponding to the list of specific frequencies.

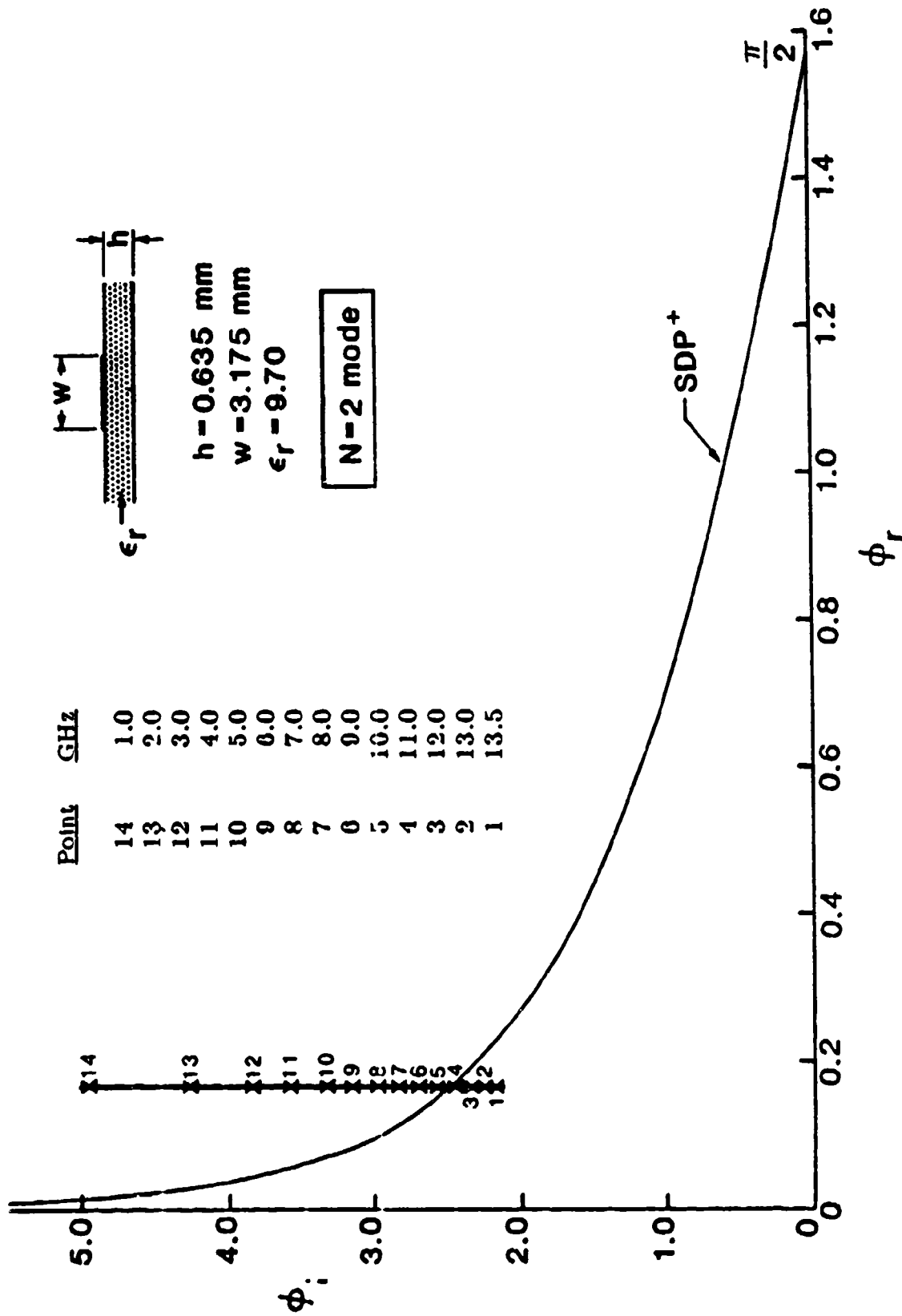


Fig. 9.23 Same as in Fig. 9.22, but for the $N = 2$ higher mode.

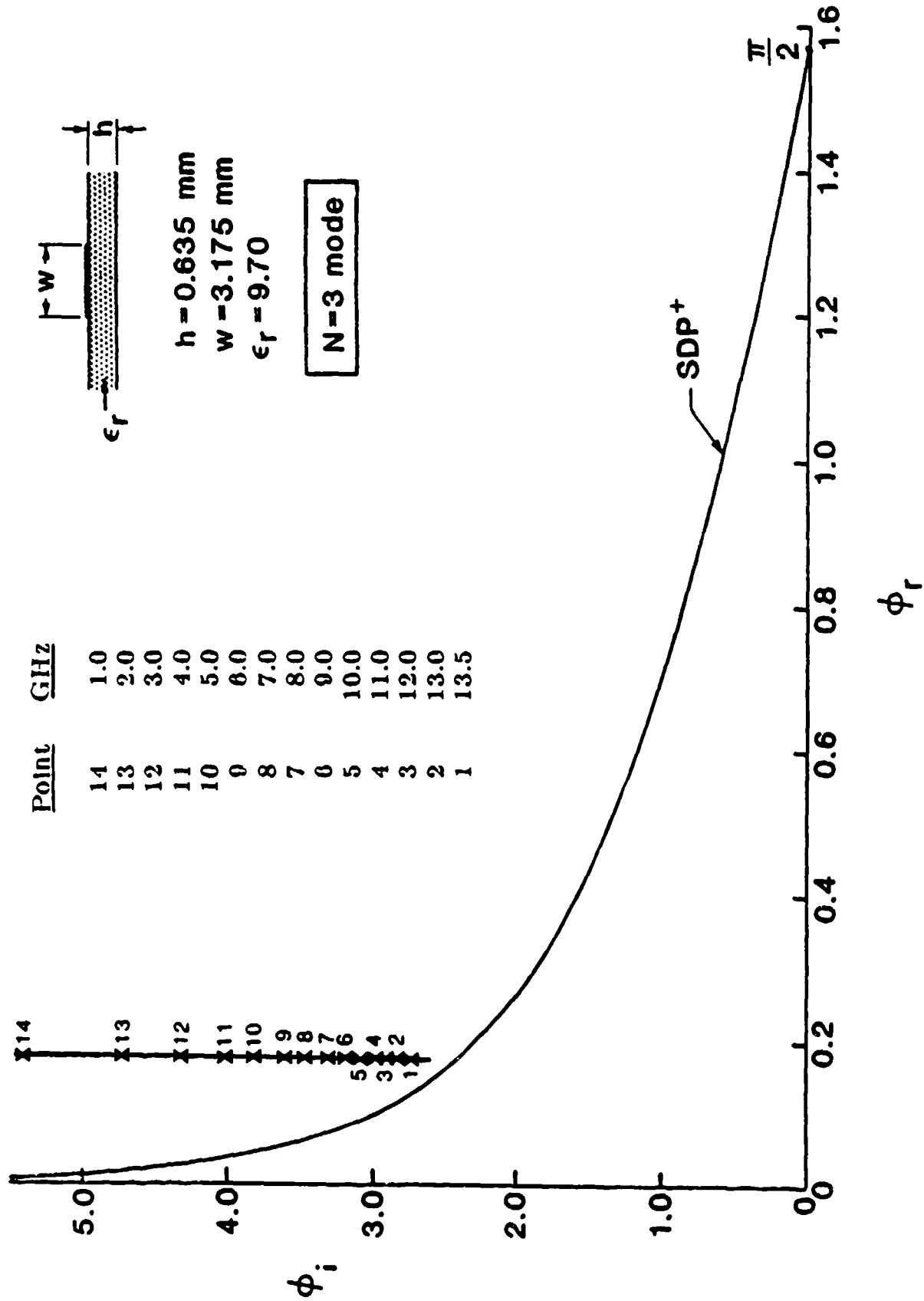


Fig. 9.24 Same as in Fig. 9.22, but for the $N = 3$ higher mode.

For the $N=2$ higher mode, we see that the pole is captured for some frequencies, but not for most. Even for those poles that *are* captured, however, corresponding to frequencies greater than 11.0 GHz, the poles for the $N=1$ mode occur much closer to the $\phi_i = 0$ axis. We thus find that the captured poles for the $N=2$ mode are located far away from the lined region in Fig. 9.17, so that they decay extremely rapidly and could contribute only over a very short distance. Compared to the $N=1$ values, therefore, they can clearly be neglected.

From the steepest-descent plots presented above, we *conclude* first that the leaky $N=1$ mode does indeed contribute to the field, and second that the other higher modes contribute negligibly, when they do at all. These were the two points we set out to determine in this section. It is therefore correct to assert, as we speculated earlier, that the "radiation" region may be represented in a highly convergent fashion by *essentially a single leaky mode*.

b. The Boukamp-Jansen Structure with a Covered Top

The structure treated in this subsection differs from that considered above only in that this one has a covered top whereas the one above has no top. The values of α/k_o and β/k_o for the structures with and without a top are only slightly different from each other, and comparisons between them were illustrated in Fig. 9.11. The *nature of the radiation* from each is quite different, however, since power leaks from the covered top structure in *surface wave* form only (when the dimensions are those chosen by Boukamp and Jansen [28]) whereas that from the open-topped structure is primarily in *space wave* form. This distinction becomes of vital importance when the steepest-descent plot is employed, especially near the onset of leakage.

When leakage occurs in *surface wave* form, the relevant plane is the xz plane, not the yz plane, as shown in Fig. 9.3 in Sec. B. A two-dimensional representation is still possible, however, when it is recognized that the equivalent of the free-space wavenumber is k_s , the surface-wave wavenumber. All expressions relating α and β to ϕ , such as (9.42), (9.46) through (9.50), and (9.52), must be appropriately modified; whenever k_o appears, it should be replaced by k_s .

With this simple but essential modification, the steepest-descent plane correctly reflects the onset of radiation and the separation between bound and leaky solutions. The steepest-descent representation for the $N=1$ (first higher) mode on the Boukamp-Jansen structure with a covered top is presented in Fig. 9.25. All of the numerical data for α and β came from their paper [28], but we transformed these data

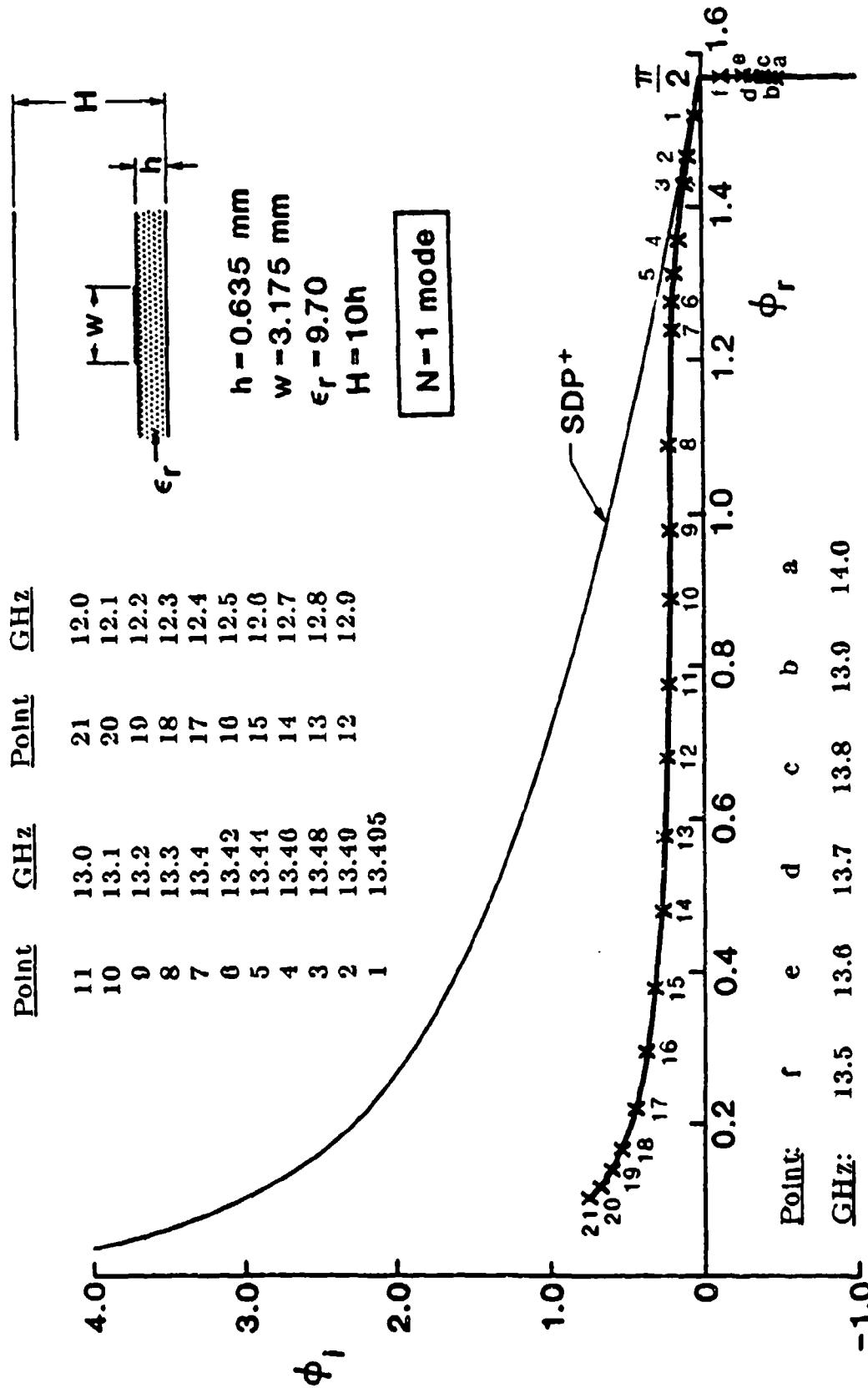


Fig. 9.25 Leaky-wave pole locations on the steepest-descent plane for a range of frequencies for the first higher mode of the Boukamp-Jansen structure with a covered top, where the leakage is in the form of a surface wave. Real k_z pole locations are present as well, on the vertical line at $\phi_r = \pi/2$.

into appropriate steepest-descent form. Results are shown for both the leaky mode range (the numbered points) and the bound mode range (the lettered points). As they should, the bound mode solutions lie on the vertical line $\phi_r = \pi/2$ and have negative values of ϕ_i ; they are "proper" solutions, and the line $\phi_r = \pi/2$ corresponds to the boundary of strip T_1 , (see Fig. 9.14). The leaky mode solutions again appear in strip B_1 , as "improper" solutions, but, for all the frequencies shown, the poles lie below the SDP^+ curve and are therefore captured when the original path P is deformed into the SDP^+ curve. It is therefore clear that the leaky mode indeed represents the "radiation" region whether the radiation is in surface-wave form or in space-wave form.

c. The Menzel Antenna Structure

The microstrip line cross-section dimensions chosen by Menzel [27] for his antenna are $h = 0.794$ mm, $w = 15.00$ mm, and $\epsilon_r = 2.32$. The structure is of course completely open at the top. These structural parameters are quite different from those selected by Boukamp and Jansen; Menzel's strip is much wider and his dielectric constant is much smaller. It was therefore considered worthwhile to see what differences occur in the steepest-descent plots for parameter values that are so dissimilar.

Values of α/k_0 and β/k_0 as a function of frequency for the first higher mode are presented in Sec. E.2; they will not be repeated here even though the frequency range covered now is somewhat wider. The pole locations in the steepest-descent plane for this $N=1$ mode are shown in Fig. 9.26 for both the bound mode range and the leaky mode range. As in Fig. 9.25, the bound mode poles are located on the vertical $\phi_r = \pi/2$ axis, and the leaky mode poles appear in strip B_1 , as in all the other plots. The use of k_0 implies that space wave radiation is assumed here, as in subsection (a). (It is understood, of course, that for a given frequency only a single pole is present.)

When we compare the trajectory of leaky-mode pole locations in Fig. 9.26 with that in Fig. 9.22 for the open-topped Boukamp and Jansen dimensions, we note two important differences. The first is that the vertical portion here occurs at a much smaller value of ϕ_r (approximately 0.05 as compared with roughly 0.15), and the second is that in the neighborhood of the onset of leakage the ϕ_i values for the pole locations are smaller here. In general, the leakage rate for the Menzel structure seems to be smaller. Also, because the vertical portion occurs closer to the $\phi_r = 0$ axis, the poles are more likely to be captured, but there is a larger frequency range over

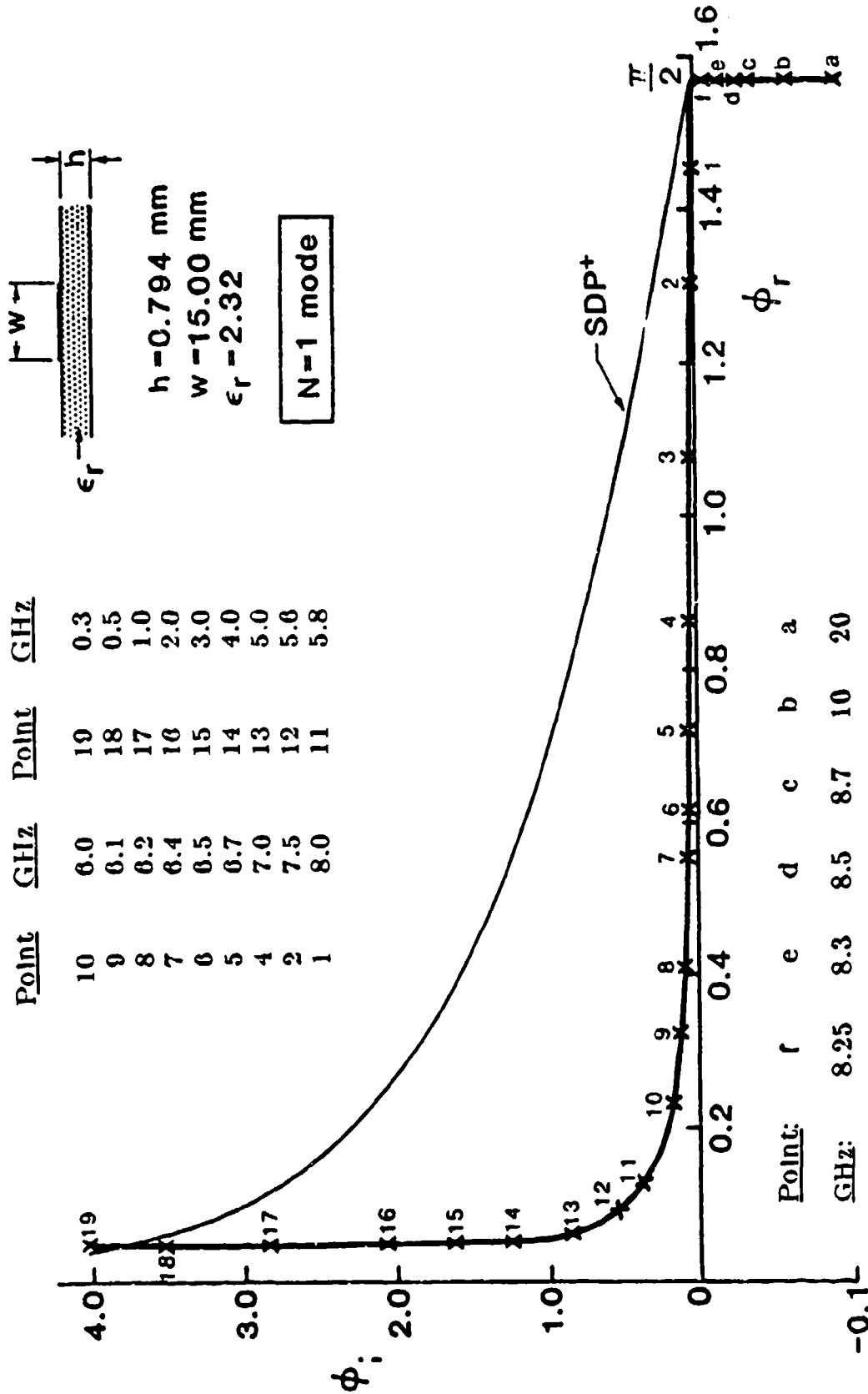


Fig. 9.26 Leaky-wave pole locations on the steepest-descent plane for the first higher mode ($N = 1$) over a very wide frequency range for the Menzel antenna structure. Some solutions in the real k_z range are also presented on the $\phi_r = \pi/2$ line.

which the poles correspond to waves that decay extremely rapidly, and are therefore not very meaningful. Menzel operated his structure as an antenna at $f = 6.70$ GHz, corresponding to point 5 in Fig. 9.26, for which $\phi_r \approx 0.7$. By reference to Fig. 9.17, frequencies for which the mode does not decay excessively vary from about 5.6 GHz to about 8.2 GHz.

Steepest-descent plots for the $N=2$ and $N=3$ higher modes for the Menzel antenna dimensions are given in Figs. 9.27 and 9.28. It is interesting to see here that the pole locations are now such that the poles are much more likely to be captured, and in principle, to be able to contribute to the field. In part, this feature is related to the above-mentioned observation that the vertical portions for the Menzel structure occur much closer to $\phi_r = 0$ axis. The poles that are captured, however, generally lie far away from the lined region in Fig. 9.17, so that they all decay extremely rapidly and are therefore not likely to contribute to the field in any significant way.

We found in subsection (a), for the Boukamp-Jansen structure without a top cover, that the higher modes (beyond the first higher mode) would contribute negligibly to the field and that, in fact, for most frequencies the poles would not even be captured. Here, for the Menzel structure, the poles would for most frequencies be captured, but the waves they represent would decay so rapidly that at most they could yield some wide-angle background radiation. It seems, therefore, that for most cases it is sufficient to consider only the first higher mode, but one should also keep in mind that the next higher modes could perhaps, under some circumstances, furnish some small contribution to the radiation pattern.

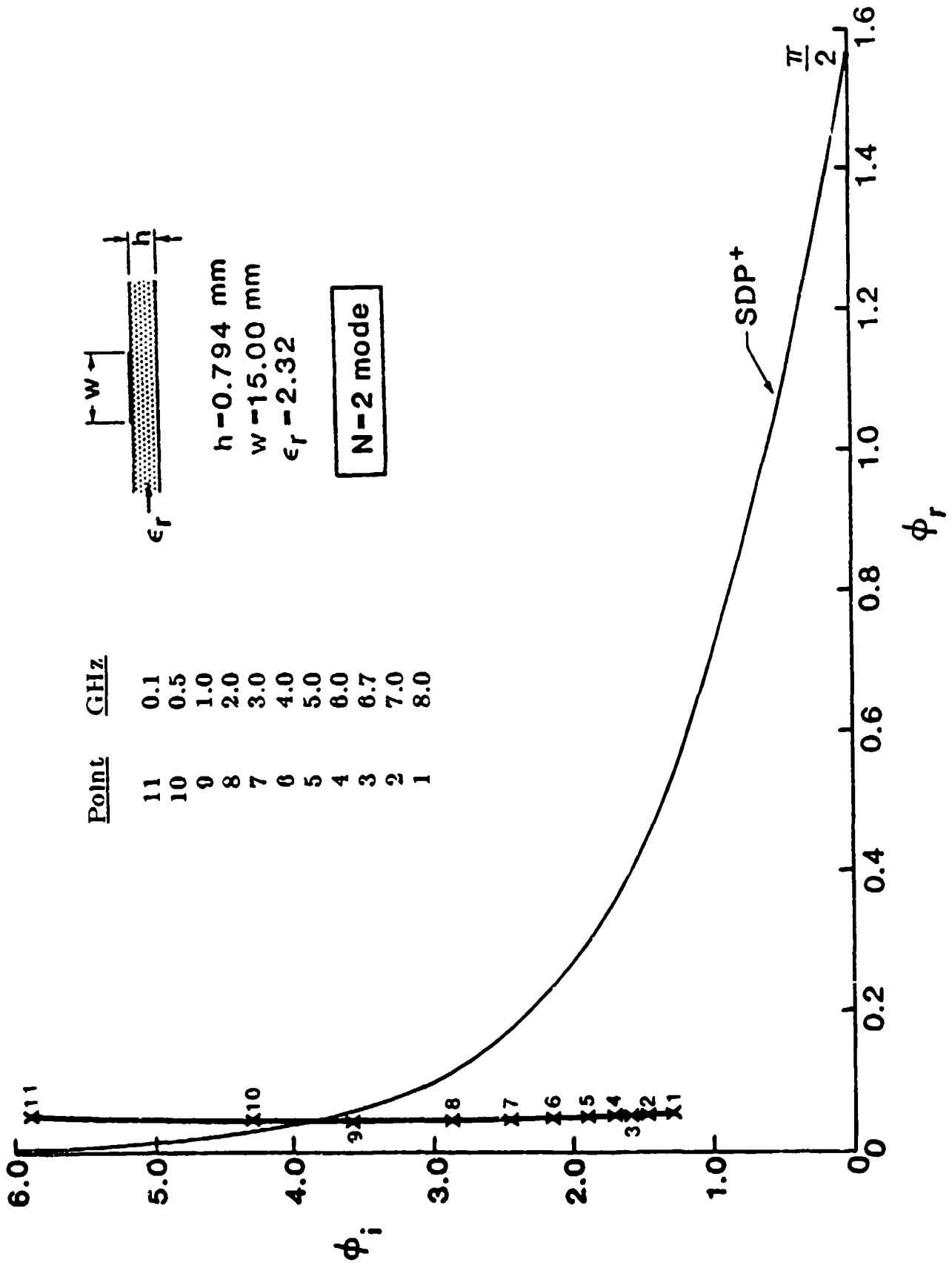


Fig. 9.27 Same as in Fig. 9.26, but for the $N = 2$ higher mode.

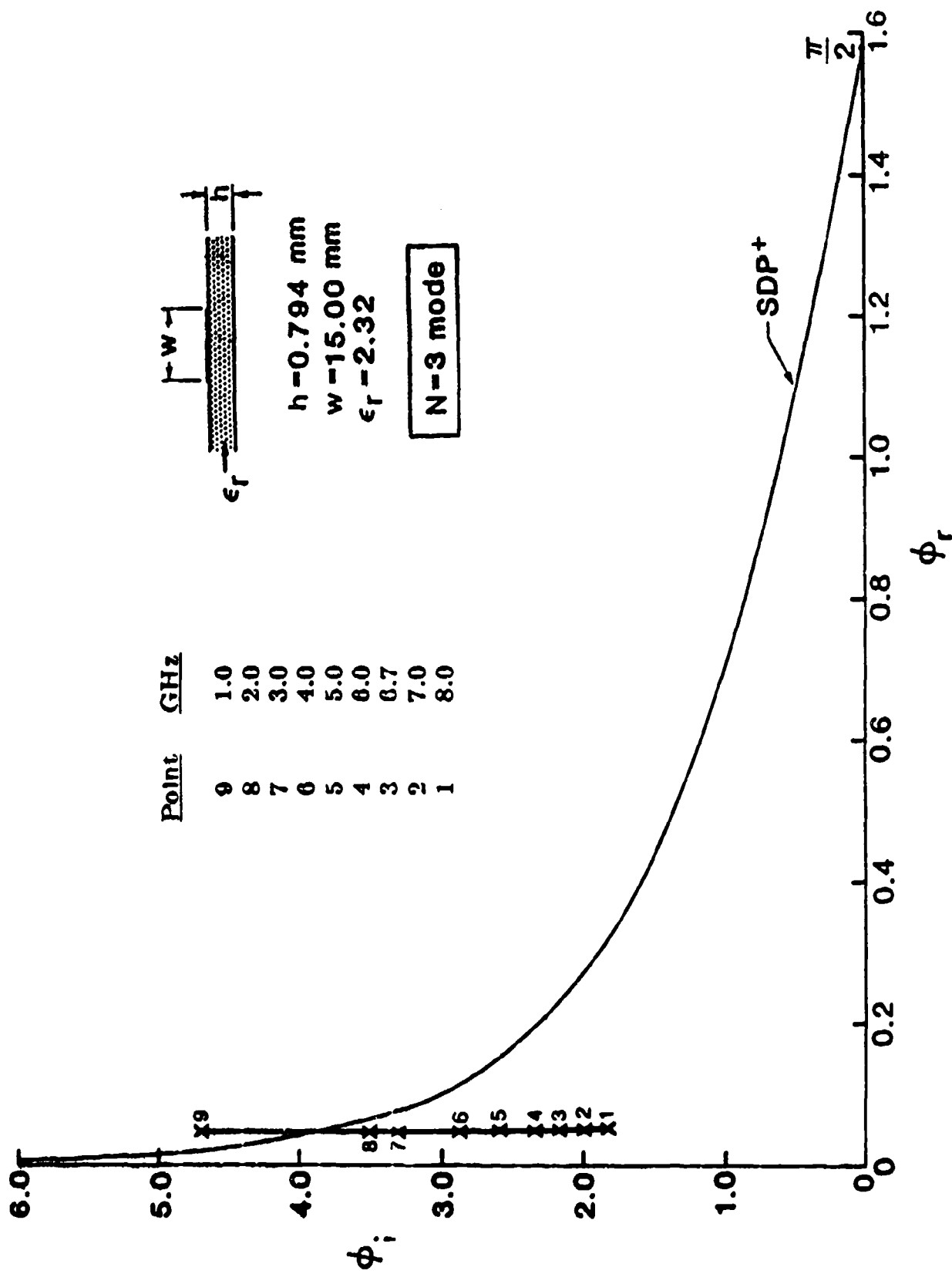


Fig. 9.28 Same as in Fig. 9.26, but for the $N = 3$ higher mode.

E. INVESTIGATIONS RELATING TO MENZEL'S ANTENNA

1. Description of Menzel's Antenna

Based on good intuition but incomplete scientific understanding, W. Menzel [27] proposed, designed and measured an antenna that consisted of a short length of microstrip line fed in its first higher mode and operated near to its "cutoff." Although it was not operated in optimum fashion, it performed reasonably well. It is of interest because of its *structural simplicity*.

As a result of the current investigations, we are now sure that the structure is basically a leaky-wave antenna. Menzel made the structure short because he conceived it as a traveling wave competitor to a microstrip patch antenna. In the next subsection, we analyze the performance of his antenna in leaky wave terms, and we show why it behaved as well as it did despite its short length, and why, from a leaky wave viewpoint, its performance would be improved if it were made longer. In this subsection, we summarize the properties of his antenna and indicate the theoretical approach that he used.

The cross-sectional shape of his antenna is of course that shown in Fig. 9.1. The aspect ratio of his antenna is unusually flat, with parameter values $h = 0.79$ mm, $w = 15.00$ mm, and $\epsilon_r = 2.32$. The antenna length is 10.00 cm and the operating frequency he chose is 6.70 GHz, so that the length becomes $2.23\lambda_0$, which is very short for customary leaky-wave antennas, where we expect lengths of 20 to 40 free-space wavelengths.

In his theoretical approach, he assumes that the propagation wavenumber k_z of the first higher mode is *purely real* but with $\beta < k_0$ and above cutoff. He calculates a value of β based on this assumption, and then further assumes that the field along the strip length has constant amplitude. The aperture distribution therefore has a constant amplitude and a traveling wave phase. From this aperture distribution, he computes a theoretical radiation pattern that appears to agree reasonably well with his measured radiation pattern. The comparison, in terms of amplitude rather than power, and plotted in polar form, is shown in Fig. 11 of his paper [27], and is reproduced here in Fig. 9.29 the same size as in his paper.

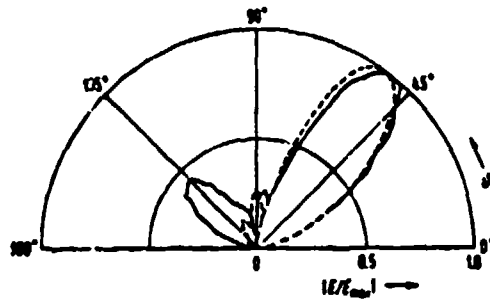


Fig. 9.29 Experimental and theoretical far field (amplitude) patterns presented by W. Menzel as Fig. 11 in his paper [27], reproduced here the same size. The antenna parameters are: $\epsilon_r = 2.32$, $h = 0.794$ mm, $w = 1.500$ cm, $L = 10.00$ cm, and $f = 6.70$ GHz.

Because this figure is so small, we made a copy double in linear size. Unfortunately, due to printing and copying distortions, the origin is not precisely centered and the vertical and horizontal axes are slightly unequal radially, making reproducibility and accurate comparison difficult. Our best estimate for the angle θ_m of maximum radiation for Menzel's *experimental* curve is $40^\circ \pm 3^\circ$, as measured from broadside (his θ is the complement of ours). The estimate is made more difficult by the fact that his experimental curve is somewhat distorted and seems to have a flat top. The 3 dB beam width of the experimental curve is estimated to be $\Delta\theta = 28^\circ \pm 3^\circ$.

His *theoretical* curve is shown dashed in Fig. 9.29, and is seen to be shifted slightly closer to broadside. An expression for that theoretical curve is given by Menzel as the H-plane portion of his Eq. (2), based upon his Eq. (1) and consistent with the aperture distribution discussion above. The value of β/k_o needed in that expression, taken from the curve in his Fig. 4 and found to be $\beta/k_o = 0.645$, is then inserted into his expression (2) to yield that dashed curve in Fig. 9.29. From our calculation, which is more accurate than the dashed curve itself in Fig. 9.29, we obtain $\theta_m = 36.2^\circ$ and $\Delta\theta = 26.1^\circ$ as Menzel's corresponding theoretical values.

The agreement with the measured curve is rather good, considering all the uncertainties and approximations. Menzel's theoretical value for θ_m is slightly low, but the beam width $\Delta\theta$ lies within the experimental uncertainty. We comment in the next section on why the agreement is as good as it is.

The other important feature evident in Fig. 9.29 is the large *back lobe*, with a maximum amplitude about 0.4 times that of the main beam, and with the angle of the maximum approximately equal to $-\theta_m$. It seems clear that much of the power reaches

the end and that some of that power travels back along the strip, radiating power into this back lobe. Menzel discusses this point, and one of his conclusions is that "efficiency is improved using longer lines." We also comment on this point in the next subsection in the context of leaky modes.

Menzel also discusses other aspects in his paper [27], such as ways to feed the antenna and measurements on an array of four strips, but we need not consider them.

2. Analysis of Menzel's Antenna in Leaky Mode Terms

Our view of the antenna structure as a leaky-wave antenna provides us with much additional insight; with this view we are able to explain the performance features of the antenna and, in addition, to know how to modify the structure to improve its performance.

As a leaky-wave antenna for which the cross-section dimensions are maintained constant, the aperture distribution along the strip in Menzel's antenna does not have constant amplitude, but one that *decays* in accordance with the leakage constant α of the leaky mode. From a leaky mode analysis of the cross-section, we compute that $\beta/k_o = 0.661$ and $\alpha/k_o = 3.78 \times 10^{-2}$ at the operational frequency of 6.70 GHz.

Let us first utilize this information to indicate the difference between his and our aperture distributions, and then, as a corollary, to obtain the power remaining at the end of the strip and to discuss the back lobe found experimentally. His assumed aperture distribution is

$$E(z) = Ae^{-j\beta z} \quad (9.53)$$

whereas our leaky wave distribution is

$$E(z) = Ae^{-\alpha z} e^{-j\beta z} \quad (9.54)$$

where A is simply a constant. From the $\exp(-\alpha z)$ factor in (9.54), we see that for a strip length L of 10.00 cm and a value of $\alpha/k_o = 3.78 \times 10^{-2}$, we have that the amplitude at the end strip is $0.588 A$, and that the power remaining at the end is 0.346 of that which is incident, or about 35%. Thus, *about 65% of the power has leaked away into the forward beam, and about 35% has reached the end of the strip.* Two interesting conclusions result from these numbers:

(a) Despite the relatively short length of the antenna, $L = 2.23\lambda_o$, almost two-thirds of the power is radiated away. That is why the antenna works as well as it does. The large radiated power follows from the fact that the α value is larger than those usually encountered in leaky-wave antennas.

(b) Since approximately one-third of the power reaches the termination of the antenna, and since Menzel states that he did not place a load at the termination, part of that power is transmitted onward and part is reflected. The reflected portion produces a leaky wave in the reverse direction, creating a *back lobe* in the radiation pattern at an angle that would be the mirror image of that for the main beam. Since we do not know how much power is reflected at the end and how much continues onward, we cannot compute theoretically the size of the back lobe; from the measured curve in Fig. 9.29, however, a back lobe amplitude of 0.4 means about 16% reflected power, which may be reasonable.

In connection with the reflected power from the end, Menzel finds experimentally (his Fig. 14) that the antenna efficiency (meaning the percentage of power radiated) decreases as the frequency is increased, and that the efficiency is increased when the antenna length is increased. The leaky wave interpretation, which includes the concept of α whereas Menzel's viewpoint did not, easily explains both of these findings. When the frequency is increased, the value of α decreases, so that less power is radiated for the same antenna length; then, when the length is increased but the frequency is kept the same, and therefore α remains the same, more power is leaked away and the efficiency improves.

Since the actual antenna aperture distribution is given by (9.54) rather than (9.53), which Menzel assumed, we can compute a more accurate radiation pattern than his by employing the *correct* aperture distribution. His theoretical expression is no longer valid, however, since it applies only to aperture distributions with constant amplitude. We need instead to use expression (2.35), the derivation of which is presented in Chap. II.

Another difference arises, and it is that the value of β/k_o used by Menzel is not quite correct. He assumed that the value of β is real within the range in which the propagation wavenumber must be complex. The actual values for both β/k_o and α/k_o as a function of frequency are shown in Figs. 9.30 and 9.31; the values were computed from the theory described in Sec. C.1, employing (9.35) together with (9.21) and its corollary relations. The general shapes of the curves are similar to those in Fig. 9.11 or in Figs. 9.20 and 9.21 over a wider range of frequencies. In Fig. 9.30 for β/k_o , however, we have added a dashed curve corresponding to Menzel's calculations; his numbers come from his Fig. 4, where we have changed the values from $(\beta/k_o)^2$ to β/k_o . It is interesting that for $f = 6.70$ GHz, the operating frequency of his antenna, the difference between his value and the correct one is small, the values being 0.645

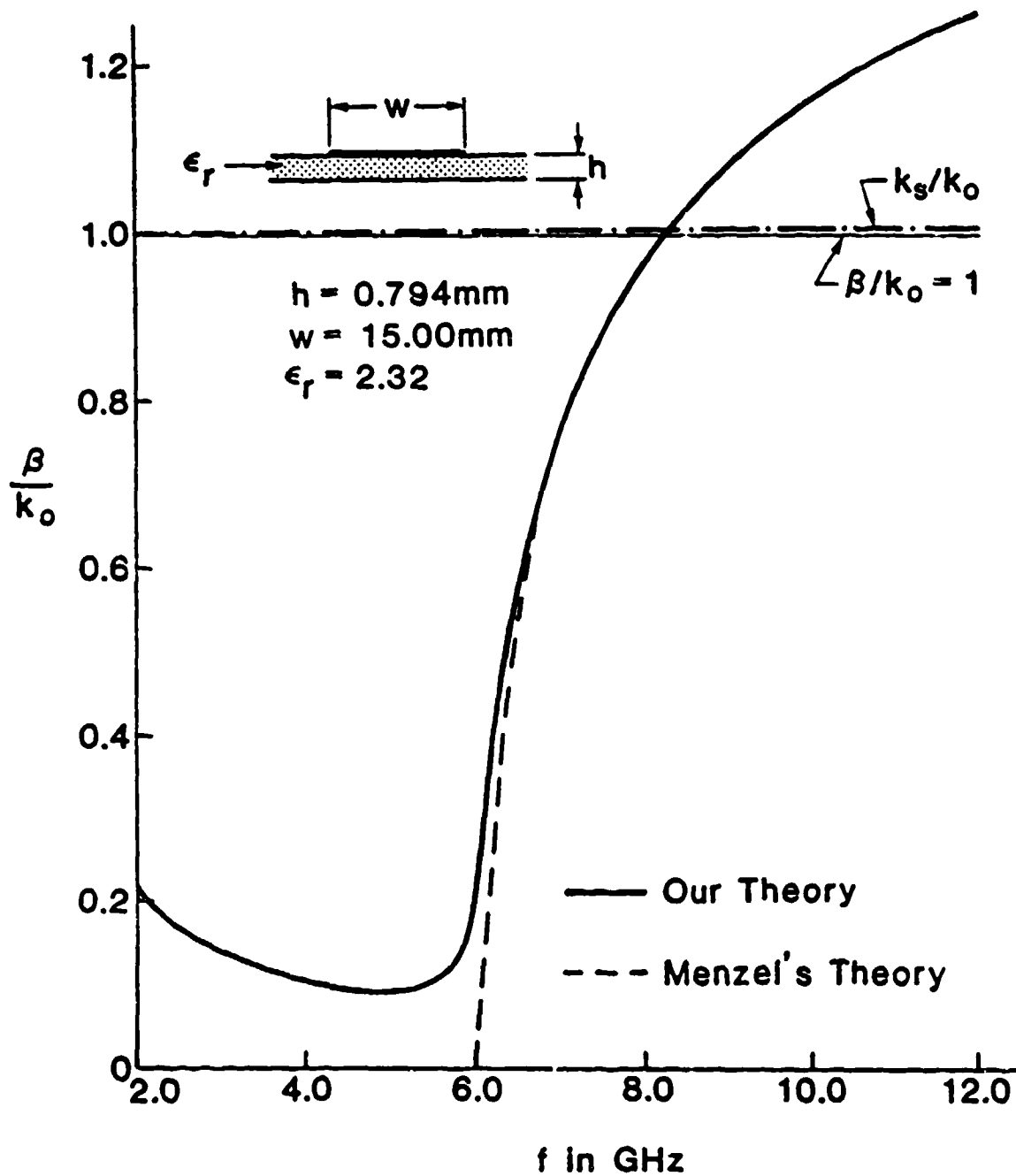


Fig. 9.30

Normalized phase constant β/k_0 as a function of frequency for Menzel's antenna structure. The solid line represents the accurate leaky wave result, while the dashed curve corresponds to Menzel's approximation in which the mode is assumed to be purely real.

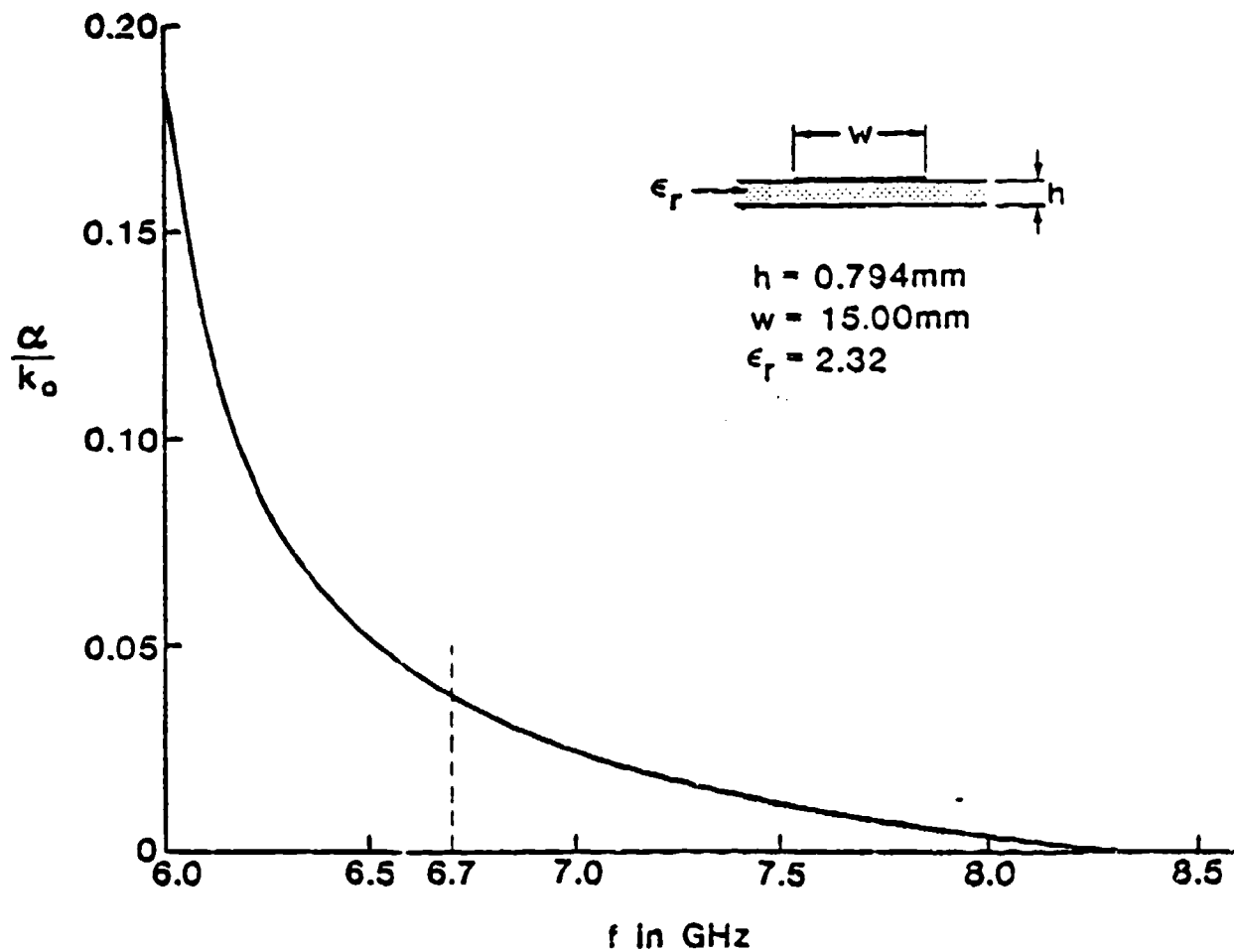


Fig. 9.31 Normalized leakage constant α/k_0 as a function of frequency for Menzel's antenna structure. His operating frequency of 6.70 GHz is indicated by the vertical dashed line.

and 0.661, respectively. For the higher frequencies, his dashed curve and our solid one are coincident; for lower frequencies, they differ strongly.

The biggest distinction between the two curves in Fig. 9.30 is conceptual, relating to the concept of *cutoff*, which has a strict and sharp significance only when the mode is lossless and purely bound. When the anticipated "cutoff" occurs in a leaky wave region, the considerations become complicated, and the "cutoff" degenerates into a spread-out region which "ends" only when the value of α becomes so high that the mode can contribute only some small wide-angle background radiation, if anything at all. These considerations are quantified in Sec. D, in the context of the steepest-descent plane.

Using our accurate values of α/k_0 and β/k_0 in expression (2.35) for the radiation pattern corresponding to aperture distribution (9.54), we obtain the amplitude pattern shown as the solid line in Fig. 9.32, which covers the complete angular range. Superimposed on this plot as a dashed line is the Menzel theoretical pattern, which is the same as the dashed pattern in his Fig. 11, except that this plot is not a polar one. These plots are seen to be very similar to each other, but two important differences should be noted. The first is that the curves are shifted with respect to each other, with the peak of the dashed-line curve, corresponding to a constant aperture distribution (Eq. (9.53)), occurring slightly closer to broadside. The second difference relates to the minima in the patterns. The pattern based on the constant aperture distribution has a null (since it is basically a $\sin x/x$ pattern), whereas that null becomes filled in when the aperture distribution has a decaying factor.

To permit a better comparison between the data in Fig. 9.32 and the original curves presented by Menzel and reproduced here as Fig. 9.29, we replot in Fig. 9.33 in *polar form* the data from Fig. 9.32. It is seen that our more accurate data appear closer to the Menzel experimental data (from Fig. 9.29) than do the theoretical values of Menzel, but the two theoretical curves agree rather well, as noted above.

In order to obtain a more accurate comparison between the two patterns with respect to θ_m and $\Delta\theta$, however, we replot in Fig. 9.34 the portion near the peaks. We then find the following:

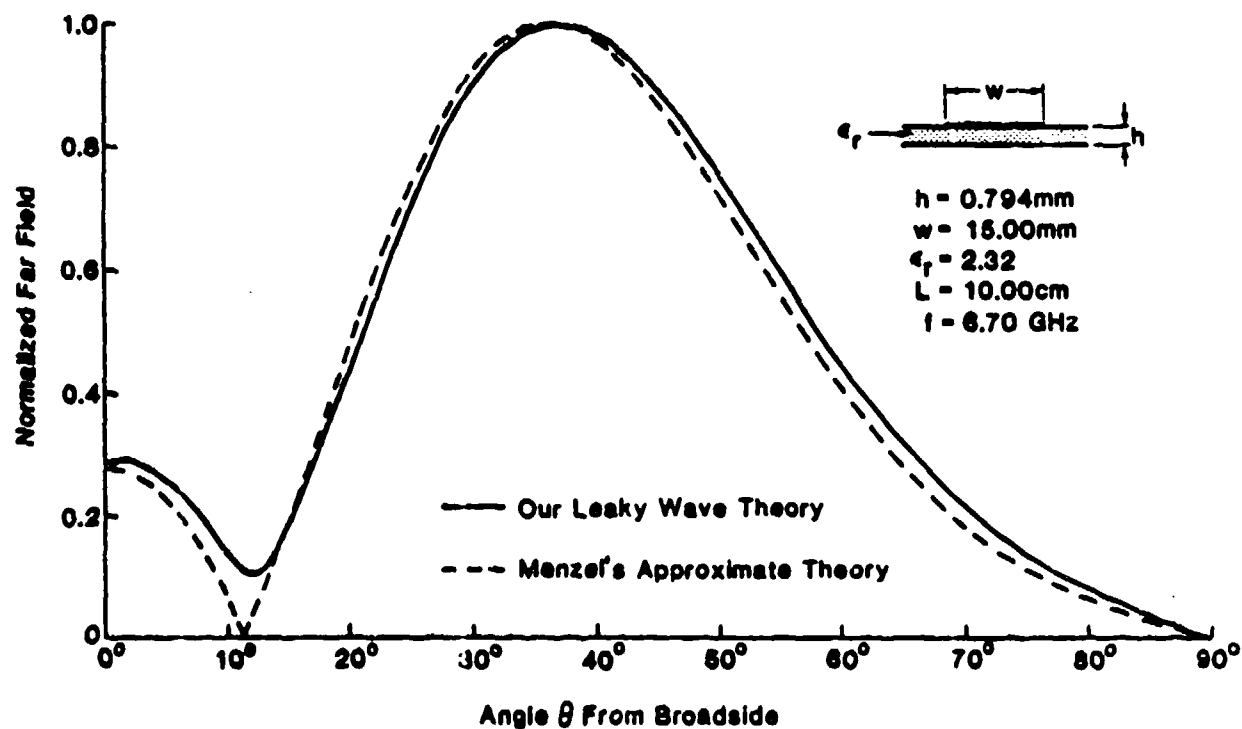


Fig. 9.32

Normalized far field over the complete angular range for the Menzel antenna [27]. The dashed line represents his theoretical calculation, assuming a constant aperture distribution, while the solid line indicates the result using the correct leaky-wave theory.

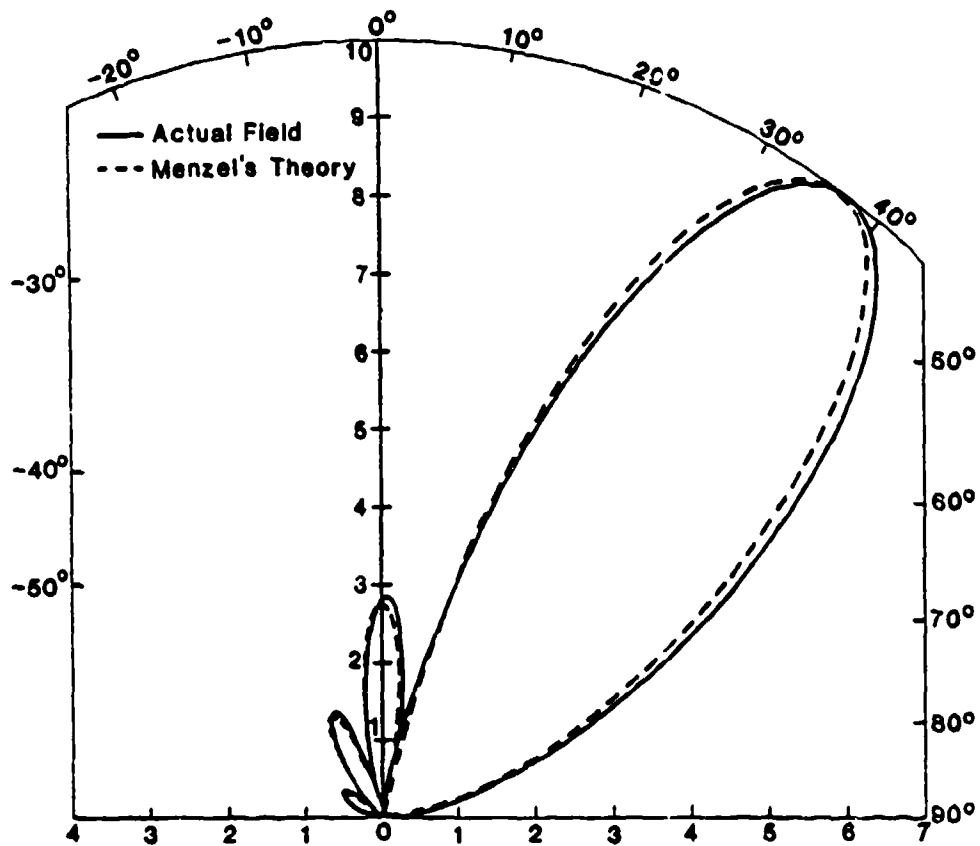


Fig. 9.33 Same as in Fig. 9.32, but plotted in polar form to permit easier comparison with Fig. 9.29.

<u>Menzel's Theory</u>	<u>Our Theory</u>	<u>Experiment</u>
$\beta/k_o = 0.645$	$\beta/k_o = 0.661$	
$\alpha/k_o = 0$	$\alpha/k_o = 3.78 \times 10^{-2}$	
<i>Aperture:</i>		
constant	exponential decay	
$\theta_m = 36.2^\circ$	$\theta_m = 37.1^\circ$	$\theta_m = 40^\circ \pm 3^\circ$
$\Delta\theta = 25.9^\circ$	$\Delta\theta = 26.5^\circ$	$\Delta\theta = 28^\circ \pm 3^\circ$

It is seen that the theoretical values of $\Delta\theta$ differ by only about $1/2^\circ$, whereas those for θ_m are about 1° apart. This distinction can be observed directly from Fig. 9.34, where the two curves appear primarily to be shifted with respect to each other. One also sees more clearly now that our theory produces results that are *slightly closer* to the experimental values.

It was pointed out above that these two theoretical results differ in *two* ways: the different aperture distributions, and the different values of β/k_o . At this stage it is not clear which of these two ways is the more important. To help us in that assessment, we have also computed the pattern that results when we assume the accurate value of β/k_o ($=0.661$) together with a constant aperture distribution. The result is illuminating; it shows that the major part of the discrepancy between the two curves in Fig. 9.34 is due to the inaccurate value of β/k_o , rather than the shape of the aperture distribution. The new values of θ_m and $\Delta\theta$ obtained from this third calculation are $\theta_m = 37.1^\circ$ and $\Delta\theta = 26.3^\circ$. The angular shift between the two curves in Fig. 9.33 or Fig. 9.34 effectively disappears when the correct value of β/k_o is employed, and the $\Delta\theta$ discrepancy is reduced, but the beam width is still slightly larger and the sidelobes are somewhat higher when the exponentially decaying aperture field is utilized.

3. Parametric Dependences for Antenna Design

We must know the parametric dependences for a given structure in order to know how to design that structure as an antenna. First of all, we must determine if it is possible to change some parameter so that the leakage rate α can be modified while simultaneously keeping the phase constant β essentially the same. If that can be done, then it is possible to taper the value of α to achieve a specified aperture distribution in

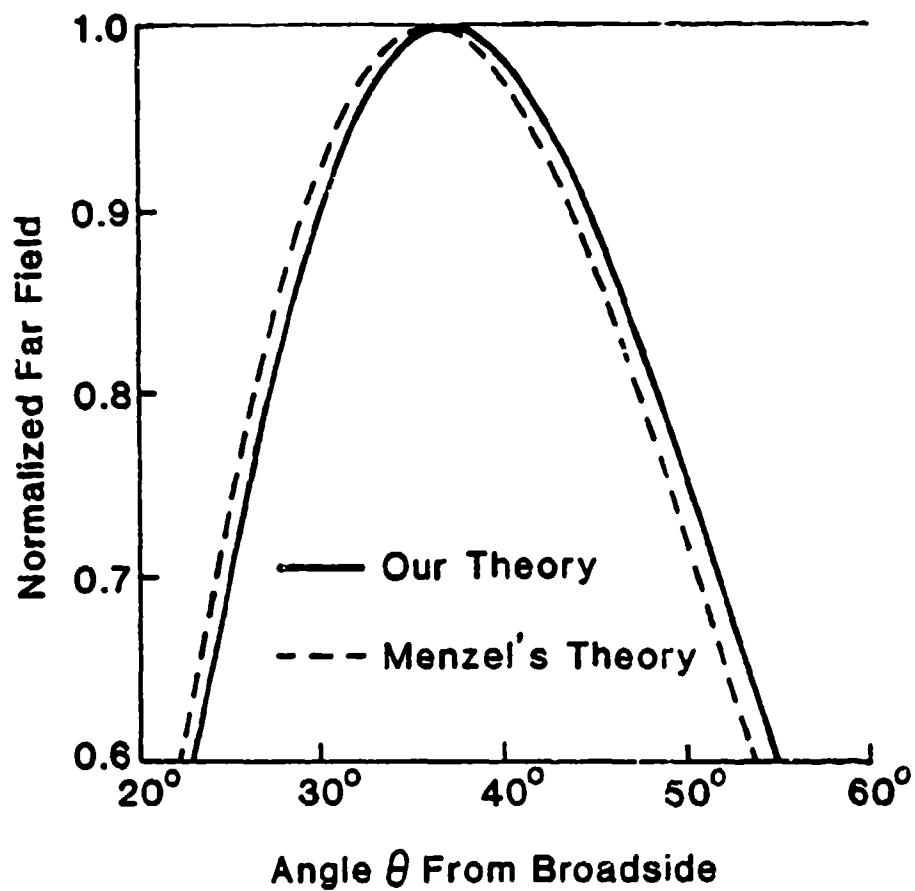


Fig. 9.34

The central portion of Fig. 9.32 near the peaks of the curves, replotted for better comparison between the two solutions.

accordance with some sidelobe requirement on the radiation pattern. If that is not possible, we must then keep the dimensions constant along the length, and be satisfied with the patterns that result from an exponentially decaying aperture distribution. One cannot then modify the sidelobe level or distribution, but at least clean narrow beams are achieved. If tapered aperture distributions are feasible, it is necessary to know the parametric dependences in more detail, but in either case one has design control only if it is known what effects are produced by various dimensional changes.

With these microstrip line leaky-wave antennas, the only parameter that can be varied easily along the antenna length is the *strip width* w . The other two parameters, the dielectric height h and the dielectric constant ϵ_r , cannot be altered easily along the antenna length but their values can be specified beforehand in the design. The strip width, however, can be readily specified as a function of distance along the antenna by lithography or other means. Let us therefore consider that parameter first.

Consider β/k_0 and α/k_0 as a function of strip width w over a wide range of widths are presented in Figs. 9.35 and 9.36, respectively. The indicated points correspond to the value of w in Menzel's antenna. The curve shapes are broadly similar to those seen in Figs. 9.30 and 9.31, where the abscissa is the frequency. The most important feature about the curves in Figs. 9.35 and 9.36 is that, when w is altered to change the leakage constant α , the phase constant β changes as well. We are thus forced to the unfortunate conclusion that we cannot taper the antenna aperture distribution, since different portions of the aperture would then point the beam in different directions. The cross-section dimensions of these leaky-wave strip antennas must therefore be maintained constant along their lengths; as a result, they will possess exponentially decaying aperture distributions, given by (9.54), for which the resulting radiation patterns can be computed from (2.35).

The variations of β/k_0 and α/k_0 with the relative dielectric constant ϵ_r are seen in Fig. 9.37; the indicated points show Menzel's value for ϵ_r . The general pattern is retained here as well; that is, when the value of α/k_0 rises, the value of β/k_0 decreases. The leakage increases as ϵ_r decreases, but here again the effect is qualitatively similar to what we find when the frequency is lowered or the width is decreased. The reason is that the electrical length of the transmission line in Fig. 9.7, corresponding to the region under the strip, is $[k_0^2 \epsilon_r - k_z^2]^{1/2} w/2$, so that all three of these parameters vary qualitatively in the same way. In Fig. 9.37, the onset of leakage occurs for ϵ_r about 3.0; if a higher value of ϵ_r is used, it is therefore necessary to reduce w appropriately, or to operate at a lower frequency.

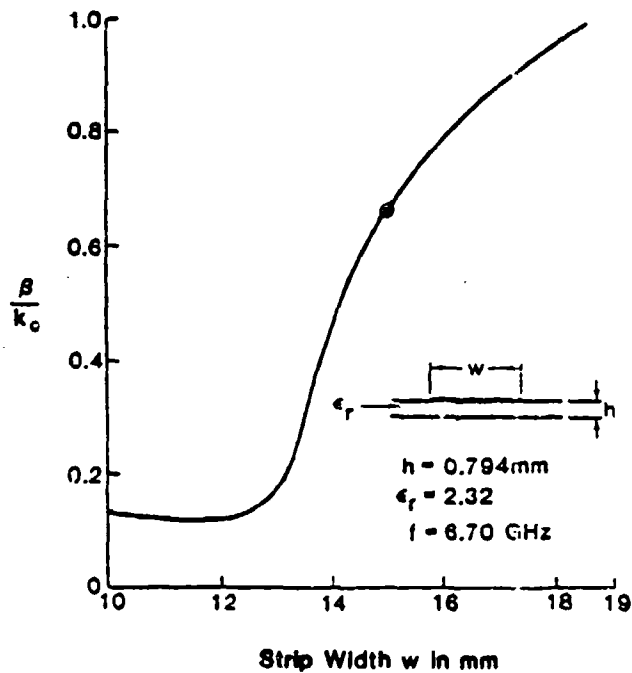


Fig. 9.35 Variation of normalized phase constant β/k_0 with strip width w of a microstrip leaky-wave antenna over a wide range of strip widths.

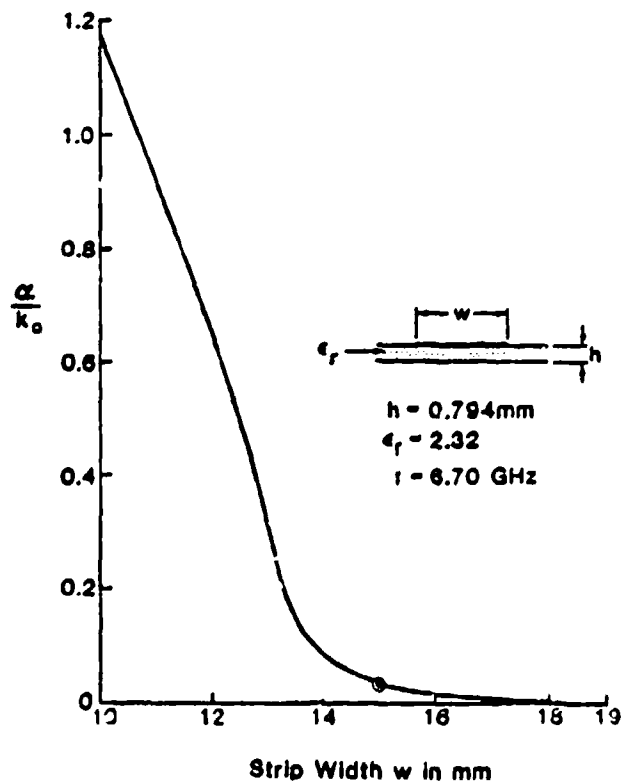


Fig. 9.36 Variation of normalized leakage constant α/k_0 with strip width w of a microstrip leaky-wave antenna over a wide range of strip widths.

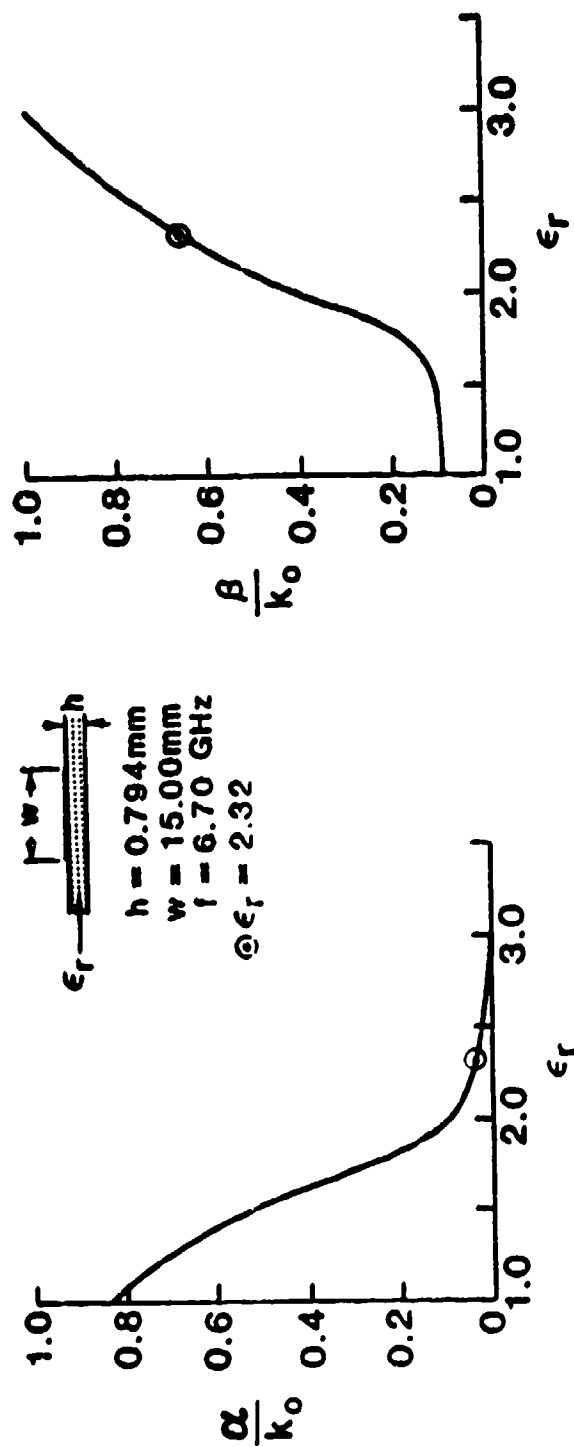


Fig. 9.37 Variations of β/k_0 and α/k_0 with relative dielectric constant ϵ_r for a microstrip leaky-wave antenna.

The behavior as a function of *dielectric height* h is somewhat different, as seen in Fig. 9.38. Even though h varies over a large range of values, α/k_o and β/k_o do not change as much as when the other parameters are altered; Menzel's value for h is indicated by the circled points. As β/k_o increases, α/k_o decreases for larger values of h , as with the other parameters, but for very thin dielectric substrates α/k_o decreases again, as though the mode were being shorted out. These variations with h are more involved, and depend more heavily on the discontinuity junction itself.

4. Performance When Properly Designed as a Leaky-Wave Antenna

We showed earlier that Menzel made his antenna too short, only $2.23\lambda_o$ long at his operating frequency of 6.70 GHz. He wanted to keep the length small to "compete" with microstrip patch antennas, but, as a result, only about 2/3 of the power was radiated away and a sizeable back lobe was produced. In addition, the short length caused a rather large beam width for a traveling wave antenna, but not a beam suitable for a patch element either. When we view the structure as a leaky-wave antenna, we automatically select a greater length so as to radiate more of the power and thereby increase efficiency. Simultaneously, the back lobe is essentially eliminated and the beam width is narrowed to a more practical value.

A common procedure for leaky-wave antennas is to choose the aperture length so that about 90% of the power is radiated; the choice is a compromise between efficiency and excessive length. When we apply that choice to the cross-section dimensions and the frequency taken by Menzel, we find that the length L of the antenna becomes 21.7 cm, actually only a bit more than twice the 10.0 cm value adopted by Menzel. The antenna is still quite short, about $4.84\lambda_o$, because the value of α is relatively high.

Since the cross-section dimensions are maintained constant along the length, the aperture field distribution is *exponentially decaying*, and the analytical expression for the radiation pattern is provided by (2.35). A linear plot of the normalized far field, similar to those in Figs. 9.32 and 9.34, appears as the solid line in Fig. 9.39. For comparison, the dashed line plot in Fig. 9.39 presents the far field behavior obtained if the aperture field distribution were *constant*, computed via (2.32). The same β/k_o value is used in computing each of these two plots.

We note first, from Fig. 9.39, that the two curves peak at essentially the same value of θ , but that the one for a constant aperture field has a slightly narrower beam width. In addition, the nulls become filled in and the side lobes are a bit higher when the

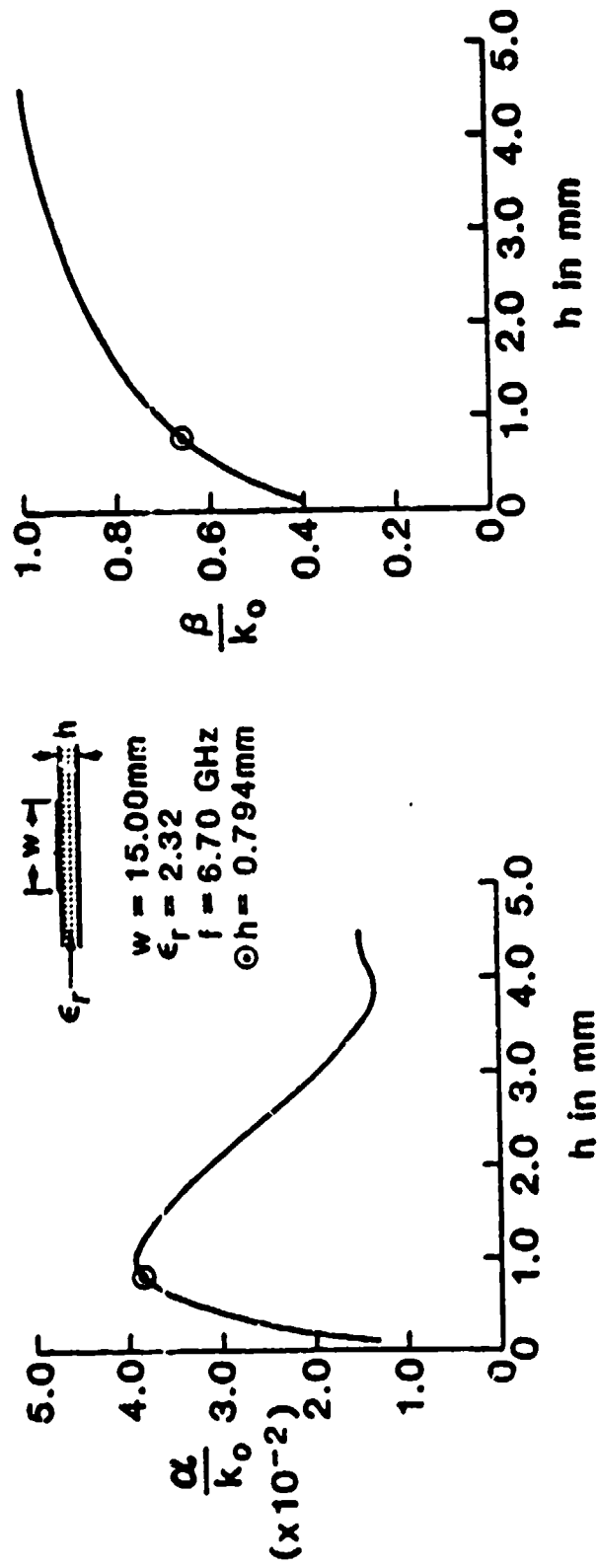


Fig. 9.38 Variations of β/k_0 and α/k_0 with dielectric height h for a microstrip leaky-wave antenna.

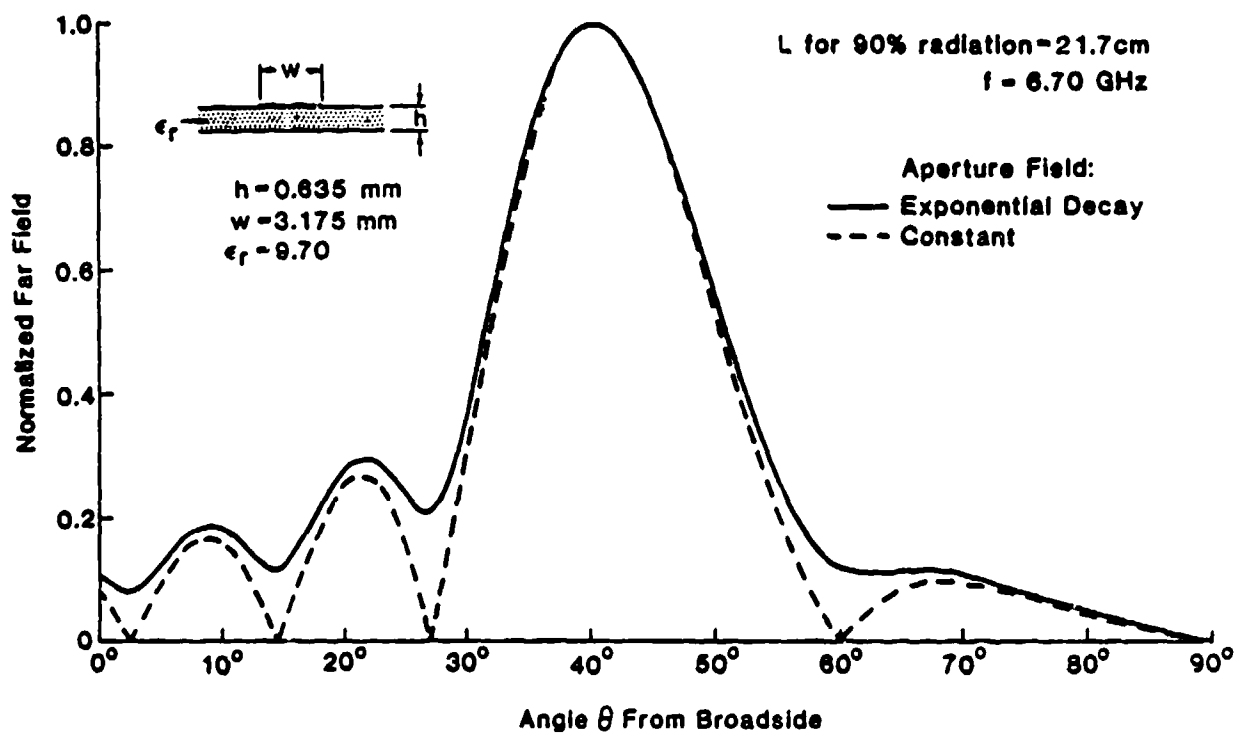


Fig. 9.39

Normalized far field vs. angle θ from broadside for a leaky microstrip structure when the length L corresponds to 90% power radiation. The solid and dashed curves correspond, respectively, to the actual, exponentially decaying, aperture distribution and an assumed constant one.

aperture field decays. Quantitatively, the θ_m and $\Delta\theta$ values for the exponentially decaying aperture field and the constant one, respectively, are $\theta_m = 40.2^\circ$ and $\Delta\theta = 14.0^\circ$ versus $\theta_m = 40.3^\circ$ and $\Delta\theta = 13.4^\circ$. As compared with the shorter Menzel structure, θ_m has moved about 3° away from broadside, which is not much, but the beam width became reduced from about 26° to about 14° , which is substantial.

Leaky-wave antennas can, of course, be *frequency scanned*. We therefore computed the far field patterns corresponding to two other frequencies, 7.50 GHz and 8.00 GHz, maintaining the same length and cross-section dimensions and changing only the frequency. The results are plotted in Fig. 9.40 in polar form, but the sidelobe information is omitted for clarity. Nothing special occurs in the sidelobes except that they increase slightly upon frequency scan. The aperture field distribution was taken to be exponentially decaying in these calculations.

We observe from Fig. 9.40 that the patterns do indeed scan with frequency, and that the beam widths remain roughly the same. A quantitative comparison reveals:

<u>f in GHz</u>	<u>θ_m</u>	<u>$\Delta\theta$</u>
6.70	40.2°	14.0°
7.50	58.0°	16.1°
8.00	66.5°	16.5°

There is a problem here, however. As the frequency is increased, the value of α/k_o decreases significantly, so that less power is radiated and antenna efficiency suffers. In fact, the power radiated at 7.50 and 8.00 GHz become only 54% and 24%, respectively. Thus, the patterns look good but the efficiency becomes poor, and back lobes will be present unless a matched load is placed at the end of the strip. We have been unfair here, however, because we placed the starting point at the low frequency end. If instead we scanned in frequency from 6.30 GHz to 7.00 GHz, about a 10% range, the values for θ_m would have gone from 28° to 50° , and the radiated powers would have been 98% and 80% at the two ends of the scan range.

Because α is such a sensitive function of frequency in this structure, we must change the length substantially if we wish to keep the radiated power at 90%. But then the beam width $\Delta\theta$ changes as well. When we change the aperture length L as well as the frequency, maintaining the efficiency now at 90%, we obtain the far field patterns shown in polar form in Fig. 9.41. The angles θ_m are now different from what

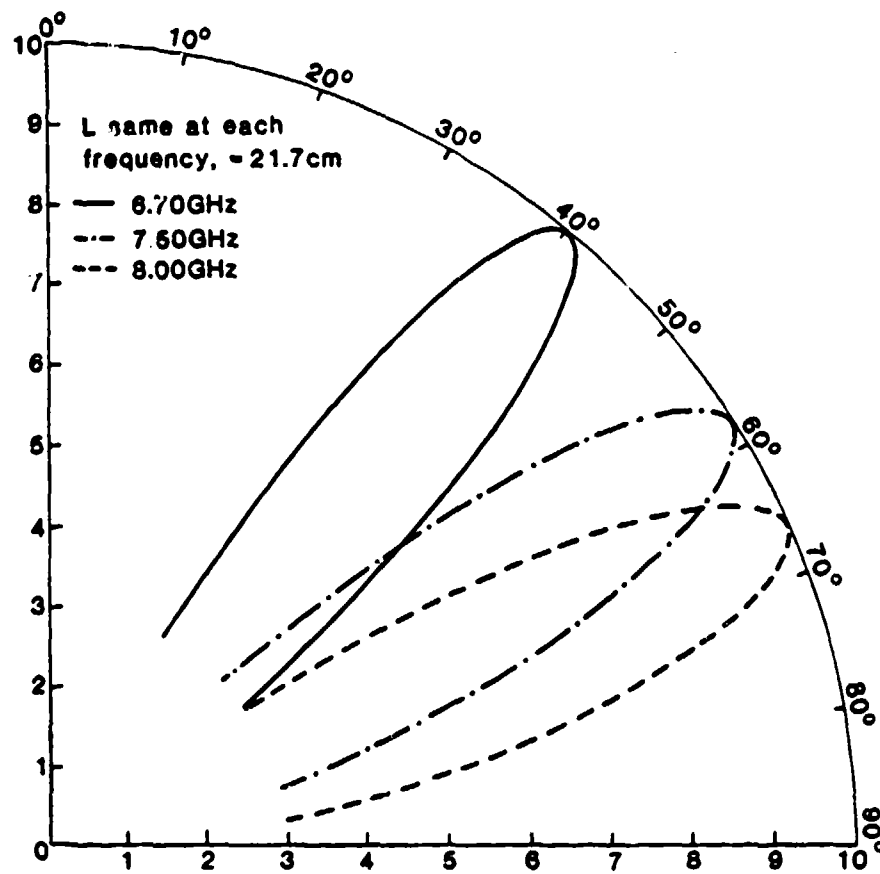


Fig. 9.40 Polar plots of normalized far field for a specific microstrip leaky-wave antenna for three different frequencies when the antenna length is maintained constant. These plots illustrate the effect of frequency scan on a given antenna.

they were in Fig. 9.40, and the beam widths $\Delta\theta$ are of course different. A quantitative comparison shows

<u>f in GHz</u>	<u>θ_m</u>	<u>$\Delta\theta$</u>	<u>L</u>
6.70	40.2°	14.0°	21.7 cm
7.50	61.1°	6.6°	65.6 cm
8.00	74.7°	3.4°	215.1 cm

It is therefore possible to achieve fairly narrow beams with these leaky-wave strip antennas, but only for angles fairly far away from broadside.

To aid in achieving an improved overall perspective with respect to a potential design, we include two additional figures, Figs. 9.42 and 9.43. In Fig. 9.42, we present the strip length L required for the antenna to radiate 90% of the power, as a function of frequency, when the cross-section dimensions are those used by Menzel. The angle θ_m of maximum radiation and the beam width $\Delta\theta$ as a function of frequency are shown in Fig. 9.43. The curves were computed from the simple rule-of-thumb relations (2.27), (2.28) and (2.29), also presented on the figure. The numbers are not as accurate for patterns with wide beams, but those for θ_m are very good for narrow beams. The values for $\Delta\theta$ depend on the actual aperture distribution. The numbers on the curve in Fig. 9.43 are based on the simplest form of relation (2.29), which reflects an "average" tapered distribution; $\Delta\theta$ is then given in radians and must be multiplied by $180/\pi$ to yield the angle in degrees. For an aperture distribution that is exponentially decaying to 0.10 of its initial power level, one should multiply the simple expression given for $\Delta\theta$ by 0.91; the resulting angles will then be accurate to three significant figures. The numbers for $\Delta\theta$ given in Fig. 9.43 are therefore 10% too large when we are concerned with microstrip line strip antennas that have untapered geometries.

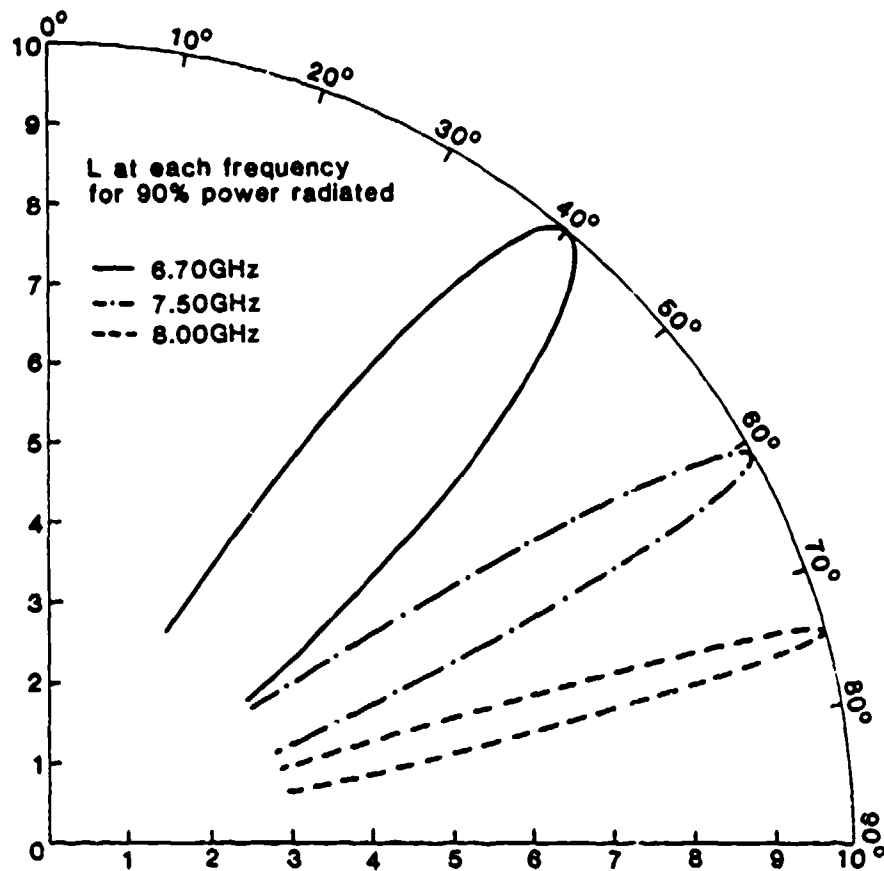


Fig. 9.41

Same as in Fig. 9.40, except that now the lengths are changed for each of the three frequencies to correspond to 90% power radiation, so that different beam widths are obtained.

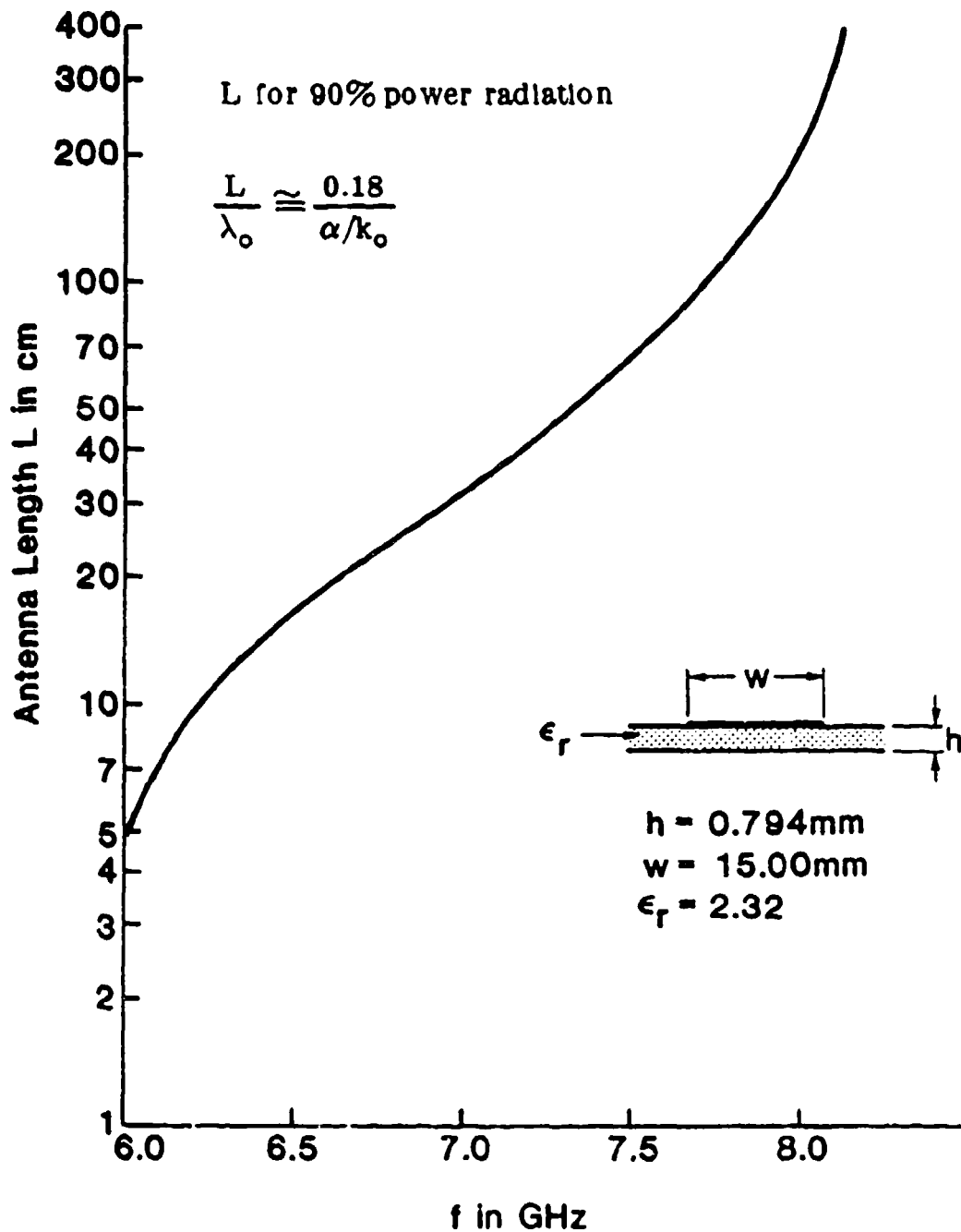


Fig. 9.42 Curve of microstrip leaky-wave antenna length L for 90% power radiation as a function of frequency for a specific cross section, that employed by Menzel [27].

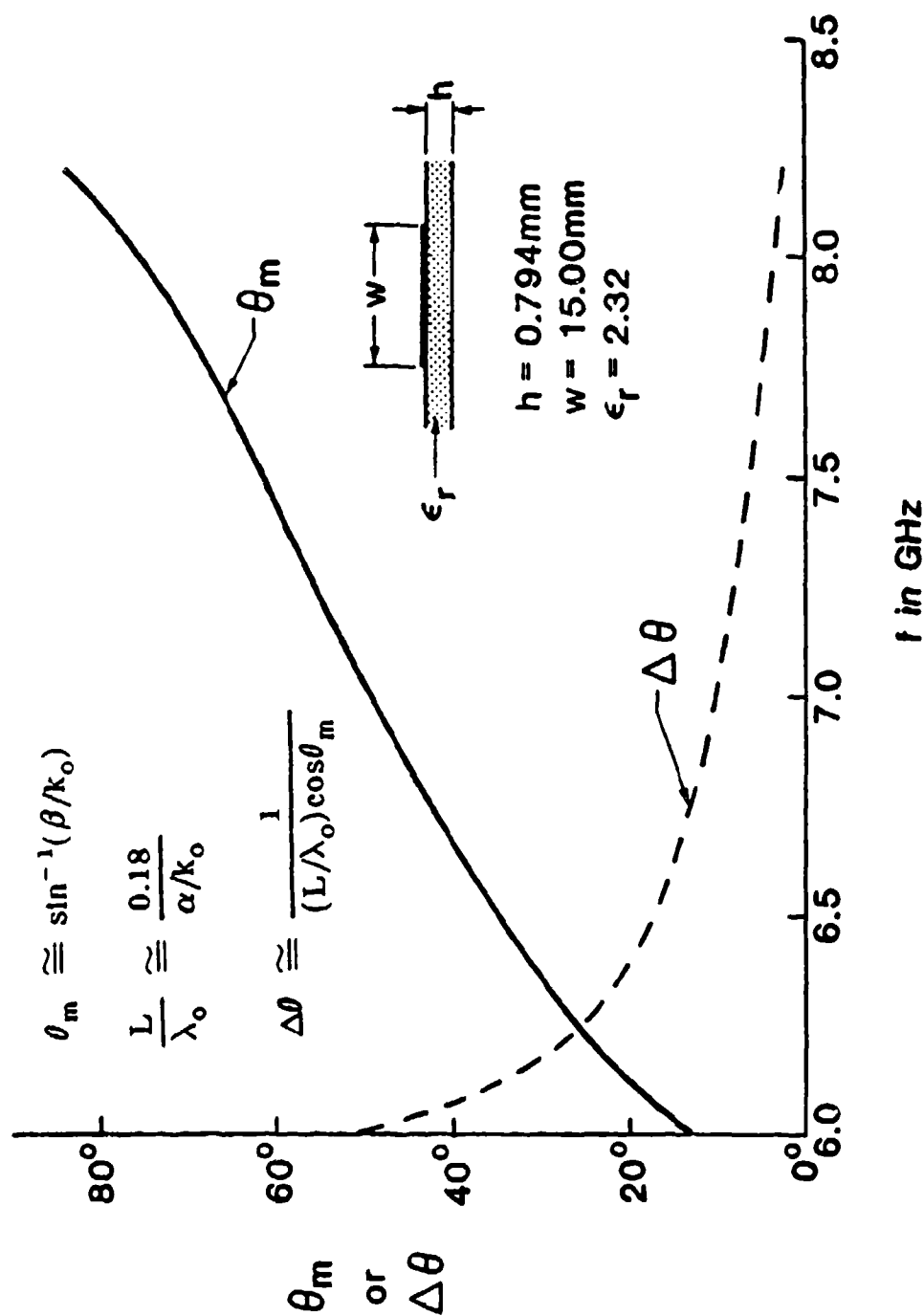


Fig. 9.43 Curves of angle θ_m for maximum radiation and beam width $\Delta\theta$ as a function of frequency for the cross section employed by Menzel [27].

X.	A NOVEL ARRAY OF PRINTED-CIRCUIT UNIFORM LEAKY-WAVE LINE SOURCES	367
A.	DESCRIPTION AND OPERATION OF THE ARRAY	369
	1. Evolution of the Array Structure	369
	2. Principle of Operation	371
B.	DERIVATION OF THE EQUIVALENT NETWORK FOR THE CONSTITUENT TEE JUNCTION	374
	1. Can the Network Form be Symmetrical?	375
	2. How the Dielectric Filling in the Main Guide is Taken into Account	376
	a. Symmetric Magnetic Field Excitation	377
	b. Symmetric Electric Field Excitation	380
	c. Small Aperture Calculation for B_a/Y_o	382
	3. Putting Together the Remaining Pieces	385
	a. The Stub Guide Contribution B_s/Y_o	385
	b. The Turns Ratio n_{cs}	387
	c. The Complete Network	390
C.	TRANSVERSE EQUIVALENT NETWORK FOR THE ARRAY OF PRINTED-CIRCUIT LINE SOURCES	393
	1. Unit Cell Properties	393
	2. Complete Transverse Equivalent Network	396
	3. The Dispersion Relation	398
D.	PERFORMANCE WITHOUT CROSS-PLANE SCAN	401
	1. Variations with Dimensional Ratios	402
	2. Variations with Frequency	419
E.	EFFECTS OF CROSS-PLANE SCANNING	434
	1. Small Cross-Plane Scan Angles	437
	2. Large Cross-Plane Scan Angles	443
	a. Variations with Stub Guide Height	443
	b. Variations with Slit Location	446
	3. Variations with Imposed Phase Shift	449
	a. Wavenumber Variations	449
	b. Conical Scan Dependence	456

X. A NOVEL ARRAY OF PRINTED-CIRCUIT UNIFORM LEAKY-WAVE LINE SOURCES

(With: Prof. P. Lampariello and Mr. F. Frezza
University of Rome, "La Sapienza," Italy)

The array described in this chapter provides a two-dimensional scan capability of the type discussed in Chap. II and described in detail in Chap. IV, where the line-source elements are NRD guides. In the present array, the leaky-wave line-source elements are in themselves new, being a printed-circuit version of what is basically the offset-groove-guide line-source antenna discussed in Chaps. VII and VIII. It evolved as a cross between that antenna and the uniform microstrip leaky-wave antenna treated in Chap. IX. The evolution of the new array, and its principle of operation, are described in Sec. A below.

The basic theoretical approach employed in the analysis of the new array is the unit-cell approach explained in Chap. II and applied in Chap. IV. However, the transverse equivalent network that is representative of this unit cell differs in several important ways from the one used in Chap. VII for the offset-groove-guide antenna. The basic tee junction network utilized there required some fundamental modifications before it could be used here because, among other features, the cross section now contains two different media and includes the periodic waveguide section. Section B contains the derivations for the elements of this modified tee junction network; the incorporation of the network into the overall transverse equivalent network, and expressions for the resulting dispersion relation, are presented in Sec. C.

From the dispersion relation, we obtain numerical values for the array performance. We first examine the parametric dependences for the simpler case for which there is no cross-plane scanning. Scanning is then possible in elevation only, but we study the radiation behavior as various dimensions are changed, and also as a function of frequency. These important results, which are presented in Sec. D, are required before any antenna designs can proceed.

The performance of the array when scanning is performed in the cross plane, resulting in conical two-dimensional scan, is described in detail in Sec. E. Several interesting and important effects occur during such scanning. They include the variation of the leakage rate with the height of the array baffles, possible coupling to another set of leaky modes, the so-called channel-guide modes, deviation from conical

scan under some conditions, and the possibility of finding blind spots. Many of these same effects were noted in Chap. IV, for the array of asymmetric NRD guide line sources, but interesting differences arise. For both arrays, however, no blind spots were found, and both are characterized by negligible cross polarization and the absence of grating lobes.

(After the completion of this chapter, it was found that the numerical values presented in this chapter were obtained using a dispersion relation that contained an error in a factor of 2. The numerical values for the phase constant are affected only slightly, but the values for the leakage constant should be 50% to 100% higher than the ones shown here. All the qualitative behaviors are the same as those shown here, and all the conclusions regarding the array performance are completely unaffected. When the contents of this chapter are submitted for publication, the correct numerical values will be included. It should be added that all of the equations presented here, including those pertaining to the dispersion relation, are correct.)

A. DESCRIPTION AND OPERATION OF THE ARRAY

1. Evolution of the Array Structure

A cross-section view of the array appears in Fig. 10.1. It is seen to consist of a parallel array of leaky-wave line sources, with each line source fed from one end, and with some imposed phase shift between them to produce the scanning in the cross plane. As explained previously for the array in Chap. IV, scanning in the elevation plane is provided by a frequency scan or an electronic scan of the leaky-wave line source, whereas scanning in the other plane is obtained in the usual phased-array manner. The combination of techniques produces a pencil beam that can be scanned over a sector of space in a conical scan fashion.

The leaky-wave line sources themselves are new. The motivation for a printed-circuit form of array arose as a result of the study in Chap. IX, where we obtained a uniform microstrip line leaky-wave line source that had a particularly simple form, consisting only of a length of uniform microstrip line operated in its first higher mode. A linear array of such line sources would be simple in form but less simple to feed. In addition, it is likely that blind spots would occur as the beam is scanned in the cross plane; however, these blind spots would most probably be eliminated by the introduction of metal baffles between the line sources.

After further manipulation of the location of the line sources relative to the baffles, it became clear that the simplest and neatest arrangement, particularly when feed problems are taken into account, is the structure whose cross section is shown in Fig. 10.1. By comparing a line source in the array with the structure in the lower part of Fig. 7.1, or the upper part of Fig. 7.4, we note that the line source in Fig. 10.1 closely resembles a printed-circuit version of the offset-groove-guide leaky-wave antenna. We therefore began with an array of microstrip uniform-strip line sources, and after a sequence of modifications emerged with an array of modified offset-groove-guide line sources. In that sense, the array in Fig. 10.1 is a combination of the two types of line source.

Despite its manner of evolution, the individual line source in the printed-circuit array in Fig. 10.1 may best be viewed as a flat dielectric-filled rectangular waveguide with an unsymmetrical continuous slit in its top wall. That point of view lends itself to an easy understanding of the principle of operation, as described immediately below.

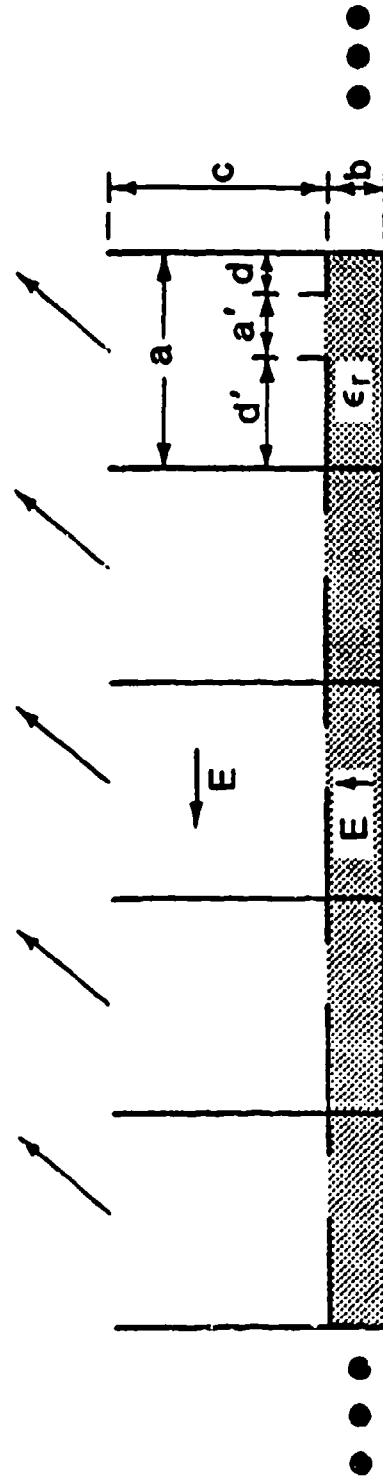


Fig. 10.1 Cross section of the linear phased array of novel leaky-wave line sources. The line sources are each fed from one end, with some imposed phase shift between each one so that scanning can be achieved in the cross plane, as shown in the figure.

2. Principle of Operation

The individual line source itself is indicated in Fig. 10.2, and we shall now view it as a dielectric-filled rectangular waveguide coupled by a slit in its top wall to an upper air-filled stub guide of finite height. Width a must be chosen so as to satisfy two conditions:

- (a) the TE_{10} mode with its vertical electric field in the dielectric-filled rectangular waveguide is *above* cutoff, and
- (b) the mode in the parallel-plate waveguide stub region with vertical electric field is *below* cutoff.

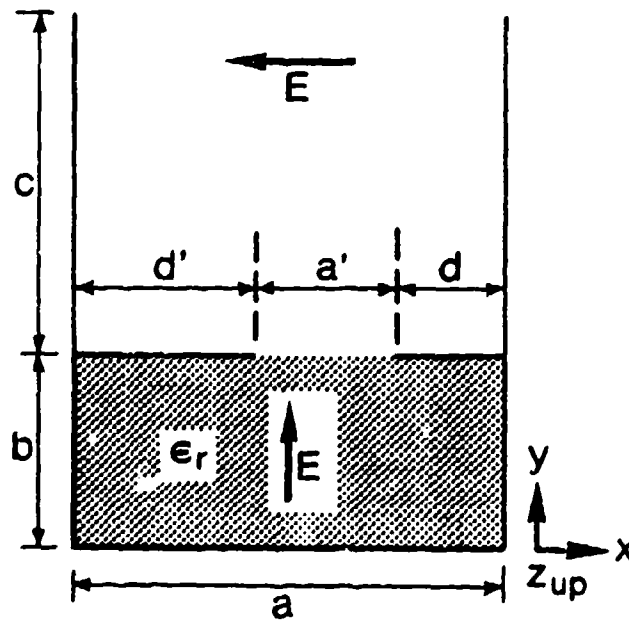


Fig. 10.2 Cross section of the line source employed in the array in Fig. 10.1.

When there is no variation along the axial direction z (along the slit), these conditions become

$$\left(\lambda_o / 2 \sqrt{\epsilon_r} \right) < a < \left(\lambda_o / 2 \right) ; \quad (10.1)$$

when such variation is present, as in our case, (10.1) becomes modified slightly to include the longitudinal phase constant β . Conditions (10.1) then become

$$\frac{\lambda_o / 2 \sqrt{\epsilon_r}}{\left[1 - (\beta / k_o)^2 \right]^{1/2}} < a < \frac{\lambda_o / 2}{\left[1 - (\beta / k_o)^2 \right]^{1/2}} \quad (10.2)$$

The rectangular waveguide, which is fed from one end, then leaks through the slit into the parallel-plate stub guide above. The asymmetric location of the slit excites both a horizontal and a vertical electric field in the stub region. The horizontal electric field corresponds to a TEM mode that travels up at an angle between the parallel plates of length c , and radiates from the open end at the top. The second condition on width a causes the mode with vertical electric field to be below cutoff, so that the radiation into space has essentially *pure* horizontal electric field polarization.

When the line source in Fig. 10.2 is operated individually, its radiated beam can be scanned in elevation either by changing the frequency or by modifying the value of β by electronic means. The angle θ_m of the beam maximum is given by β / k_o and the width of the beam in elevation is proportional to α / k_o ; simple expressions that relate these quantities are given in Chap. II as (2.27) to (2.29). Although the beam is narrow in the elevation plane, it is of course wide in the cross plane. Arranging the line sources in the form of the array shown in Fig. 10.1 will narrow the beam in the cross plane in proportion to the number of line sources in the array. If phase shifts are introduced between each line source, the beam will then be scanned in the cross plane, and therefore in azimuth, in proportion to the phase shift. The arrows in Fig. 10.1 indicate a typical beam scan due to this cause.

It should also be noted that the second of the two conditions on width a eliminates any grating lobes with respect to scan in the cross plane. To be completely accurate, that condition should also include the phase shift itself. If the phase shift per unit cell is $k_{xop} a$, then the fully accurate expression is given by (2.8) of Chap. II, which is repeated here for convenience:

$$a \leq \frac{\lambda_o}{\left[1 - (\beta/k_o)^2\right]^{1/2} + (k_{xop}/k_o)} \quad (10.3)$$

for grating lobes to be avoided.

The structure in Fig. 10.1 would be neater and simpler if the stubs were not present. The antenna would then still radiate, but the radiation would be cross polarized. In addition, there would very likely be blind spots present in the array application. *With* the stubs present, however, our accurate analysis indicates that *no blindness effects occur*. The stubs are a structural nuisance, of course, but they serve to eliminate both cross polarization and blindness problems. It is highly likely that the introduction of such stubs into other forms of phased arrays (where scanning in both planes is obtained using phase shifters) would also produce both benefits and thereby improve performance.

If the slit were centered within width a there would be no radiation. Small shifts of the slit off center result in small leakage rates, whereas larger shifts result in larger leakage per unit length. Since the width of the radiated beam is directly proportional to this leakage rate, we have available a very simple mechanism to control the beam width. Furthermore, the beam width can readily be varied over a wide range by simply changing the location of the slit within the width a . The structure therefore yields versatile performance in addition to pure polarization, no grating lobes, and no blind spots.

B. DERIVATION OF THE EQUIVALENT NETWORK FOR THE CONSTITUENT TEE JUNCTION

In order to obtain numerical information regarding the performance properties of the array of printed-circuit line sources under scan conditions, we need to determine the transverse equivalent network for the array structure, and from the network to derive the dispersion relation for the propagation characteristics. A key constituent of the required transverse equivalent network is a representation of the tee junction formed by the asymmetrical slit that couples the lower dielectric-filled region and the upper air-filled stub guide. The same geometric form occurs in the individual line source (Fig. 10.2) and in the array (Fig. 10.1). That constituent E-plane tee junction is shown in Fig. 10.3.

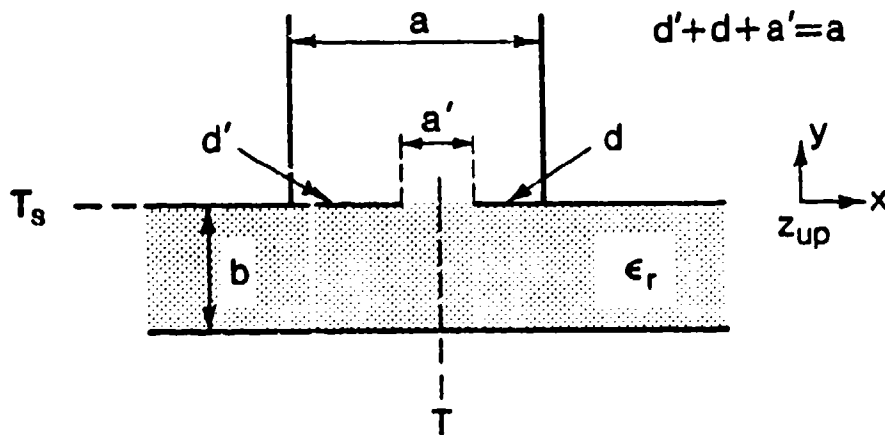


Fig. 10.3 The constituent tee junction that appears in the cross sections of both the line source in Fig. 10.2 and the full array in Fig. 10.1.

This tee junction is similar in a basic way to the tee junction that is a constituent of the offset-groove-guide antenna treated in Chap. VII. That constituent tee junction is seen in Fig. 5.2 of Chap. V, and the equivalent network representation for it is the one

shown in Fig. 5.3, and discussed in detail in Chap. V. Its incorporation into the transverse equivalent network for the offset-groove-guide antenna is exhibited in Fig. 7.4 of Chap. VII. Despite the basic similarity between the tee junctions in Fig. 5.3 and Fig. 10.3, the one in Fig. 10.3 differs from the other one in several important ways. First, the main guide portion in Fig. 10.3 is dielectric-filled; next, the aperture is not wide open, but contains a slit; and finally, the slit is not centered. The added complications in the structure in Fig. 10.3 require a series of detailed considerations with respect to whether or not the equivalent network in Fig. 5.4 can be modified appropriately so as to be valid for the structure in Fig. 10.3. It turns out that such modifications can indeed be made, not rigorously but to a high degree of accuracy. The reasoning followed, and the derivation of the modifications, are presented here. The resulting network is then incorporated into the transverse equivalent network for the array in Sec. C.

In the discussion below, the series of considerations involved in the derivation of the final network parameters is treated sequentially.

1. Can the Network Form be Symmetrical?

The first problem relates to the *form* of the equivalent network. Can it be symmetrical, even though the structure is not symmetrical, that is, the parallel-plate stub guide is located asymmetrically with respect to the "center" plane T (see Fig. 10.3)?

Let us examine the effects of *antisymmetric* and *symmetric* electric field excitations in the main guide portion of the tee structure. First, for *antisymmetric excitation* the plane T would become an electric wall, or a short-circuit plane, as indicated in Fig. 10.4. The position of the stub guide (moving it over or not) would not change the character of that electric wall because the "TEM mode at an angle" that propagates in the stub guide has its electric field perpendicular to that plane. The effective susceptance of the coupling slit will change if the stub guide is shifted over, but nothing else will be affected. (We are, of course, assuming that only the lowest mode can be above cutoff in the stub guide.)

We next examine the effects due to *symmetric electric field excitation*, as shown in Fig. 10.5. The plane T then becomes a magnetic wall (open-circuit plane) due to this excitation. An inspection of the field components in the center of the slit region reveals that the H_z components (along the slit), due to the excitation from opposite sides, will cancel, whereas the H_x components (across the slit) and the E_y components will add. Neither of these two components, however, will couple to the dominant

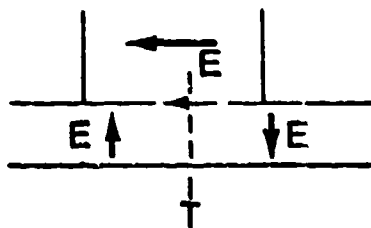


Fig. 10.4 The effect of *anti-symmetric* electric field excitation in the main guide of the tee junction in Fig. 10.3; plane T becomes an electric wall, or short-circuit plane.

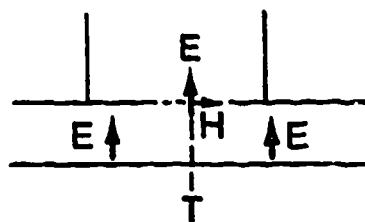


Fig. 10.5 The effect of *symmetric* electric field excitation in the main guide of the tee junction in Fig. 10.3; plane T becomes a magnetic wall, or open-circuit plane.

mode in the stub guide, since these components are orthogonal to those of that dominant mode. The first higher mode, which would be excited, is below cutoff. Thus, this excitation does not produce anything different from what it would if the slit were centered, except for some modifications in the higher mode content of the slit susceptance due to this excitation.

Because of the simple nature of the dominant mode in the stub guide, we have here a situation that permits us to employ a *symmetric form* of equivalent network to characterize a special type of asymmetric tee junction, provided that the expressions for the network elements correctly take the stub guide asymmetry into account.

The network form is basically the same as that in Fig. 5.4, but it is phrased now, in Fig. 10.6, in a slightly more complicated form because of the derivations below. We must obtain expressions for all of these network elements, and we will attempt to use the results we derived earlier in Chap. V wherever possible.

2. How the Dielectric Filling in the Main Guide is Taken Into Account

The main guide portion of the tee junction is filled with dielectric material of dielectric constant ϵ_r , and our second problem is how to take this fact into account in some simple way, or ways, so that we do not have to reevaluate the various susceptances. Some approximations are required, but we must also assess how important they are.

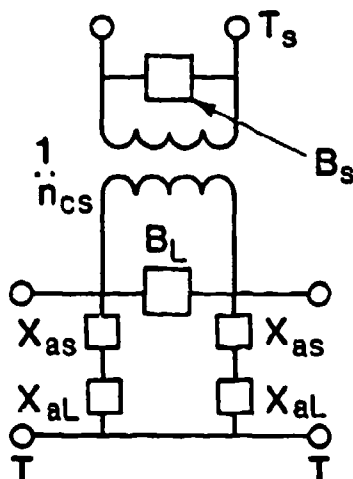


Fig. 10.6

The equivalent network form that is used to represent the constituent tee junction in Fig. 10.3. The form is symmetrical even though the structure is not because of the reasons given in the text. The elements X_{as} and X_{al} are utilized in reactance form to aid in the derivations to follow.

Since the network parameters are related to the type of main guide excitation, we treat the two basic excitation types separately.

a. Symmetric Magnetic Field Excitation

We begin with the *symmetric magnetic field* excitation case (SH case), which is of course the same as the *antisymmetric electric field* excitation case. An electric field is excited directly across the slit, as seen in Fig. 10.4, and this slit field will in turn excite *higher TM modes* in the main guide section (and in the stub guide portion as well).

A short-circuit bisection of the network in Fig. 10.6, corresponding to this field excitation, yields a two-port network with a shunt susceptance equal to

$$2B_L + (1/n_{cs}^2)2B_x + 1/(X_{as} + X_{aL}) = 2B_{sh} \quad (10.4)$$

where the subscript *sh* signifies "symmetric magnetic". An expression in variational form for B_{sh} is given in symbolic notation in (5.6) of Chap. V; more explicitly, it is

$$j \frac{B_{sh}}{Y_o} = \frac{j \iiint \underline{M}_{sh} \cdot (\underline{B}_L + \underline{B}_s) \cdot \underline{M}_{sh}^* dS dS'}{Y_o \left| \iint \underline{M}_{sh} \cdot \underline{h}^{(1)*} dS \right|^2} \quad (10.5)$$

where

$$\underline{M}_{sh}(x, z) = \underline{y}_o \times \underline{E}_{slit} \quad (10.6)$$

$$\underline{h}^{(1)}(x, z) = \underline{h} \cos k_x x \quad (10.7)$$

and the *z* dependence in both \underline{M}_{sh} and $\underline{h}^{(1)}$ is $\exp(k_z z)$. The integrations are over the slit in *x* and per unit length in *z*, and *x* and *y* begin at the center of the slit. The Green's function dyadics \underline{B}_L and \underline{B}_s correspond to the main guide and the stub guide, respectively.

These Green's function dyadics are proportional to the sum of the higher modes in each of the two regions, in the form

$$\underline{B} \propto \sum Y_n \underline{h}_n \underline{h}_n^* \quad (10.8)$$

where the \underline{h}_n terms are the mode functions for the higher modes in each region, and Y_n represents the higher mode characteristic (or modal) admittance for mode *n*. As long as the waveguide cross section is filled with dielectric material or is empty, the \underline{h}_n terms are independent of the dielectric constant ϵ_r . The Y_n terms, however, do depend on ϵ_r .

We wish first to consider \underline{B}_L for the *main guide*, which is filled with dielectric material. Since, for symmetric magnetic field excitation, the *higher modes* excited in the main guide are *TM modes*, Y_n takes the form

$$Y_n = \frac{\omega \epsilon_0 \epsilon_r}{k_{xn}} = \left[j \frac{\omega \epsilon_0}{|k_{xn}|} \right] \epsilon_r \quad (10.9)$$

Since only higher TM modes are excited, the ϵ_r factor will multiply every term in the sum in (10.8), and it can therefore be taken out of the sum. We may therefore write

$$(B_L)_{\epsilon_r} = \epsilon_r (B_L)_{\epsilon_r=1} \quad (10.10)$$

For the *main guide portion* of B_{sh}/Y_o , therefore, we have

$$\left[(B_{sh}/Y_o)_L \right]_{\epsilon_r} = \epsilon_r \left[(B_{sh}/Y_o)_L \right]_{\epsilon_r=1} \quad (10.11)$$

where the result for $\epsilon_r = 1$ is what we have used previously, as in (7.2) of Chap. VII, for example. The explicit expression then becomes

$$\left[\left(\frac{B_{sh}}{Y_o} \right)_L \right]_{\epsilon_r} = \left[\frac{B_L}{Y_o} + \frac{1}{2} \frac{B_a}{Y_o} \right]_{\epsilon_r} = \frac{\epsilon_r}{n_c^2} \left(\frac{k_x b}{\pi} \right) \left[\ln \left(1.43 \frac{b}{a'} \right) + \frac{1}{2} \left(\frac{k_x b}{\pi} \right)^2 \right] \quad (10.12)$$

where

$$n_c = \frac{\sin k_x a'/2}{k_x a'/2} \quad (10.13)$$

which is the same as (7.3). The various dimensions are indicated in Fig. 10.3.

It is important to recognize that two *approximations* have been introduced into the reasoning above. The first is the implicit assumption that the aperture field remains the same when the dielectric medium is inserted into the main guide region. The field does actually change slightly, but for variational expressions, as used here, the effect of the change should be minimal.

The second assumption is that $|k_{xn}|$ in (10.9) is independent of ϵ_r for all higher modes. Actually, $|k_{xn}|$ is given by

$$|k_{xn}| = \left[k_{in}^2 - k_o^2 \epsilon_r \right]^{1/2} \quad (10.14)$$

where $k_{in}^2 = k_{yn}^2 + k_z^2$ in the main guide parallel-plate region. For modes with very

high values of n , $k_{m1}^2 \gg k_o^2 \epsilon_r$, so that $|k_{xm}| \approx k_{m1} \approx k_{ym} = n\pi/b$, which is certainly independent of ϵ_r . But, for the first few higher modes, k_{m1}^2 is not much greater than $k_o^2 \epsilon_r$, and the $|k_{xm}|$ values for these modes may be slightly dependent on ϵ_r . The error in (10.11) is expected to be small.

For the *stub guide portion* of B_{sh} we do not multiply by ϵ_r because the stub guide region is air-filled. As an additional consideration, the stub guide structure used in Chaps. VI and VII resembles that in Fig. 5.1 (or Fig. 5.2), whereas the one we employ now, in Fig. 10.3, is of the type in Fig. 5.4. The contribution to B_{sh} from the stub guide in Chaps. VI and VII was therefore taken to be zero, but now it is clearly finite and non-negligible. In fact, it can be taken from a result appearing in the Waveguide Handbook [8], as described in Chap. V; the contribution is derived later in this section.

b. Symmetric Electric Field Excitation

We next consider the effect of *symmetric* electric field excitation, which produces a magnetic wall at T in Fig. 10.5, with E_y and H_x present at the midplane of the slit. This excitation produces only *higher TE modes* in the main and stub guides, in contrast to the previously considered excitation, which created only higher TM modes.

This excitation corresponds to an open-circuit bisection of the network in Fig. 10.6, and it produces a one-port termination, of reactance

$$X_{se} = X_{aL} + X_{as} \quad (10.15)$$

where the subscript *se* means "symmetric electric". The expression in variational form comparable to (10.5) for B_{sh} is

$$j \frac{X_{se}}{Z_o} = \frac{j \iiint \underline{M}_{se} \cdot (\underline{B}_L + \underline{B}_S) \cdot \underline{M}_{se}^* dS dS'}{Y_o \left| \iint \underline{M}_{se} \cdot \underline{h}^{(2)*} dS \right|^2} \quad (10.16)$$

where

$$\underline{M}_{se}(x, z) = \underline{y}_o \times \underline{E}_{slit} \quad (10.17)$$

$$\underline{h}^{(2)}(x, z) = \underline{h} \sin k_x x \quad (10.18)$$

The other comments made after (10.7) are applicable here as well. It should be added

that X_{se}/Z_o is the same as the negative reciprocal of B_a/Y_o , a fact that will be utilized below. We use the reactance form now because we wish to consider separately the contributions from the main guide and the stub guide.

The Green's function dyadics are still of the form in (10.8), proportional to the sum of the higher modes. Again, the mode functions are independent of the dielectric constant ϵ_r , so that only the Y_n terms need be considered. Since the discontinuity excites higher TE modes as a result of symmetric electric field main guide excitation, we write for Y_n

$$Y_n = \frac{k_{xn}}{\omega\mu_o} = -j \frac{|k_{xn}|}{\omega\mu_o} \quad (10.19)$$

which does *not* involve ϵ_r explicitly. Therefore, there is no factor of ϵ_r to be concerned about. Of course, $|k_{xn}|$ is still slightly dependent on ϵ_r for the lowest few of these higher modes, and we should remember that we have made such an approximation. Within this approximation, however, the contribution to X_{se}/Z_o from the main guide, which is X_{aL}/Z_o , should be the *same* whether or not the dielectric is present.

In the derivation of the expression for $B_a/Y_o (= -1/(X_{se}/Z_o))$ used in Chaps. VI and VII, the dyadic Green's functions in (10.16) were each approximated by dyadic half-space Green's functions. The net effect of that approximation is to neglect the presence of the nearby walls. The terms B_L and B_S are thus taken to be the same in (10.16), and the contributions from each to the total stored power are also the *same*. Thus, the expression for X_{aL}/Z_o (for the main guide) and that for X_{as}/Z_o (for the stub guide) turn out to be identical, consistent with this approximation. In addition, we showed above that the expressions are essentially unaffected by whether or not the main guide region is filled with dielectric material. We can therefore write

$$X_{aL}/Z_o = X_{as}/Z_o = \frac{1}{2} X_{se}/Z_o \quad (10.20)$$

and

$$\frac{B_a}{Y_o} = - \frac{1}{X_{se}/Z_o} \quad (10.21)$$

The final expression for B_a/Y_o is thus the same as the one given as (7.1) of Chap. VII, namely,

$$\frac{B_a}{Y_o} = -\frac{\pi}{16} \frac{a'}{b} \left(k_x \frac{a'}{2} \right) J_o^2 \left(k_x \frac{a'}{2} \right) \quad (10.22)$$

The approximation which substitutes the half-space Green's function for the actual guide Green's function may at first seem severe, but the approximation is a good one because the aperture field for symmetric electric field excitation is confined primarily to the region near the slit. In Chap. V, expression (5.3) for B_a/Y_o , which was derived employing this approximation, is applied to the case of a slit-coupled tee junction in rectangular waveguide. Table 5.1 presents comparisons between numerical values computed using (5.3) and measured values for three different slit widths, and the agreement is seen to be very good.

Lastly, it is sometimes necessary to have available an expression for network element B_L/Y_o separately. Since B_a/Y_o is not affected by the presence or absence of dielectric material in the main guide, we may write

$$\left[\frac{B_L}{Y_o} \right]_{\epsilon_r} = \left[\frac{B_L}{Y_o} + \frac{1}{2} \frac{B_a}{Y_o} \right]_{\epsilon_r} - \frac{1}{2} \frac{B_a}{Y_o} \quad (10.23)$$

where explicit expressions for the two terms on the right-hand side of (10.23) appear in (10.12) and (10.22).

c. Small Aperture Calculation for B_a/Y_o

This subsection is a parenthetical one, motivated by the use of half-space Green's functions in [10.16] for the evaluation of B_a/Y_o . Since small aperture theory is in part based on a similar assumption, it is of interest to see what result for B_a/Y_o would be furnished by that theory.

The geometry under consideration is the lower portion of Fig. 10.3, which consists of the main guide portion of the tee junction; the field excitation employed is the symmetric electric field excitation. We shall use the simple procedure summarized in [46], and the formulas presented therein, in the derivation of the susceptance for this longitudinal aperture discontinuity. As a result of the symmetric electric field excitation, the field components present in the slit are H_x and E_y . The expression for B_a/Y_o then involves only two terms:

$$B_a/Y_o = \omega\mu_o Y_o M_x h_{xo} \dot{h}_{xo} - \omega\epsilon_o \epsilon_r Z_o P_y e_{yo} \dot{e}_{yo} \quad (10.24)$$

where h_{xo} and e_{yo} are the mode functions for the incident dominant mode evaluated at the center of the slit, M_x and P_y are the magnetic and electric polarizabilities of the slit, and $Y_o (= 1/Z_o)$ is the dominant mode characteristic admittance.

In (10.24) the characteristic admittance Y_o corresponds to that of the dominant mode, which is a TE mode since the TEM mode is traveling at an angle. We therefore have

$$Y_o = 1/Z_o = k_x/\omega\mu_o \quad (10.25)$$

The polarizabilities are those for a slit of width a' ; using notation consistent with that in (10.24), we write

$$M_x = P_y = \frac{\pi}{16} (a')^2 \quad (10.26)$$

The remaining terms are the mode functions, which must be normalized appropriately.

Following the notation in [46], we write

$$\underline{e}(z) = \underline{e}_o E_o e^{-jk_z z} \quad (10.27)$$

since there is no variation in the y direction. Using (10.27) in the normalization condition

$$\int_0^b \int_0^b \underline{e} \cdot \underline{e}^* dy dz = 1 \quad (10.28)$$

yields

$$e_y(z) = \frac{1}{\sqrt{b}} e^{-jk_z z} \quad (10.29)$$

and

$$e_{yo} \dot{e}_{yo}^* = 1/b \quad (10.30)$$

For mode function h_x , which is a bit more complicated, we have from (5) of [46],

$$h_x(z) = -j \frac{Z_o}{\omega \mu_o} k_c^2 \psi(z) \quad (10.31)$$

where $k_c = k_z$ is the cutoff wavenumber, and ψ is subject to the normalization

$$\iint \psi \psi^* dS = 1/k_z^2 \quad (10.32)$$

From (32) of [46], we have

$$\psi(z) = \frac{1}{k_z \sqrt{b}} e^{-jk_z z} \quad (10.33)$$

so that h_x becomes

$$h_x(z) = -j \frac{k_z}{k_x} \frac{1}{\sqrt{b}} e^{-jk_z z} \quad (10.34)$$

on use of (10.25), and we find

$$h_{xo} h_{xo}^* = \left(\frac{k_z}{k_x} \right)^2 \frac{1}{b} \quad (10.35)$$

When (10.25), (10.26), (10.30) and (10.35) are inserted into (10.24) we obtain

$$\frac{B_a}{Y_o} = \frac{\pi}{16} \frac{(a')^2}{bk_x} (k_z^2 - \epsilon_r k_o^2) \quad (10.36)$$

In the dielectric-filled main guide parallel-plate region we have

$$k_o^2 \epsilon_r - k_z^2 = k_x^2 \quad (10.37)$$

so that B_a/Y_o becomes

$$\frac{B_a}{Y_o} = -\frac{\pi}{8} \frac{a'}{b} \left(\frac{k_x a'}{2} \right) \quad (10.38)$$

We recall that the geometry for which (10.38) is valid is only the main guide portion of the tee junction. B_a/Y_o in (10.38) therefore corresponds to $-1/(X_{aL}/Z_o)$. When we utilize (10.20) we recognize that the value for B_a/Y_o that is valid for *both* the main guide and stub guide contributions is actually one-half of that in (10.38), namely,

$$\frac{B_a}{Y_o} = -\frac{\pi}{16} \frac{a'}{b} \left(\frac{k_x a'}{2} \right) \quad (10.39)$$

Before comparing this final result with what was derived earlier, we should note that result (10.38) is independent of ϵ_r , even though the main guide was taken to be dielectric-filled. If it were air-filled, then the ϵ_r factor in the second term in (10.24) would be unity, so that the ϵ_r that appears in both (10.36) and (10.37) would also become unity. Thus, any influence due to ϵ_r is removed, consistent with our earlier conclusion.

Now we wish to compare the small aperture result (10.39) with the variational result (10.22). We note that they differ only in the added factor $J_o^2(k_x a'/2)$ in (10.22), which accounts for larger slit widths. That factor is an important one that provides significantly better numerical agreement with measurements in Table 5.1, for example, but it is interesting that the simple and easily derived small aperture expression contains all the major dependences, and agrees asymptotically with the more accurate result when the slit width a' is small.

3. Putting Together the Remaining Pieces

a. The Stub Guide Contribution B_s/Y_o

Variational expression (10.5) for B_{sh}/Y_o consists of two parts, one involving B_L , the dyadic Green's function for the main guide, and the other based on B_s , for the stub guide. The considerations in subsection 2.a concerned only the first part; the derivation yielded an expression for $(B_L/Y_o + B_a/2Y_o)$ that takes into account the presence of dielectric filling in the main guide. It was stated there that the stub guide

contribution would be considered later, but that in any case it would not be multiplied by ϵ_r because the stub guide region is air-filled.

There are two features of concern in this connection. One is how an expression for B_s/Y_o can be obtained from information already available in the literature, and the second involves the fact that the Y_o values for the main and stub guides are not the same.

In Fig. 5.4 of Chap. V a slit-coupled E-plane tee junction is presented in which the upper portion is similar to the upper portion of the structure in Fig. 10.3, the differences between them being the geometry in the direction perpendicular to the page and the fact that the slit is centered in Fig. 5.4 but asymmetrically located in Fig. 10.3. Those differences, however, do not affect the approach employed to determine the network parameters. Expression (5.6) is a symbolic representation of (10.5), so that the numerator in (10.5) represents the stored powers on both sides of the slit, with the part involving B_s corresponding to the stored power in the stub guide. It is then explained in Chap. V, by reference to Figs. 5.4 and 5.5, that the stored power in the stub guide is essentially the same as that in one-half of a transverse slit in a waveguide of the same width as the stub guide. If B_t is the susceptance corresponding to the stub guide portion of B_{sh} , and if Y_o is the characteristic admittance of the stub guide, then

$$\frac{B_s}{Y_o} = \frac{1}{2} \frac{B_t}{Y_o} \quad (10.40)$$

where B_t/Y_o is the normalized susceptance of the corresponding transverse slit in a parallel-plate waveguide. Since the slit in Fig. 10.3 is off-center in the stub guide, we require for B_t/Y_o the normalized susceptance of an *asymmetrically* located transverse slit in parallel-plate guide when a TEM mode is incident on it at an angle. That result is given (with the minor substitution of k_y for $2\pi/\lambda_g$) by equation (1a) on p. 218 of the Waveguide Handbook [8]; incorporating that expression into (10.40) we obtain

$$\frac{B_s}{Y_o} = \frac{k_y b}{\pi} \ln \left[\csc \frac{\pi a'}{2a} \csc \frac{\pi}{2a} (a' + 2d') \right] \quad (10.41)$$

using the notation in Fig. 10.3.

We next take into account the fact that the Y_o values for the main and stub guides

are different, and that the denominator of (10.5), which is basically a voltage squared, is also different from that used in the corresponding expression for B_s/Y_o . The denominator of the relation in (10.5) may be written as

$$Y_o \left| \iint \underline{M}_{sh} \cdot \underline{h}^{(1)*} dS \right|^2 = Y_{om} |V_m|^2 \quad (10.42)$$

whereas the corresponding denominator in an expression for B_s/Y_o similar to (10.5) is

$$Y_o \left| \iint \underline{M}_{sh} \cdot \underline{h}_s^* dS \right|^2 = Y_{os} |V_s|^2 \quad (10.43)$$

Then, if we carefully break up (10.5) into its constituent parts, we find

$$\frac{B_{sh}}{Y_{om}} = \left[\frac{B_{sh}}{Y_{om}} \right]_{main\ guide} + \left[\frac{B_{sh}}{Y_{om}} \right]_{stub\ guide} \quad (10.44)$$

where

$$\left[\frac{B_{sh}}{Y_{om}} \right]_{stub\ guide} = \frac{B_s}{Y_{os}} \frac{Y_{os} |V_s|^2}{Y_{om} |V_m|^2} \quad (10.45)$$

since the stored powers (numerators) are the same.

The factor multiplying B_s/Y_{os} in (10.45) can be incorporated into the turns ratio n_{cs} in Fig. 10.6; it is derived below in the next subsection.

b. The Turns Ratio n_{cs}

The factor that multiplies B_s/Y_{os} in (10.45) includes a ratio of characteristic admittances and a ratio of voltage terms. The propagating mode in both the main guide and the stub guide is the same, being a TEM mode propagating at an angle, and therefore a TE mode. The difference between them is that the mode propagation direction is horizontal (x) in the main guide and vertical (y) in the stub guide. The ratio of the characteristic admittances is therefore

$$\frac{Y_{om}}{Y_{os}} = \frac{k_x / \omega \mu_0}{k_y / \omega \mu_0} = \frac{k_x}{k_y} \quad (10.46)$$

In the offset-groove-guide antenna, $k_x = k_y$. Here, because of the dielectric filling of the main guide, they are different and are given by

$$k_x^2 = k_o^2 \epsilon_r - k_z^2 \quad (10.47)$$

$$k_y^2 = k_o^2 - k_z^2 \quad (10.48)$$

The voltage ratio involves the mode functions in both the main and stub guides, and the form of the electric field in the slit. Combining relations (10.42), (10.43) and (10.7), we may write

$$\frac{V_m}{V_s} = \frac{\int_{-a'/2}^{a'/2} \int_0^{a'/2} \underline{M} \cdot \underline{h}^{(1)*} dx dz}{\int_{-a'/2}^{a'/2} \int_0^{a'/2} \underline{M} \cdot \underline{h}_s^* dx dz} \quad (10.49)$$

where

$$\underline{h}^{(1)}(x, z) = \underline{h}_m(z) \cos k_x x \quad (10.50)$$

Mode function \underline{h}_m for the main guide is subject to the same normalization as that shown in (10.28) for \underline{e} ($=\underline{e}_m$); following (10.29), we therefore write for \underline{h}_m

$$\underline{h}_m(z) = \frac{1}{\sqrt{b}} e^{-jk_z z} \quad (10.51)$$

Similarly, but for the stub guide cross section, we have

$$\underline{h}_s(z) = \frac{1}{\sqrt{a}} e^{-jk_z z} \quad (10.52)$$

Both $\underline{h}_m(z)$ and $\underline{h}_s(z)$ have units of per unit length in the z direction.

For simplicity, we assume that the aperture electric field, and therefore \underline{M} from (10.6), is a constant across the slit. The same quantity appears in both numerator and denominator, and the result for V_m/V_s is not sensitive to the form of \underline{M} . This approximation was used previously in the evaluation of n_c in Chap. V, and with success. With this simple approximation, the result for V_m/V_s follows readily on use of (10.50) through (10.52) in (10.49).

When we define turns ratio n_{csn} in the manner

$$\frac{1}{n_{csn}^2} = \frac{Y_{os} |V_s|^2}{Y_{om} |V_m|^2} \quad (10.53)$$

we find, from (10.46) and (10.49),

$$n_{csn} = \frac{\sqrt{k_x a}}{\sqrt{k_y b}} \frac{\sin k_x a'/2}{k_x a'/2} \quad (10.54)$$

Expression (10.54) for n_{csn} permits us to utilize the network in Fig. 10.6 in the most logical and straightforward way. In practice we must work with *normalized* susceptances or reactances, which is the way in which they occur physically. To use n_{csn} in the form (10.54) would then require us (and permit us) to employ *normalized* susceptances in the equivalent network of Fig. 10.6, rather than the artificial *absolute* values for them, which is the customary procedure. Then, we would work only with normalized quantities, and all the susceptances in the stub guide, including B_s and the termination on that guide, would be normalized with respect to Y_{os} of the stub guide; similarly, the quantities B_L , B_a , and the terminations in the main guide would be normalized to Y_{om} of the main guide. The transition between the main guide and the stub guide is absorbed completely into the n_{cs} term.

On the other hand, since it is customary to employ *absolute* susceptances or reactances in equivalent networks, it might cause confusion *not* to do so. It would be prudent, therefore, to leave the susceptances in the networks in absolute form, and modify the turns ratio accordingly. In that case, we would use n_{cs} , rather than n_{csn} , where that last subscript (n) signifies "normalized." The only difference is to leave out the ratio of characteristic admittances in the definition for the turns ratio. If absolute values were to be employed, (10.45) would become

$$\left[B_{sh} \right]_{\substack{\text{stub} \\ \text{guide}}} = B_s \frac{|V_s|^2}{|V_m|^2} \quad (10.55)$$

so that the definition for turns ratio n_{cs} is

$$\frac{1}{n_{cs}^2} = \frac{|V_s|^2}{|V_m|^2} \quad (10.56)$$

and n_{cs} is found to be

$$n_{cs} = n_{csn} \sqrt{k_y/k_x} \quad (10.57)$$

where n_{csn} is given by (10.54).

c. The Complete Network

We are now able to present the final form of the equivalent network for the tee junction shown in Fig. 10.3, and to present expressions for all of the elements in this network. The structure itself differs in several ways from the earlier tee junction employed in Chaps. VI and VII; in particular, the main guide is filled here with dielectric material, and the slit is located asymmetrically within the stub guide, leading to the various complications addressed above.

The final form of the equivalent network is presented in Fig. 10.7. As explained above, we have the alternative of expressing the network elements in Fig. 10.7 in absolute form, which is customary, and then using n_{cs} (as given in (10.57)) for the turns ratio, or employing the normalized form for the network elements and utilizing n_{csn} , as presented in (10.54). We have chosen here to use the absolute form, simply because it is customary; the alternative may cause confusion.

The expressions for the individual network elements emerge naturally in normalized form, and that is the way they are summarized below. To use them in the network in Fig. 10.7, we must multiply them by their characteristic admittances; for example, we must write $B_a = (B_a/Y_{om})Y_{om}$, or $B_s = (B_s/Y_{os})/Y_{os}$. In the transverse resonance relation, derived in Sec. C.3, we encounter the ratio Y_{om}/Y_{os} ,

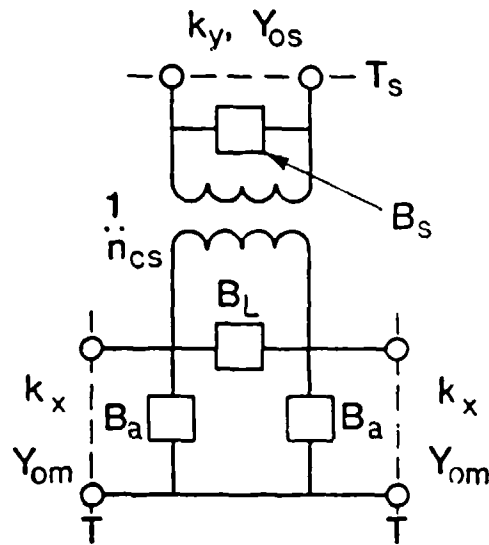


Fig. 10.7 The final form of the equivalent network for the constituent tee junction shown in Fig. 10.3.

which is given below and in (10.46). If we used the normalized form of the elements in the equivalent network, this ratio would not enter explicitly because it is already incorporated into n_{csn} . Either way, of course, one obtains the identical result for the resonance relation.

Normalized expressions for the various network elements in Fig. 10.7 are obtained from (10.22), (10.12), (10.13), (10.23), (10.41) and (10.57). Some have been given explicitly and some not. For convenience, we present all of them in explicit form in the following summary:

$$\frac{B_a}{Y_{om}} = \frac{\pi}{16} \frac{a'}{b} \left(k_x \frac{a'}{2} \right) J_o^2 \left(k_x \frac{a'}{2} \right) \quad (10.58)$$

$$\begin{aligned} \frac{B_L}{Y_{om}} = \frac{\epsilon_r}{n_c^2} \left(\frac{k_x b}{\pi} \right) \left[\lg \left(1.43 \frac{b}{a'} \right) + \frac{1}{2} \left(\frac{k_x b}{\pi} \right)^2 \right] \\ + \frac{\pi}{32} \frac{a'}{b} \left(k_x \frac{a'}{2} \right) J_o^2 \left(k_x \frac{a'}{2} \right) \end{aligned} \quad (10.59)$$

with

$$n_c = \frac{\sin(k_x a'/2)}{k_x a'/2} \quad (10.60)$$

$$\frac{B_s}{Y_{os}} = \frac{k_y b}{\pi} \ln \left[\csc \frac{\pi a'}{2a} \csc \frac{\pi}{2a} (a' + 2d') \right] \quad (10.61)$$

$$n_{cs} = n_c \sqrt{a/b} \quad (10.62)$$

where n_c is given by (10.60).

$$Y_{os}/Y_{om} = k_y/k_x \quad (10.63)$$

$$k_x^2 = k_o^2 \epsilon_r - k_z^2 \quad (10.64)$$

$$k_y^2 = k_o^2 - k_z^2 \quad (10.65)$$

C. TRANSVERSE EQUIVALENT NETWORK FOR THE ARRAY OF PRINTED-CIRCUIT LINE SOURCES

When we use the unit-cell approach to the analysis of the array of leaky-wave line sources, the transverse equivalent network for the array reduces to a transverse equivalent network for a single unit cell. The unit-cell approach is described in general terms in Chap. II, and its application to the array of NRD guide line sources is discussed in detail in Chap. IV. The analysis here of the array of printed-circuit line sources is similar in the main to that employed in Chap. IV, but of course the transverse equivalent network used is quite different. The dispersion relation is substantially different as well, in that here the dispersion relation can be explicitly displayed in an analytic closed form, whereas the analysis in Chap. IV leads via its mode-matching procedure to numerical results directly.

In the discussion below, we first summarize the relevant unit cell properties, then obtain the complete transverse equivalent network, and finally derive the dispersion relation.

1. Unit Cell Properties

In the unit-cell approach, the array is replaced by a single unit cell, where the space above the array is represented by a periodic waveguide with phase-shift walls. When the unit cell is properly characterized, all mutual coupling effects are automatically taken into account. The unit cell for the array in Fig. 10.1 is shown on the left-hand side of Fig. 10.8. The lower portion of this unit cell, with metal outer walls, is the same as the structure of an individual line source of the array, which was presented in Fig. 10.2. The upper portion of the unit cell, with the phase-shift walls, is completely different; the radiating open end in Fig. 10.2 is now replaced by a junction between the parallel-plate stub region and the periodic unit cell with phase-shift walls.

In the transverse resonance that yields the dispersion relation, the transmission direction in the stub and periodic regions is the y direction. The dominant mode in that direction in both of these regions is a TEM mode at an angle. In the stub region, the propagation wavenumber is k_{yos} , where the subscripts o and s refer to "lowest mode" and "stub", respectively; in the periodic region, the wavenumber is k_{yop} , where subscript p means "periodic." In Chap. IV, these wavenumbers were given as k_{yog} and k_{yop} ; here we refer to the air-filled parallel-plate region as a "stub", rather than a "guide." Wavenumber k_{yos} is then related to the free-space wavenumber k_o and the longitudinal (axial) wavenumber k_z by

$$k_{yos}^2 = k_o^2 - k_z^2 \quad (10.66)$$

where $k_z (= \beta - j\alpha)$ is the unknown that we ultimately seek in the analysis. A corresponding expression for the higher modes in that region is

$$k_{yms}^2 = k_o^2 - k_z^2 - (m\pi/a)^2 \quad (10.67)$$

where m is the mode number of the higher mode. Expressions (10.66) and (10.67) are analogous to (4.1) and (4.2).

In the periodic (upper) region, with the phase-shift walls, the lowest mode is a TEM mode that propagates in the y direction, but at an angle in the z direction due to leaky-wave scan in elevation, and at an angle in the x direction corresponding to scan in the cross plane (and hence in azimuth). The wavenumber components in the y and x directions are k_{yop} and k_{xop} , respectively. The value of wavenumber k_{xop} is related to the phase shift Φ_C between the opposite walls of the unit cell of width a , which in turn depends on the phase shift *imposed* between the successive parallel line sources in the array. Thus, we may define

$$\Phi_C = k_{xop} a = \text{phase shift per unit cell} . \quad (10.68)$$

When all the line sources are fed in phase, $k_{xop} = 0$ and there is no scan in the cross plane, and therefore in azimuth. In Sec. E below, we use Φ_C as a measure of the scan in the cross plane.

As explained in Sec. B of Chap. II, and used in Sec. B of Chap. IV, space harmonics are created in the periodic region, where each space harmonic in the x direction corresponds to a mode in the y direction in the unit cell. The n th space harmonic k_{xnp} is related to k_{xop} by

$$k_{xnp} = k_{xop} + 2\pi n/a \quad (10.69)$$

and wavenumbers k_{yop} and k_{ynp} for the lowest mode and the higher modes in the periodic region are then given by

$$k_{yop}^2 = k_o^2 - k_{xop}^2 - k_z^2 \quad (10.70)$$

and

$$k_{yp}^2 = k_o^2 - k_z^2 - k_{xp}^2 \quad (10.71)$$

from (10.69). From (10.66) and (10.70) we obtain the simple but useful relation

$$k_{yop}^2 = k_{yos}^2 - k_{xop}^2 \quad (10.72)$$

Relations (10.69) through (10.72) correspond to (4.3) through (4.6) of Chap. IV.

As pointed out in Chap. IV in the discussion following (4.6), the beam undergoes conical scan as k_{xop} increases from zero. Wavenumber k_{xop} is real and is assumed given. Using Fig. 2.13 of Chap. II and the relations in (2.9) between the wavenumbers and angles θ and ϕ of the polar coordinate system, we observe that the beam scans in azimuth (given by ϕ) and increases in θ (meaning that the beam approaches closer to the ground) as k_{xop} increases. When k_{xop} reaches k_{yos} the beam hits the ground and all radiation ceases, in accordance with (10.72). The angles at the two extremes of the conical scan range are related in a simple way, as given in (2.16) or (2.17).

2. Complete Transverse Equivalent Network

The transverse equivalent network corresponding to the unit cell of the array shown on the left-hand side of Fig. 10.8 is presented on the right-hand side of that figure. The difficult portion of the unit cell to represent in network form is the asymmetrical slit that couples the dielectric-filled lower region to the air-filled stub region above it. That representation in the form of an E-plane tee is derived in Sec. B, and shown in Fig. 10.7. As seen, it forms the central portion of the transverse equivalent network in Fig. 10.8; to complete the network, we need only to add the appropriate terminations.

The terminations on the main guide sections of the tee network are simple, being only short circuits. The asymmetric location of the slit in the dielectric-filled region is accounted for by the two different line lengths $(d + a'/2)$ and $(d' + a'/2)$ in the main guide arms; the length $a'/2$ must be added because the network in Fig. 10.7 is valid at the reference planes located at the midplane of the slit. The expressions for the elements of the tee network are listed in (10.58) through (10.62). They are given in normalized form, exactly the way they would arise naturally, even though the susceptance elements in the network are shown in absolute form, which is customary. The characteristic admittances represent TE modes in each line, and their ratio is presented in (10.46) as

$$\frac{Y_{om}}{Y_{os}} = \frac{k_x}{k_y} \quad (10.73)$$

where the wavenumbers are related by

$$k_x^2 = k_o^2 \epsilon_r - k_z^2 \quad (10.74)$$

$$k_y^2 = k_o^2 - k_z^2 \quad (10.75)$$

The difficult termination to represent is the one shown as Y_{op} , together with the length δ by which the stub guide length c has been shortened. That termination represents the junction between the stub guide with metal side walls and the periodic guide with the phase-shift walls, and then the infinite length of periodic guide beyond it. The characteristic admittance Y_{op} serves as the termination because that line is infinitely long. The mode in the periodic guide, when k_{xop} is nonzero, is an LSE or $H^{(2)}$ -type mode, and its characteristic admittance is in the form given by (2.18). Using (2.18) for Y_{op} together with (10.46) for Y_{os} , we have

$$\frac{Y_{op}}{Y_{os}} = \frac{(k_o^2 - k_z^2)/\omega\mu k_{yop}}{k_{yos}/\omega\mu}$$

or

$$\frac{Y_{op}}{Y_{os}} = \frac{k_{yos}}{k_{yop}} \quad (10.76)$$

when (10.66) is employed.

The equivalent network representation for the junction between those two guides was discussed in detail in Chap. IV, where it was indicated that the network was available in the Waveguide Handbook (Sec. 5.22, pp. 289-292) for the case of normal incidence ($k_z = 0$) in the stub guide. The required analytic continuation for the case $k_z \neq 0$, the changes in notation involved, the modifications in going from a longitudinal to a transverse problem, and the needed interpretation of the results, are all presented in Chap. IV. The steps are all simple ones in themselves, but one must be careful and consistent. Two differences in notation appear between what we employ here and what was chosen in Chap. IV. The first is that the subscript for the stub guide here is s , where g was used there; the second is that the length by which the stub guide length

c is shortened was d' in Chap. IV, whereas here d' means something else (related to the offcenter location of the slit) so that we employ δ instead.

From the detailed discussion in Chap. IV, we may obtain the expression for δ that we still require. From (4.14), after changing $k_{yos} d'$ to $k_{yos} \delta$, we have

$$k_{yos} \delta = 2x' \ln 2 + \sin^{-1} 2x' - \sin^{-1} \frac{x'}{1+y} - \sin^{-1} \frac{x'}{1-y} \\ + S_2(2x'; 0, 0) - S_2(x'; 0, -y) - S_2(x'; 0, y) \quad (10.77)$$

where

$$S_2(x'; 0, b) = \sum_{n=2}^{\infty} \left[\sin^{-1} \frac{x'}{n-b} - \frac{x'}{n} \right] \quad (10.78)$$

and where y and x' are symbols used in the Waveguide Handbook which here signify (from (4.12))

$$y = \frac{ak_{xop}}{2\pi}, \quad x' = \frac{ak_{yos}}{2\pi} \quad (10.79)$$

We now have expressions for all the constituents of the transverse equivalent network in Fig. 10.8.

3. The Dispersion Relation

Because the elements in the transverse equivalent network in Fig. 10.8 are all in closed form (S_2 in (10.78) converges extremely rapidly), it is possible to derive the transverse resonance relation, or dispersion relation, in analytical closed form. To obtain the transverse resonance relation, we first choose as the reference plane location a plane just below the transformer in Fig. 10.8; then we set equal to zero the sum of the admittances looking up and looking down from this reference plane. Looking up, we have

$$Y_{up} = (1/n_{cs}^2) (j B_s + Y_{ins}) \quad (10.80)$$

where B_s is written as $B_s = (B_s/Y_{os})Y_{os}$, and Y_{ins} is given by

$$\frac{Y_{ins}}{Y_{os}} = \frac{j + (Y_{op}/Y_{os}) \cot k_{yos} (c - \delta)}{\cot k_{yos} (c - \delta) + j(Y_{op}/Y_{os})} \quad (10.81)$$

The expression for B_s/Y_{os} appears in (10.61); the k_y there is now written k_{yos} . Expressions for n_{cs} , Y_{op}/Y_{os} , and δ are given by (10.62), (10.76), and (10.77) through (10.79), respectively.

Looking down, we obtain

$$Y_{down} = j B_L + \frac{(j B_a + Y_R)(j B_a + Y_L)}{j 2 B_a + Y_R + Y_L} \quad (10.82)$$

where

$$Y_R = -j Y_{om} \cot k_x (d + a'/2) \quad (10.83)$$

$$Y_L = -j Y_{om} \cot k_x (d' + a'/2) \quad (10.84)$$

and where we write $B_L = (B_L/Y_{om})Y_{om}$ and $B_a = (B_a/Y_{om})Y_{om}$. Expressions for B_L/Y_{om} and B_a/Y_{om} appear as (10.59) and (10.58).

When the normalized forms are substituted into (10.80) and (10.82), Y_{os} and Y_{om} multiply all terms in Y_{up} and Y_{down} , respectively. Then, when Y_{up} and Y_{down} are summed to zero, the ratio Y_{os}/Y_{om} enters as a multiplier of $(1/n_{cs})^2$, in effect changing n_{cs} to n_{csn} , in accordance with (10.57) and the discussion surrounding it, when (10.46) is used. We thus see, as expected, that the same result is achieved whether we use n_{cs} and absolute susceptances or n_{csn} and normalized susceptances directly.

Since there are three different regions in the cross section of the unit cell of the array, the dielectric-filled region at the bottom, the air-filled parallel-plate region in the middle, and the periodic region at the top, the resulting transverse resonance relation contains three different transverse wavenumbers, k_x , k_{yos} and k_{yop} . These transverse wavenumbers are related to each other and to k_o and k_z , the free-space and longitudinal wavenumbers, respectively, by (10.64), (10.66), (10.70) and (10.72). The transverse resonance relation can be rephrased in a variety of ways to exclude some of these wavenumbers and include others. We have found it convenient to phrase it to contain k_o , k_x and k_{xop} , using (10.70) to replace k_{yop} with k_{xop} , since the

latter is given and is real. Effectively, then, the relation contains only the unknown k_x . The other wavenumbers, particularly $k_z (= \beta - j\alpha)$, which is the ultimate goal, follow simply from the wavenumber relations quoted just above. The dispersion "relation" is then the transverse resonance relation taken together with the other wavenumber relations.

D. PERFORMANCE WITHOUT CROSS-PLANE SCAN

When all the line-source elements in the array are fed in phase, $k_{xop} = 0$, and the cross-plane scan angle is zero. The phase shift across the unit cell is then zero, so that the phase-shift walls reduce to electric walls in view of the electric field direction. The periodic region then becomes identical to the air-filled parallel-plate stub guide region that connects to it; as a result, length c loses its meaning, the metal vertical walls effectively extend to infinity, and the modified unit cell becomes that shown in Fig. 10.9.

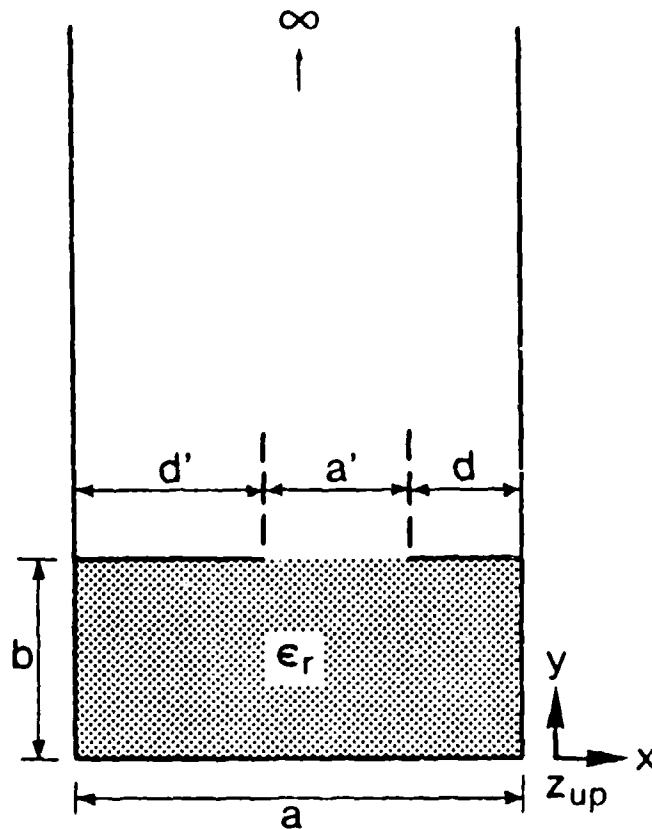


Fig. 10.9

The form to which the unit cell reduces when there is no cross-plane scan ($k_{xop} = 0$).

The array is capable of two types of scanning: leaky-wave scanning in elevation, and phase-shift scanning in the cross plane. The latter produces conical scanning of the beam, so that the beam moves in azimuth and also gets nearer to the ground in elevation. When the cross-plane scan is zero, as in this section, the beam is at its highest position in elevation, and that position can be altered by changing the frequency or by modifying β/k_o in some other way. The zero cross-plane scan case therefore represents the *best case* for an examination of the *leaky-wave* properties of the array. Such an examination is conducted in this section; the modifications in performance that arise when k_{xop} is no longer zero are treated in Sec. E.

We present results below for the dependence of the performance on dimensional ratios in the array cross section and on frequency.

1. Variations with Dimensional Ratios

We recall that the angle θ_m of the maximum of the beam is given by the value of β/k_o , the normalized phase constant, and that the beam width $\Delta\theta$ is related to the value of α/k_o , the normalized leakage constant. (See relations (2.27) to (2.29).) We are therefore interested in the behavior of β/k_o and α/k_o as various dimensions in the cross section are changed. In particular, we wish to know which dimensions to vary so that β/k_o remains fairly constant while α/k_o changes greatly.

The two best candidates to vary in order to modify α/k_o strongly are the relative slit width a'/a and its location in the cross section, measured as d/a , as seen in Fig. 10.9. Let us first obtain the *dependence on d/a* when the width a and then the height b of the dielectric-filled region (which is actually the feed guide region) are varied as parameters.

We first present the variations of β/k_o and α/k_o vs. d/a for three different values of *feed guide width a* . The curves in Figs. 10.10, 10.11 and 10.12 correspond to values of a equal to 2.50 mm, 2.25 mm and 2.20 mm, for a frequency of 50.0 GHz. Other parameter values are indicated in the inset. The curves in Fig. 10.10 for $a = 2.50$ mm are the least desirable because the values of α/k_o are the smallest and the values of β/k_o are too close to unity, meaning an angle too close to endfire (for example, $\beta/k_o = 0.90$ corresponds to an angle of 26° from endfire). The behaviors in Figs. 10.11 and 10.12, for $a = 2.25$ mm and 2.20 mm, are rather similar to each other; we selected $a = 2.25$ mm as the guide width for further calculations, but we could just as well have chosen $a = 2.20$ mm.

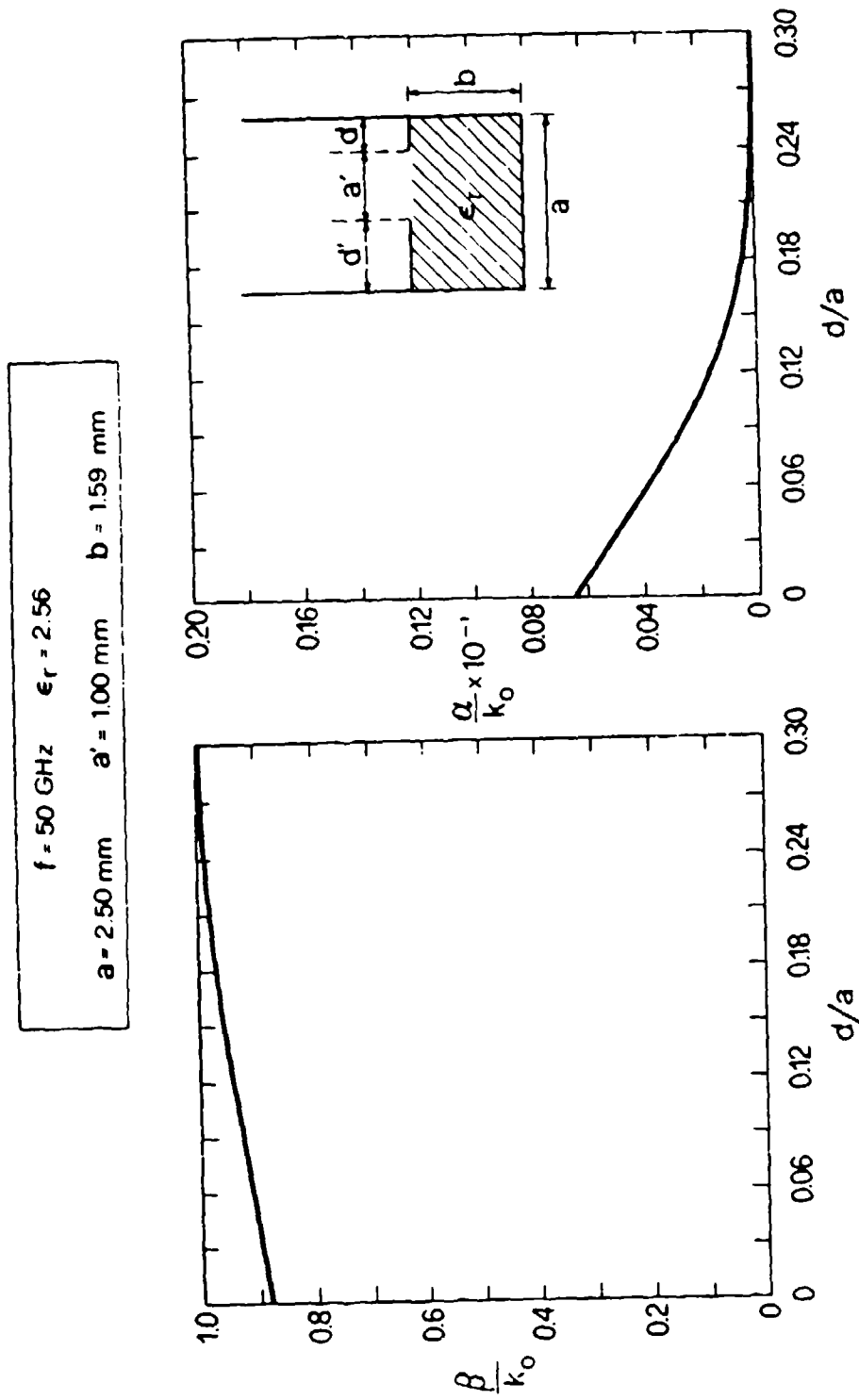


Fig. 10.10 Variations of the normalized phase and leakage constants as a function of slit location in the cross section, for guide width $a = 2.50$ mm.

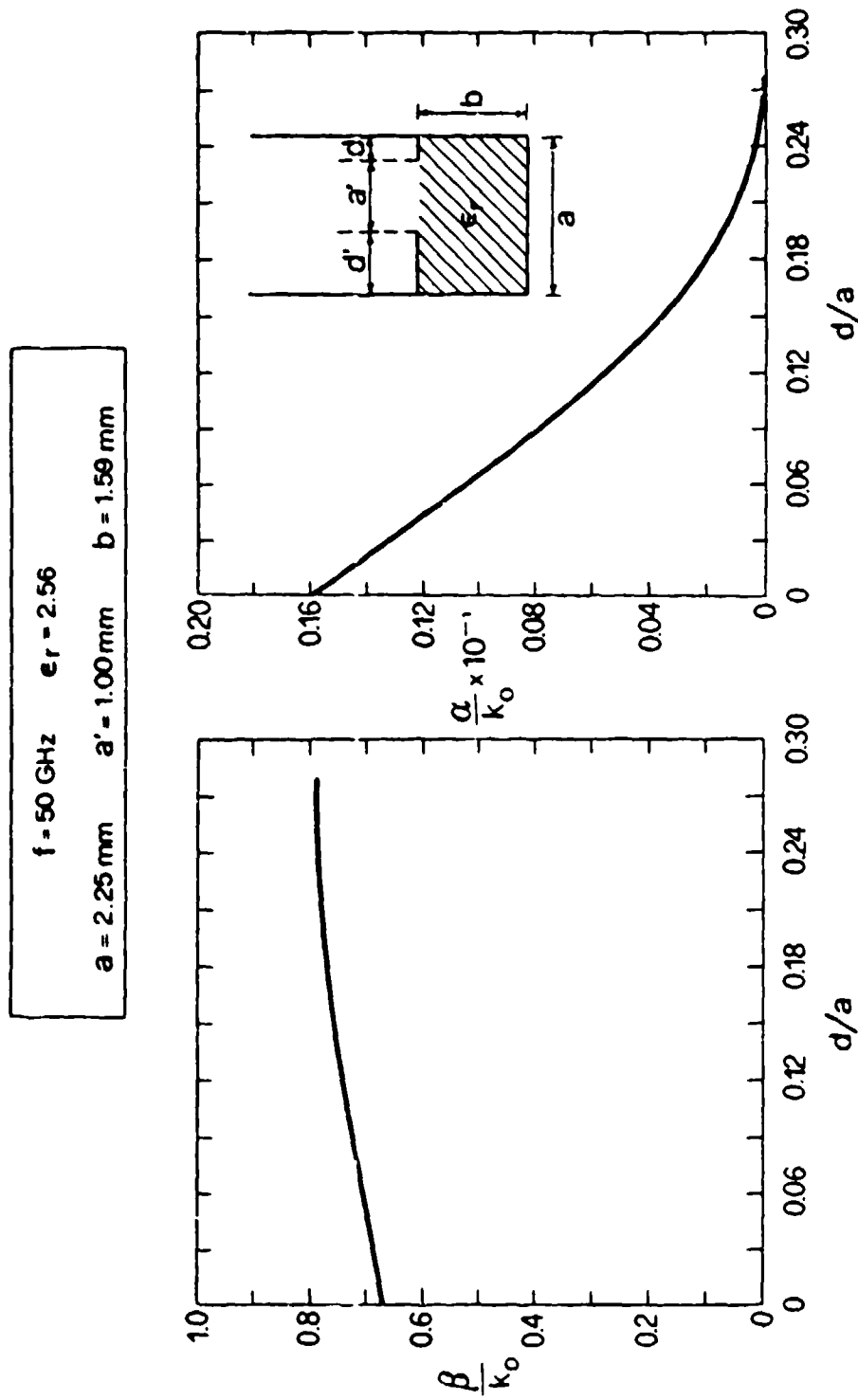


Fig. 10.11 Same as Fig. 10.10, but for guide width $a = 2.25 \text{ mm}$.

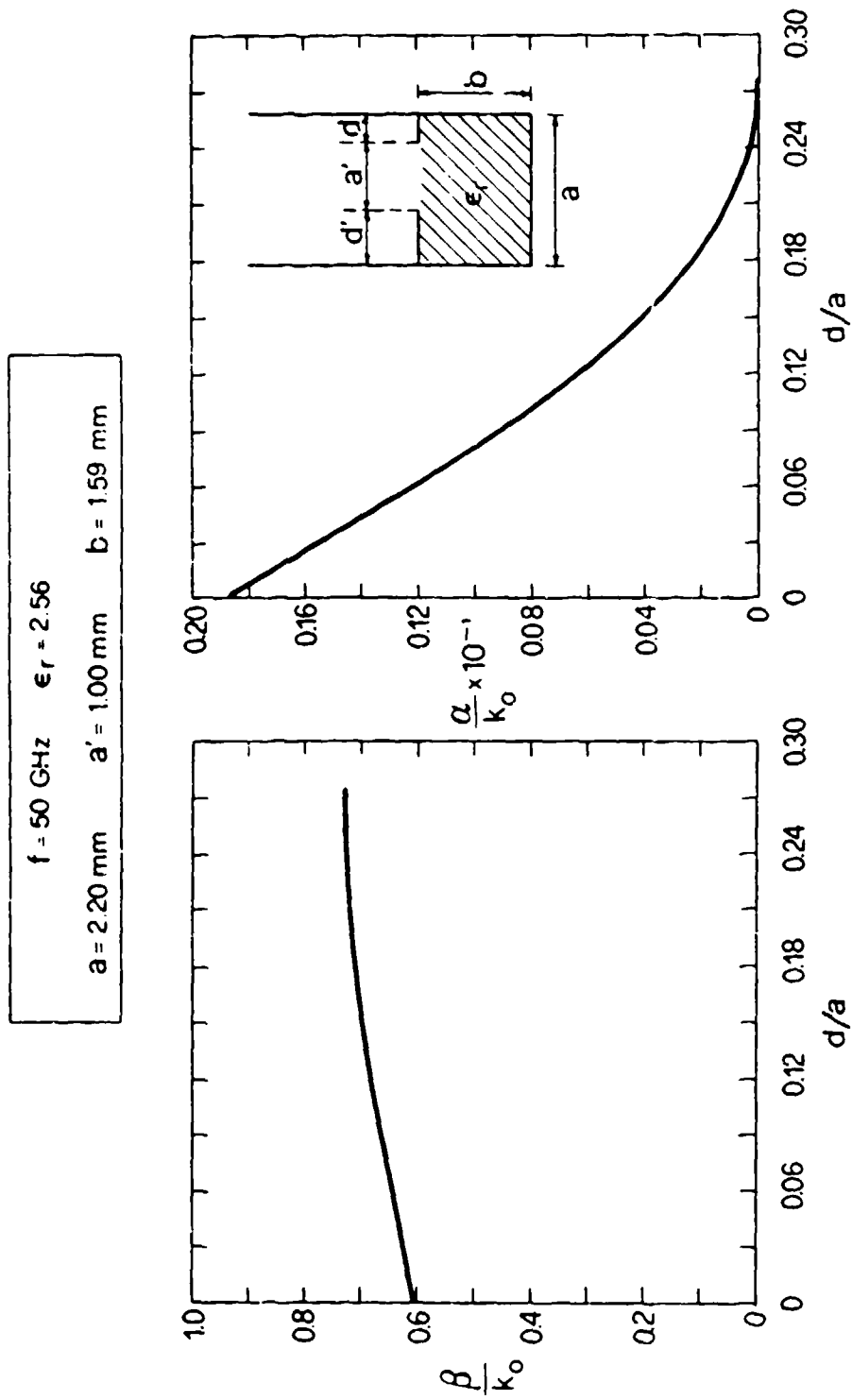


Fig. 10.12 Same as Fig. 10.10, but for guide width $a = 2.20 \text{ mm}$.

As expected from similar numerical results for the offset-groove-guide antenna in Chap. VII, the value of α/k_o varies monotonically and smoothly over a very wide range of values as d/a is changed. The value of β/k_o over this range varies only a little, but we would have hoped for it to be flatter.

The value of *feed guide height* b in Figs. 10.10 to 10.12 is 1.59 mm, which corresponds to a 1/16 inch thick printed-circuit board. That height is a very convenient one, but in Fig. 10.13 we examined the behavior vs. d/a when thickness b was increased slightly to 2.00 mm. We observe that, as compared with the curves in Fig. 10.11, the values of β/k_o are flatter, but the α/k_o values are much lower. The corresponding curves for beam angle θ_m and beam width $\Delta\theta$ are shown in Fig. 10.14 (using (2.27) to (2.29)), where it is seen that θ_m varies only about 4° or 5° over the full range of d/a , whereas $\Delta\theta$ varies monotonically from zero to a maximum of about 2.3° , which is not that large. This dimensional combination is therefore useful only for rather narrow beams. To permit greater flexibility in beam width, and also because it corresponds to easily available 1/16 inch printed-circuit board, we will stay with $b = 1.59$ mm.

The next set of curves varies the *slit width* a' as the parameter, from $a' = 0.40$ mm to $a' = 1.30$ mm in four steps, corresponding to relative slit width values of $a'/a = 0.178, 0.311, 0.444$ and 0.578 . Figures 10.15, 10.17, 10.19 and 10.21 present the variations of β/k_o and α/k_o vs. d/a for $a' = 0.40$ mm, 0.70 mm, 1.00 mm and 1.30 mm, respectively. Figures 10.16, 10.18, 10.20 and 10.22 show how θ_m and $\Delta\theta$ vary with d/a for the same set of a' values. The abscissa scales are the same for each curve; the curves for larger values of a' therefore cover a smaller range of d/a . Inspection of these curves shows that, of the four values of a' being compared, the value of $a' = 1.00$ mm seems optimum, corresponding to a maximum beam width of just over 6° . (These beam widths are obtained for line-source lengths for which 90% of the power is radiated, consistent with (2.28) and (2.29).)

So far, the abscissa variation was for d/a , a measure of the offcenter location of the slit. We next consider the abscissa variation for a'/a , the *relative slit width*. For an arbitrary choice of $d = 0.20$ mm, the behavior of β/k_o and α/k_o vs. a'/a is depicted in Fig. 10.23. We observe that β/k_o remains rather *flat* as a'/a is changed from 0.4 to 0.8, and that over this range of a'/a the values of α/k_o vary monotonically over a wide range. The corresponding behaviors for θ_m and $\Delta\theta$ are shown in Fig. 10.24, where it is seen that θ_m is indeed flat from $a'/a = 0.4$ to 0.8, while $\Delta\theta$ varies from about 3.5° to nearly zero over the same range. The maximum

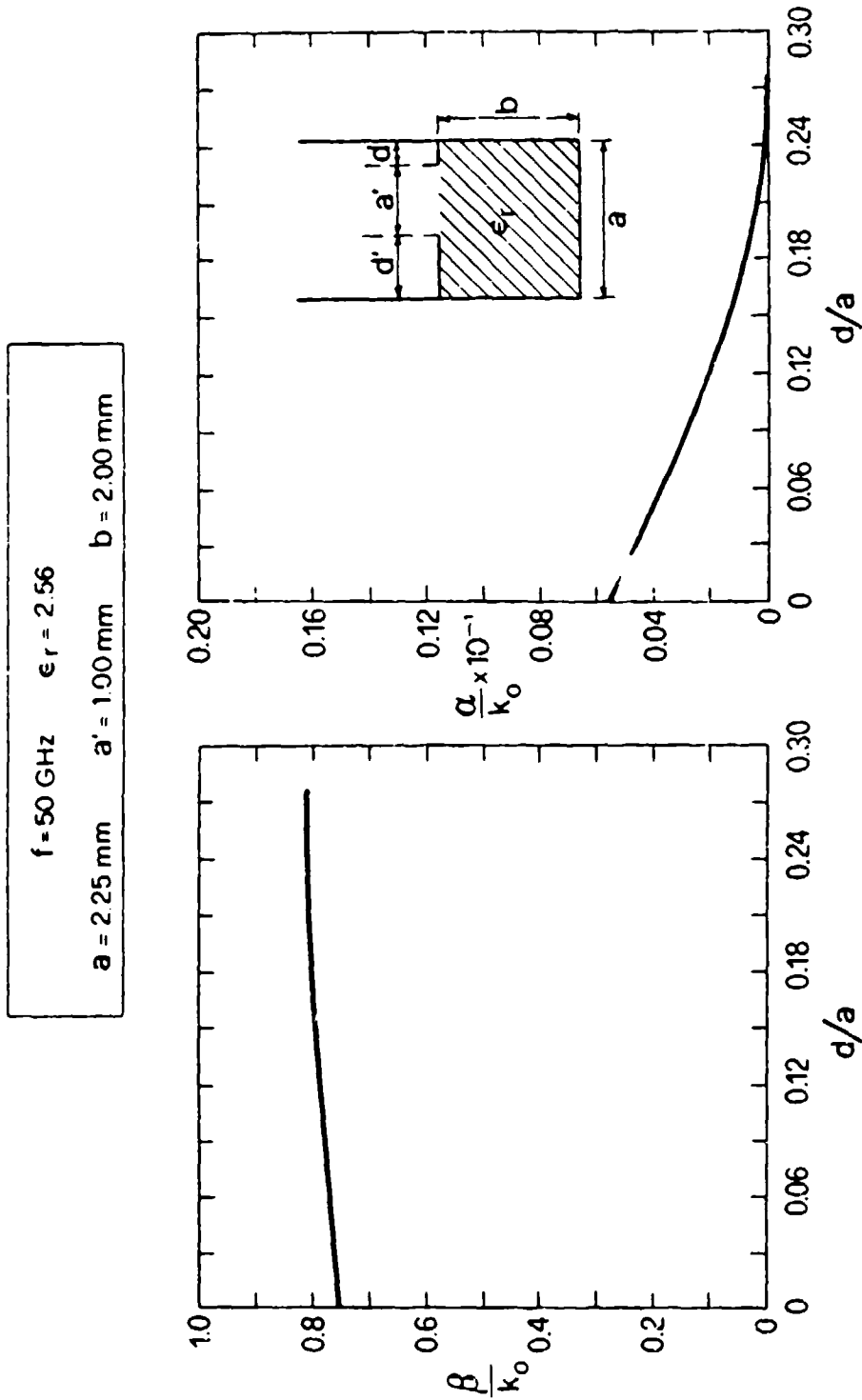


Fig. 10.13 Same as Fig. 10.11, but for the height b of the dielectric-filled portion equal to 2.00 mm instead of 1.59 mm, which corresponds to a 1/16 inch printed-circuit board.

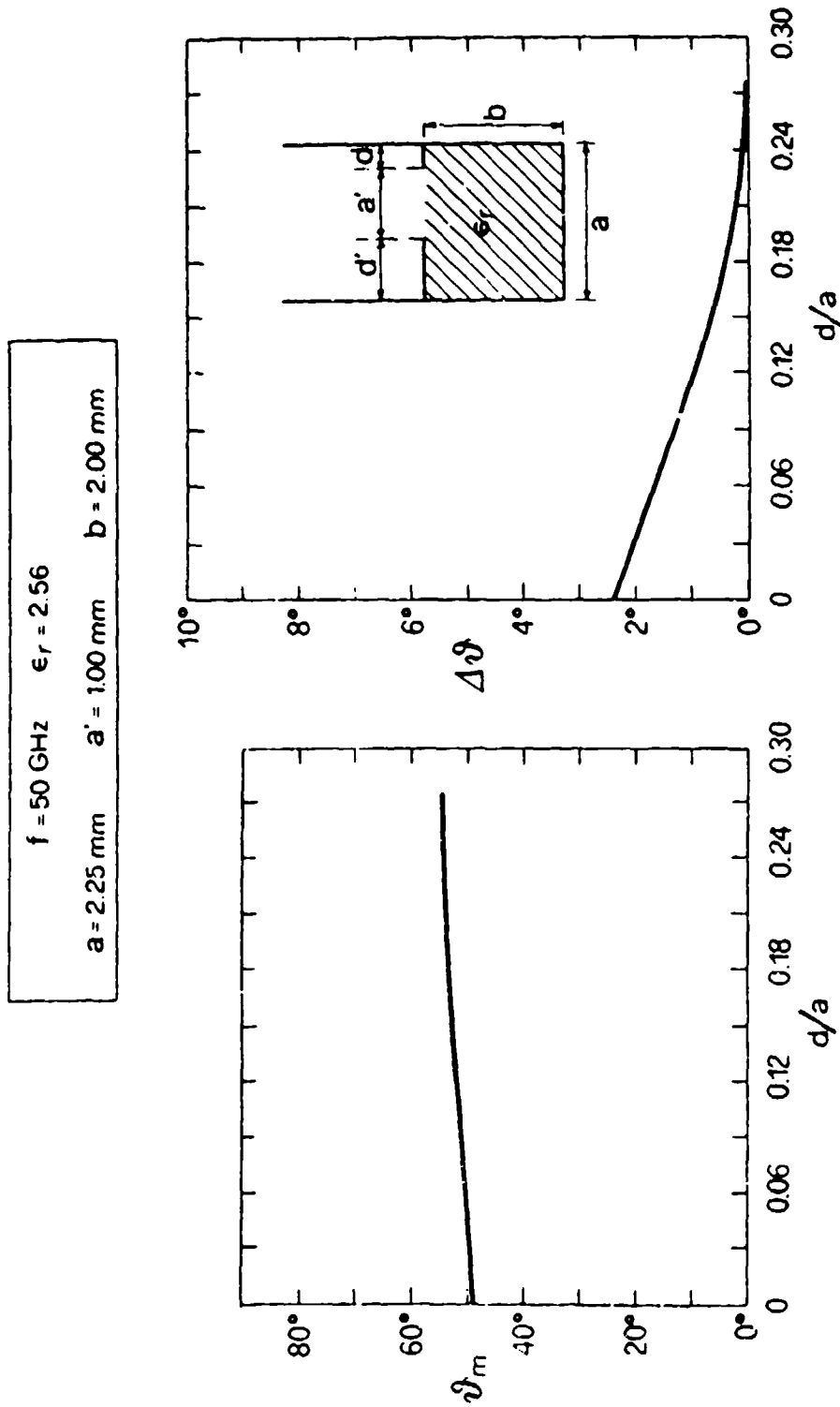


Fig. 10.14 Variations of the beam elevation angle θ_m and the beam width $\Delta\theta$ as a function of slit location in the cross section, for height $b = 2.00 \text{ mm}$.

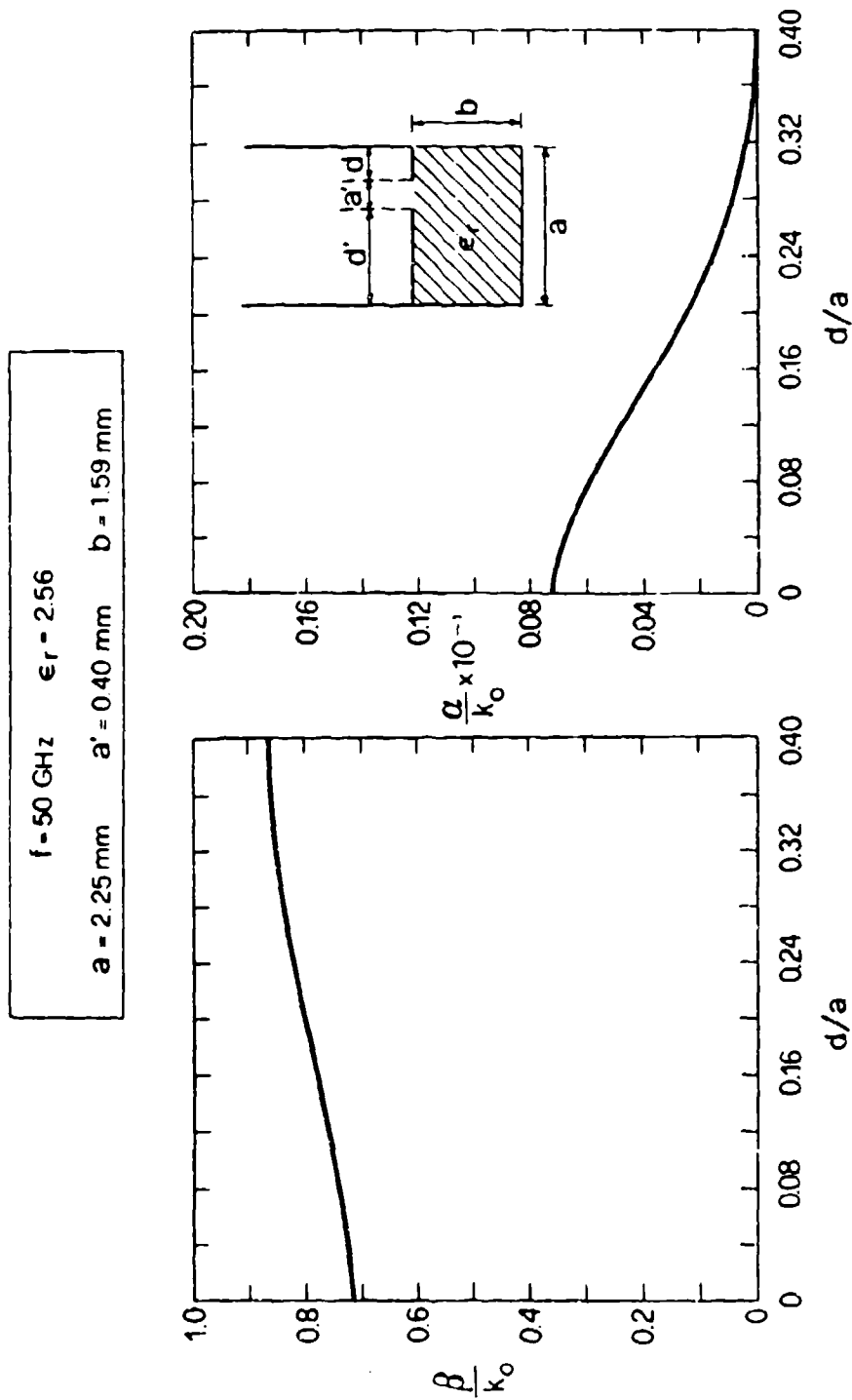


Fig. 10.15 Variations of the normalized phase and leakage constants as a function of slit location in the cross section, for slit width $a' = 0.40$ mm.

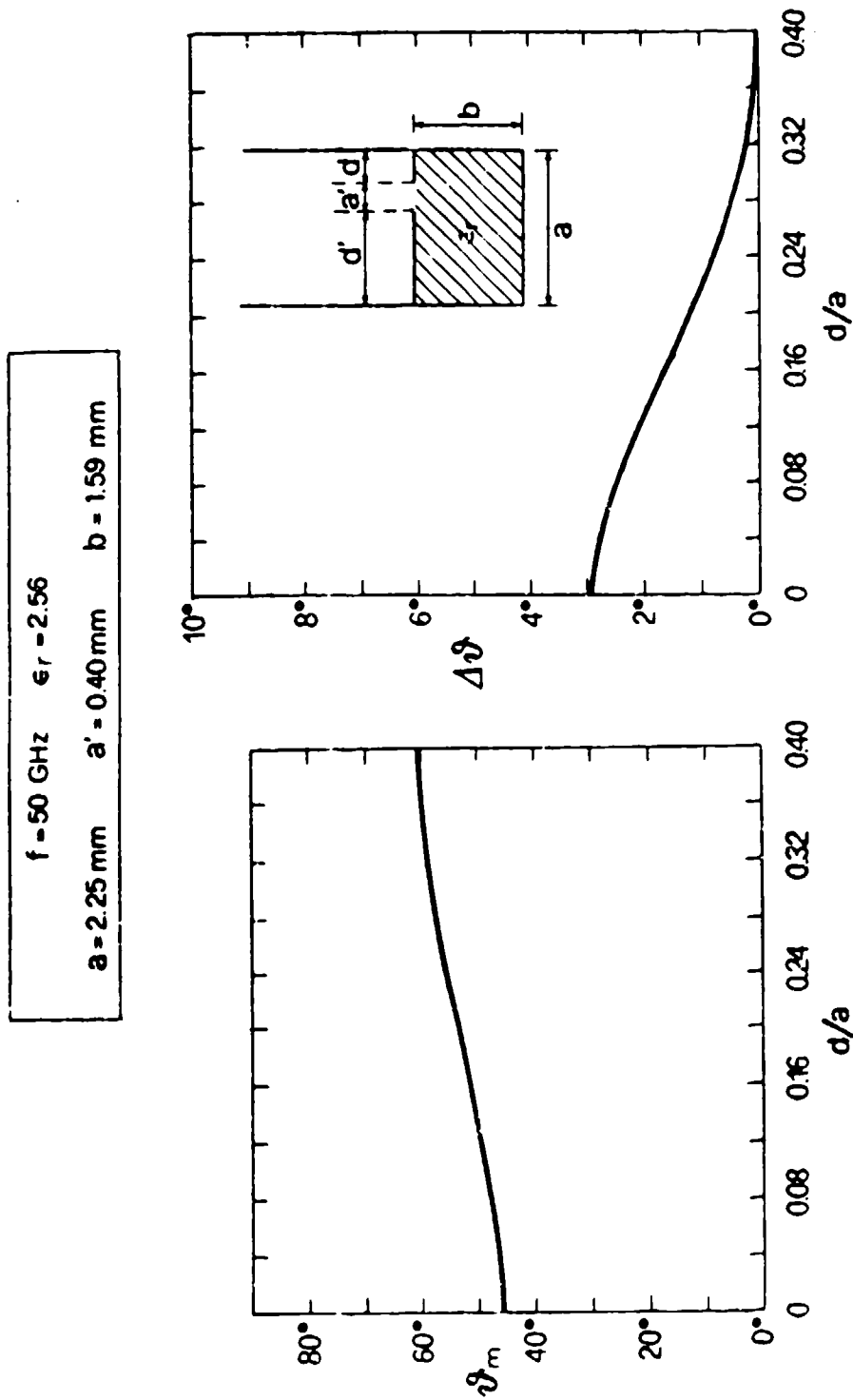


Fig. 10.16 Variations of the beam elevation angle θ_m and the beam width $\Delta\theta$ as a function of slit location in the cross section, for slit width $a' = 0.40$ mm.

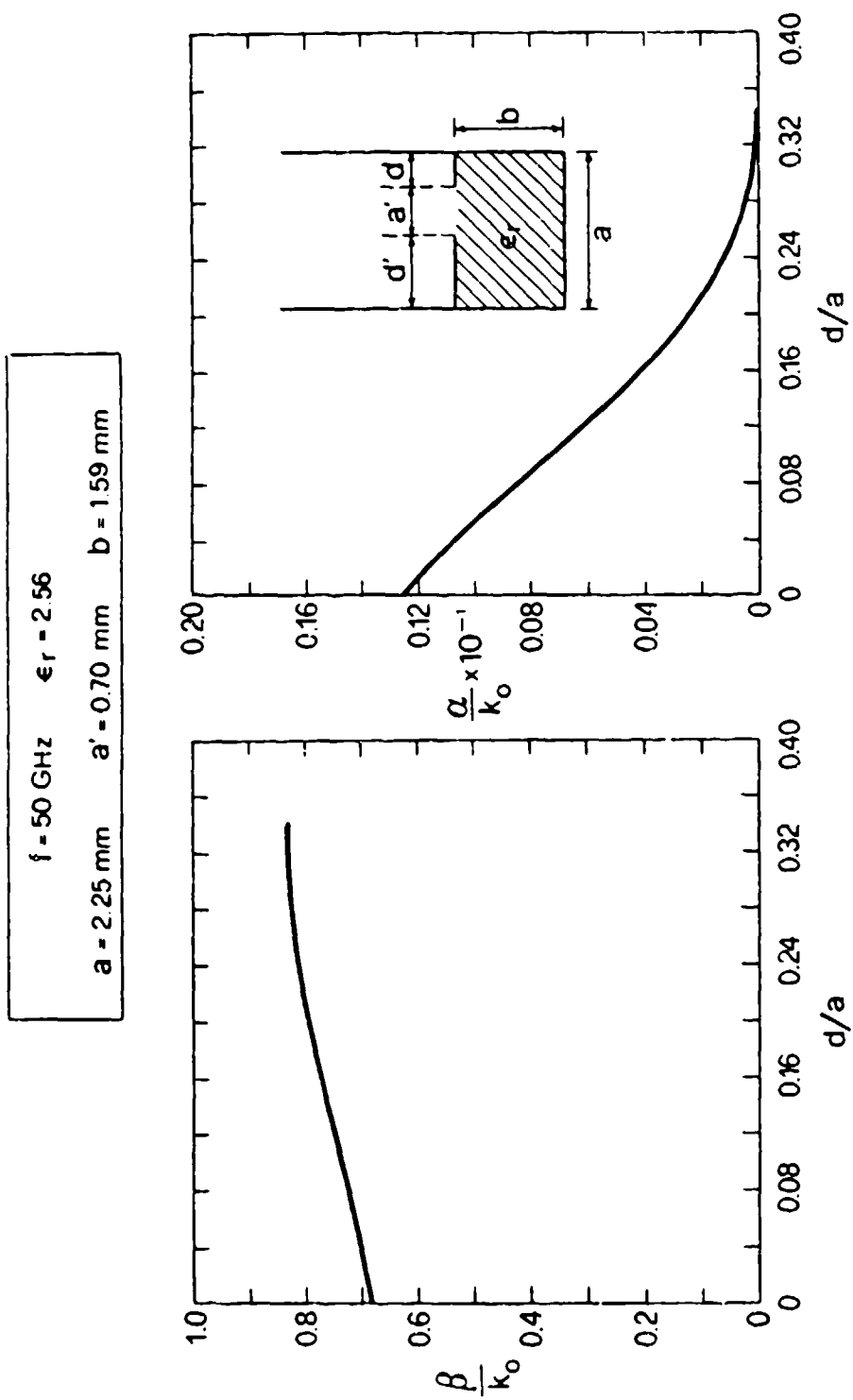


Fig. 10.17 Same as Fig. 10.15, but for slit width $a' = 0.70 \text{ mm}$.

$f = 50 \text{ GHz}$ $\epsilon_r = 2.56$
 $a = 2.25 \text{ mm}$ $a' = 0.70 \text{ mm}$ $b = 1.59 \text{ mm}$

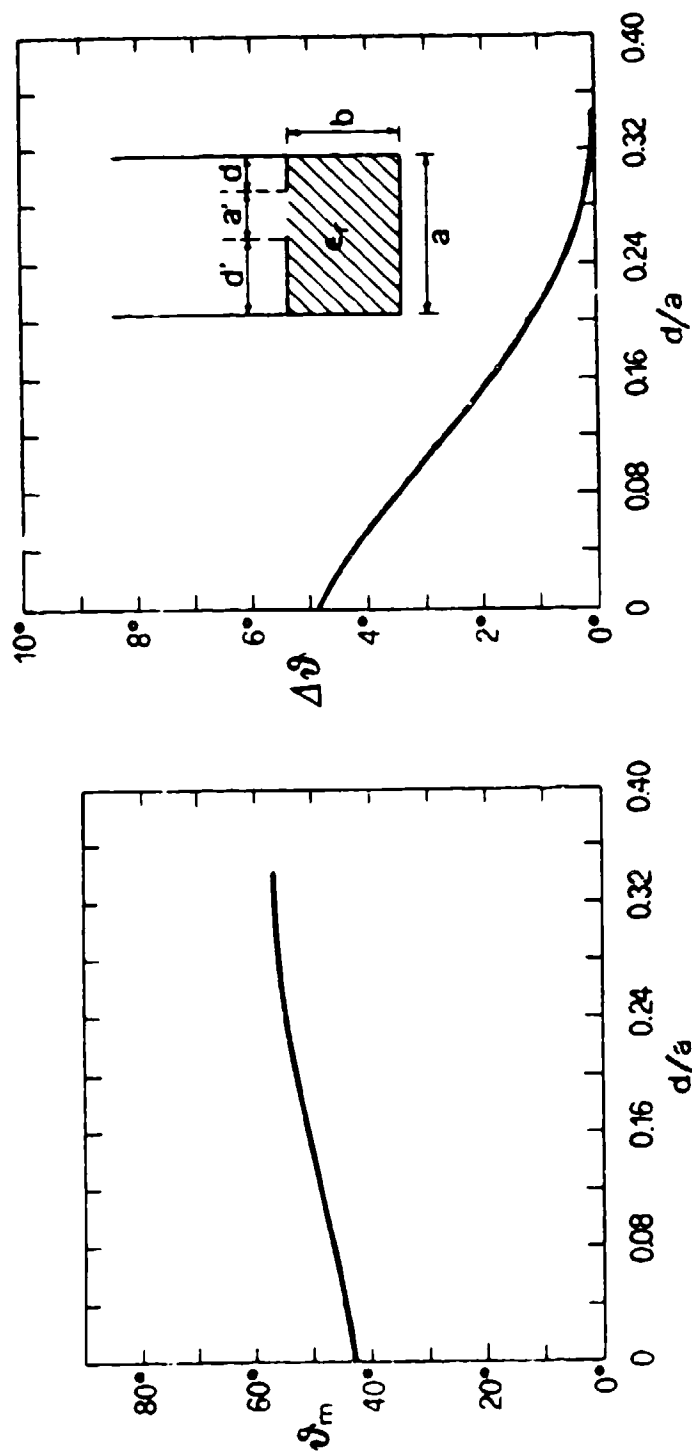


Fig. 10.18 Same as Fig. 10.16, but for slit width $a' = 0.70 \text{ mm}$.

$f = 50 \text{ GHz}$ $\epsilon_r = 2.56$
 $a = 2.25 \text{ mm}$ $a' = 1.00 \text{ mm}$ $b = 1.59 \text{ mm}$

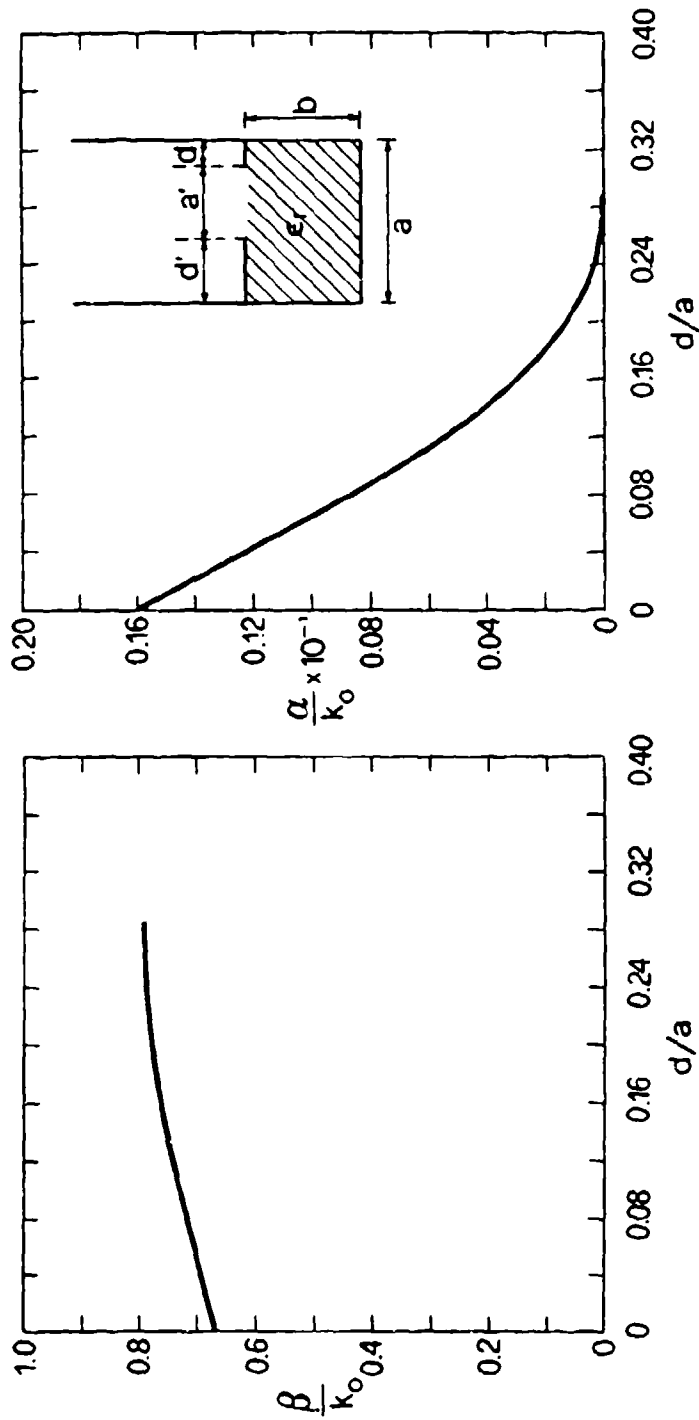


Fig. 10.19 Same as Fig. 10.15, but for slit width $a' = 1.00 \text{ mm}$.

$f = 50 \text{ GHz}$ $\epsilon_r = 2.56$
 $a = 2.25 \text{ mm}$ $a' = 1.00 \text{ mm}$ $b = 1.59 \text{ mm}$

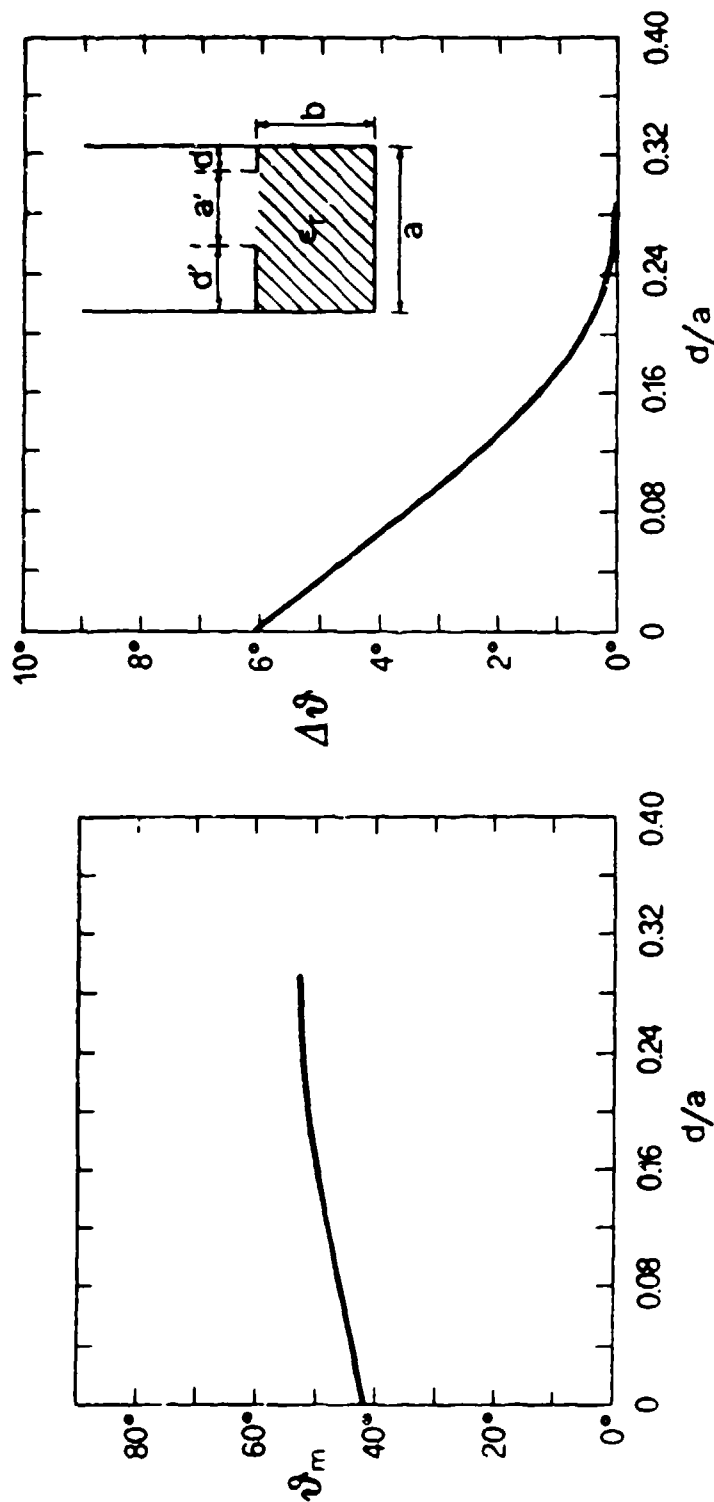


Fig. 10.20 Same as Fig. 10.16, but for slit width $a' = 1.00 \text{ mm}$.

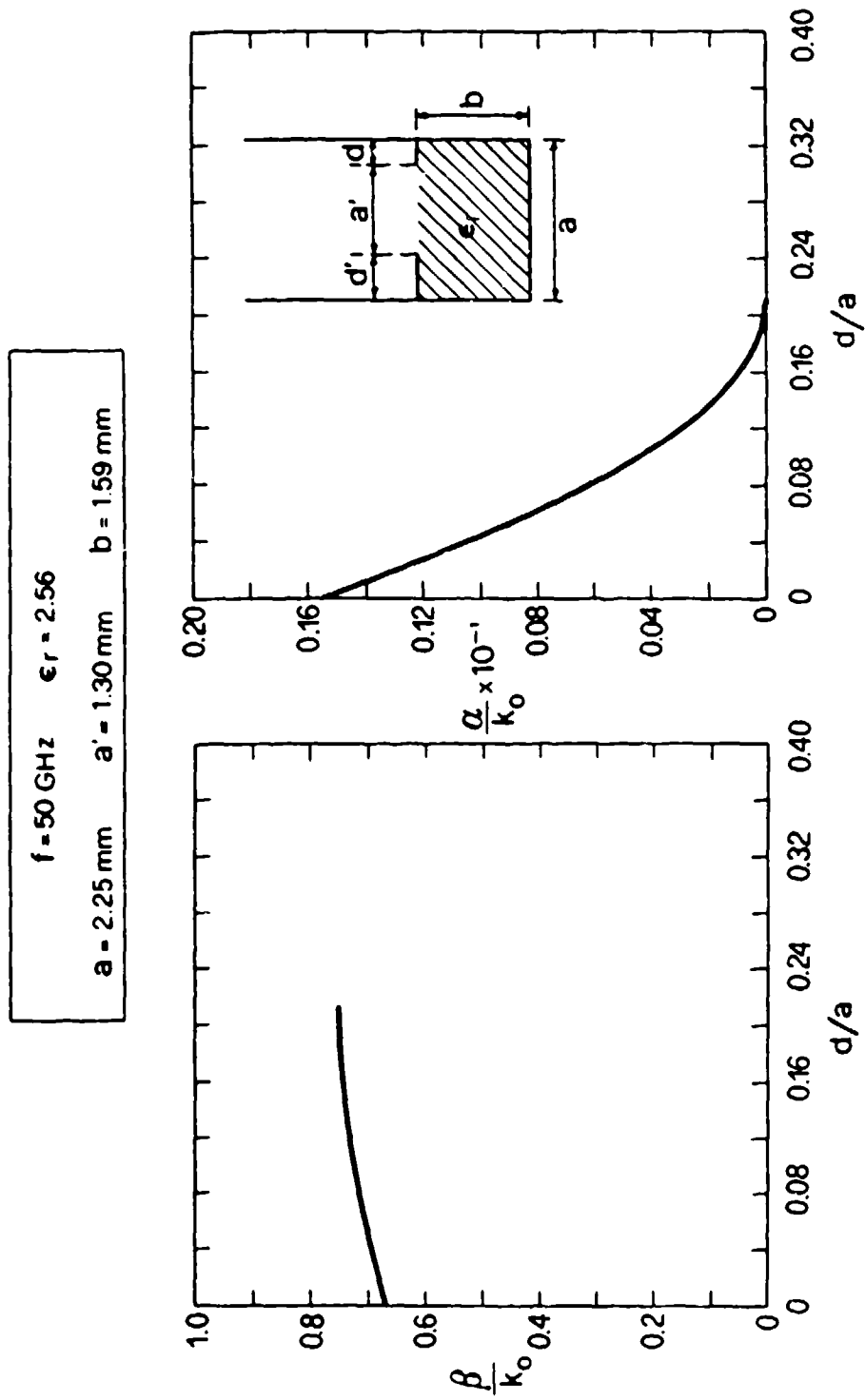


Fig. 10.21 Same as Fig. 10.15, but for slit width $a' = 1.30 \text{ mm}$.

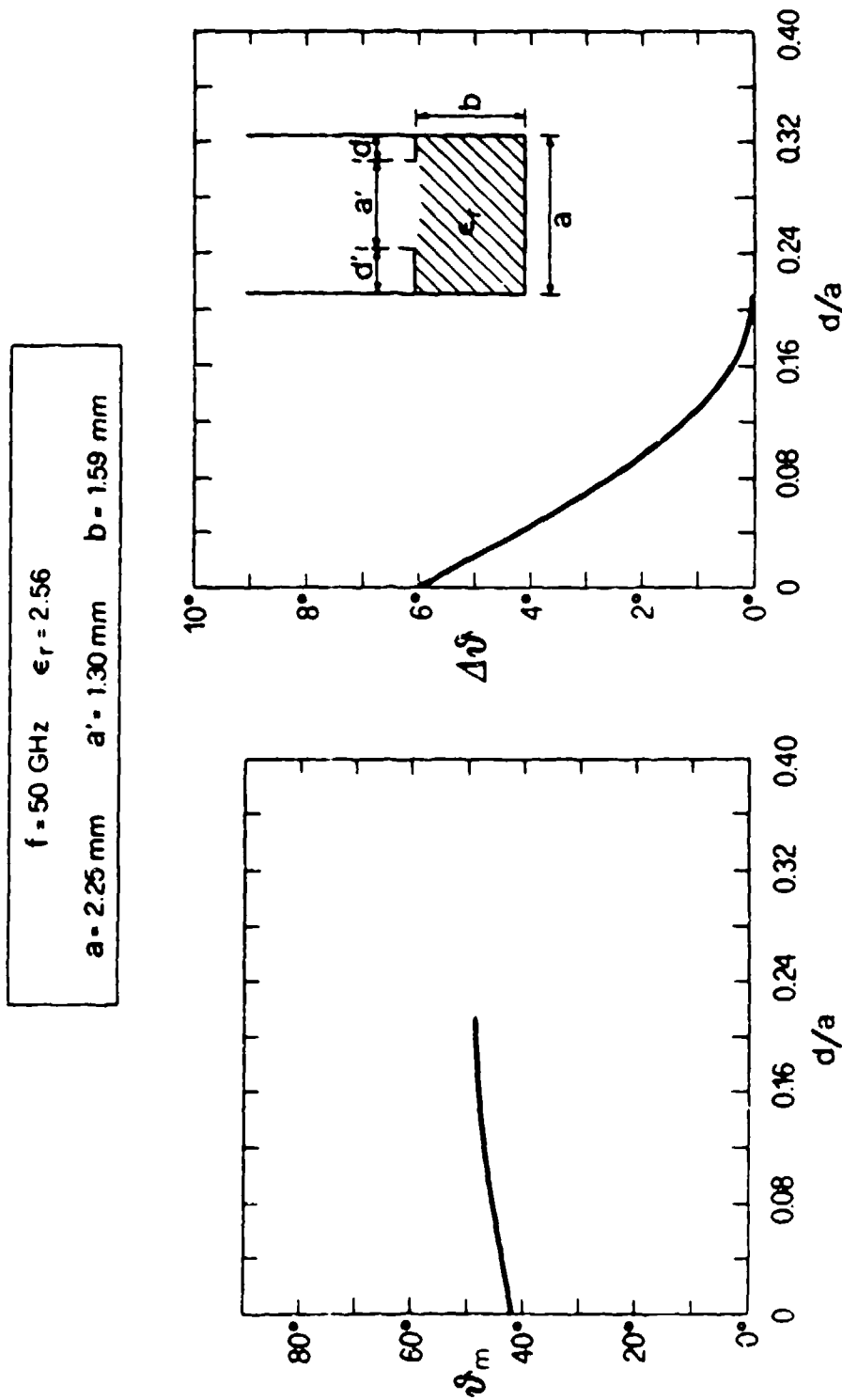


Fig. 10.22 Same as Fig. 10.16, but for slit width $a' = 1.30 \text{ mm}$.

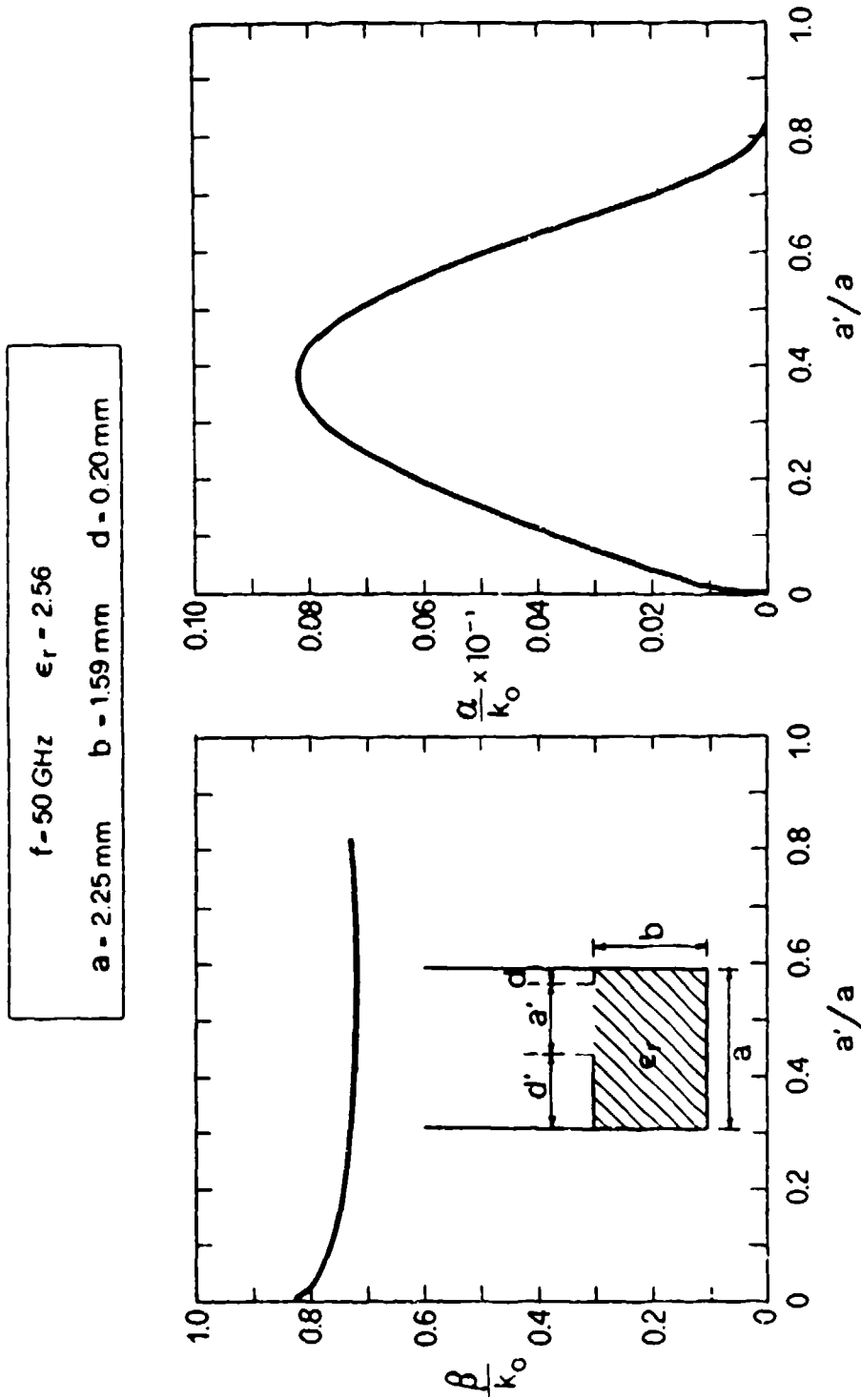


Fig. 10.23 Variations of the normalized phase and leakage constants as a function of relative slit width.

$f = 50 \text{ GHz}$ $\epsilon_r = 2.56$
 $a = 2.25 \text{ mm}$ $b = 1.59 \text{ mm}$ $d = 0.20 \text{ mm}$

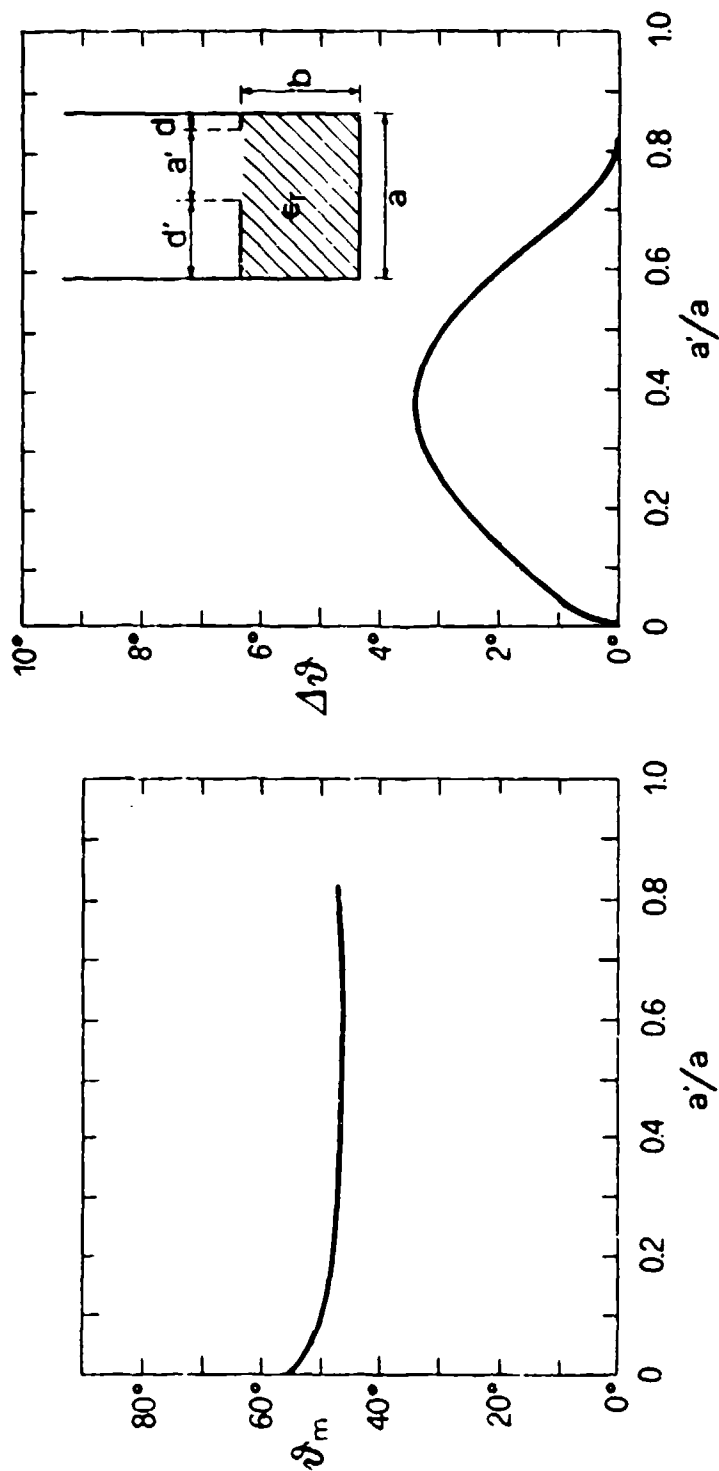


Fig. 10.24 Variations of the beam elevation angle θ_m and the beam width $\Delta\theta$ as a function of relative slit width.

value for $\Delta\theta$ could be increased by simply choosing a smaller value for d , in accordance with Fig. 10.20.

The last set of dimensional variations involves the ratio b/a , the *relative height* of the dielectric-filled feed guide. The dependences of β/k_o and α/k_o on b/a are presented in Fig. 10.25, and the corresponding behaviors of θ_m and $\Delta\theta$ are shown in Fig. 10.26. It is seen that varying b/a changes both β/k_o and α/k_o simultaneously, increasing one while decreasing the other. The 1/16 inch printed-circuit board height corresponds to $b/a = 0.707$. Making the guide aspect ratio flatter serves to widen the beam, and also to raise the beam closer to broadside. We have not, however, examined how the other dependences would be affected by making b/a smaller. We suspect that they would be more sensitive, that is, β/k_o would be less flat as d/a or a'/a were varied, but we have not checked the behavior.

From the point of view of sidelobe control or pattern shaping, where we would need to vary α/k_o while maintaining β/k_o the same, we find from the above numerical results that a'/a is the best parameter to vary, although d/a is not bad. It is important to note that both of those dimensional parameters can be tapered along the line source length by employing lithographic means, which would permit a mask to deposit or etch away at one time the whole structure on the dielectric interface.

2. Variations with Frequency

The variations of β/k_o and α/k_o with frequency are shown in Fig. 10.27. There are three separate frequency ranges, and they are best recognized by looking at the curve for β/k_o . For the *highest* range of frequencies, when f is greater than 56.75 GHz for the set of dimensions given in the inset, the value of β/k_o exceeds unity, because the guided wave is then purely bound and not leaky at all. In that frequency range, we correspondingly find that $\alpha/k_o = 0$. This behavior cannot occur for the offset-groove-guide antenna, discussed in Chap. VII, where the corresponding curves appear in Fig. 7.12. The slow-wave behavior here is made possible by the presence of the dielectric material in the feed guide portion.

In the *second* frequency range, from about 43 GHz (the value is not sharply defined) to 56.75 GHz, the guided mode is above cutoff, with a fast phase velocity. The mode is leaky within that range, and the values of α/k_o increase monotonically as the frequency is decreased. Below about 43 GHz the mode goes below cutoff, in the *third* range. The α/k_o values continue to increase strongly, but the attenuation is now predominantly reactive rather than radiative. The β/k_o curve does not approach zero,

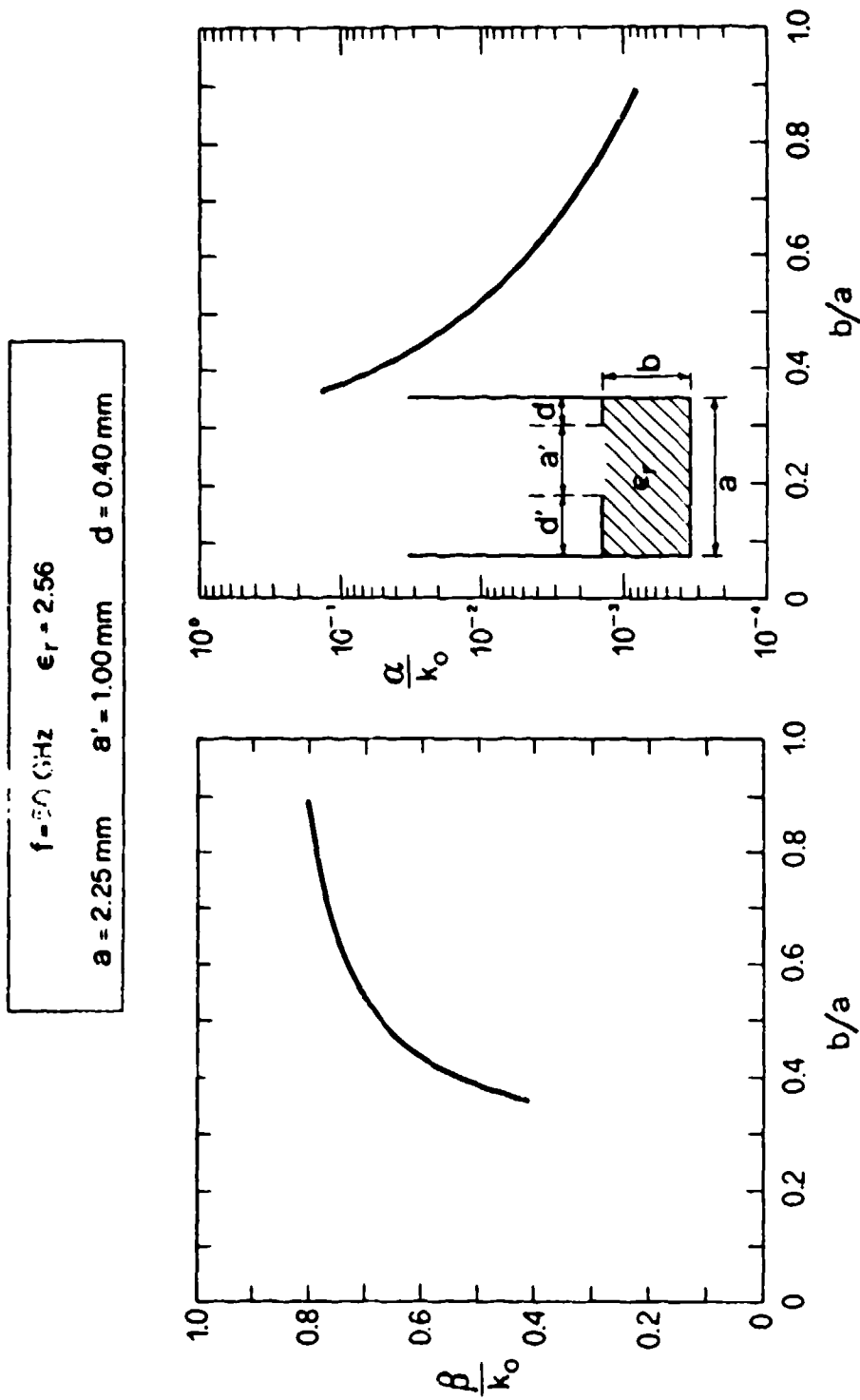


Fig. 10.25 Variations of the normalized phase and leakage constants as a function of the feed guide aspect ratio.

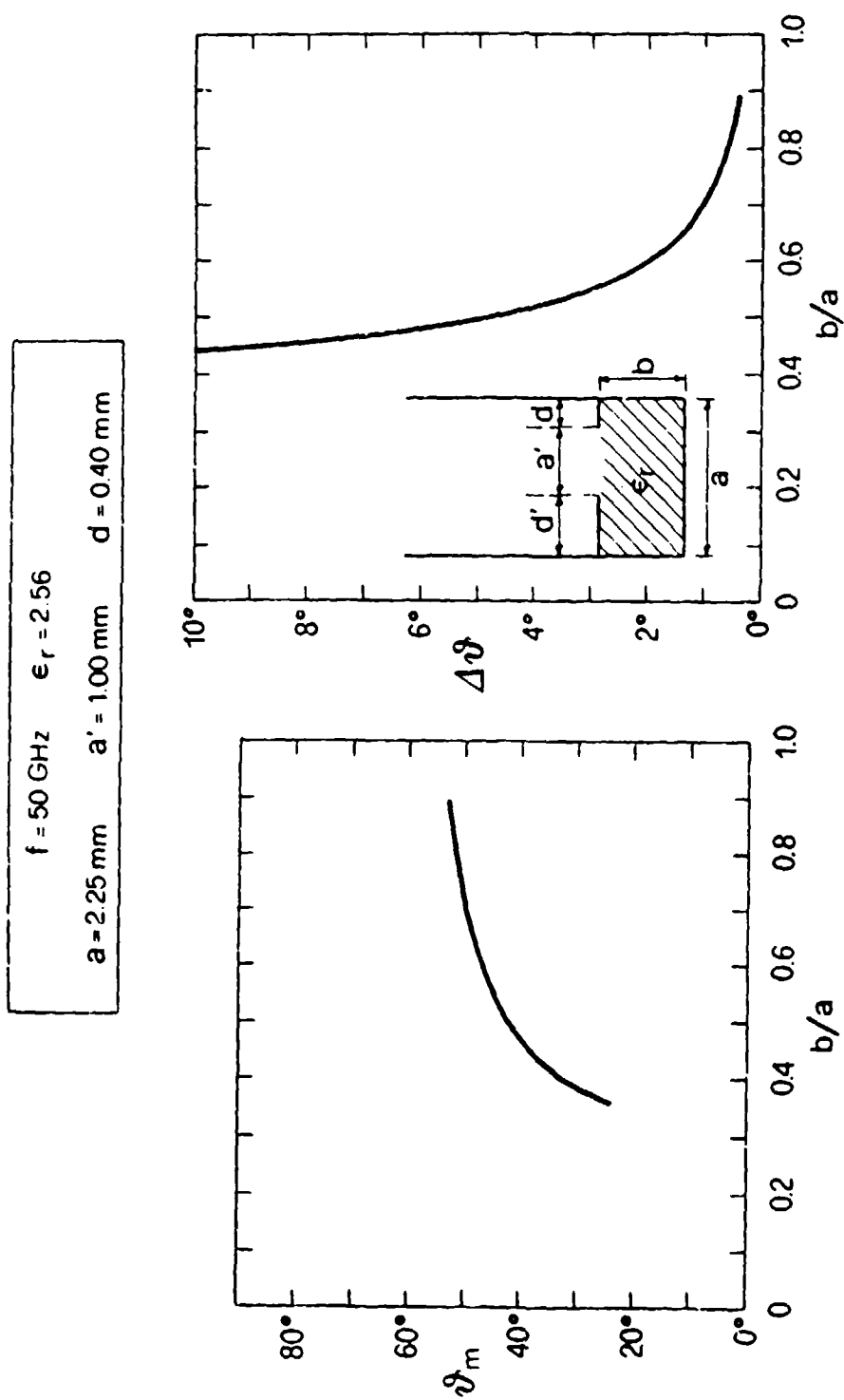


Fig. 10.26 Variations of the beam elevation angle θ_m and the beam width $\Delta\theta$ as a function of the feed guide aspect ratio.

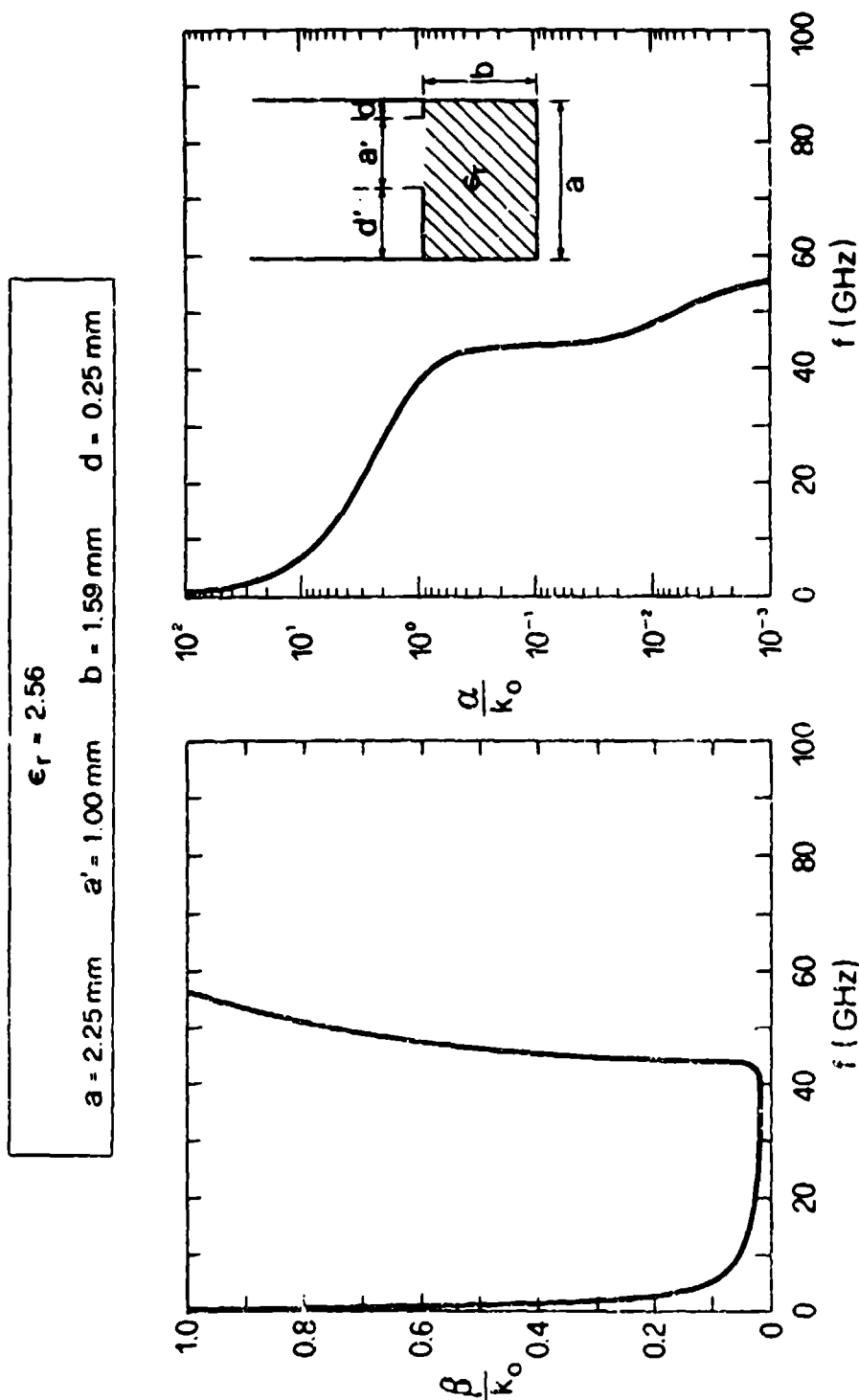


Fig. 10.27 Variations of the normalized phase and leakage constants as a function of frequency over a very wide range, for $d = 0.25 \text{ mm}$, a measure of the slit location.

but slowly turns up again and eventually, at very low frequencies, crosses the $\beta/k_o = 1$ line. It was proved analytically for the offset groove guide in Sec. B,3 of Chap. VII that such seemingly odd behavior for β/k_o should be expected, and the same bases are applicable here. Similar behavior was found in the case of the uniform microstrip line leaky-wave antenna, where it was shown in Sec. D,3 of Chap. IX that the crossing of the $\beta/k_o = 1$ line corresponds to the condition for which the pole is no longer captured in the steepest-descent plane and thus can no longer contribute to the total field.

In Fig. 10.28 similar data are reported for a slit that is more symmetrically located, and therefore leaks much less. We see that the values of α/k_o in the above-cutoff frequency range are much *lower* as compared with those in Fig. 10.27, and also that the β/k_o values below cutoff approach zero more closely at the minimum. Qualitatively, the performances are similar.

Plots of the *unnormalized* phase constant β and leakage constant α as a function of frequency are presented in Fig. 10.29. It is seen clearly that both β and α approach constant values as the frequency approaches zero. Thus, when we divide by k_o , which goes to zero linearly with the frequency, it is evident that the curves for β/k_o and α/k_o in Figs. 10.27 and 10.28 must continue to increase as the frequency approaches zero.

The variations in the values of the *beam angle* θ_m and the *beam width* $\Delta\theta$ as a function of frequency in the range above cutoff are shown in Fig. 10.30. For θ_m we observe that the beam angle changes rather quickly with frequency, making frequency scan in elevation effective for this array. It is possible to cover essentially the whole angular range by varying the frequency about ± 7 GHz, centered at 50 GHz. The frequency range below 50 GHz seems more attractive because $\Delta\theta$ varies more slowly there; we note that we can scan from about 5° from broadside to about 40° in about 5 GHz, or a 10% change. Because of the presence of the dielectric material, however, we have lost the very desirable property possessed by the offset-groove-guide antenna, namely, that $\Delta\theta$ remains constant with frequency. Here, $\Delta\theta$ is seen to change substantially with frequency, as we also found for the uniform microstrip leaky-wave antenna in Sec. E of Chap. IX.

The behavior of θ_m and $\Delta\theta$ vs. frequency for a larger value of d , meaning a lower leakage rate, is shown in Fig. 10.31. These dimensional values are the same as those for Fig. 10.28. The θ_m dependence on frequency is essentially the same as that found in Fig. 10.30, but the $\Delta\theta$ values are smaller, as expected.

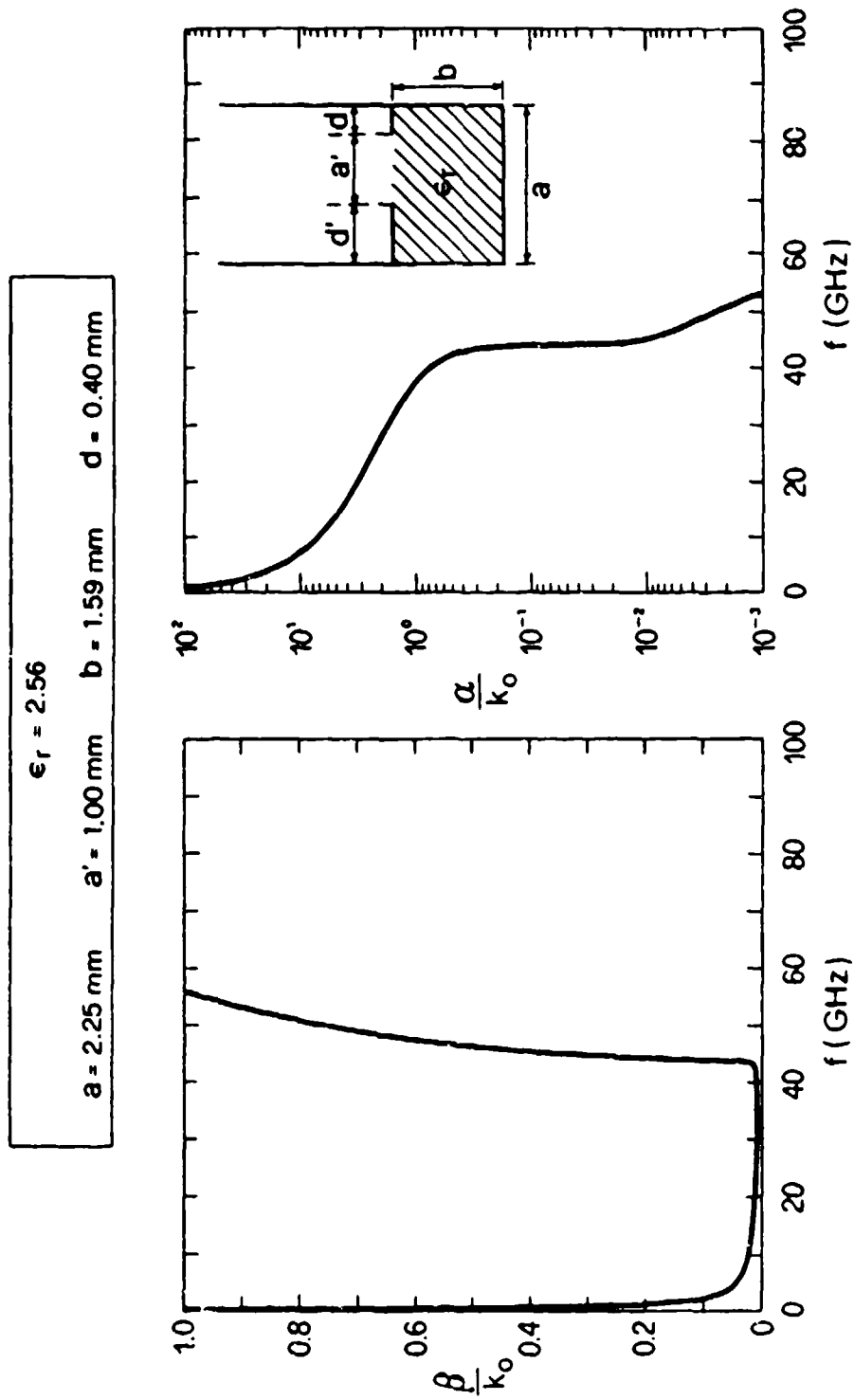


Fig. 10.28 Same as Fig. 10.27, but for $d = 0.40 \text{ mm}$, which yields a smaller leakage rate.

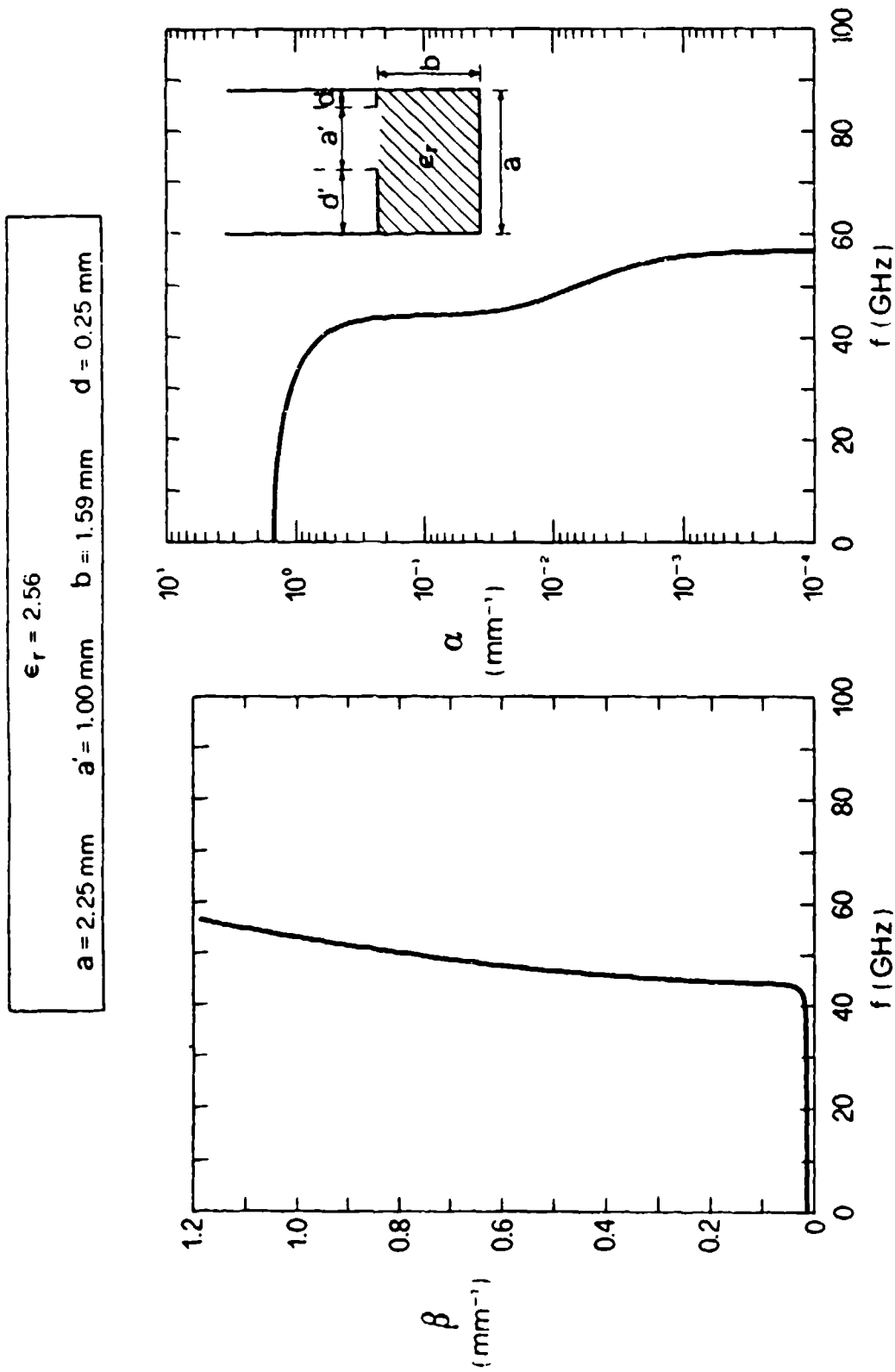


Fig. 10.29 Variations of the unnormalized phase and leakage constants, β and α , as a function of frequency over a wide range.

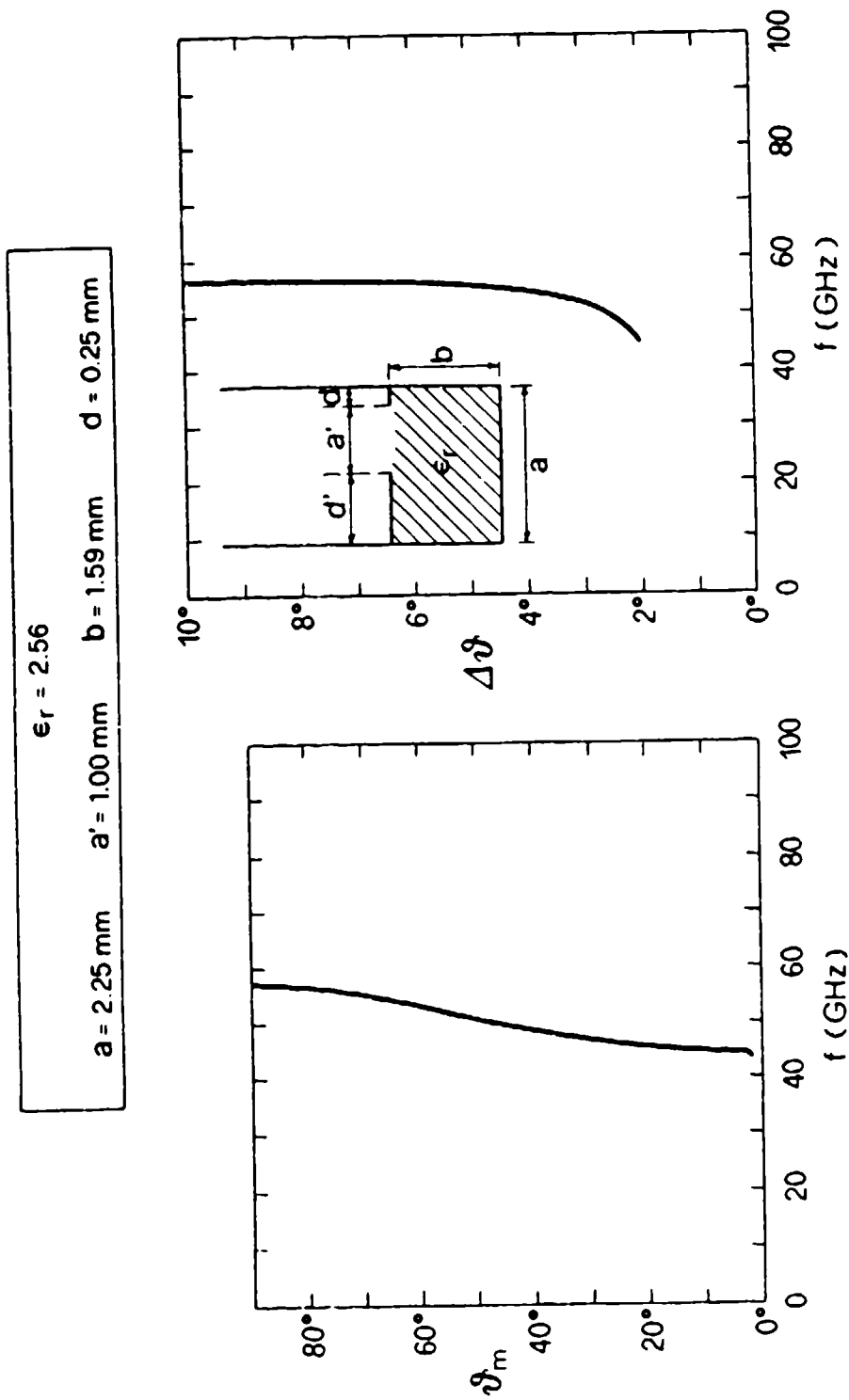


Fig. 10.30 Variations of the beam elevation angle θ_m and the beam width $\Delta\theta$ as a function of frequency, for $d = 0.25 \text{ mm}$.

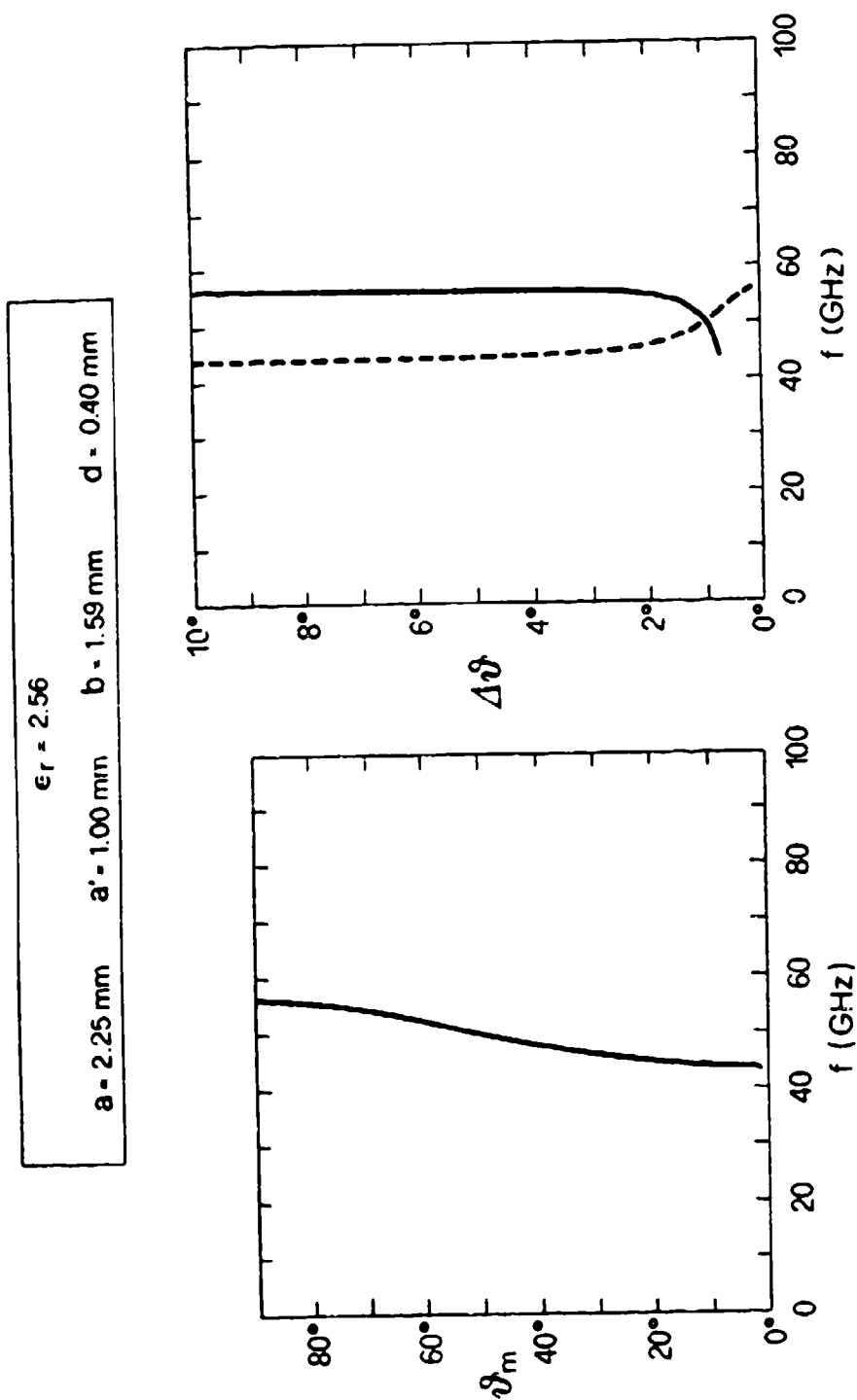


Fig. 10.31 Same as Fig. 10.30, but for $d = 0.40 \text{ mm}$, which yields a lower leakage rate. The dashed line for $\Delta\theta$ is new to this figure. For the distinction between the solid and dashed lines for $\Delta\theta$, see text.

Moreover, two curves are shown for $\Delta\theta$, to indicate that different behavior is obtained for different methods of operation. The solid curve here, and the curve in Fig. 10.30, assume that one chooses a length L for the antenna and then maintains that value of L as the frequency is changed. The dashed curve assumes that at each frequency the length L is changed so that 90% of the power is radiated at each frequency. From (2.28) and (2.29), we may write the relations that correspond to the solid and the dashed lines:

$$\text{solid line: } \Delta\theta = \frac{52.1}{(L/\lambda_o) \cos \theta_m} \quad (10.85)$$

$$\text{dashed line: } \Delta\theta = 285 \frac{\alpha/k_o}{\cos \theta_m} \quad (10.86)$$

where $\Delta\theta$ is in degrees in both relations. The value of L/λ_o to be used in (10.85) depends on the frequency chosen, since L/λ_o is determined from (2.28) and α/k_o varies with frequency. For the curve for $\Delta\theta$ in Fig. 10.30, the center frequency of 50.0 GHz was selected, and L/λ_o became 29.7. It is seen from Fig. 10.31 that these two different ways to compute $\Delta\theta$ actually produce oppositely directed dependences. The more meaningful method of operation, if indeed frequency scanning is intended, is the one corresponding to the solid line.

The last set of curves relating to behavior with frequency is concerned with the *transverse wavenumbers*. We consider only the wavenumber in the air region, which is k_{yos} in the parallel-plate region with metal walls and k_{yop} in the periodic region; when $k_{xop} = 0$, corresponding to zero cross-plane scan, they are of course equal to each other, as explained above. For the offset-groove-guide antenna, we found in Chap. VII that the transverse wavenumber, although complex, was indeed independent of frequency. Here there are two different media in the cross section, so that k_{yop} must be frequency dependent.

The variations of $\text{Re } k_{yop}$ and $\text{Im } k_{yop}$ with frequency are presented in Fig. 10.32. The values for both the real and imaginary parts are seen to approach constants as the frequency nears to zero, but to decrease monotonically as the frequency increases, reaching zero when β/k_o becomes equal to unity, which is the transition between the fast and slow wave ranges of behavior. For still higher frequencies in the slow wave region, $\text{Re } k_{yop}$ remains zero since there is no leakage, and $\text{Im } k_{yop}$ becomes negative, corresponding to exponential decay away from the air-dielectric interface.

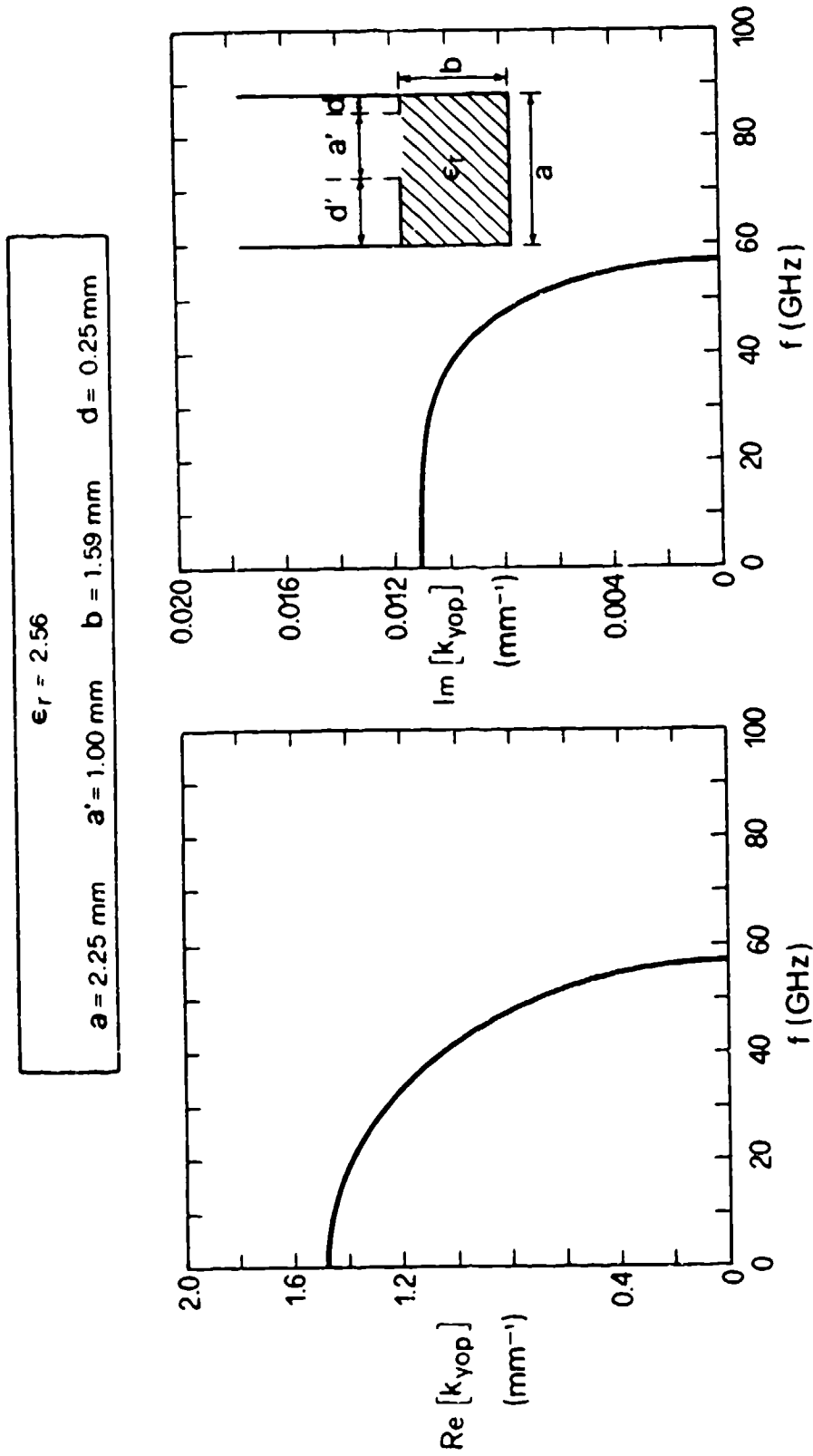


Fig. 10.32 Variations as a function of frequency of the real and imaginary parts of the transverse wavenumber k_{yop} , which is the propagation wavenumber in the periodic guide, for $d = 0.25 \text{ mm}$.

Figure 10.33 indicates the behavior of k_{yop}/k_o vs. frequency. When normalized to k_o , both the real and imaginary parts increase without limit as the frequency approaches zero, as we would expect. The behaviors of the unnormalized and normalized values of k_{yop} for a different value of offcenter slit location, corresponding to a lower leakage rate, are given in Figs. 10.34 and 10.35, respectively. It is interesting to note that the $\text{Re } k_{yop}$ values, when Figs. 10.32 and 10.34 are compared, are not much different; similarly for the normalized values. The $\text{Im } k_{yop}$ values, however, are very different, by almost a factor of three.

The reason for the different behavior becomes clear when we examine the relations between the real and imaginary parts of k_{yop} and k_o . From

$$k_o^2 = (\beta - j\alpha)^2 + (\text{Re } k_{yop} + j \text{Im } k_{yop})^2 \quad (10.87)$$

we separate the real and imaginary parts, to obtain

$$k_o^2 = \beta^2 - \alpha^2 + (\text{Re } k_{yop})^2 - (\text{Im } k_{yop})^2 \quad (10.88)$$

and

$$\alpha\beta = (\text{Re } k_{yop})(\text{Im } k_{yop}) \quad (10.89)$$

When $k_o \rightarrow 0$, $\alpha^2 \gg \beta^2$ and $(\text{Re } k_{yop})^2 \gg (\text{Im } k_{yop})^2$, as seen from Figs. 10.29 and 10.32. Under those conditions, (10.88) reduces to

$$\text{Re } k_{yop} \approx \alpha \quad (10.90)$$

Employing (10.90) in (10.89) yields

$$\text{Im } k_{yop} \approx \beta \quad (10.91)$$

When we compare Figs. 10.29 and 10.32, we see that the ordinate values in each do approach constant values. By an inspection of the curves we may check relations (10.90) and (10.91), although more precise values may be found from Fig. 10.32. We find, for $f \rightarrow 0$:

$$\text{Re } k_{yop} = 1.48; \quad \alpha = 1.5$$

$$\text{Im } k_{yop} = 0.011; \quad \beta = 0.01$$

The computer output results for α and β are 1.479/mm and 0.0111/mm. Relations (10.90) and (10.91) are therefore very accurate.

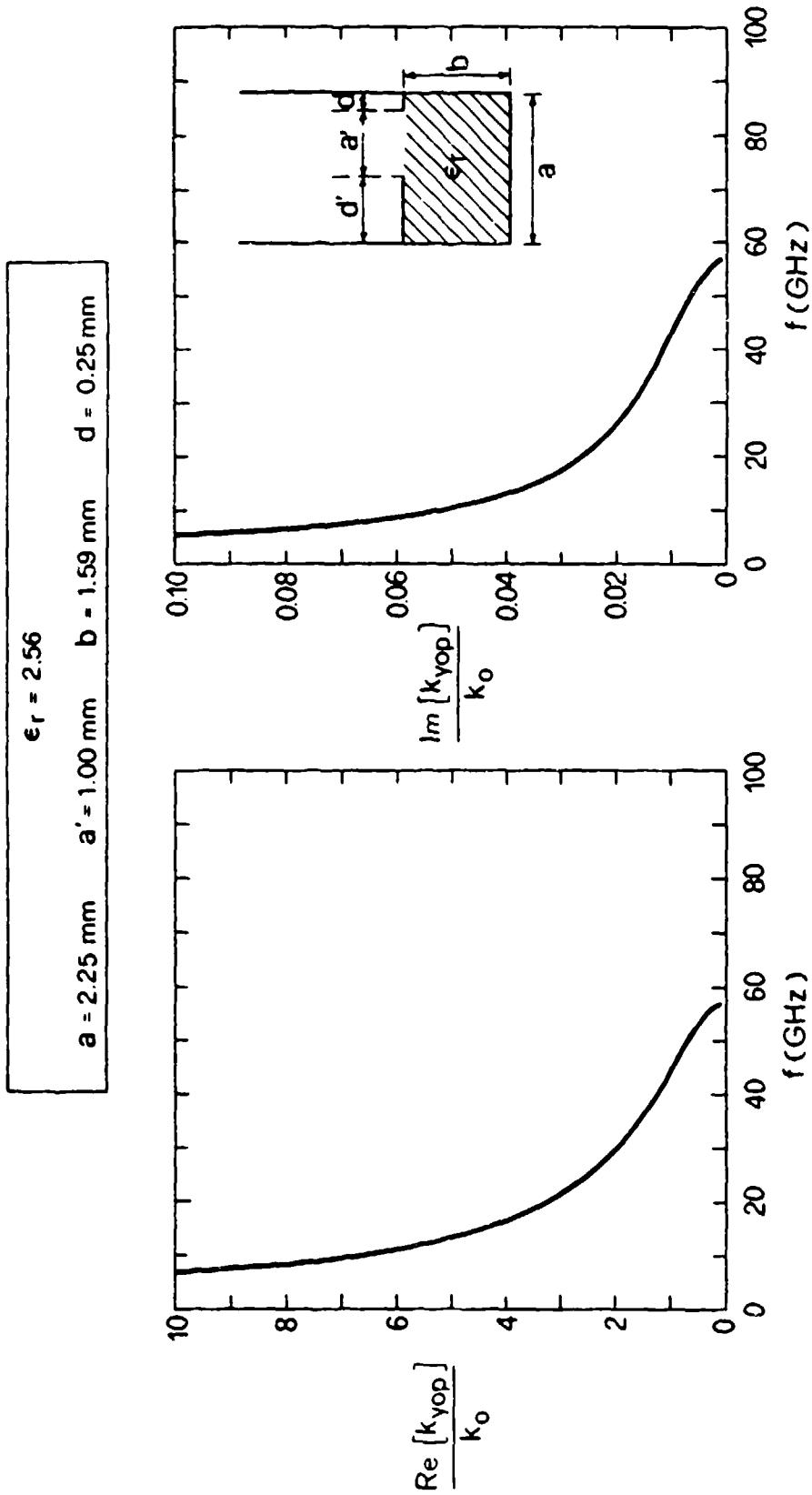


Fig. 10.33 Variations as a function of frequency of the real and imaginary parts of the normalized transverse wavenumber k_{yop}/k_0 , for $d = 0.25 \text{ mm}$.

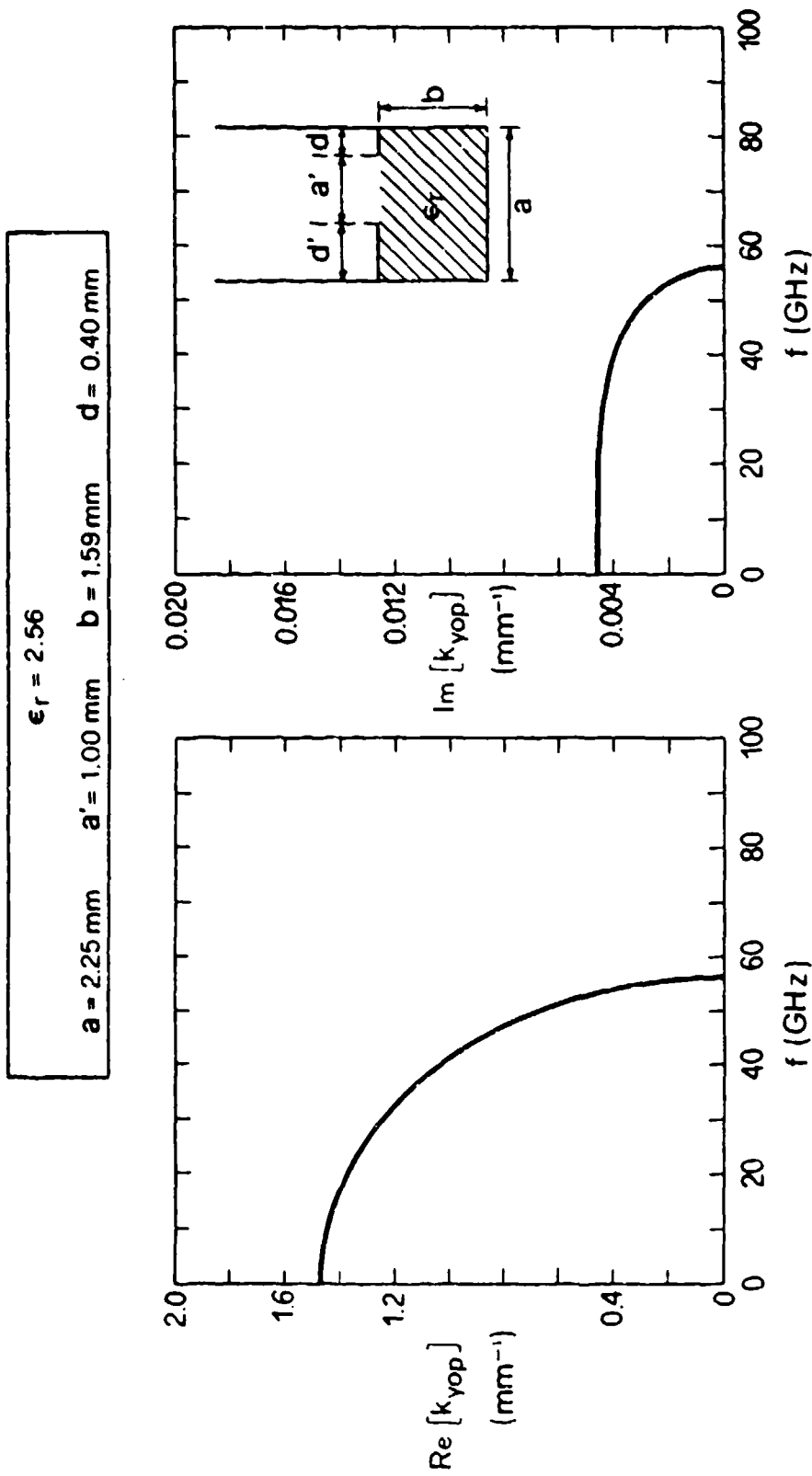


Fig. 10.34 Same as Fig. 10.32, but for $d = 0.40 \text{ mm}$.

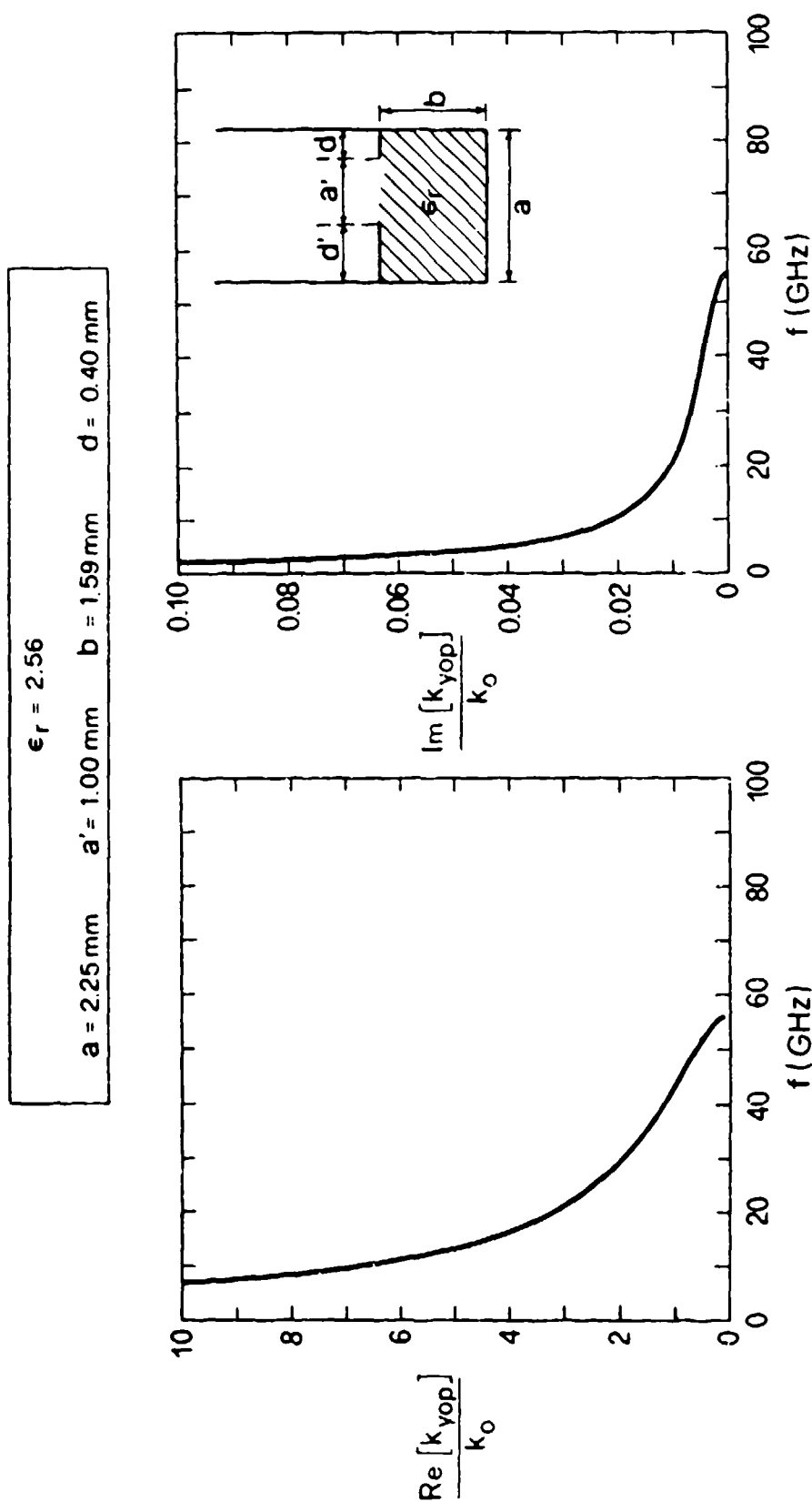


Fig. 10.35 Same as Fig. 10.33, but for $d = 0.40 \text{ mm}$.

E. EFFECTS OF CROSS-PLANE SCANNING

Cross-plane scanning, and therefore scanning in the azimuth plane, is achieved by imposing a phase shift between successive parallel line sources in the array. This phase shift per unit cell, Φ_C , is defined in (10.68) as

$$\Phi_C = k_{xop} a \quad (10.92)$$

where a is the unit cell width and k_{xop} is the wavenumber component in the x direction. When $k_{xop} = 0$, there is no cross-plane scanning, and the junction between the stub guide with metal walls and the periodic guide with phase-shift walls disappears. As a result, the phase-shift walls become electric walls, and the stub guide becomes effectively infinitely high, as discussed in Sec. D.

When $k_x \neq 0$, and cross-plane scan is present, the junction between the stub guide and the periodic guide becomes significant. The larger the phase shift introduced per unit cell, the bigger is the effective discontinuity due to that junction. Two primary effects are introduced by the junction discontinuity; the first is that a *standing wave* is introduced into the stub guide region, between the slit of width a' located at the air-dielectric interface and the above-mentioned junction, and the second is that a *new set of leaky modes* is introduced, the so-called channel-guide modes. These channel-guide modes also occur in antenna structures treated in other chapters of this report, and have been discussed in detail in Chaps. IV and VII. Due to the standing wave, subsidiary effects are also introduced, including a small *deviation from conical scan* and a *variation in the leakage rate* as k_{xop} is changed.

When the cross-plane scan angle is small, the junction discontinuity is small, so that the standing wave is mild and the interaction between the desired leaky mode and the unwanted channel-guide modes is negligible or completely absent. When the cross-plane scan angle is large, however, all the effects are magnified, and the interaction with the channel-guide modes must be taken into account. In the treatment below, we first select two separate phase-shift values, one corresponding to a small cross-plane scan angle and the other to a large one, to illustrate the performance differences.

Before we can select the two typical phase shift values corresponding to large and small scan angles, we must know the value of phase shift that causes the beam to reach the end of the conical scan range. During the conical scan, the beam begins at azimuth angle $\phi = 0$; then, as k_{xop} or Φ_C increases, ϕ increases and θ also increases,

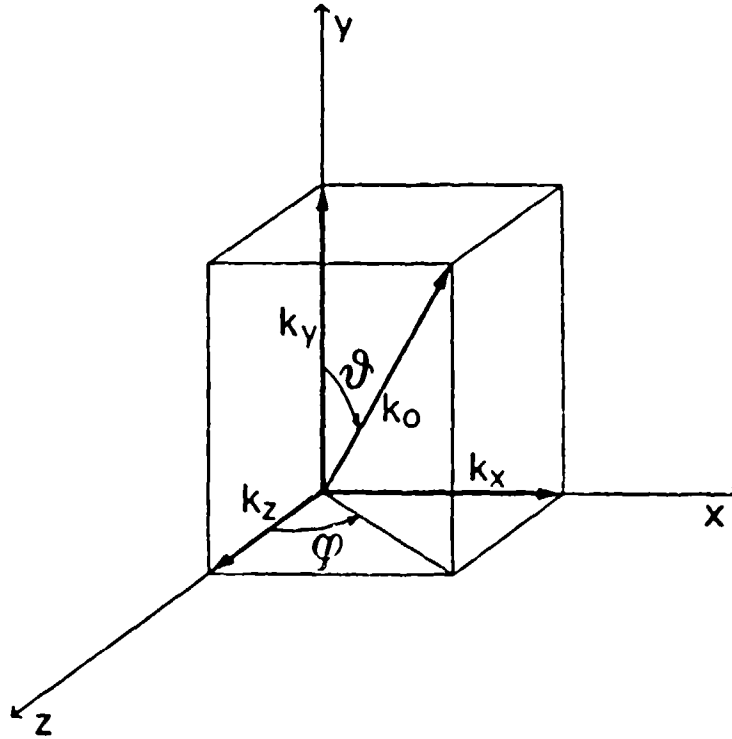


Fig. 10.36 Polar coordinate diagram, showing the relationships between the various wavenumbers and angles θ and ϕ .

meaning that the beam gets closer to the ground. When Φ_C reaches its maximum value, $\theta = 90^\circ$, ϕ is at its maximum value, and all radiation ceases. The relation between the angles ϕ and θ at the two extremes has been derived in Chap. II as

$$\phi_{\theta = 90^\circ} = 90^\circ - \theta_{\phi = 0} \quad (10.93)$$

which is (2.16).

With the aid of the polar coordinate diagram in Fig. 10.36, we see that

$$\sin \theta_{\phi=0} = k_z / k_o \approx \beta / k_o \quad (10.94)$$

and

$$\sin \phi_{\theta=90^\circ} = k_x / k_o = k_{xop} / k_o \quad (10.95)$$

Combining (10.93) to (10.95), we find for the largest permissible value of k_{xop}

$$k_{xop} / k_o = \cos(\sin^{-1} \theta_{\phi=0}) \quad (10.96)$$

The value of $\theta_{\phi=0}$ is seen from (10.94) to depend on the properties of the leaky-wave line source, so that the maximum value of k_{xop} will change as the dimensions of the line-source cross section are altered. It is also a function of frequency.

For a center frequency of 50.0 GHz, and for $a = 2.25$ mm, $a' = 1.00$ mm, $b = 1.59$ mm, and $d = 0.25$ mm, a typical case for which we have many numerical results in Sec. D, we know that $\beta / k_o = 0.737$. For that value of β / k_o , we have from (10.94) and (10.96) that

$$\theta_{\phi=0} = 47.5^\circ, \text{ and } k_{xop} / k_o = 0.676.$$

Since $k_o = 1.047/\text{mm}$ at 50.0 GHz, and $a = 2.25$ mm, we have obtained for the maximum value of the phase shift per unit cell, from (10.92),

$$(\Phi_C)_{\max} = 91.3^\circ$$

for this set of dimensions. When $d = 0.40$ mm, with all other dimensions the same, we find that the maximum value of phase shift per unit cell becomes 86.6° . It is therefore reasonable to select $\Phi_C = 35^\circ$ and 70° as phase shift values that correspond to small and large cross-plane scan angles, respectively.

In the figures presented below, the numerical values first demonstrate that for small, but not negligible, cross-plane scan angles (corresponding to $\Phi_C = 35^\circ$), a mild standing wave effect is present but no interactions with channel-guide modes occur. Next, for $\Phi_C = 70^\circ$, interesting interactions with channel-guide modes are found, and we indicate how to avoid their influence. Numerical values are also presented for several quantities as a function of stub guide location d/a , showing that the variations are similar but numerically a bit different, as compared with the case of zero cross-plane scan. Finally, we examine the performance as a function of phase shift Φ_C per unit cell, to show that the conical scan is affected slightly, and that no blind spots occur.

1. Small Cross-Plane Scan Angles

The dispersion relation from which the numerical values presented below are obtained is given by summing to zero relations (10.80) and (10.82), using the various supporting expressions in that vicinity. The discontinuity appearing at the junction between the stub guide and the periodic waveguide is accounted for rigorously. That discontinuity permits the presence of a *standing wave* in the stub guide region between it and the slit of width a' at the air-dielectric interface. The extent of that standing wave and its effect on the phase and leakage constants are illustrated in Fig. 10.37 by varying the length c of the stub guide.

In Fig. 10.37 the phase shift per unit cell Φ_C is 35° . The azimuth angle ϕ corresponding to that phase shift value is readily obtained from the following simple considerations. From the polar coordinate expression in (2.9) of Chap. II, we write

$$k_{xop} = k_o \sin \theta \sin \phi \quad (10.97)$$

while we note from the polar coordinate diagram in Fig. 10.36 that

$$k_o \sin \theta = [k_{xop}^2 + \beta^2]^{1/2} \quad (10.98)$$

where we have set $\beta \approx k_z$. Combining these two expressions, we have

$$\sin \phi = \frac{k_{xop}/k_o}{[(k_{xop}/k_o)^2 + (\beta/k_o)^2]^{1/2}} \quad (10.99)$$

We may therefore compute the elevation and azimuth angles θ and ϕ of the main beam from (10.98) and (10.99), respectively, once β/k_o is known.

We do not yet know if β/k_o will change as k_{xop} increases, but for small values of k_{xop} , and therefore small cross-plane scan angles, we may assume for now that it remains almost the same as its value for $k_{xop} = 0$. On that assumption, $\beta/k_o = 0.737$ for the set of parameters given in the inset in Fig. 10.37. Furthermore, for $\Phi_C = 35^\circ$, $k_{xop}/k_o = 0.259$, since $k_o = 1.047/\text{mm}$ and $a = 2.25 \text{ mm}$. Using (10.98), we find that the azimuth scan angle $\phi = 19.4^\circ$, which is fairly small, but not extremely so.

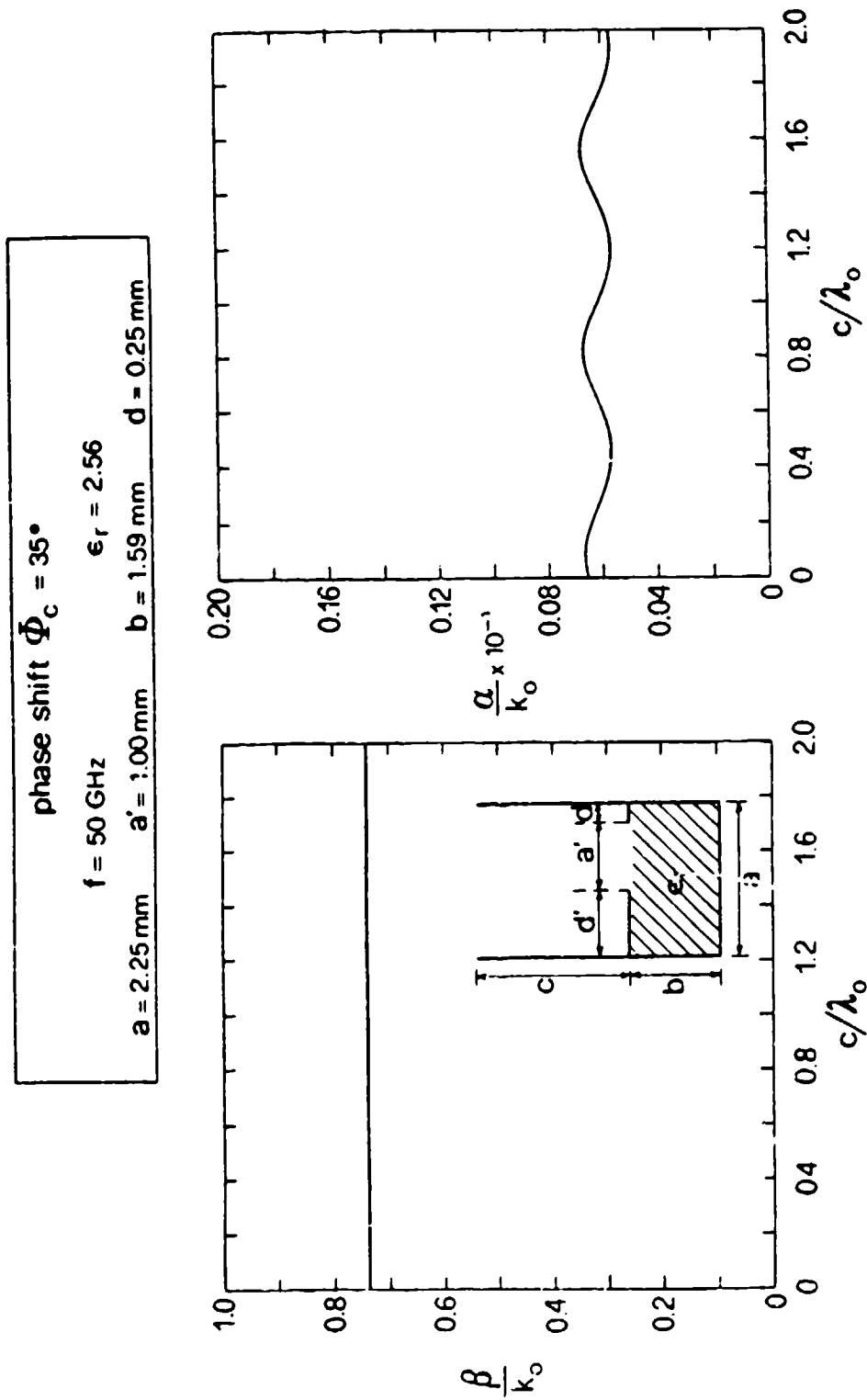


Fig. 10.37 Variations of the normalized phase and leakage constants as a function of the relative stub guide height, for $d = 0.25 \text{ mm}$ and for $\Phi_c = 35^\circ$, a relatively small phase shift per unit cell.

The variations of the normalized phase constant β/k_o and the normalized leakage constant α/k_o as a function of the normalized stub guide height c/λ_o are presented in Fig. 10.37 for phase shift $\Phi_C = 35^\circ$. We observe that β/k_o remains essentially flat with c/λ_o , whereas α/k_o undergoes a "periodic" variation with c/λ_o , as one would expect in view of the standing wave we know to be present in the stub guide region. The period of the standing wave is approximately $\lambda_{yos}/2\lambda_o$, but k_{yos} ($\approx 2\pi/\lambda_{yos}$) is complex (and given by (10.66)). A careful inspection of the standing wave pattern in the curve of α/k_o vs. c/λ_o reveals that the amplitude of the pattern *increases* slowly with c/λ_o , consistent with the complex nature of k_{yos} and the improper nature of leaky-wave poles for which the field increases to infinity in the transverse direction.

The standing wave is a mild one, consistent with the statement that the discontinuity is a small one when the cross-plane scan angle is small. For larger scan angles, the amplitude in the α/k_o plot would increase and a similar ripple would appear in the β/k_o plot, as was found for the array of NRD guide line sources discussed in Chap. IV. For still larger scan angles, as is seen later, coupling to channel-guide modes also occurs.

The angular coordinates θ_m and ϕ_m of the maximum of the radiated beam are computed from (10.98) and (10.99), using the value of β/k_o obtained from Fig. 10.37. Since β/k_o is essentially flat with c/λ_o , we should expect that θ_m and ϕ_m will also be essentially independent of c/λ_o . These expectations are borne out in Fig. 10.38. We may also note that the azimuth scan angle ϕ is slightly smaller than 20° , in close agreement with the calculation of 19.4° obtained above by assuming that β/k_o does not change when Φ_C is increased from zero to 35° . The assumption seems to be a good one; the actual variation is shown later for several geometric parameter values.

The slit offset position d in Figs. 10.37 and 10.38 is 0.25 mm. When d is reduced to 0.10 mm, corresponding to greater offset, or asymmetry, the value of β/k_o changes a bit and that of α/k_o increases substantially, almost doubling. The variations of β/k_o and α/k_o with c/λ_o are shown in Fig. 10.39. The qualitative behavior is the same as that found in Fig. 10.37, but the amplitude of the α/k_o variation seems a bit more pronounced and the β/k_o curve seems on the verge of oscillating periodically (the curve is a copy of the actual computer plot, not a tracing of plotted points).

Figure 10.40 is analogous to Fig. 10.38 for θ_m and ϕ_m vs. c/λ_o , but for $d = 0.10$ mm rather than $d = 0.25$ mm. The behavior is again qualitatively similar; the greater leakage rate corresponding to Fig. 10.40 seems to raise the beam slightly in elevation

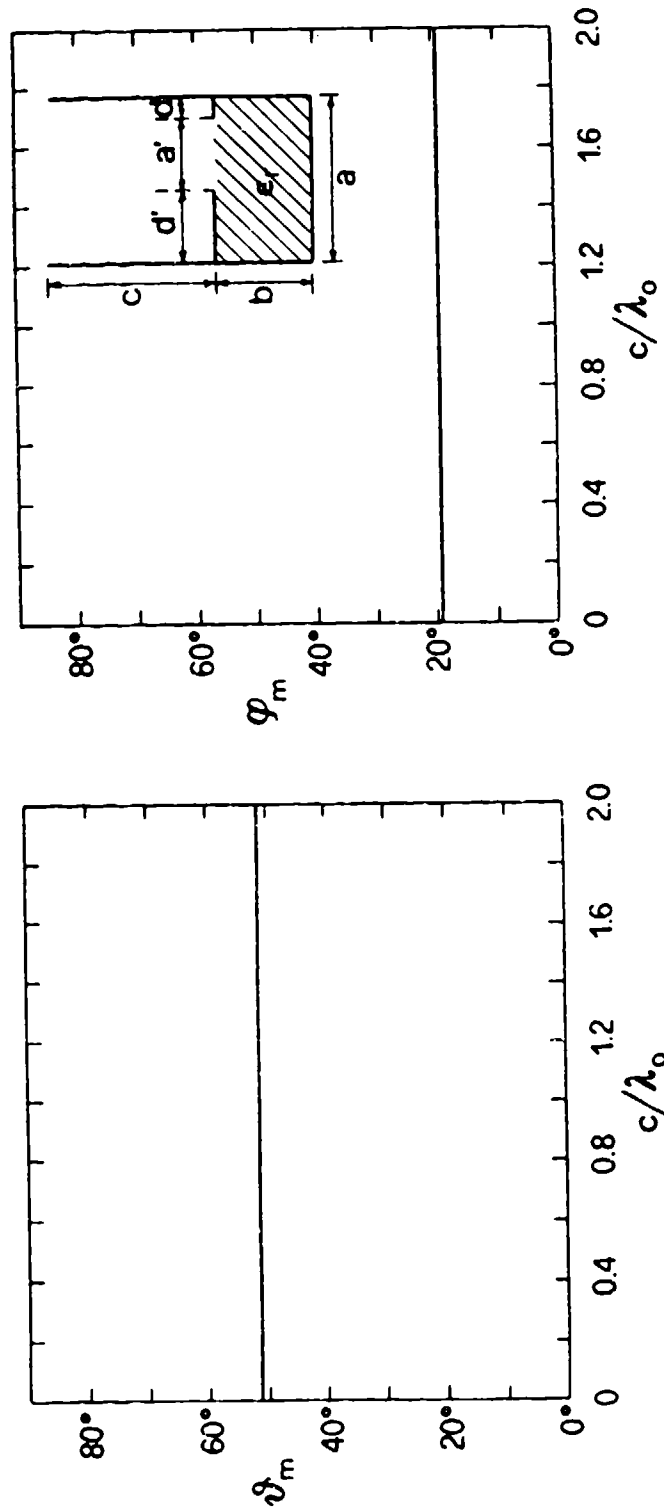
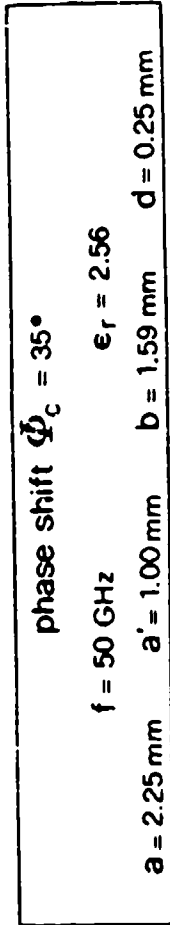


Fig. 10.38 Variations of the beam elevation angle θ_m and azimuth angle ϕ_m as a function of relative stub height, for $d = 0.25 \text{ mm}$ and for $\Phi_c = 35^\circ$, a relatively small phase shift per unit cell.

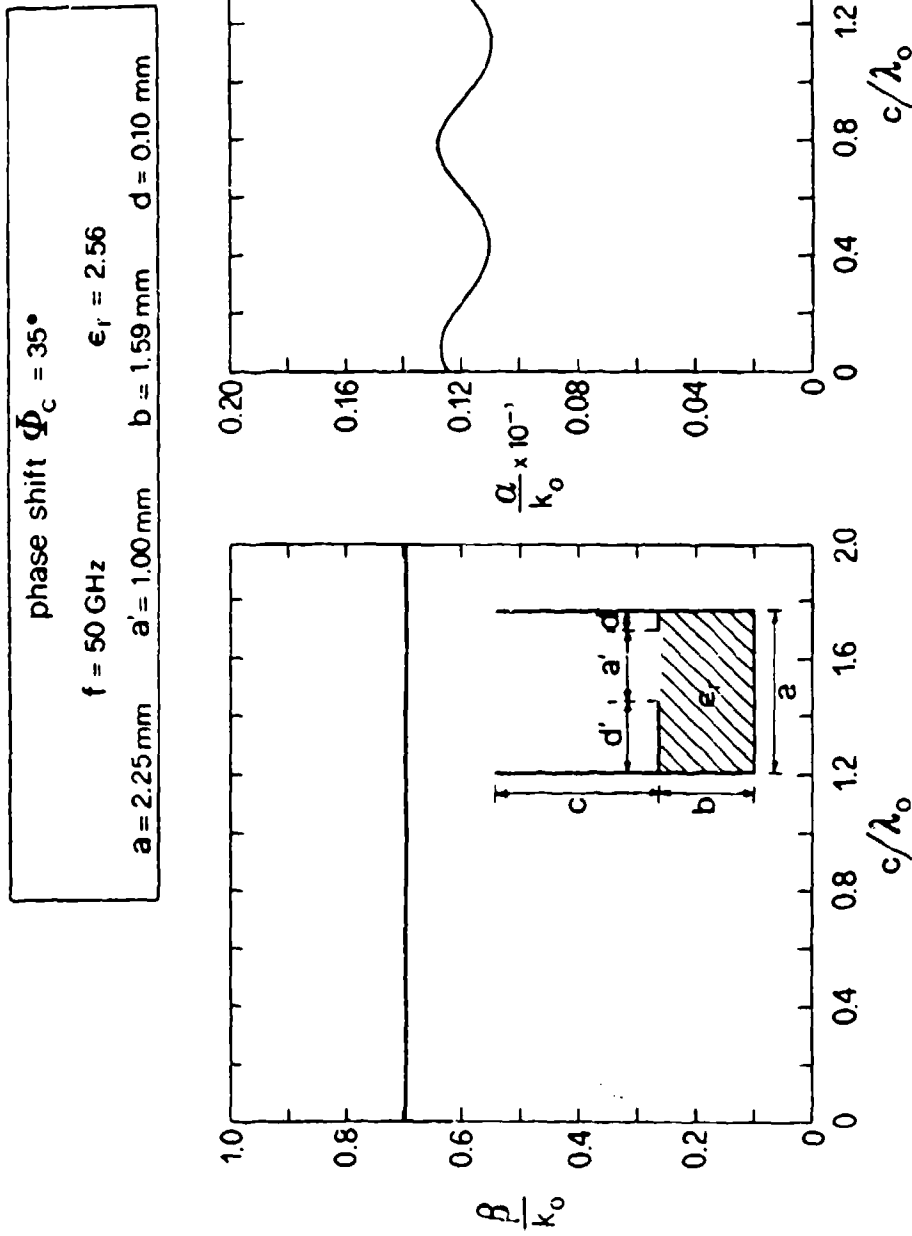


Fig. 10.39 Same as Fig. 10.37, but for $d = 0.10 \text{ mm}$, for which the leakage rate is higher.

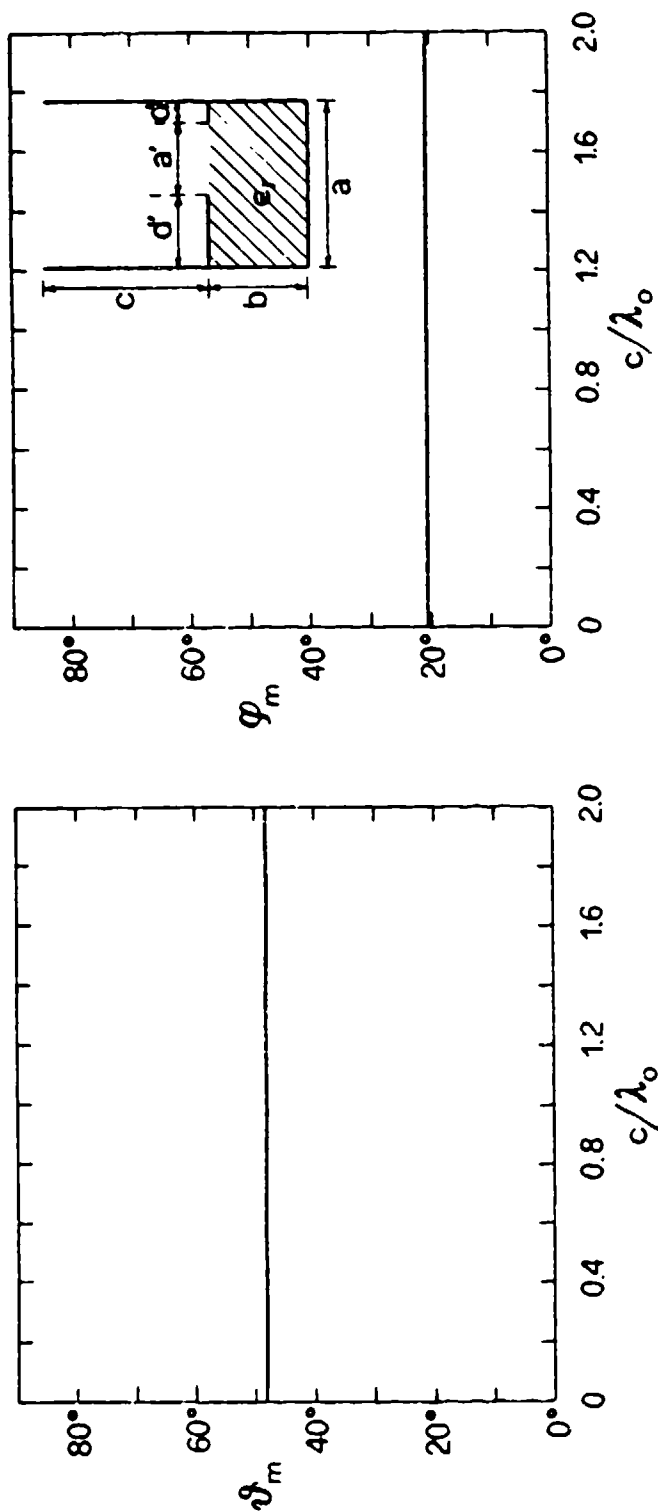
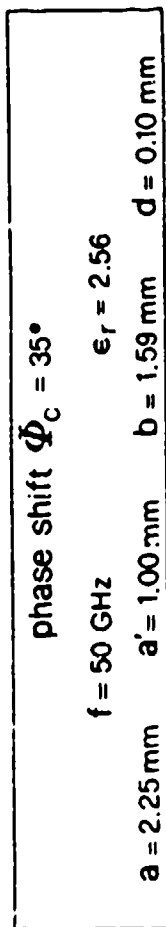


Fig. 10.40 Same as Fig. 10.38, but for $d = 0.10 \text{ mm}$, for which the leakage rate is higher.

and slightly increase the azimuth scan angle.

2. Large Cross-Plane Scan Angles

Large cross-plane scan angles, and therefore large azimuth scan angles, are produced by introducing larger phase shifts between successive line sources in the array. For this next set of curves, we have chosen the phase shift per unit cell Φ_C to be 70° , rather than 35° . As a result, the junction discontinuity between the stub guide and the periodic guide is greatly increased. The standing wave effect discussed above is enhanced, but we now also must take into account the interactions between the desired leaky mode and the set of channel-guide leaky modes.

The latter set of modes is discussed in detail in other chapters, but we wish here to point out the principal distinction between these modes and the desired one, that of the field polarization in the feed guide portion, as shown in Fig. 10.41. The electric field in the dielectric-loaded region is vertically polarized initially, giving rise to the horizontally-polarized field in the stub guide and the periodic guide because the coupling slit at the air-dielectric interface is located asymmetrically. The fields of the channel-guide leaky mode are horizontally polarized in all of the regions, and are affected very little by the asymmetry of the slit, as shown in detail in Chap. VII for the offset-groove-guide antenna. The primary seat of the coupling between the two mode types is the junction discontinuity between the stub guide and the periodic guide, which is more pronounced when the phase shift is greater. Of course, the modes will couple only when both the β and α values of each mode type are equal.

a. Variations with Stub Guide Height

The dependence of β/k_o and α/k_o on the normalized stub guide height c/λ_o when the phase shift per unit cell is large is shown in Fig. 10.42. For small values of c/λ_o , we have only the original desired mode, which we call $n = 0$ in that range. The channel-guide modes before they couple are designated as $n = 1$ through $n = 6$. No coupling occurs until c/λ_o equals about 2.8, although the presence of the $n = 2$ channel-guide mode nearby distorts the α/k_o curve slightly near $c/\lambda_o = 2.2$. The first real coupling occurs between the desired $n = 0$ mode and the $n = 3$ channel-guide mode; we find the usual gap in the β/k_o curves and the cross-over behavior in the α/k_o curves. Since this type of behavior has been discussed in detail in earlier chapters of this report, we will not comment on it here.

A new feature is present in Fig. 10.42, however, and it is concerned with the behavior of the channel-guide modes for lower values of c/λ_o . In the plots in other

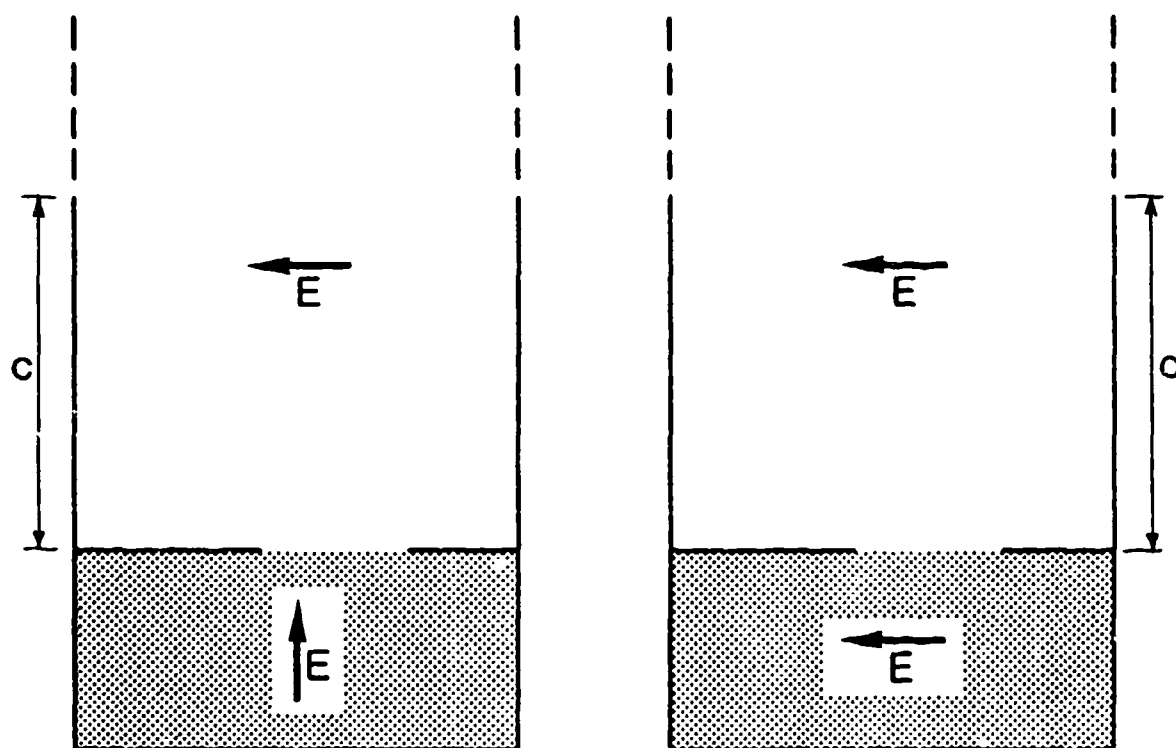


Fig. 10.41

Electric field directions in the array unit cell for the desired leaky mode, on the left-hand side, and for a channel-guide leaky mode, on the right-hand side. The polarizations are similar in the stub guide and periodic guide air regions but opposite in the dielectric region.

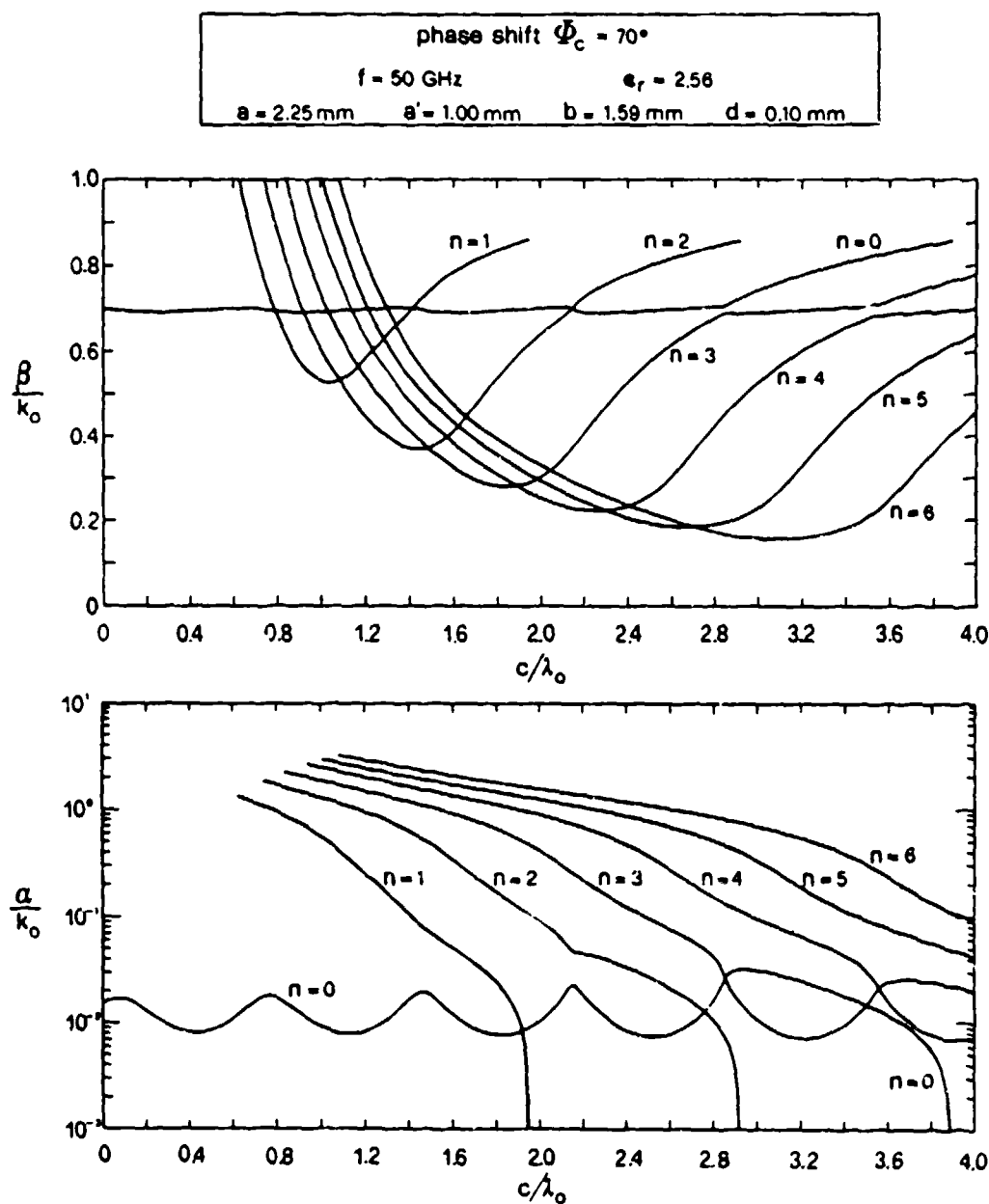


Fig. 10.42 Variations of the normalized phase and leakage constants as a function of relative stub guide height, for $\Phi_C = 70^\circ$, a relatively large phase shift per unit cell. (See text for identification of the various curves.)

chapters the curves were stopped before they reached this region. Now we have continued them until the value of c/λ_o is too small for these channel-guide modes to remain above cutoff. As these modes go *below cutoff*, however, their very *high* values of attenuation constant cause the turn-around in the β/k_o values to occur rather quickly, and their minimum values to be rather large. We believe that this is the first time that this feature relating to the channel-guide modes has been investigated, or even recognized.

As to how to use these curves to insure that the mode we are employing is the desired one and not one of the channel-guide modes, we follow the advice given in Chap. VII, namely, that we choose only those portions of the curves corresponding to the flat regions in the β/k_o plot.

The corresponding curves for elevation and azimuth scan angles θ_m and ϕ_m as a function of c/λ_o are presented in Fig. 10.43. Here, again, we must employ only those portions of the curves that are essentially flat. We then see that the values of θ_m and ϕ_m vary a little when c/λ_o is changed, but not much.

b. Variations with Slit Location

In Sec. D numerical values were presented for the variations of β/k_o , α/k_o and other quantities with various dimensional parameters for the special case of $\Phi_C = 0$. The principal dimensional parameter that was varied was d/a , where d is a measure of the location of the slit in the guide cross section, and therefore a measure of the asymmetry. Now, we present numerical results for some of the same variations, but for the case of $\Phi_C = 70^\circ$, a large phase shift value, to compare the behaviors.

First, in Fig. 10.44, β/k_o and α/k_o are plotted as a function of d/a for the same parameter values as in Fig. 10.11, except that now $c = 1.00$ mm instead of being effectively infinite. When we compare Figs. 10.44 and 10.11 with regard to the curves for β/k_o , we find that they are very similar. The curves for α/k_o are qualitatively similar, but the values in Fig. 10.44 are roughly 20% higher.

The reason for higher values for α/k_o in Fig. 10.44 may be understood by examining Fig. 10.42. For $c = 1.00$ mm at 50.0 GHz, we have $c/\lambda_o = 0.167$. At that value of c/λ_o , the curve of α/k_o vs. c/λ_o is near to a crest in the periodic variation, and therefore higher than the average value. If c/λ_o were chosen to be 0.40, for example, the curve would be at a trough, and the values of α/k_o in a plot equivalent to that in Fig. 10.44 would yield values lower than those in Fig. 10.11.

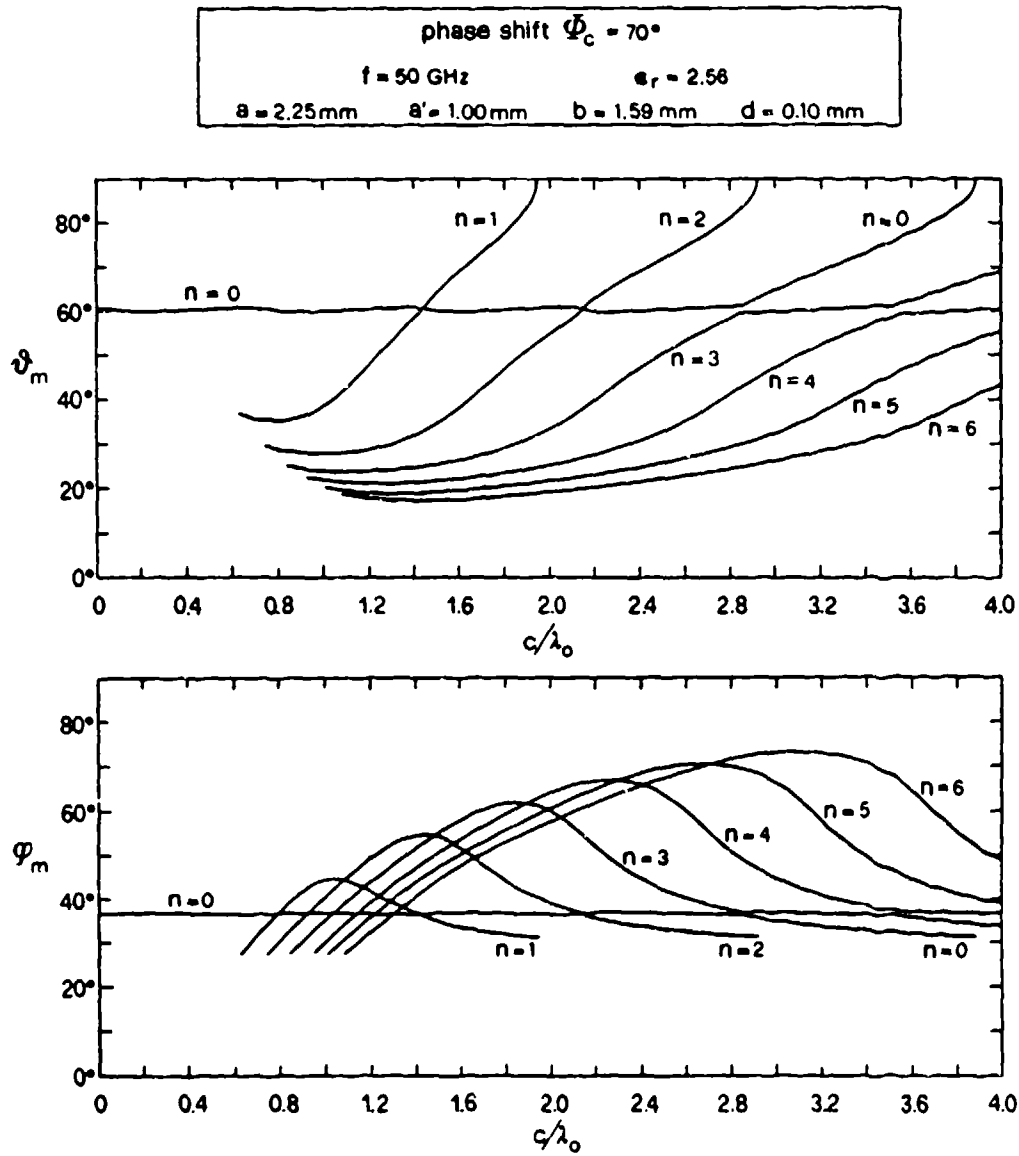


Fig. 10.43 Same as Fig. 10.42, except that the ordinate quantities are now the elevation and azimuth angles.

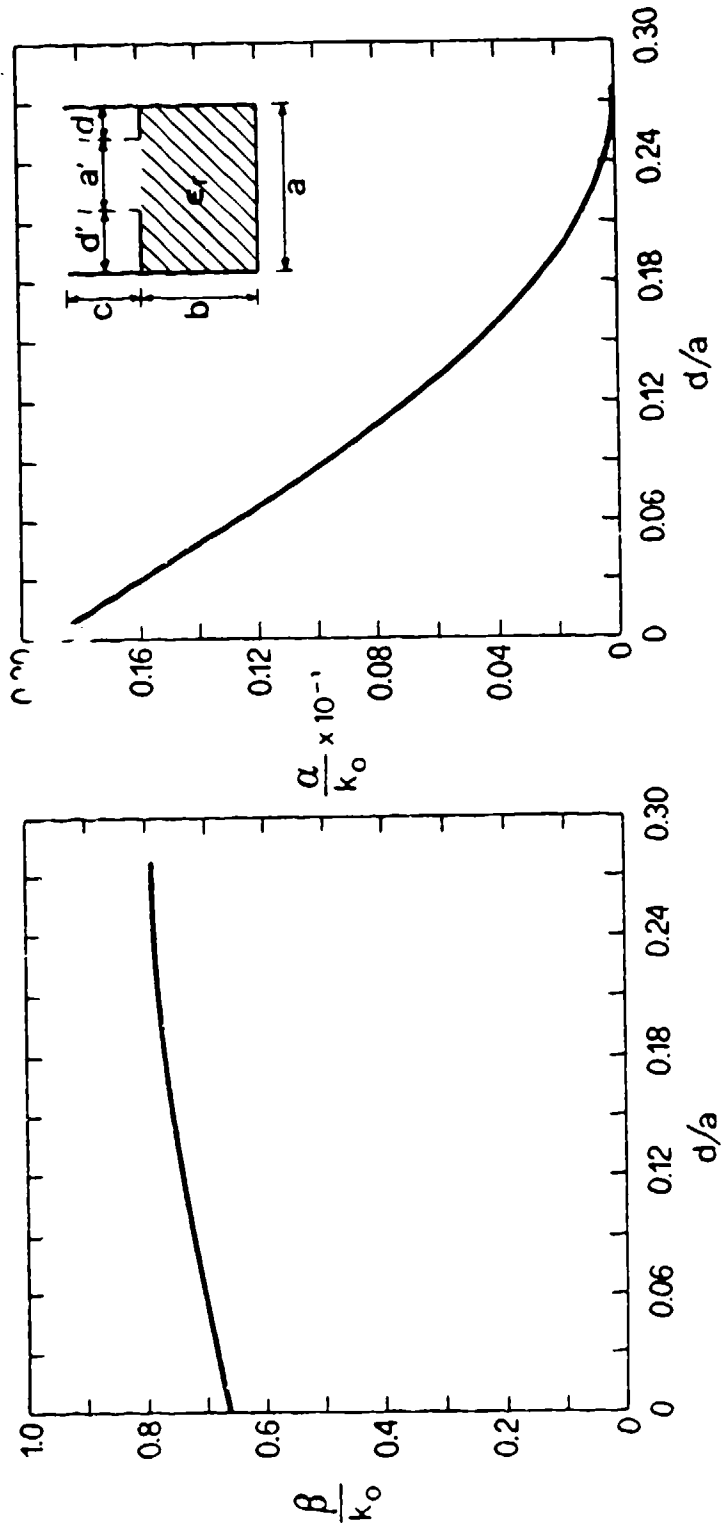
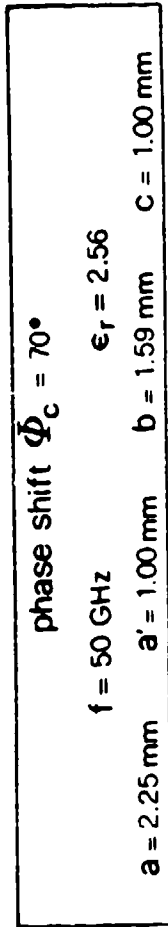


Fig. 10.44 Variations of the normalized phase and leakage constants as a function of slit location in the cross section, when $\Phi_c = 70^\circ$, a large phase shift per unit cell.

As a separate consideration, the value $c = 1.00$ mm is actually too small for practical purposes. The length c must be long enough so that the vertically polarized component of electric field has effectively decayed to zero, to insure negligible cross polarization in the radiated beam. We had determined earlier that $c/\lambda_o \approx 0.5$ is sufficient. With respect to Fig. 10.42, therefore, one can choose any value of c/λ_o greater than 0.5 or so, but if one wishes to maximize the leakage rate a value of c/λ_o near 0.8 may be selected.

The next curves, in Fig. 10.45, show how the elevation and azimuth scan angles θ_m and ϕ_m change as d/a is varied. The qualitative behaviors for θ_m in Figs. 10.45 and 10.20 are seen to be similar, but the actual values must be different because θ_m is computed using (10.98), and the values of k_{xop} are quite different for the two cases. A point on the curves for θ_m and ϕ_m in Fig. 10.45 must agree with corresponding points on the curves in Fig. 10.43. The points in Fig. 10.43 correspond to $c = 1.00$ mm, or $c/\lambda_o = 0.167$; those in Fig. 10.45 correspond to $d = 0.10$ mm, or $d/a = 0.044$. Direct inspection of the relevant curves show that they are in agreement.

3. Variations with Imposed Phase Shift

In the two preceding subsections we presented the behavior of key quantities under the conditions of small, and then large, cross-plane scan angles. Here we consider the behavior as we change the scan angle *continuously over its whole range*. In the process, we are concerned about two basic features: the extent of deviation from strict conical scan, and the possible presence of blind spots. As we see below, the deviation is actually very small, and no blind spots are found.

a. Wavenumber Variations

The quantities β/k_o and α/k_o are measures of the leaky-wave behavior, and therefore of the elevation angle in the longitudinal principal plane (the yz plane, see Fig. 10.8 or 10.36) and the vertical beam width in that plane. As the beam scans in azimuth, the elevation angle changes (in keeping with conical scan) and the beam width becomes modified. As the beam scans in azimuth, the properties of the discontinuity between the stub guide and the periodic guide change, so that the termination on the equivalent network representing the unit cell (see Fig. 10.8) becomes modified. As a result, the values of β/k_o and α/k_o change, and it is important to know the nature of these changes.

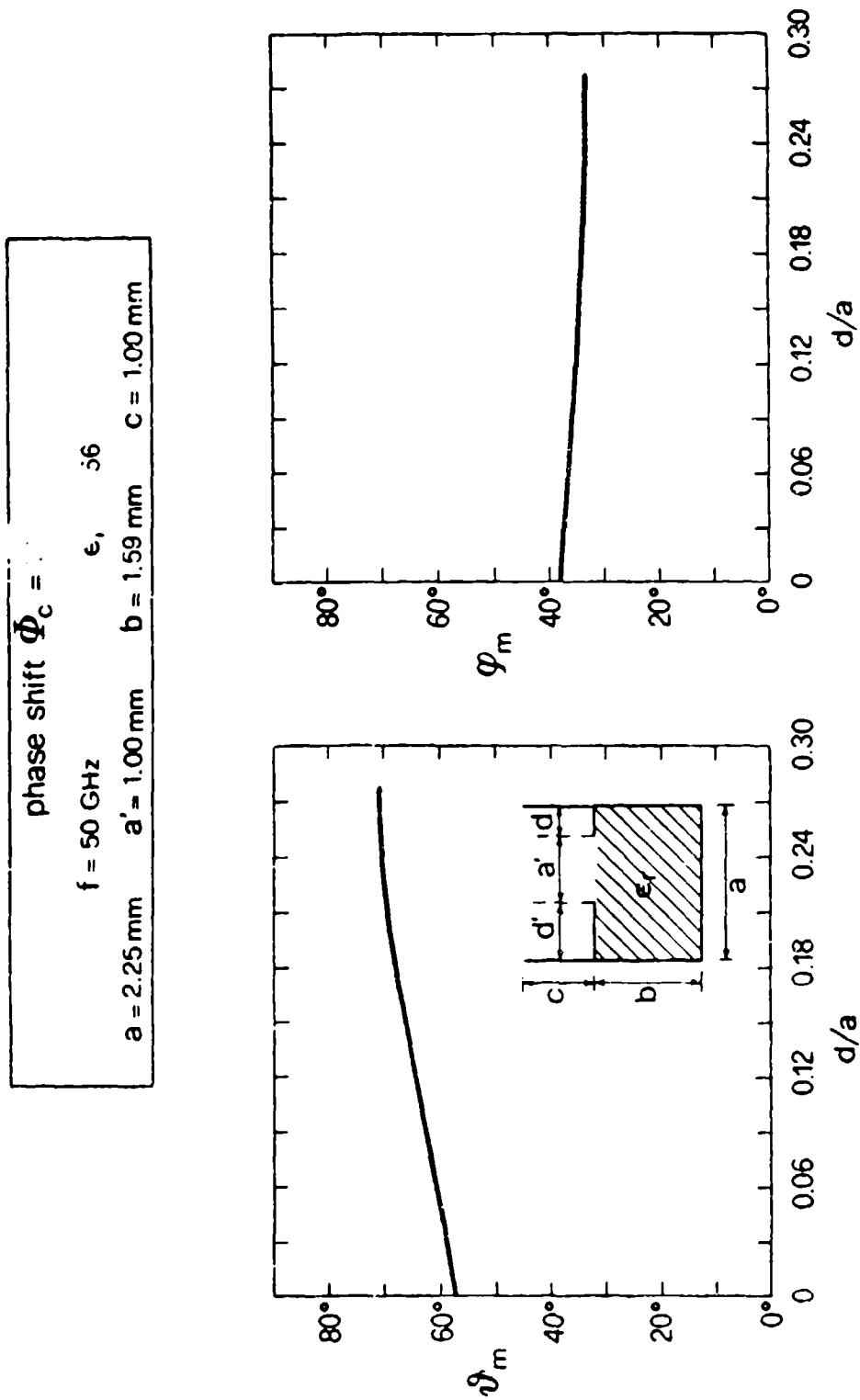


Fig. 10.45 Variations of the elevation and azimuth angles as a function of slit location in the cross section, when $\Phi_c = 70^\circ$, a large phase shift per unit cell.

In Figs. 10.46 through 10.49 we present the variations of β/k_o and α/k_o as a function of Φ_C , the phase shift per unit cell, over the whole range of permissible values, for four separate cases. From these four figures, certain qualitative features may be observed immediately. First, the curves of β/k_o are seen to be *essentially flat* in all cases. For some, the curves droop down slightly, and for one of them (Fig. 10.47) a sharp change occurs near the end of the scan range, as the beam approaches the ground. The flatness implies that the deviation from conical scan will be small, as we shall see below.

The curves for α/k_o vs. phase shift are seen to change in interesting ways from one case to the next, but for all of them it is clear that no sharp dips occur anywhere during the scan range. (Of course, all the curves go to zero at the end of the scan range, when the beam hits the ground and all radiation ceases.) The absence of any drops during the scan range shows that *no blind spots* occur.

In order to explain why two of the curves for α/k_o rise near the end of the scan range (Figs. 10.46 and 10.47), while another (Fig. 10.48) remains pretty flat and the last (Fig. 10.49) drops off, we must determine the specific values of c in each case and examine, in Figs. 10.37, 10.39 and 10.42, how that value of c corresponds to the crest and trough nature of the periodic variation with c . In Fig. 10.46, $c = 1.00$ mm, so that $c/\lambda_o = 0.167$; in all three of Figs. 10.37, 10.39 and 10.42 that value of c/λ_o corresponds to a point near the crest of the periodic curve. As the phase shift increases, the amplitude of the variation increases (since the geometric discontinuity becomes more pronounced); thus, a point located near a crest gets pushed higher, so that the curve for α/k_o will increase as the phase shift becomes large. Since the stub guide height is rather small, however, the amplitude increase as the phase shift increases is only modest; as a result, the rise in α/k_o will be small in this case.

For the three remaining figures (Figs. 10.47, 10.48 and 10.49), the values of c are 4.80 mm, 6.00 mm and 7.20 mm, so that $c/\lambda_o = 0.80$, 1.00 and 1.20, respectively. Inspection of Figs. 10.37, 10.38 and 10.42 shows that for each of these figures the values $c/\lambda_o = 0.80$, 1.00 and 1.20 correspond to points near a crest, near the middle, and near a trough, respectively. From the reasoning above, we would therefore expect that the curves of α/k_o vs. phase shift would show, respectively, a rise, a flat behavior, and a drop. The curves in Figs. 10.47 to 10.49 follow our expectations.

The increase in Fig. 10.47 is sharper than that in Fig. 10.46 because the value of c/λ_o for it is closer to the maximum of the crest, as well as corresponding to a higher

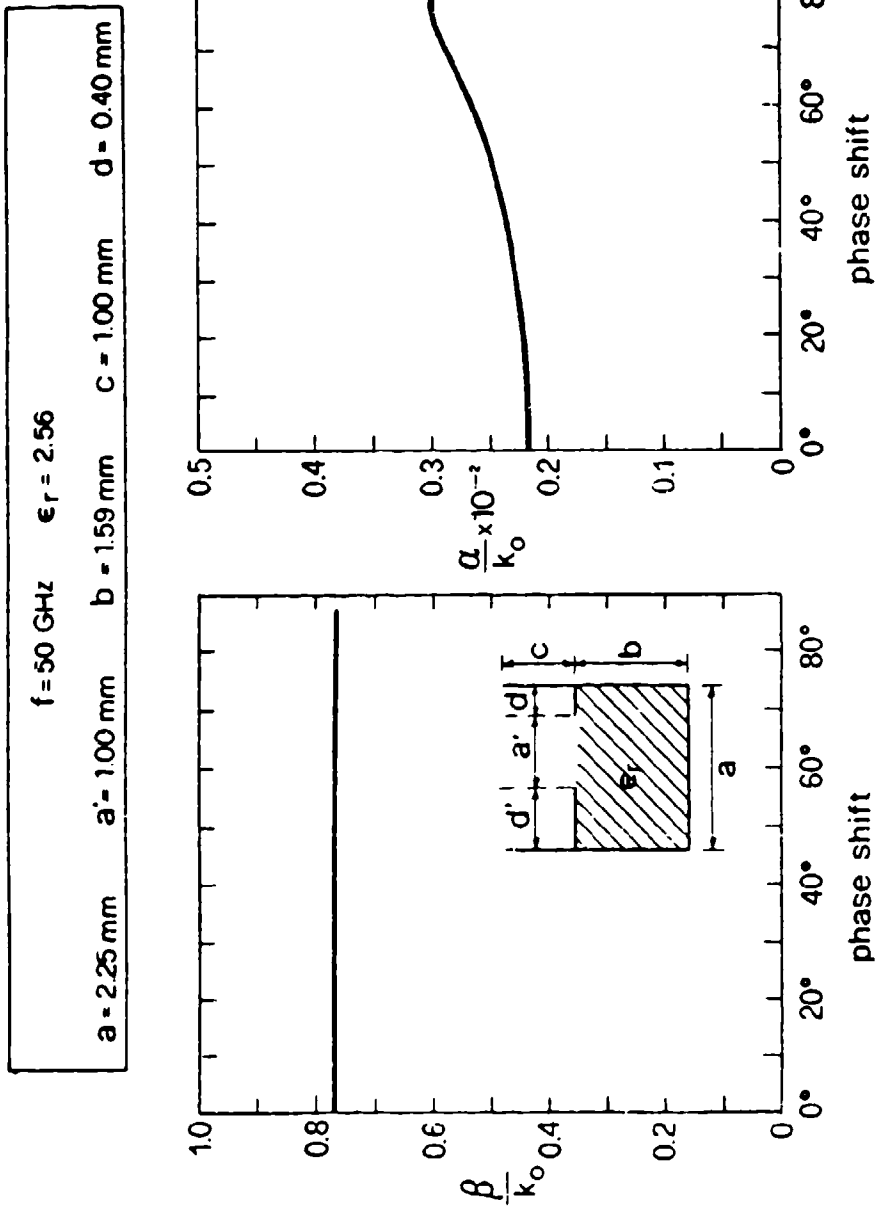


Fig. 10.46 Variations of the normalized phase and leakage constants as a function of phase shift per unit cell, for $d = 0.40 \text{ mm}$ and stub guide height $c = 1.00 \text{ mm}$.

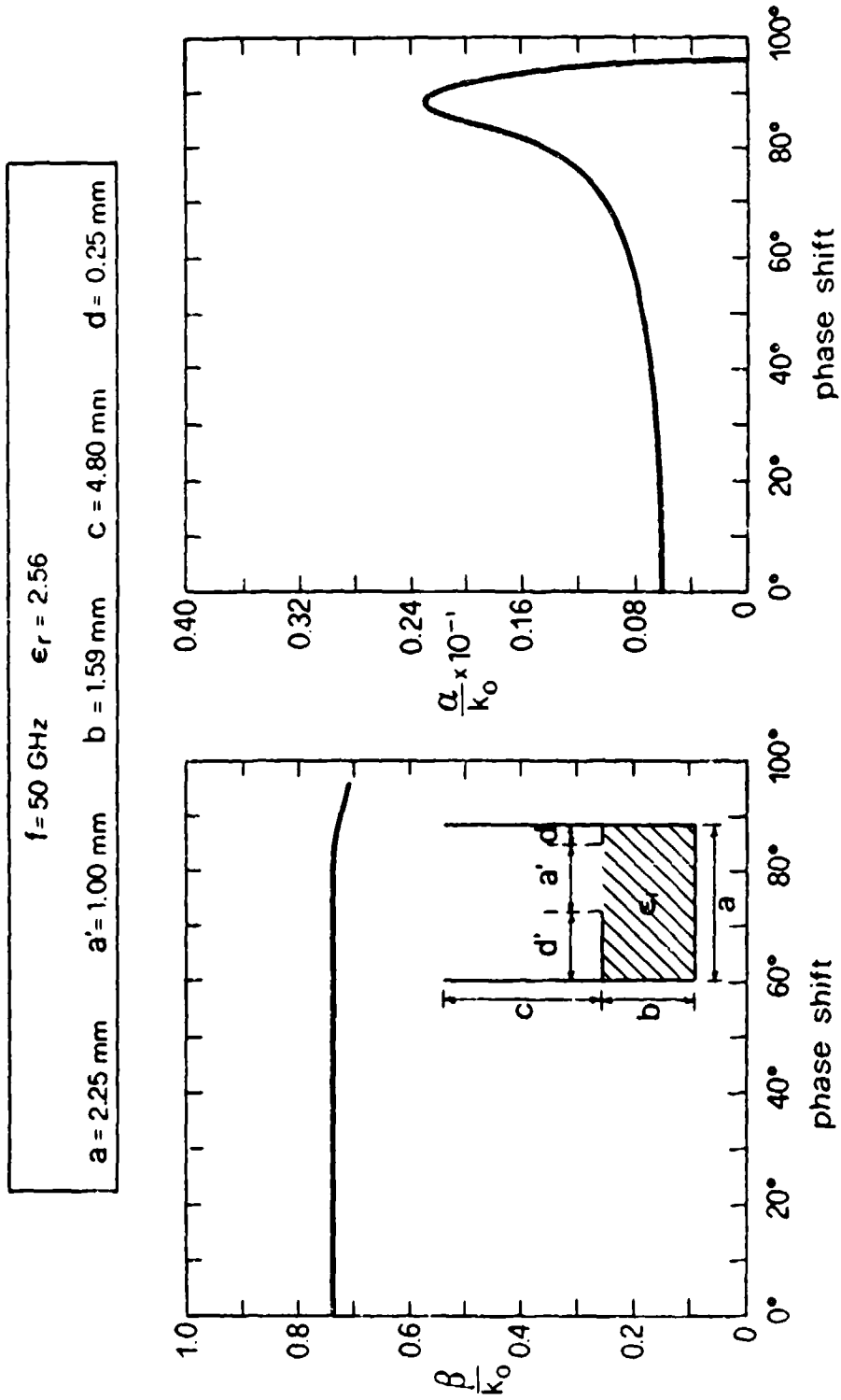


Fig. 10.47 Same as Fig. 10.46, but for $d = 0.25 \text{ mm}$ and $c = 4.80 \text{ mm}$.

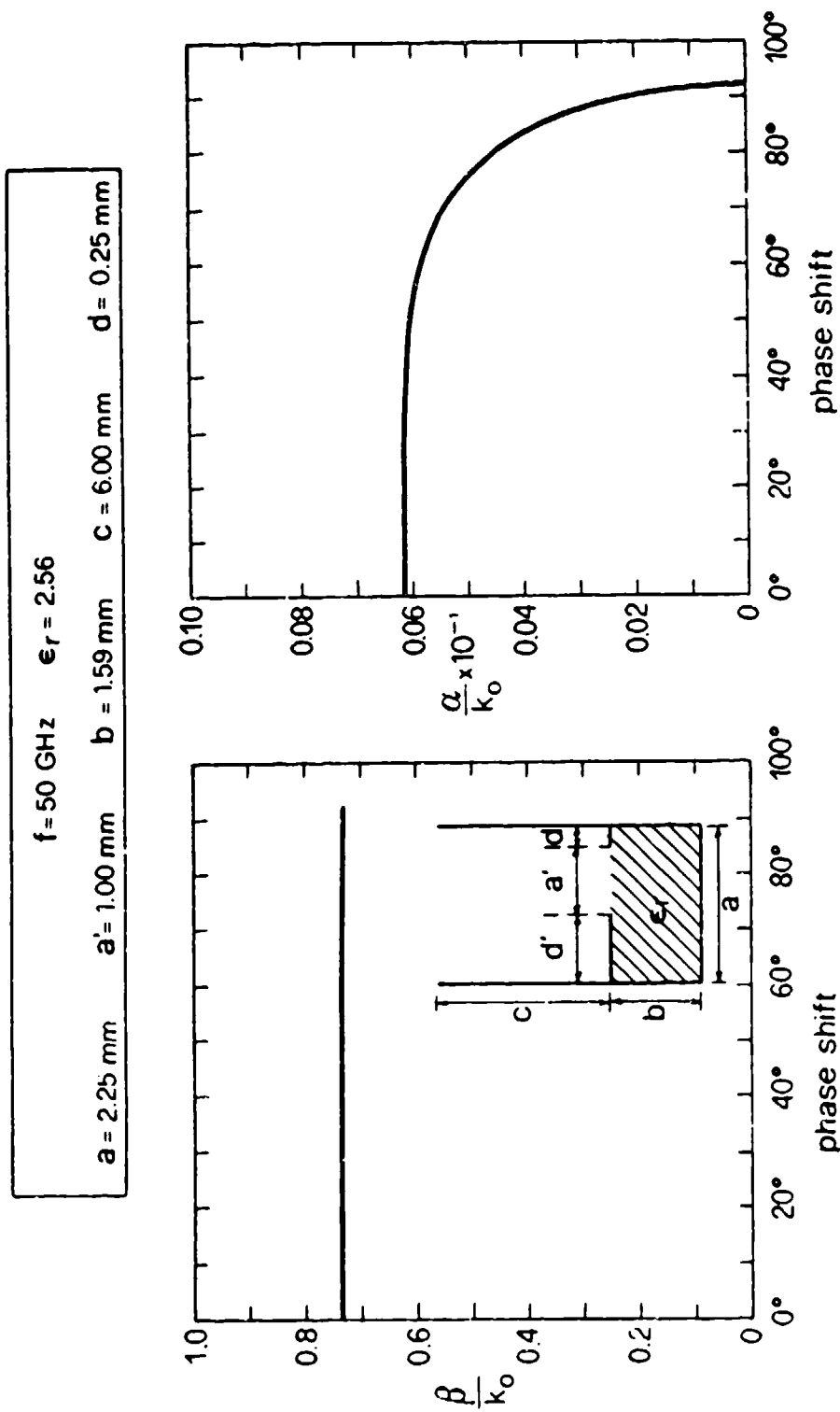


Fig. 10.48 Same as Fig. 10.47, but for $c = 6.00 \text{ mm}$.

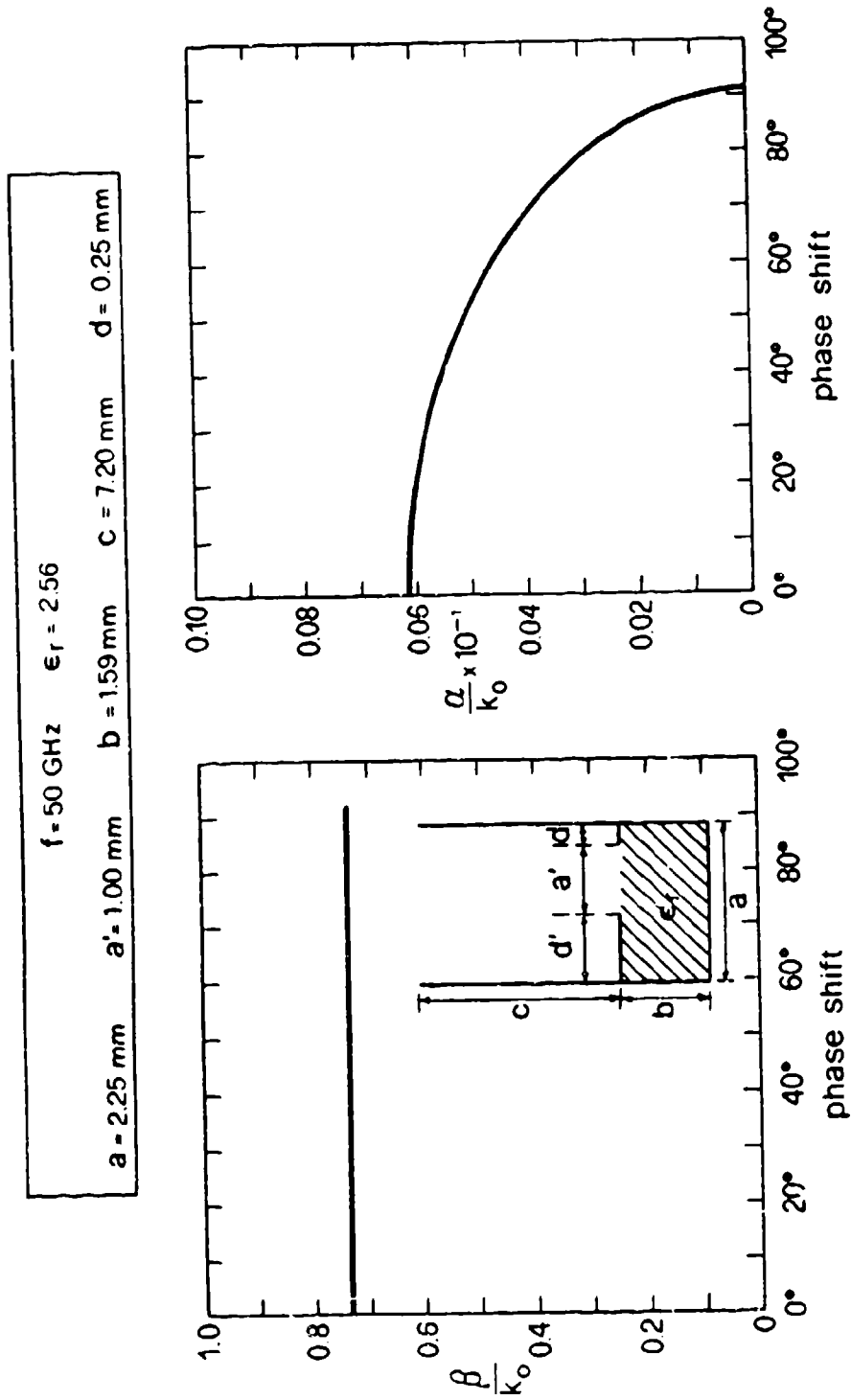


Fig. 10.49 Same as Fig. 10.47, but for $c = 7.20 \text{ mm}$.

stub guide. The value of c/λ_o for Fig. 10.48 actually occurs a bit below the middle (or average) of the periodic curve, and the curve for α/k_o in Fig. 10.48 therefore droops somewhat, though much less than the curve in Fig. 10.49. A slightly smaller value of c/λ_o would probably permit the flatness to continue for larger values of phase shift.

We therefore see that we can explain the nature of the variations in these curves, but, even more, by referring to a curve of α/k_o vs. c/λ_o we are able to design beforehand the curve shape of α/k_o vs. phase shift.

b. Conical Scan Dependence

As the phase shift per unit cell, Φ_C , increases, the value of azimuth scan angle ϕ_m increases from zero, and that of the elevation scan angle θ_m also increases, but the beam actually drops since θ_m is measured from broadside. To first order, that is, when α is neglected, θ_m and ϕ_m depend only on k_{xop}/k_o and β/k_o , and may be calculated using (10.98) and (10.99). Though approximate, these expressions are believed to be rather accurate under most conditions in practice.

For the four cases considered in Figs. 10.46 through 10.49, we present the scan behavior vs. phase shift in Figs. 10.50 through 10.53. The elevation angle is plotted as $90^\circ - \theta_m$, rather than as θ_m directly, to show that this angle goes to zero as the beam hits the ground at the end of the scan range. The qualitative behavior is similar for all of the curves for $90^\circ - \theta_m$ and for ϕ_m , respectively. Furthermore, since the curves for β/k_o vs. phase shift were found to be rather flat, and since k_{xop} is linear with the phase shift, the *deviations from conical scan are very small*.

The only noticeable deviation occurs in Fig. 10.51 at the end of the scan range. It is noted that, above 83° or so for the phase shift, a minor bump appears in the curves for both $90^\circ - \theta_m$ and ϕ_m , and the scan range itself becomes extended by a few degrees. Except for these two features, the curves in Fig. 10.51 agree very closely with those in Figs. 10.52 and 10.53, for which all the geometric parameters except c are the same. The reason for the different behavior at the end of the scan range in Fig. 10.51 may be understood from the curves in Fig. 10.47, where one sees that the value of α/k_o increases by more than a factor of three and that the value of β/k_o begins to drop noticeably for phase shift values greater than 83° or so. A drop in the value of β/k_o should raise the beam in elevation, increase it in azimuth, and extend the scan range. All three of these effects occur in Fig. 10.51, as compared with what we observe in Figs. 10.52 and 10.53, consistent quantitatively with the β/k_o behavior in Fig. 10.47.

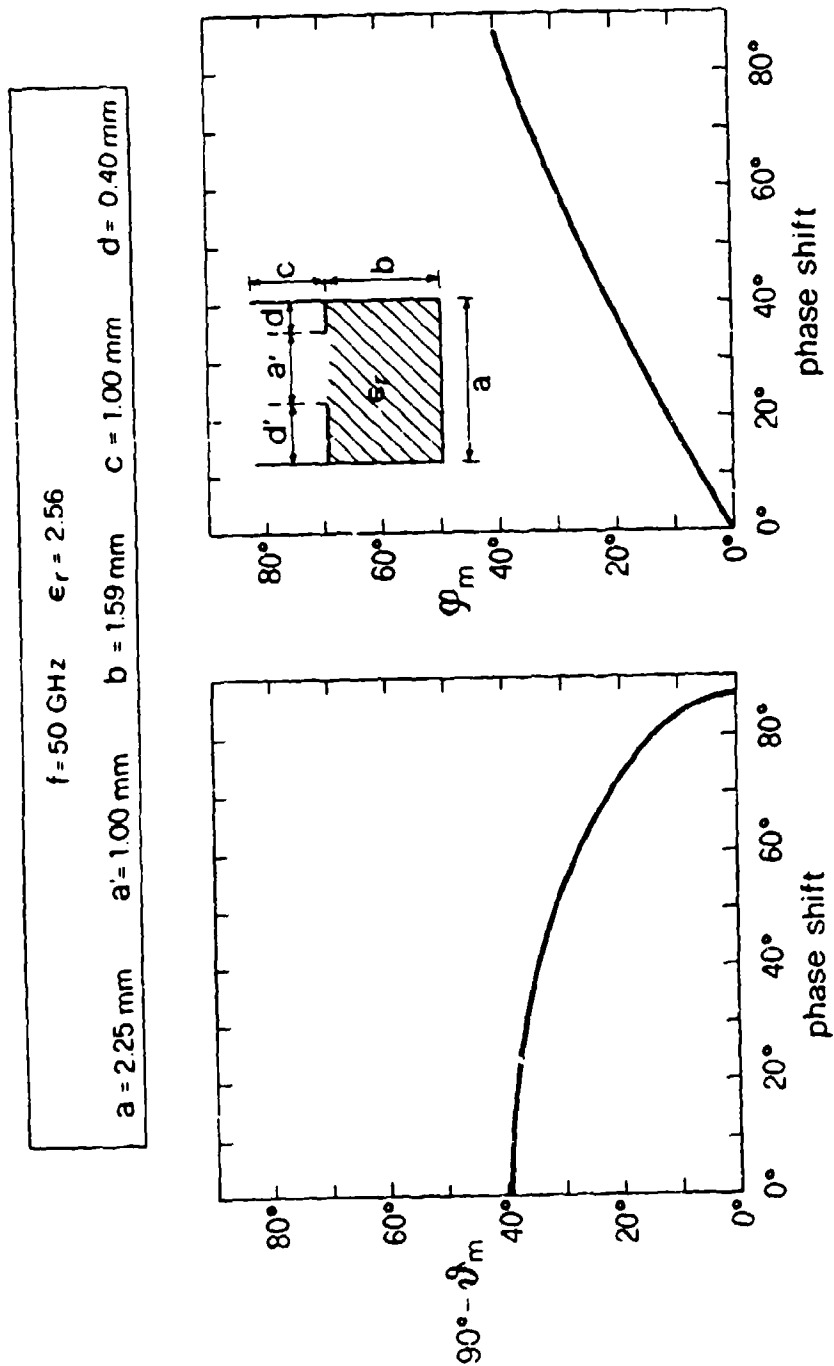


Fig. 10.50 Variations of the elevation angle $90^\circ - \theta_m$ and azimuth angle ϕ_m as a function of phase shift per unit cell, for $d = 0.40 \text{ mm}$ and stub guide height $c = 1.00 \text{ mm}$.

$f = 50 \text{ GHz}$	$\epsilon_r = 2.56$
$a = 2.25 \text{ mm}$	$a' = 1.00 \text{ mm}$
$b = 1.59 \text{ mm}$	$c = 4.80 \text{ mm}$
$d = 0.25 \text{ mm}$	

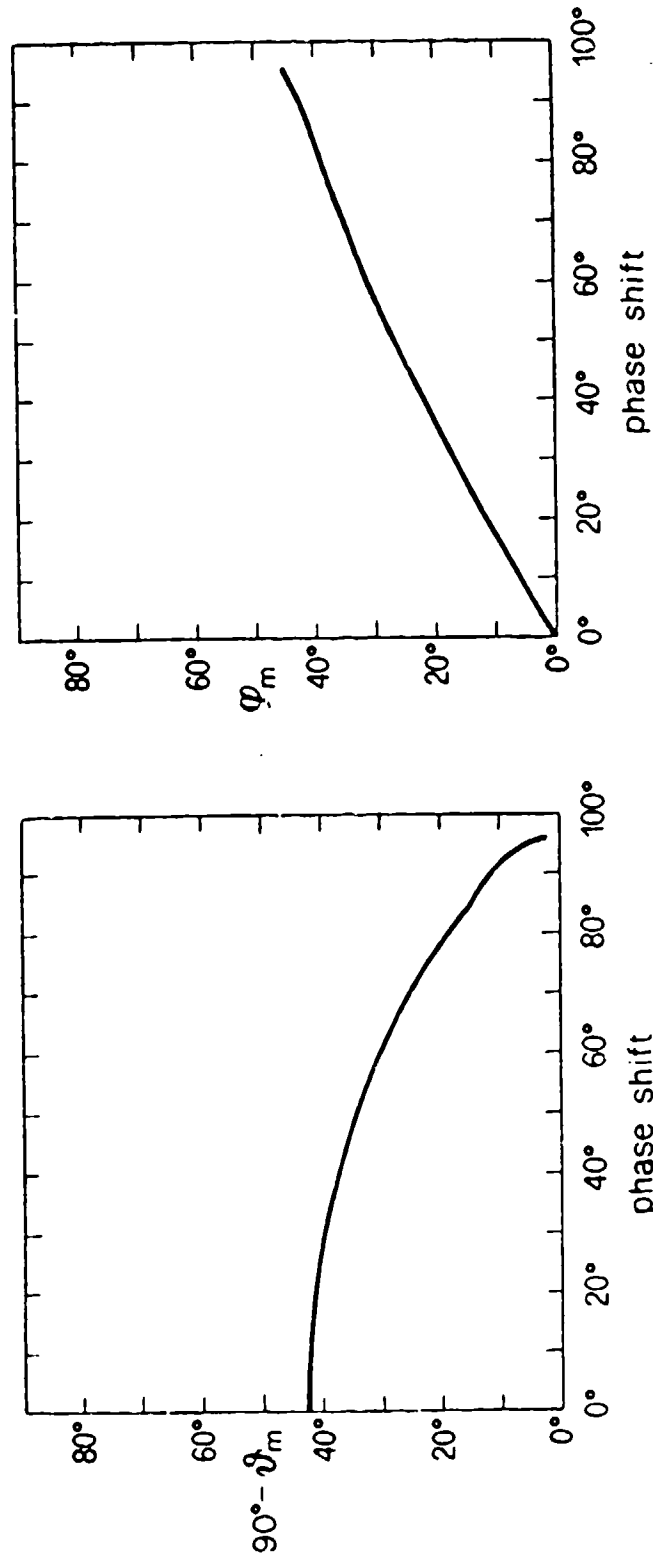


Fig. 10.51 Same as Fig. 10.50, but for $d = 0.25 \text{ mm}$ and $c = 4.80 \text{ mm}$.

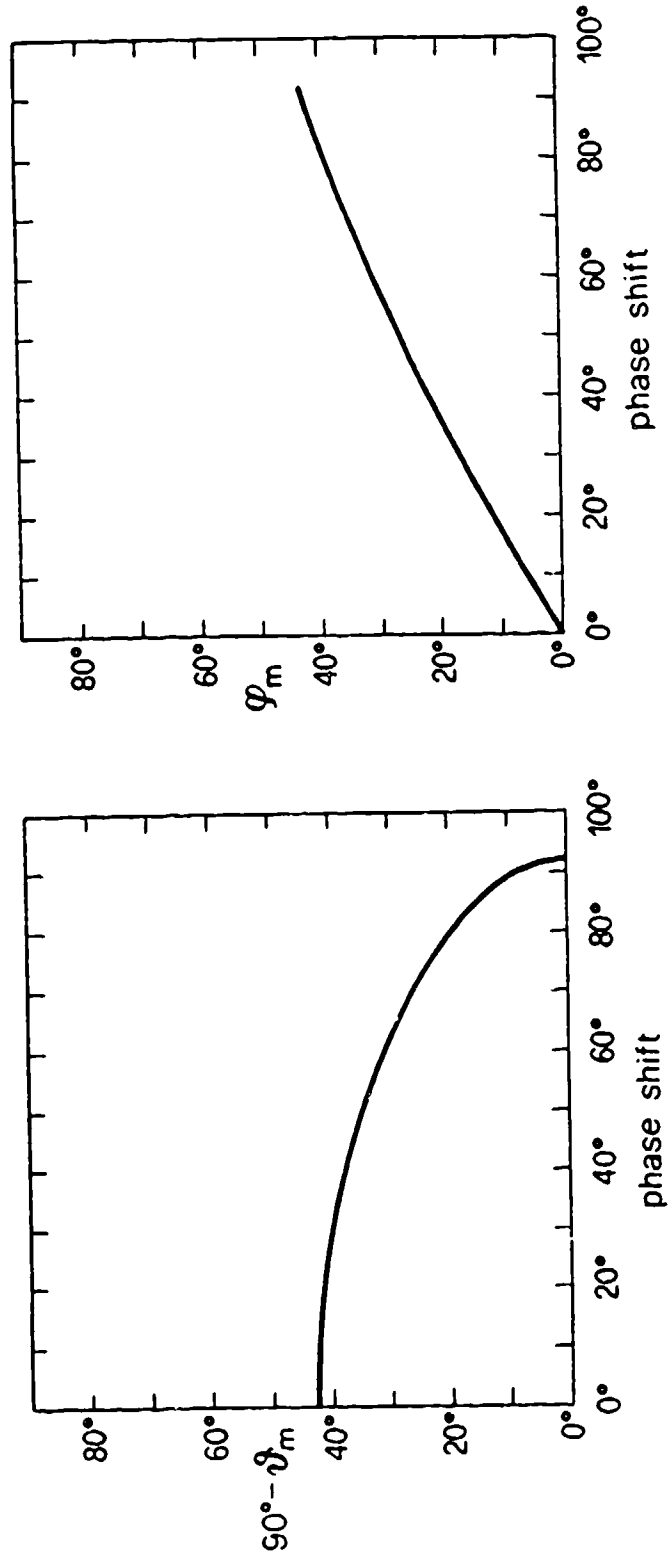
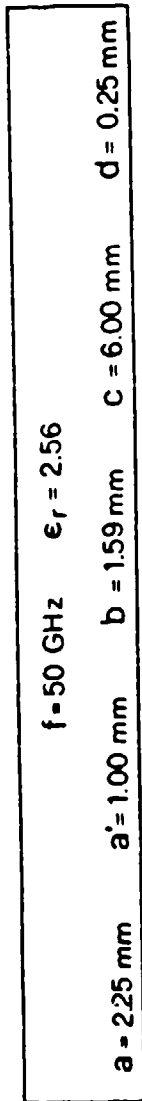


Fig. 10.52 Same as Fig. 10.51, but for $c = 6.00 \text{ mm}$.

$f = 50 \text{ GHz}$ $\epsilon_r = 2.56$			
$a = 2.25 \text{ mm}$	$a' = 1.00 \text{ mm}$	$b = 1.59 \text{ mm}$	$c = 7.20 \text{ mm}$ $d = 0.25 \text{ mm}$

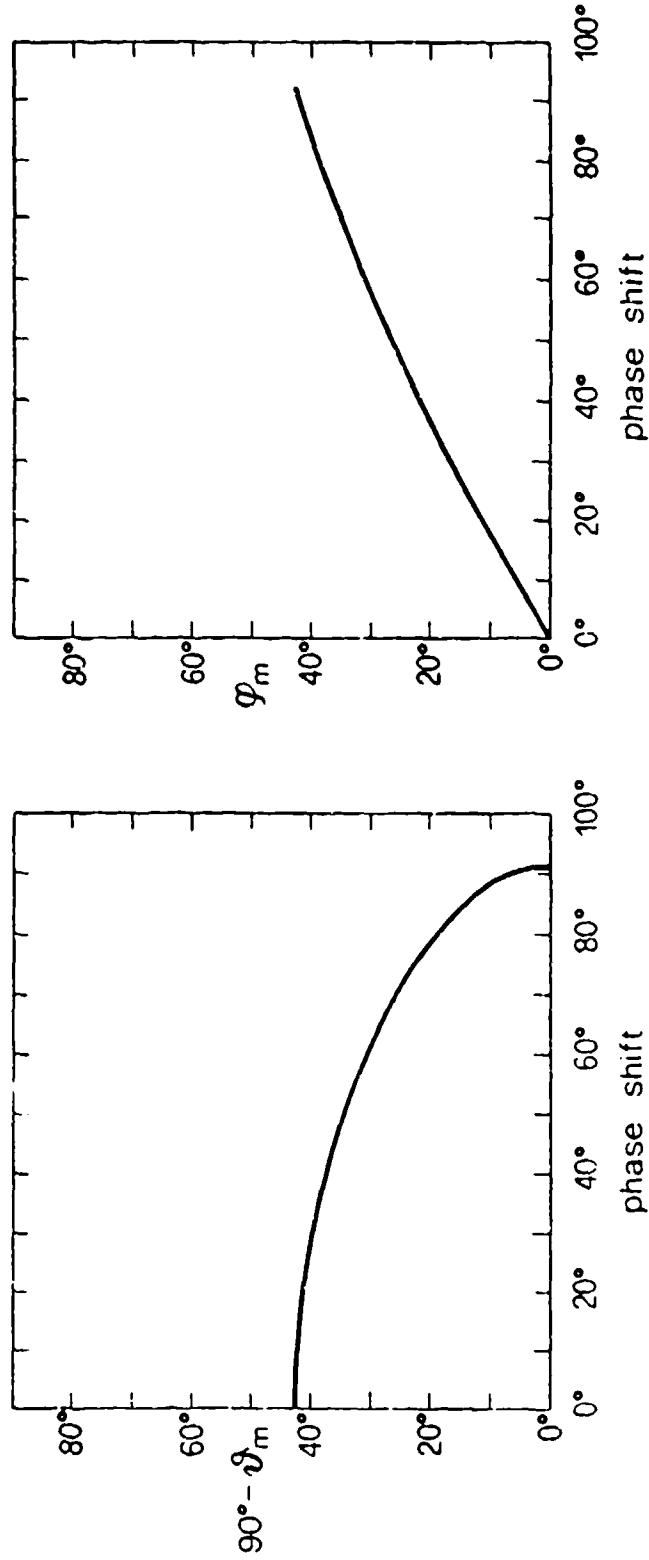


Fig. 10.53 Same as Fig. 10.51, but for $c = 7.20 \text{ mm}$.

The details of the behavior in the various curves have been explained, but the two chief points that should be stressed with respect to this subsection on variations with phase shift are that no blind spots occur and that deviations from conical scan are very small.

XI.	A NOVEL ARRAY OF PRINTED-CIRCUIT PERIODIC LEAKY-WAVE LINE SOURCES	465
A.	STRUCTURE AND PRINCIPLE OF OPERATION	467
B.	GENERAL PERFORMANCE CONSTRAINTS USING THE k_o vs. β_n DIAGRAM	471
	1. Description of the k_o vs. β_n Diagram	471
	2. Some Constraint Conditions	474
C.	TRANSVERSE EQUIVALENT NETWORK	479
	1. Equivalent Network for the Array of Periodic Slits on a Metal-Coated Air-Dielectric Interface	479
	2. The Full Transverse Equivalent Network	484
D.	ELEVATION ANGLE PERFORMANCE WITHOUT CROSS SCAN	489
E.	EFFECTS OF CROSS-PLANE SCANNING	501

XI. A NOVEL ARRAY OF PRINTED-CIRCUIT PERIODIC LEAKY-WAVE LINE SOURCES

(With: Prof. M. Guglielmi, Polytechnic University)

All of the line sources treated so far in this report are longitudinally *uniform*, to comply with the need at millimeter wavelengths for structures of simple configuration. The line source (and the array of them) in Chap. X went further in that the portion that controlled the radiation was in printed-circuit form, thus permitting its fabrication by lithographic means. Such fabrication methods actually allow us to utilize somewhat more complicated printed-circuit structures if there are advantages involved.

Although longitudinally uniform line sources offer simplicity in structure, they introduce an important restriction in the *scan range* available. For the line source itself, the beam can be scanned in the forward quadrant only, and then in only part of that. For example, the offset-groove-guide antenna in Chaps. VII and VIII possesses wonderful advantages in versatility of performance, including constancy of beamwidth during frequency scan, but one cannot approach endfire or broadside too closely, so that the scan range is limited. The printed circuit version in the array discussed in Chap. X permits closer access to endfire, but in all of the uniform line-source arrays we must accept the fact that the two-dimensional conical scan that is available covers a limited range in space -- very useful and convenient within that range, but limited in coverage.

The problem with uniform line sources posed in the paragraph above leads us to the array structure discussed in this chapter, in which the line sources are longitudinally *periodic*, rather than uniform. To form an array of these new line sources, we proceed as in Chaps. IV and X, that is, we again take a linear phased array of them, and we obtain scanning in the cross plane by introducing a phase shift between successive parallel line sources.

The principle underlying these periodic *line sources* is the following. One employs a dielectric section, for two purposes: to establish a slow basic wave, and to provide an air-dielectric interface on which a printed-circuit periodic structure may be deposited (or etched away). The longitudinally periodic structure then introduces space harmonics, and the frequency and dimensions are so chosen that only one of these space harmonics is radiating. As the beam corresponding to that space harmonic is scanned, it covers the range from backward endfire, through broadside, and into part

or all of the forward quadrant. In principle, therefore, the linear phased array of such line sources can provide two-dimensional scan coverage of up to the whole of space, except for narrow regions near broadside and endfire. In practice, one may wish to be more modest in the coverage, but clearly a much wider range is available than that provided by the longitudinally uniform line sources, which would typically be a cone in the forward quadrant with elevation and azimuth angles extending to 70° or 75° from the longitudinal axis of the line sources, and excluding the region near to endfire.

It is evident that a variety of structures may be devised that can provide an array of longitudinally periodic line sources. In the remainder of this chapter we present *one example*, which we feel is simple in configuration and for which we can provide a very accurate theoretical analysis. It retains the periodic baffle arrangement employed in the structures described in Chaps. IV and X (although in principle it does not need to) because we then know that the antenna will not suffer from blind spots. With this structure, the array will also radiate with negligible cross polarization and with no grating lobes.

A. STRUCTURE AND PRINCIPLE OF OPERATION

The array structure proposed here, which is longitudinally *periodic* rather than uniform in order to provide greater scan coverage, is shown in Fig. 11.1. It consists of a linear phased array of line sources, in which a phase shift is introduced between each of the successive parallel line sources to provide scanning in the cross plane. The principles behind the cross-plane scanning have been described in Chap. II and they have been applied in Chaps. IV and X to the specific arrays treated there. We will therefore not repeat any of those results, but we will instead concentrate on the new features here.

The array in Fig. 11.1 may be viewed as arising in the following way. We begin with a wide dielectric-filled parallel-plate waveguide placed horizontally; the guide height is then equal to b . A series of periodic parallel slits is then cut into the upper plate of this parallel-plate guide. The mode introduced into the parallel-plate guide

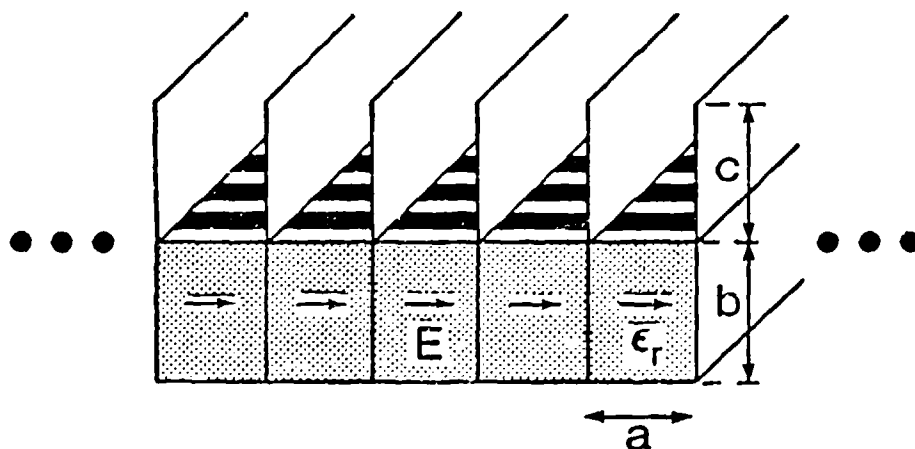


Fig. 11.1 A new array structure in which the individual line sources are longitudinally periodic, rather than uniform, in order to provide greater scan coverage.

has a horizontal electric field, and is the lowest TE mode in that guide. Height b must therefore be large enough to support that mode above cutoff. (We could alternatively have begun with a dielectric layer on a ground plane, thick enough to support the lowest surface wave with horizontal electric field polarization, which would then have a periodic array of strips deposited on the top surface.) To create the array, we then insert an array of metal plates spaced a apart, as shown in Fig. 11.1 The spacing a is arbitrary because the electric field is everywhere perpendicular to the plates, but a should be small enough to avoid any grating lobes, and it could be taken to be equal to $b/2$ if the individual elements in the array are each fed by dielectric-filled rectangular waveguides rotated through 90° (at millimeter wavelengths the aspect ratio of rectangular waveguides is two by one).

Dimensions a and b can thus be determined by those of feed rectangular waveguides corresponding to the frequency and the value of ϵ_r , with their ratio equal to $1/2$. Height c should be just sufficient to damp out any higher modes that might be excited. Because the electric field in this structure is always unidirectional, height c could perhaps be safely reduced to zero without causing any cross-polarized radiation. However, blind spots could be created over part of the cross-plane scanning range. Our analysis retains the upper baffles of height c , so that no blind spots occur. We have not checked whether or not any blind spots appear when $c=0$, but they may not; if they don't, the structure can be simplified without any deterioration in performance.

Two geometrical parameters remain to be determined: the period of the slits or strips on the air-dielectric interface, and the ratio of slit width to period. These dimensions are indicated on Fig. 11.2, which shows the structure before the vertical metal walls (spaced a apart) are inserted.

Before we can specify those dimensions, we need to review the *principle of operation* of the line source, which in this problem is the same as the structure of infinite width. Let us approach the performance from the *small-aperture* viewpoint, meaning that we begin with a completely metallized top, for which no radiation occurs, and then open up the slits gradually in the periodic array of slits cut in this top wall. The slit is of width a' in a period of width p . For this electric field orientation, the slit is actually a small-aperture perturbation of the upper wall, so that a gradual opening of the slit, or of the ratio a'/p , permits a gradual control over the leakage rate of the radiation.

When periodicity is introduced in the z direction, an infinite set of space harmonics is produced, where the propagation wavenumber of the n th space harmonic is related to that of the basic slow wave by

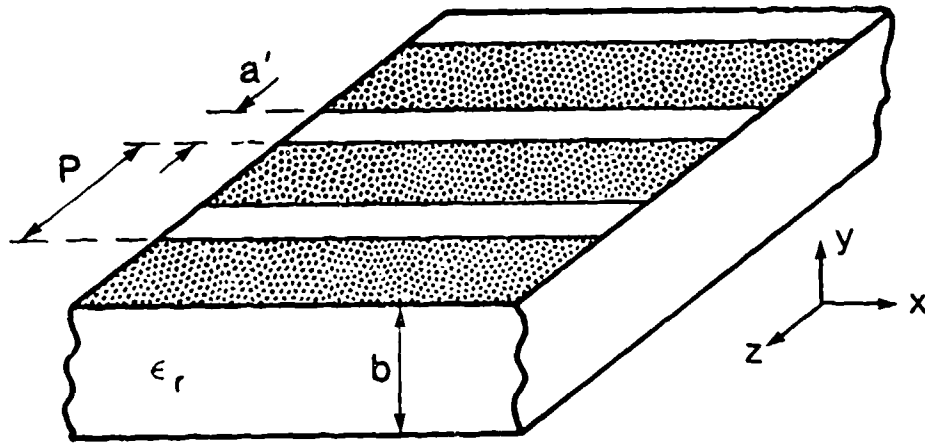


Fig. 11.2 The structure before the vertical metal baffles are inserted, showing the metallic grating with its periodic array of slits.

$$k_{zn} = k_{zo} + 2n\pi/p, \quad n = 0, \pm 1, \pm 2, \dots \quad (11.1)$$

When there is leakage of power, both k_{zo} and k_{zn} are complex with the *same* attenuation constant α , so that (11.1) becomes

$$\beta_n = \beta_o + 2n\pi/p \quad (11.2)$$

In the small-aperture limit, the value of β_o is close to the propagation constant of the TE_1 mode in the dielectric-filled parallel-plate guide of height b , so that

$$\beta_o/k_o \approx \left[\epsilon_r - (\lambda_o/2b)^2 \right]^{1/2} \quad (11.3)$$

with $\beta_o/k_o > 1$, so that the basic guided wave is a slow wave, and therefore nonradiating.

When p is selected so that one (or more) of the space harmonics becomes fast, the guided mode becomes leaky and radiation occurs. For practical antenna operation, we wish that only the $n = -1$ space harmonic is fast, with

$$\frac{\beta_{-1}}{k_o} = \frac{\beta_o}{k_o} - \frac{\lambda_o}{p} < 1 \quad (11.4)$$

The period p is thus selected relative to the wavelength so that (11.4) is satisfied; the elevation angle θ_{-1} of the radiation is then given by

$$\sin \theta_{-1} = \beta_{-1}/k_o \quad (11.5)$$

where θ_{-1} is measured from broadside, consistent with the designation for beam angle in the other chapters. By changing the wavelength in (11.4), the angle θ_{-1} can be scanned into either the backward or the forward quadrant.

Relation (11.1) is similar to expression (2.2) in Chap. II, which applies to the space harmonics produced by the periodic array of line sources in the *cross* plane. The basic physics regarding the space harmonics is the same, but two important differences are present. The first is related to the direction of the periodicity relative to the propagation direction. The power is first fed into the individual periodically modulated line sources in the longitudinal (z) direction, and the periodicity is in the *same* direction. The power leaked as a result of that periodicity emerges in the yz plane, moving basically upwards. The periodicity in the line-source array is then located at the top of the array structure, where that periodicity (in x) is *transverse* to the direction of the leakage, which is in the yz plane. The more important difference is that in the line-source array the basic $n=0$ term is propagating and the intention is to prevent the other space harmonics from radiating (no grating lobes), whereas in the periodic line source the basic $n=0$ mode is nonradiating and we wish the $n=-1$ term to radiate.

We shall see in Sec. D below that the angle in elevation of the radiated beam is determined essentially by the value of period p relative to the wavelength (in accordance with (11.4) and (11.5)), although the value of β_o , and therefore β_{-1} , is also influenced somewhat by other geometric parameters. The width of the beam is, as usual, determined primarily by the value of the leakage constant α , which in turn depends predominantly on the relative slit size a'/p . The azimuth scan angle is of course determined by the phase shift introduced between the successive line sources.

Clearer insight into how one may select the optimum value for period p is obtained by the discussion in Sec. B, where use is made of the k_o vs. β_n diagram.

B. GENERAL PERFORMANCE CONSTRAINTS USING THE k_o vs. β_n DIAGRAM

1. Description of the k_o vs. β_n Diagram

In attempting to optimize the set of dimensional parameters for the design of the array of periodically modulated line sources, several aspects must be kept in mind. First, we wish to have the $n = -1$ space harmonic be fast and correspond to a radiated beam, but we want it to be the *only* space harmonic to do so over its complete scan range. Second, we wish the feed waveguide to carry only *one* mode, the dominant one, over the frequency range of operation (corresponding to the scan range).

A simple and convenient way to gain the necessary insights is to use the k_o vs. β_n diagram, shown in Fig. 11.3. The diagram is periodic in $2\pi/p$ in the horizontal direction along β_n , and only the first two periods centered about $\beta_n = 0$ are included. The $\pm 45^\circ$ lines are defined by $k_o = \pm \beta_n$, or shifts in them by $\pm 2\pi/p$. The lower solid curve labelled $n = 0$ represents the basic $n = 0$ space harmonic of the lowest mode. Exactly parallel to it but shifted by $-2\pi/p$ is the (identical) curve labelled $n = -1$, which represents the $n = -1$ space harmonic of that mode. Higher up we note the $n = 0$ and $n = -1$ space harmonic curves for the second mode, which we wish to remain below cutoff. The dashed straight lines, parallel to each other but shifted from each other by $2\pi/p$, represent the asymptotes for the $n = 0$ and $n = -1$ curves for both the lowest and the second modes. Finally, the dashed curve represents a portion of the $n = -2$ space harmonic for the lowest mode.

The abscissa is labelled β_n because it applies to all the values of n provided we select the proper curve. For example, broadside radiation occurs when $\beta_o = 2\pi/p$, but it also corresponds to $\beta_{-1} = 0$. As we see, those points correspond to the same value of k_o .

The convenience associated with this phrasing of the k_o vs. β_n diagram becomes particularly clear when we consider the "radiation region", shown in Fig. 11.3 as occurring between the $\pm 45^\circ$ lines centered at the origin. If the point on the dispersion curve lies within that region, the relevant space harmonic is a radiating one. If any point lies within that region, the mode is leaky, with a complex propagation wavenumber.

Let us next examine the meaning of the various circled points, labelled 1 through 8. Point 1 shows the cutoff of the lowest mode in the parallel-plate guide, which is

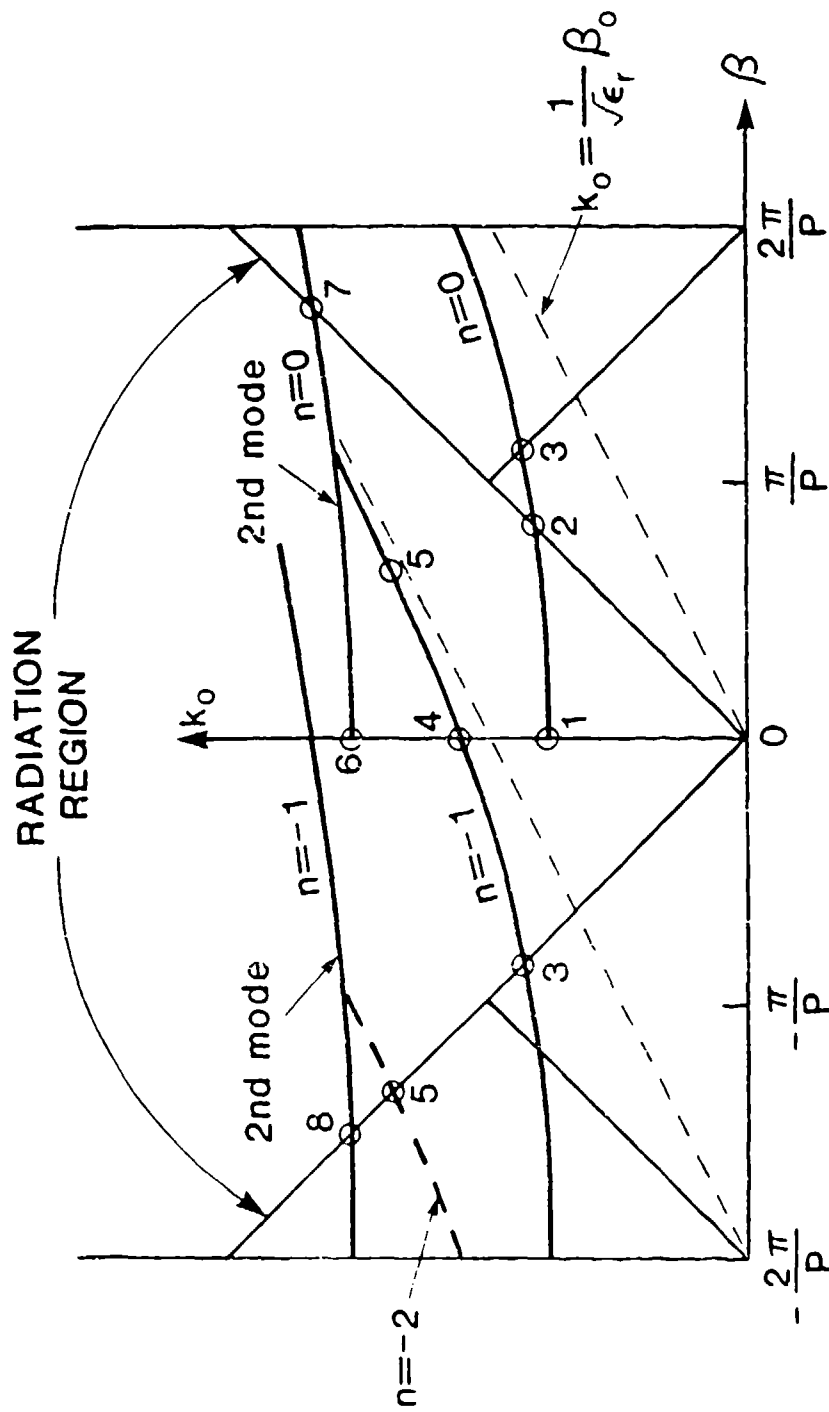


Fig. 11.3 The k_0 vs. β_n diagram, which can provide physical insight into the elevation angle behavior as a function of frequency, and which is useful for a preliminary design of the line source for the array.

dielectric filled and has a periodic array of slits on its top wall. For simplicity in the discussion below, we shall assume that these slits are very narrow, so that radiation can occur but the perturbation on the guide's properties is small. For frequencies (k_o) just above cutoff, in the range between points 1 and 2, the lowest mode is a fast mode, and radiation will occur in the $n = 0$ space harmonic. After point 2 the curve leaves the radiation region, and the mode becomes a slow wave ($\beta_o > k_o$). After point 3, however, the $n = -1$ space harmonic enters the radiation region, and as k_o increases further the $n = -1$ curve is seen to continue further into the radiation region.

Point 3 is located on the line $\beta_{-1} = -k_o$, so that, from (11.5), the angle of the radiated beam corresponding to that point is -90° , or backward endfire. (From $\sin \theta_o = \beta_o / k_o$ we recognize that the beam for the $n = 0$ space harmonic moves from broadside to forward endfire, as the $n = 0$ curve is traversed from point 1 to point 2, the latter lying on the line $\beta_o = k_o$.) As k_o is increased, and we follow the $n = -1$ curve, the angle of the radiated beam due to the $n = -1$ space harmonic moves up from backward endfire towards broadside, which it reaches at point 4. After point 4, the beam points in the forward quadrant.

At this stage, we must take into account the $n = -2$ space harmonic, and determine when it enters the radiation region. A portion of the curve for the $n = -2$ space harmonic is shown dashed in Fig. 11.3, and it is seen to enter the radiation region at point 5. Since $\beta_{-2} = -k_o$ at point 5, the beam due to the $n = -2$ space harmonic will then point at backward endfire. At that frequency, point 5 also occurs on the $n = -1$ curve, which corresponds to some angle in the forward quadrant. The frequency corresponding to point 5 represents the highest useful frequency for this set of conditions, and the corresponding angle for the $n = -1$ beam represents the limit of the useful scan range.

The above considerations assume that point 5 occurs at a lower value of k_o than point 6, which is the cutoff for the second mode. Either point may come first, however, and it then determines the end of the useful scan range. When the second mode is just above cutoff, it is seen to be right in the middle of the radiation region, and the $n = 0$ space harmonic of that mode will radiate. The $n = 0$ space harmonic will continue to radiate, traversing the forward quadrant, until point 7 is reached. For frequencies very near to point 6, however, the $n = -1$ space harmonic for the second mode does not radiate. That space harmonic enters the radiation region at point 8, which is seen to occur at a lower value of k_o than that for point 7, indicating that for a narrow frequency range both the $n = 0$ and $n = -1$ space harmonics for the second mode will radiate, although at different angles. Clearly, we must insure that that mode

remains below cutoff.

2. Some Constraint Conditions

In order to keep the conditions simple, we shall assume that the periodic array of slits exerts only a small perturbation on the wavenumber values; we may thus employ the equations corresponding to the "closed" waveguide. (We will find later, in Sec. D, that this assumption is rather accurate.) We can then immediately write down simple expressions that correspond to the various circled points 1 through 8 on the k_o vs. β_n diagram in Fig. 11.3.

Since the lowest mode is the TE_1 mode in dielectric-filled parallel-plate guide of height b , the value of k_o at the mode cutoff, which is point 1, is

$$k_o = \frac{\pi}{b} \frac{1}{\sqrt{\epsilon_r}} \quad (11.6)$$

The value of k_o at the cutoff of the second mode (the next mode with the same polarization), which corresponds to point 6, is

$$k_o = \frac{2\pi}{b} \frac{1}{\sqrt{\epsilon_r}} \quad (11.7)$$

At point 2, where the basic ($n=0$) space harmonic of the lowest mode changes from fast to slow, we have $\beta_o = k_o$, where β_o is given by

$$\beta_o = \left[k_o^2 \epsilon_r - (\pi/b)^2 \right]^{1/2} \quad (11.8)$$

The value of k_o at point 2 is thus

$$k_o = \frac{\pi}{b} \frac{1}{\sqrt{\epsilon_r - 1}} \quad (11.9)$$

For point 3, we must consider the $n = -1$ space harmonic, which is related to the $n = 0$ one by

$$\beta_{-1} = \beta_o - 2\pi/p \quad (11.10)$$

Since point 3 is characterized by $\beta_{-1} = -k_o$, we have that k_o is then obtained from

$$k_o = 2\pi/p - \left[k_o^2 \epsilon_r - (\pi/b)^2 \right]^{1/2} \quad (11.11)$$

which is a quadratic equation for k_o . Point 4 corresponds to broadside radiation, for which $\beta_{-1}=0$; on use of (11.8) and (11.10), we have

$$k_o = \frac{1}{\sqrt{\epsilon_r}} \left[\left(\frac{2\pi}{p} \right)^2 + \left(\frac{\pi}{b} \right)^2 \right]^{1/2} \quad (11.12)$$

For point 5, which corresponds to the onset of radiation for the $n = -2$ space harmonic, we specify

$$k_o = -\beta_{-2} = -\beta_o + 4\pi/p \quad (11.13)$$

where β_o is taken from (11.8). If one wishes the values of k_o corresponding to points 7 and 8, which we will not need, they may be obtained in the manner used above for points 2 and 3, respectively, but for the second mode.

For the antenna to perform properly, the $n = -1$ space harmonic of the lowest mode should produce the *only* radiating beam. We will next arrive at a *simple criterion* for determining the range of values within which period p must be in order that this condition is satisfied within certain limits.

We first note that, when the $n = -1$ space harmonic begins to radiate, the $n = 0$ space harmonic must be slow. That is the same as saying that points 2 and 3 in Fig. 11.3 must lie below the top of the triangle on which they appear. If p is made *larger*, these two points approach the top of the triangle. Hence, the *maximum* value that we can allow p to have is the one for which points 2 and 3 have the same value of k_o ; at this maximum value, k_o must satisfy relations (11.9) and (11.11) simultaneously. Their simultaneous solution yields the simple condition

$$p_{\max} = b \sqrt{\epsilon_r - 1} \quad (11.14)$$

Another condition relates to the onset of the *second mode*. Certainly we wish the second mode to remain below cutoff during the scan range. Relation (11.7) for the cutoff of the second mode, which corresponds to point 6 in Fig. 11.3, is independent of period p . The value of k_o corresponding to point 4, at broadside, is seen from (11.12) to increase if p is made *smaller*. A weak condition for the *minimum* value of p is then obtained by asserting that the smallest value of p that we can tolerate is the one for which the second mode is at cutoff when the $n = -1$ beam radiates at broadside. (At least we can scan over one-half of space then.) We then equate the values of k_o in

(11.7) and (11.12) to obtain

$$p_{\min} = 2b/\sqrt{3} \quad (11.15)$$

If we are to be able to select a value of p that lies between the p_{\min} and p_{\max} values, we must have, at the least

$$p_{\max} > p_{\min}$$

or, from (11.14) and (11.15),

$$\epsilon_r > 2.33 \quad (11.16)$$

An alternative condition for p_{\min} , which is a stronger condition than the one in (11.15), may be obtained by requiring that the k_o value corresponding to point 6 be greater than or equal to that for point 5, rather than point 4. That is, the frequency at which the second mode is at cutoff should be equal to or greater than that for which the $n = -2$ space harmonic begins to radiate. To establish that condition, we equate the values of k_o in (11.7) and (11.13) to obtain

$$p_{\min} = \frac{4b \sqrt{\epsilon_r}}{2 + \sqrt{3} \sqrt{\epsilon_r}} \quad (11.17)$$

If we then employ (11.14) and (11.17) to set p_{\max} greater than p_{\min} , we find the condition

$$2\sqrt{\epsilon_r - 1} + \sqrt{3} \sqrt{\epsilon_r} \sqrt{\epsilon_r - 1} - 4\sqrt{\epsilon_r} > 0 \quad (11.18)$$

which is satisfied for

$$\epsilon_r > 2.89 \quad (11.19)$$

Other conditions or constraints can also be specified to cover more precise requirements. For our purposes, however, it seems sufficient to select a value of $\epsilon_r = 4.00$ for our calculations, and to follow the p_{\max} and p_{\min} constraints in (11.14) and (11.15).

We need next to select a frequency range of operation, and from it to choose the cross-section dimensions. Taking the frequency range of about 40 GHz to about 60 GHz, corresponding to an air-filled rectangular waveguide with cross-section dimensions 2.388 mm by 1.194 mm, which we will employ as the basic feed waveguide, our dielectric-filled region will have $b = 2.40$ mm and $a = 1.20$ mm, since $\epsilon_r = 4.00$ (note that b and a in Fig. 11.1 are reversed from the usual rectangular waveguide b and a ,

to be consistent with the notation in previous chapters in this report). The recommended operating range of this waveguide is then 39.3 GHz to 59.7 GHz, and the cutoff frequency of the second mode is 62.8 GHz. (Actually, the 62.8 value corresponds to a nominal guide width of 4.775 mm; when we choose $b = 2.40$ mm, then $b\sqrt{\epsilon_r} = 4.80$ mm, which corresponds to a cutoff frequency of 62.5 GHz for the second mode, but these differences are of the order of the fabrication tolerances.)

Consistent with these dimensions, we then need to select a value for the period p . From (11.14) and (11.15), we find $p_{\min} = 2.77$ mm and $p_{\max} = 4.16$ mm. Taking an average of these two values, which is a satisfactory but arbitrary procedure, we obtain $p = 3.45$ mm.

Corresponding to this set of dimensions and to $\epsilon_r = 4.00$, we find the following values for k_o , λ_o and f for the various circled points in Fig. 11.3.

Point 1, the cutoff of the lowest mode (from (11.6)):

$$k_o = 0.654/\text{mm} , \lambda_o = 9.60 \text{ mm} , f = 31.3 \text{ GHz}$$

Point 2, where the $n = 0$ space harmonic goes from fast to slow (from (11.9)):

$$k_o = 0.756/\text{mm} , \lambda_o = 8.31 \text{ mm} , f = 36.1 \text{ GHz}$$

Point 3, where the $n = -1$ space harmonic begins to radiate, at backward endfire (from (11.11)):

$$k_o = 0.822/\text{mm} , \lambda_o = 7.64 \text{ mm} , f = 39.3 \text{ GHz}$$

Point 4, where the radiating $n = -1$ space harmonic reaches broadside (from (11.12)):

$$k_o = 1.120/\text{mm} , \lambda_o = 5.61 \text{ mm} , f = 53.5 \text{ GHz}$$

Point 5, where the $n = -2$ space harmonic begins to radiate, at backward endfire (from (11.13)):

$$k_o = 1.329/\text{mm} , \lambda_o = 4.73 \text{ mm} , f = 63.5 \text{ GHz}$$

Point 6, the cutoff of the second mode (from (11.7)):

$$k_o = 1.308/\text{mm} , \lambda_o = 4.80 \text{ mm} , f = 62.6 \text{ GHz}$$

The useful scan range corresponds to the frequency range from point 3 to beyond point 4, approaching point 6. Point 3, by coincidence, corresponds exactly to the low end of the recommended frequency range for this feed waveguide. Point 4, where the beam is near broadside, occurs near the middle of the waveguide's frequency range. It is also seen that the beam can scan past broadside into the forward quadrant. A reminder should be given about the broadside region itself; it corresponds to an open "stop band" region, so that one must avoid the narrow frequency range exactly in the neighborhood of broadside. A clearer picture of just what happens there is provided by the numerical results presented in Sec. D.

The end of the useful scan range for the $n = -1$ space harmonic corresponds to either point 5 or point 6, whichever comes first as we raise frequency. It does not matter which it is because one no longer has a single radiating beam in either case. For *this* set of numbers, point 6 arrives before point 5, but they are close to each other. We can readily determine how far into the forward quadrant the $n = -1$ beam goes before these two points are reached. We simply determine the value of β_{-1}/k_o for each point, using (11.8) and (11.10), and then find the angle θ_{-1} from (11.5).

For point 6, the cutoff of the second mode, we find

$$\theta_{-1} = 20.1^\circ \quad (11.20)$$

whereas for point 5, where the $n = -2$ space harmonic begins to radiate, the value is

$$\theta_{-1} = 21.7^\circ \quad (11.21)$$

The *total scan range in elevation* for this type of leaky-wave antenna, for the set of dimensions chosen above, extends from backward endfire, through broadside, and 20.1° into the forward quadrant.

Obviously, by adjusting parameters such as the period p , and the combination of b and ϵ_r , one can move these critical points around to extend the scan range further into the forward quadrant, or to have point 5 occur before point 6, etc. The important point that is made here is that it is possible to control the performance characteristics by employing the approach and the simple relations presented above.

C. TRANSVERSE EQUIVALENT NETWORK

The treatment in Sec. B provides a road map that tells us what dimensions to choose in order to achieve the scan range we wish over the frequency range of interest. It yields approximate values for the radiation angles as a function of frequency on the assumption that the radiating slits perturb the basic guided wave only slightly. It cannot, of course, provide any information about leakage rates or beam widths. In order to obtain accurate numerical values for the leakage rates and the radiation angles, we must develop an accurate transverse equivalent network and then examine its resonances.

The transverse equivalent network must be complete and must take into account all portions of the antenna's cross section. The array is viewed here in the same way as it is in Chaps. IV and X, i.e., in terms of a unit-cell approach, which automatically takes into account all mutual coupling effects. The transverse equivalent network therefore needs to include only the contents of a typical unit cell; the description of the unit cell, its phase-shift walls, its modes, etc., have been presented in Chap. II, and applied in detail in Chaps. IV and X. As before, the unit cell is composed of three basic sections: the dielectric-filled section at the bottom, the air-filled parallel-plate section in the middle, and the periodic section, representing the radiating region, at the top. On the air-dielectric interface, at the transition between the bottom and middle sections, we have an array of periodic slits, as seen in Fig. 11.1 and described further in Fig. 11.2. We shall first discuss the equivalent network representation of that array of periodic slits, which is a basic constituent of the unit cell, and then incorporate it into the transverse equivalent network for the full cross section.

1. Equivalent Network for the Array of Periodic Slits on a Metal-Coated Air-Dielectric Interface

Since the electric field in this antenna is perpendicular to the vertical metal planes, we may remove these planes without affecting the field distribution. It is more convenient, then, to regard that array as a set of infinitely long slits, cut into a metal-covered air-dielectric interface, with the electric field parallel to the long dimension of the slits, as shown in Fig. 11.2, except that at this stage the height b is not being considered. We seek a representation now for only the array at the interface, which we view as a *key constituent* in the full transverse equivalent network.

Recognizing that space harmonics along the z direction, along the plane, correspond to modes in the y direction, perpendicular to the plane, we require the *multimode* equivalent network that couples the modes in the air region with those in

the dielectric region. In the air region, only *one* mode is above cutoff, corresponding to the $n = -1$ space harmonic, since we wish to have one radiating beam. In the dielectric region, we will have at least two modes above cutoff, for $n = -1$ and $n = 0$, but there may also be some others, depending on ϵ_r and the geometric parameters.

We require an analytical formulation for the equivalent network parameters since we wish to employ this formulation in a transverse resonance, and it would be nice if it were also simple and in closed form. Such an analytical formulation, for multimode operation, on a structure with different dielectrics on each side of the interface, is not yet available in the literature. We have, however, developed such an analytical solution recently [47] in a different context. The solution there was actually the dual of that employed here, with an array of long strips on the interface, and with the magnetic field parallel to those strips. For application here, we adapt that solution in the small argument range, and take the dual form for both the network form and the expressions for the parameters of the network. A detailed derivation of the integral equation that was solved, together with the new equivalent network developed from it, are included in a two-part paper that has been accepted for publication [48,49].

The constituent problem that is considered now is shown in Fig. 11.4, and is phrased as a plane wave incident at an arbitrary angle on a grating of slits with the electric field parallel to the slits. Superscripts (1) and (2) represent the two different media, p is the grating period, and a' is the slit width. The aperture integral equation is formulated rigorously in terms of a kernel that consists of a sum of static, rather than dynamic, modes, and with the incident excitation correspondingly modified. The modes are *TE* modes, so that the dynamic characteristic admittances are

$$Y_{oe,n} = k_{ye,n} / \omega \mu_o, \quad Y_{oa,n} = k_{ya,n} / \omega \mu_o \quad (11.22)$$

where

$$k_{ye,n} = \left[k_o^2 \epsilon_r - k_{z,n}^2 \right]^{1/2}, \quad k_{ya,n} = \left[k_o^2 - k_{z,n}^2 \right]^{1/2} \quad (11.23)$$

The subscripts are to be interpreted in the following way. The subscript o in the characteristic admittances mean that they are "dynamic", the subscript y represents the transmission direction in the cross section, subscripts ϵ and a signify the dielectric region and the air region, respectively, and the n at the end indicates the number of the space harmonic, or mode in the y direction. The wavenumber $k_{z,n}$, which is the same in each region, is

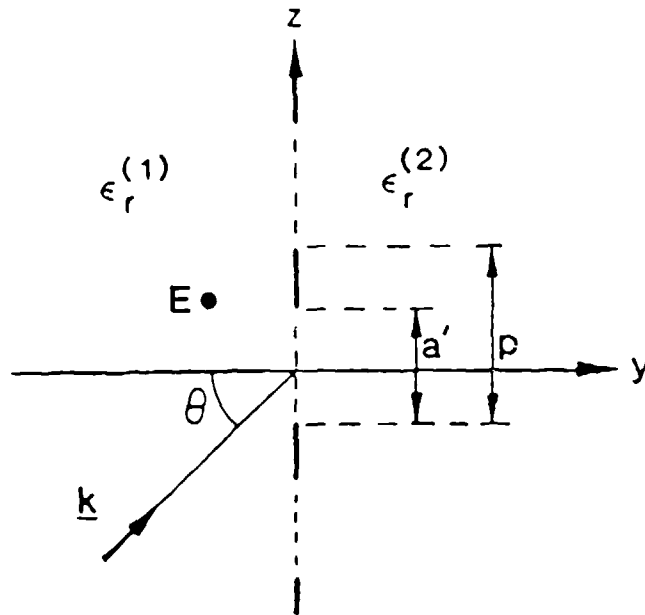


Fig. 11.4 A constituent problem in the derivation of the transverse equivalent network: the scattering of an incident plane wave by a multimode metal grating on an air-dielectric interface.

$$k_{z,n} = \beta_0 - j\alpha + 2\pi n/p \quad (11.24)$$

The "static" characteristic admittances are defined as

$$Y_{se,n} = \frac{\lim_{\omega \rightarrow 0} (k_{ye,n})}{\omega \mu_0}, \quad Y_{sa,n} = \frac{\lim_{\omega \rightarrow 0} (k_{ya,n})}{\omega \mu_0} \quad (11.25)$$

On use of (11.23) and (11.24), $Y_{se,n}$ and $Y_{sa,n}$ reduce to

$$Y_{se,n} = Y_{sa,n} = Y_{s,n} = -j \frac{2\pi |n|}{\omega \mu_0 p} \quad (11.26)$$

where the subscript s signifies that the characteristic admittance is a "static" one.

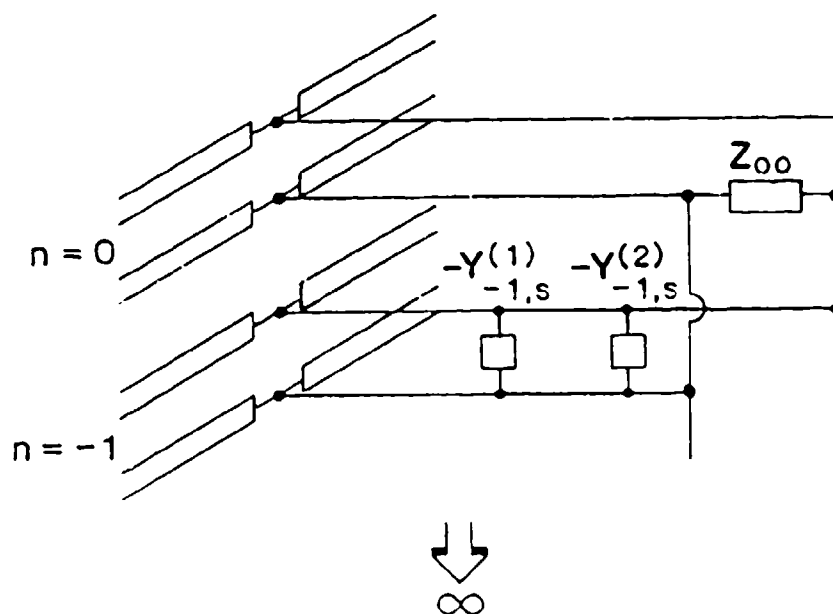


Fig. 11.5 A novel and simple equivalent network that provides a useful solution to the constituent multimode scattering problem posed in Fig. 11.4.

When these terms are applied to the constituent scattering problem outlined in Fig. 11.4, with its different notation (following the usage in [48,49]) the different media are represented by superscripts (1) and (2), rather than subscripts ϵ and a , so that (11.26) would be written

$$Y_{s,n}^{(1)} = Y_{s,n}^{(2)} = -j \frac{2\pi |n|}{\omega \mu_0 p} \quad (11.27)$$

and wavenumber $k_{z,o}$ would become

$$k_{z,o} = \beta_o = k_o^{(1)} \sin \theta^{(1)} = k_o^{(2)} \sin \theta^{(2)} \quad (11.28)$$

When the integral equation is solved in the small-aperture range ($a/p \ll 1$), a very simple equivalent network representation is obtained, in which the network elements are given by surprisingly simple but accurate expressions. The network is shown in Fig. 11.5, where it is seen to take a planar form at the air-dielectric interface.

Transmission lines are shown for only two modes, the $n=0$ and the $n=-1$ modes, but others may be added on as indicated, in straight-forward fashion.

The expressions for the network elements are

$$Z_{oo} = \frac{j\omega\mu_o p}{4\pi} \left[\frac{\pi}{2} \frac{a'}{p} \right]^2 \quad (11.29)$$

$$Y_{s,n}^{(1)} = Y_{s,n}^{(2)} = \frac{2\pi |n|}{j\omega\mu_o p} = \frac{1}{Z_{s,n}} \quad (11.30)$$

Expression (11.29) may be rewritten as

$$Z_{oo} = \frac{Z_{s,1}}{2} \left[\frac{\pi}{2} \frac{a'}{p} \right]^2 \quad (11.31)$$

where

$$Z_{s,1} = j \frac{\omega\mu_o p}{2\pi} = j \frac{p}{\lambda_o} \sqrt{\mu_o/\epsilon_o} \quad (11.32)$$

where $\sqrt{\mu_o/\epsilon_o} = 120\pi \text{ ohms}$, and is the characteristic impedance of free space. In (11.31) and (11.32) we are returning to the notation in (11.26), since we will be using that form in the full transverse equivalent network. Expression (11.30) may also be rephrased as

$$Y_{s,n} = -j \frac{\lambda_o}{p} \frac{|n|}{\sqrt{\mu_o/\epsilon_o}} = \frac{1}{Z_{s,n}} \quad (11.33)$$

The equivalent network in Fig. 11.5 is rapidly convergent with respect to the addition of transmission lines corresponding to further modes. When $|n|$ becomes large, and the modes are below cutoff, the dynamic characteristic admittances $Y_{o,n}$ and the static characteristic admittances $Y_{s,n}$ are almost the same. When the transmission lines are below cutoff, and they are terminated by their reactive characteristic admittances, the input admittance at the interface plane is $2Y_{o,n}$. But, the elements $-2Y_{s,n}$ (or $-(Y_{s,n}^{(1)} + Y_{s,n}^{(2)})$) shown in the planar network are then added to the $2Y_{o,n}$ value, and the result approaches zero as $|n|$ increases. Thus, the added transmission lines have an increasingly negligible effect.

The validity and accuracy of this network and the associated expressions have been verified in [49].

2. The Full Transverse Equivalent Network

The full unit cell consists of three sections, or regions, as stated above. In the dielectric region, two or more modes with respect to the vertical (y) direction are above cutoff; those two are the $n=0$ and $n=-1$ modes. In the air region, only the $n=-1$ mode is permitted to be above cutoff, since we wish only a single radiating beam. The same is true for the periodic region above, in which the radiation actually occurs. Since the periodic region is assumed to be unbounded, we can terminate the propagating transmission line that represents that region with its characteristic admittance, $Y_{op,-1}$.

In the dielectric-filled and air-filled parallel-plate guide regions the modes in the y direction are TE modes. After the higher modes in the vicinity of the grating at the air-dielectric interface have decayed to negligible values in the air region, the only mode remaining above cutoff is a TE mode that is actually a TEM mode propagating at an angle in the y and z directions. With respect to the space harmonics along z , it corresponds to the $n=-1$ space harmonic. The wavenumber of that mode is given by

$$k_{ya,-1}^2 = k_o^2 - k_{z,-1}^2 \quad (11.34)$$

where

$$k_{z,-1} = \beta_o - j\alpha - 2\pi/p \quad (11.35)$$

which are consistent with (11.23) and (11.24). The modal characteristic admittance follows from (11.22) as

$$Y_{oa,-1} = k_{ya,-1}/\omega_o \mu_o \quad (11.36)$$

where the subscript a signifies the air region.

When the metal baffles are present, and separated by spacing a , the radiating beam can be scanned in the cross plane, and therefore in azimuth, by inserting a phase shift between the successive line-source sections in the array. That phase shift per unit cell, Φ_c , is related to the wavenumber in the x direction by

$$\Phi_c = k_{xp,-1}a \quad (11.37)$$

Wavenumber $k_{xp,-1}$ is real and is imposed on the system to produce the cross-plane scan; it is exactly the same as the wavenumber k_{xop} in Chaps. IV and X, which means

it corresponds to the *lowest mode in the periodic waveguide*. The subscript -1 corresponds to the original $n = -1$ space harmonic in the z direction, associated with the periodic grating at the air-dielectric interface. When the metal baffles are present, a second periodic structure is introduced, at right angles to the first, but they are displaced from each other by height c (see Fig. 11.1) and they therefore do not interact directly. Of the set of space harmonics set up in the x direction, only the $n = 0$ term is above cutoff in the y direction in the periodic region. We then write for the transmission wavenumber in the y direction in the periodic region

$$k_{yp,-1}^2 = k_o^2 - k_{z,-1}^2 - k_{xp,-1}^2 \quad (11.38)$$

which may then be restated as

$$k_{yp,-1}^2 = k_{ya,-1}^2 - k_{xp,-1}^2 \quad (11.39)$$

in view of (11.34).

The fields of the propagating mode in the periodic region have components of electric and magnetic field in both the x and y directions when $k_{xp,-1} \neq 0$, but there is only a component of magnetic field in the z direction. With respect to the y direction, therefore, the mode is hybrid, but it can be characterized as an $H^{(z)}$ -type mode or an *LSE* mode with respect to the xy plane. The mode has been discussed in detail in Sec. B,2 of Chap. IV, where it is shown that the characteristic admittance for the mode is, from (2.18),

$$Y_{op,-1} = \frac{k_o^2 - k_{z,-1}^2}{\omega \mu_o k_{yp,-1}} \quad (11.40)$$

so that we may write

$$\frac{Y_{op,-1}}{Y_{oa,-1}} = \frac{k_{ya,-1}}{k_{yp,-1}} = \frac{1}{\sqrt{1 - (k_{xp,-1}/k_{ya,-1})^2}} \quad (11.41)$$

on use of (11.36), (11.34) and (11.39).

To complete the transverse equivalent network, we still require a representation for the *junction discontinuity* between the air-filled parallel-plate guide and the periodic waveguide. That discontinuity, however, is identical with one that we encounter in a similar fashion in the arrays treated in Chaps. IV and X. We will therefore not repeat the material here, but instead refer to the discussion in Sec. B,2 of Chap. IV.

The representation for the discontinuity is rigorous, is taken from the Waveguide Handbook [8] after an analytic continuation, and is shown in Fig. 4.3 of Chap. IV. It is conveniently in the form of a reference plane shift d' from the actual discontinuity plane, and the expression for d' is presented in (4.14) and (4.15), with some of the terms defined in (4.12). We must be careful in using these expressions from Chap. IV, however, to employ the correct terms since the notation used here for the wavenumbers is slightly different. The following substitutions are required: change k_{yog} and k_{xop} to $k_{ya,-1}$ and $k_{xp,-1}$.

We are finally in a position to put all the pieces together and to construct the full transverse equivalent network, which appears in Fig. 11.6. Three modes are shown in the network, the $n=0$, $n=-1$ and $n=1$ modes, but more can be added in the simple fashion shown. The planar network representing the grating at the air-dielectric interface is shown coming off at angle; that network is the same as the one presented in Fig. 11.5, but slightly modified and employing the present notation. The transmission lines representing the modes in the dielectric-filled region are shown in full because they may be above or below cutoff; even if they are below cutoff, they may still "see" the short-circuit termination. For the air-filled region, we know that only the $n=-1$ mode is above cutoff, and length c is chosen such that all the other modes have decayed to negligible values at the radiating junction. Thus, the below-cutoff modes in the air region may be safely terminated by their (reactive) characteristic admittances, and only the transmission line for the $n=-1$ mode needs to be explicitly indicated.

The discontinuity at the radiating junction, between the air-filled parallel-plate region and the periodic region, is accounted for by the reduction by d' of the height c of the parallel-plate metal baffles. Finally, the termination on that transmission line is $Y_{op,-1}$ because the periodic region is assumed to continue on into the far field. The expression for $Y_{op,-1}$ is given by (11.40).

The diminishing contribution made by adding modes with higher values of n may be assessed by the following. As the value of n increases, the input admittance to the short-circuited below-cutoff transmission line in the dielectric region approaches $Y_{oe,n}$, which in turn becomes the same as $Y_{oa,n}$, and they both approach the static characteristic admittance $Y_{s,n}$. Therefore, the sum of that input admittance and $Y_{oa,n}$, when added to the term $-2Y_{s,n}$ that is in shunt with them in the network, produces a result that approaches zero as n increases.

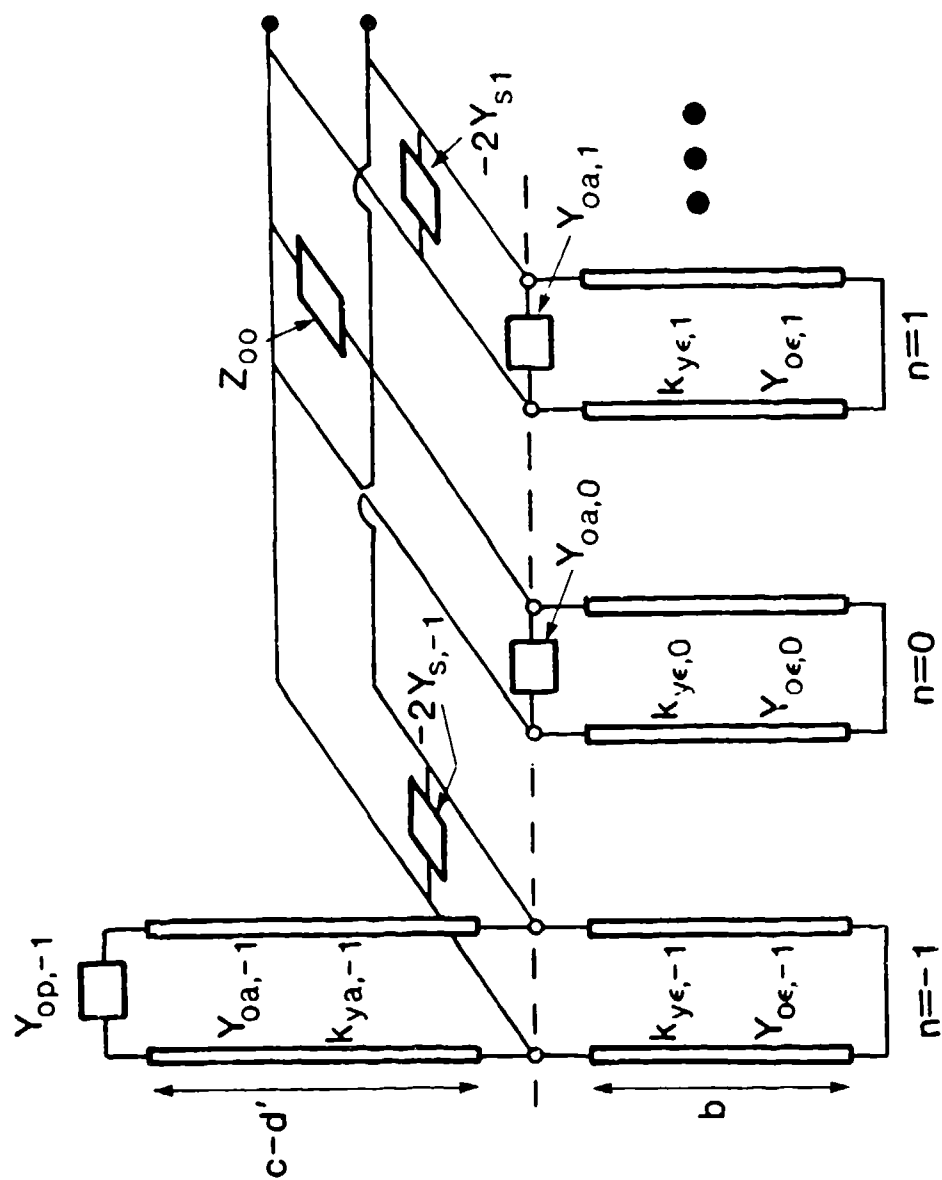


Fig. 11.6 The complete transverse equivalent network for the full array structure shown in Fig. 11.1.

D. ELEVATION ANGLE PERFORMANCE WITHOUT CROSS SCAN

When a phase shift is introduced between successive parallel line sources in the array, and when this phase shift per unit cell is varied, the beam undergoes a conical scan. The highest elevation angle for the beam, or the largest scan range in elevation for the beam, occurs when the cross-plane scan is zero. It is thus best to examine the elevation angle capability under this condition, and that is the objective in this section.

The unit cell structure simplifies under the condition of zero phase shift per unit cell because the phase-shift walls then become electric walls, in view of the electric field direction. This simplification was also found in the array structures treated in Chaps. IV and X. The transverse equivalent network becomes correspondingly simplified because the transmission line representing the propagating $n = -1$ transverse mode in Fig. 11.6 then becomes infinitely long. We do not have to treat the junction discontinuity, since it has disappeared, so that the input admittance to that transmission line becomes its characteristic admittance. The principal complexity in that network has therefore been removed. In the calculations that follow we have employed 6 modes in the dispersion relation (meaning that 6 transmission lines have been included in the transverse equivalent network in Fig. 11.6), namely, the $n = -3, -2, -1, 0, 1$ and 2 modes.

The first piece of information we seek is whether or not there is a geometrical parameter we can vary which will permit us to control the leakage constant α without changing the phase constant β at the same time. The candidate we have in mind is the relative slit width a'/p of the grating on the air-dielectric interface (see Fig. 11.2). Before examining the performance numerically, however, we must specify a frequency. Since we wish to achieve a large elevation angle, we therefore select a frequency corresponding to an angle near broadside.

The k_o vs. β_n diagram in Fig. 11.3 provides convenient physical insight into how such a selection is made, but we can determine it directly by simply using relations (11.3) to (11.5). In any case, let us employ the numerical determinations already made in Sec. B in connection with the various points indicated on the k_o vs. β_n diagram. First, we must specify the dimensions of the elements in the array. Referring to Figs. 11.1 and 11.2, the dimensions specified in Sec. B as corresponding to the frequency range of 40 GHz to 60 GHz are:

$$a = 1.20 \text{ mm} , \epsilon_r = 4.00$$

$$b = 2.40 \text{ mm} , p = 3.45 \text{ mm}$$

For these dimensions, the frequency corresponding to broadside radiation, evaluated in the small aperture limit, was found to be 53.5 GHz, corresponding to a value $k_o = 1.120 \text{ mm}^{-1}$. When the beam begins to radiate, at backward endfire, we had $f = 39.3 \text{ GHz}$ and $k_o = 0.822 \text{ mm}^{-1}$.

Calculations are presented in Figs. 11.7 through 11.10 for the normalized phase constant β_o/k_o and the normalized leakage constant α/k_o as a function of the relative slit width a'/p for two different values of k_o corresponding to radiation near to broadside. The value of $k_o = 1.096 \text{ mm}^{-1}$ is employed in Figs. 11.7 and 11.8, whereas $k_o = 1.099 \text{ mm}^{-1}$ was selected for the other two figures.

The variation of β_o/k_o with a'/p is seen in Fig. 11.7 to be relatively slight, although it does increase a little as the slit width increases. It varies from $\beta_o/k_o = 1.60$ at one end to 1.64 at the other. The $n=0$ space harmonic does not radiate, so its value of normalized phase constant *should* be greater than unity. The radiating beam corresponds to β_{-1}/k_o , which may be computed from (11.4), and the elevation angle of the radiation follows from (11.5). For the values at the two ends of the curve in Fig. 11.7 we obtain $\theta_{-1} = -3.4^\circ$ and $\theta_{-1} = -1.1^\circ$; these angles are very close to broadside, but slightly in the backward quadrant. The angular change from one end of the range of a'/p to the other end is really quite small, however.

From Fig. 11.8, on the other hand, we observe that the normalized leakage constant α/k_o varies very substantially and rather rapidly as a'/p exceeds 0.20 or so. The simple expressions (11.31) through (11.33) that were used in the dispersion relation are known to be valid up to $a'/p = 0.3$ or so, and we have therefore performed computations up to that value. We note, however, that the beam width corresponding to $a'/p = 0.3$ in Fig. 11.8 already corresponds to $\Delta\theta = 9.4^\circ$, which is a rather wide beam. (The beam width $\Delta\theta$ can be obtained by writing

$$\Delta\theta \approx 285 \alpha/k_o \quad (11.42)$$

where $\Delta\theta$ is in degrees, by combining (2.28) and (2.29), and recognizing that θ_{-1} is almost zero, being close to broadside.)

The data in Figs. 11.9 and 11.10 are similar to those in Figs. 11.7 and 11.8 except that they apply to a value of k_o even closer to that for broadside. The values of β_o/k_o are almost exactly the same in Figs. 11.9 and 11.7, but the α/k_o values in Fig. 11.10 are

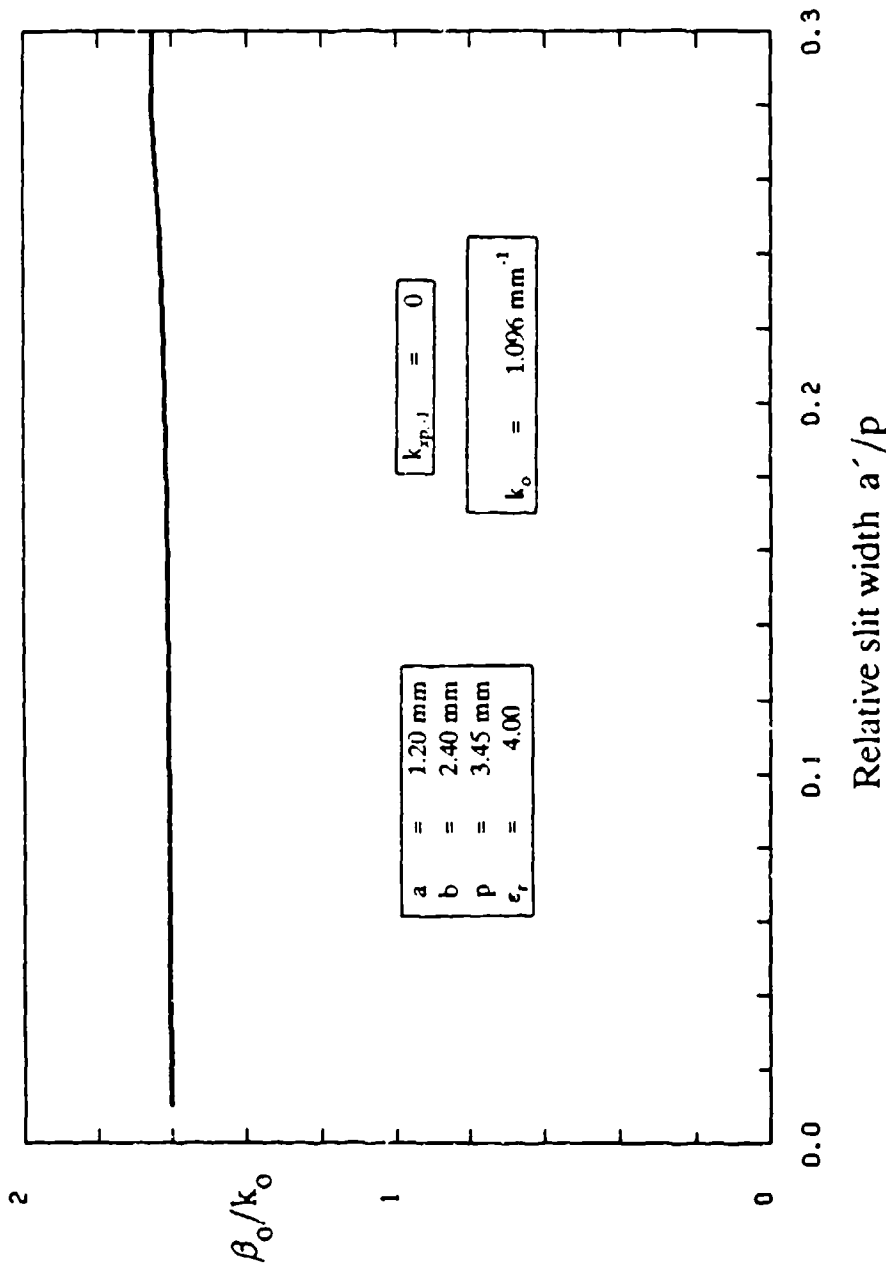


Fig. 11.7 The variation of β_0/k_0 , the normalized phase constant of the basic $n = 0$ space harmonic, as a function of a'/p , the relative slit width of the grating on the air-dielectric interface, in the absence of cross-plane scan. The free-space wavenumber k_0 in this case is 1.096 mm^{-1} , corresponding to a beam angle very close to broadside. The variation is seen to be slight.

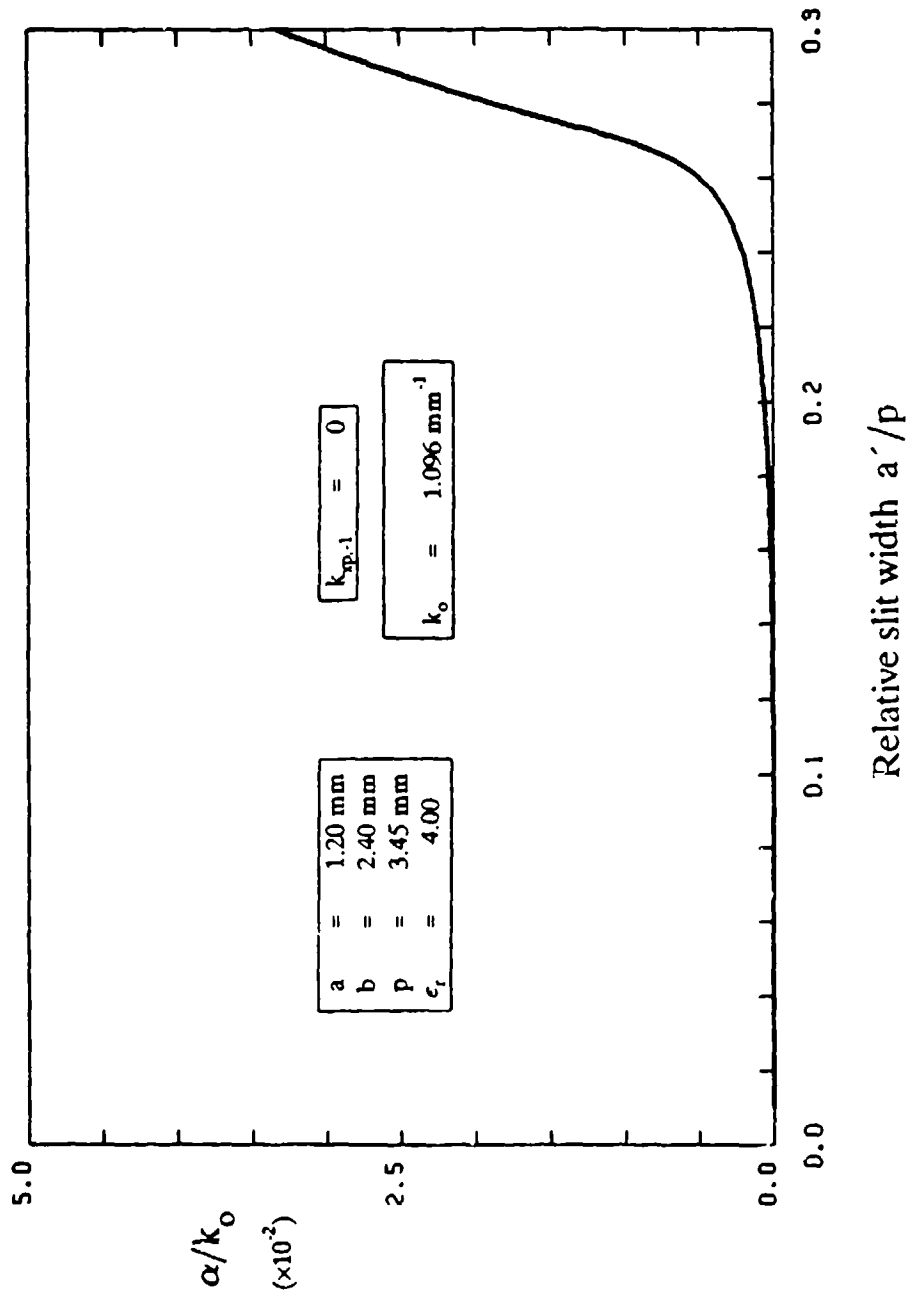


Fig. 11.8 The variation of α/k_0 , the normalized leakage constant, as a function of a'/p . The other parameters correspond to those in Fig. 11.7.

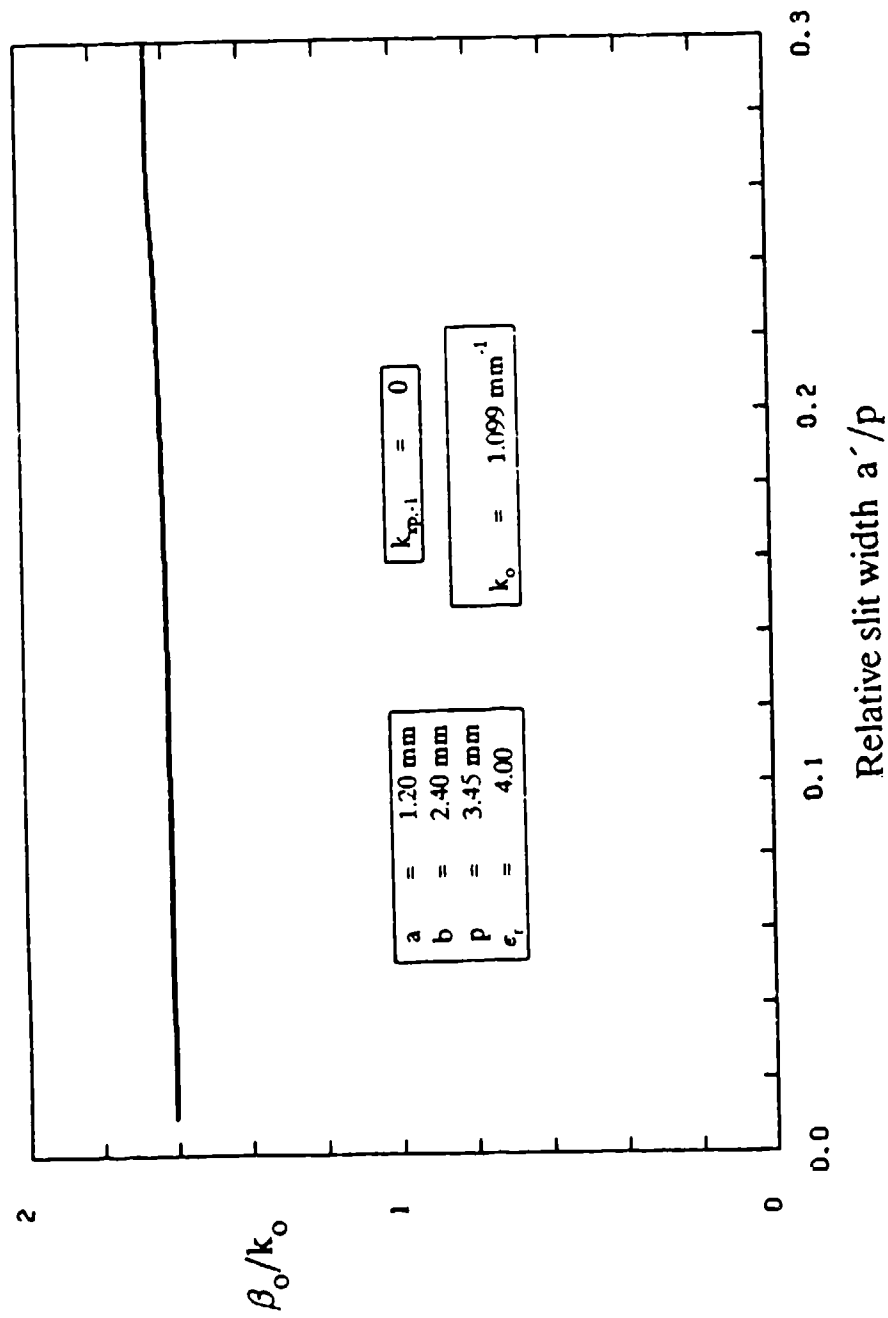


Fig. 11.9 Same as Fig. 11.7, but for $k_o = 1.099 \text{ mm}^{-1}$, corresponding to a beam angle slightly closer to broadside

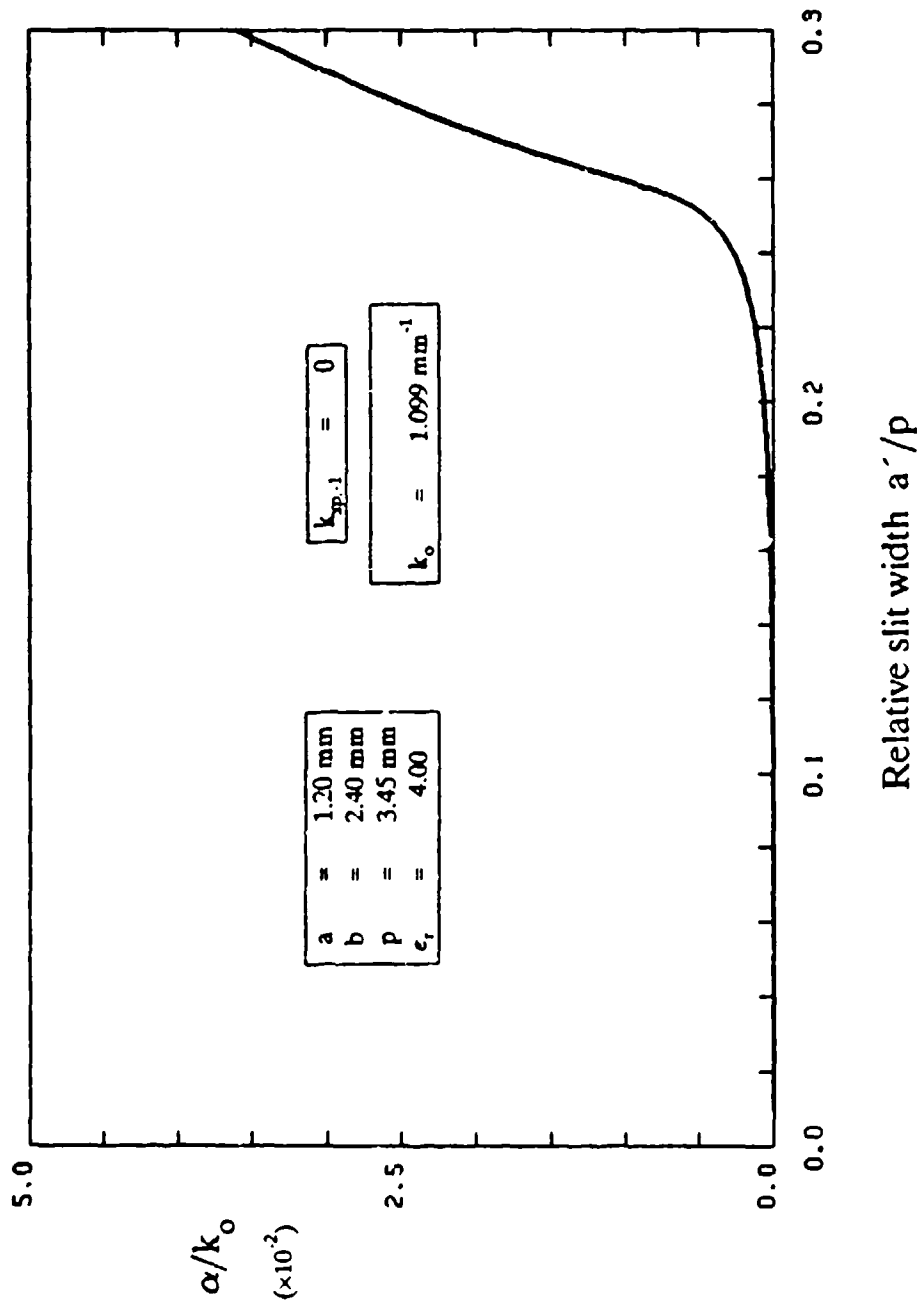


Fig. 11.10 Same as Fig. 11.8, but for $k_0 = 1.099 \text{ mm}^{-1}$, corresponding to a beam angle a little closer to broadside, resulting in larger values of leakage constant, but otherwise similar behavior, as compared with Fig. 11.8.

seen to be noticeably larger than those in Fig. 11.8. The value corresponding to $a'/p = 0.30$ is now 3.6×10^{-2} , for which the beam width is 10.3° , rather than the 9.4° obtained from Fig. 11.8. A much bigger change is observed for values for $a'/p = 0.26$ or 0.28 ; for 0.26 , for example, α/k_o has changed from 0.50×10^{-2} to 1.00×10^{-2} , effectively doubling. Such a large change occurs because the angle is so near to broadside; at angles away from broadside the modifications in α/k_o as we vary k_o by small amounts would be much less pronounced.

The important conclusions from this set of four curves are that, as the relative slit width is varied, the value of β_o/k_o changes very little and that of α/k_o changes very strongly. Thus, the beam angle is determined primarily by the relative values of λ_o, b, p and ϵ_r , and the beam width by those of a'/p , assuming that the antenna length is chosen so that some specified percentage, like 90%, of the power is radiated.

The next set of curves presents the way the radiation angle and the leakage constant vary as k_o is changed. The vertical axis in each figure represents the values of the free-space wavenumber k_o , the right-hand-side abscissa shows the values of α/k_o , and the left-hand-side abscissa indicates the behavior of the beam angle θ_{-1} . The parameter a'/p is different in each of the figures.

We begin with the largest value of a'/p in the set, namely, $a'/p = 0.27$, in Fig. 11.11. As we go vertically along the k_o axis, we first reach the onset of radiation at which the beam is at backward endfire, i.e., $\theta_{-1} = -90^\circ$. The curve for θ_{-1} , on the left-hand side, is plotted in polar coordinate fashion, where θ_{-1} can only be positive, so that one reads the value as 90° rather than -90° . However, the direction of the curve reverses after it crosses broadside in this plot. Thus, as k_o increases, we see that the beam moves in the backward quadrant from 90° to zero, at broadside, and then, after lingering there for a bit, the beam continues on into the forward quadrant.

At the same time, the value of leakage constant α/k_o increases from zero at the onset of radiation but then rises sharply and dramatically when the beam approaches broadside. Only about 1/3 of the full extent of the spike-type rise is shown in Fig. 11.11. The sharp peak corresponds to the open "stop band" near broadside, at which the $n = 0$ and $n = -2$ space harmonics become equal in amplitude but are oppositely directed. (All the other space harmonics pair off in like fashion.) The rise in α is predominantly reactive, not radiative, so that a sharp increase is observed in reflected power, together with pattern deterioration. The narrow region near broadside is to be avoided in practice, but, unless the beam is rather narrow, one can scan through the region and hardly notice any effect. Just on the other side of the spike in α/k_o , the

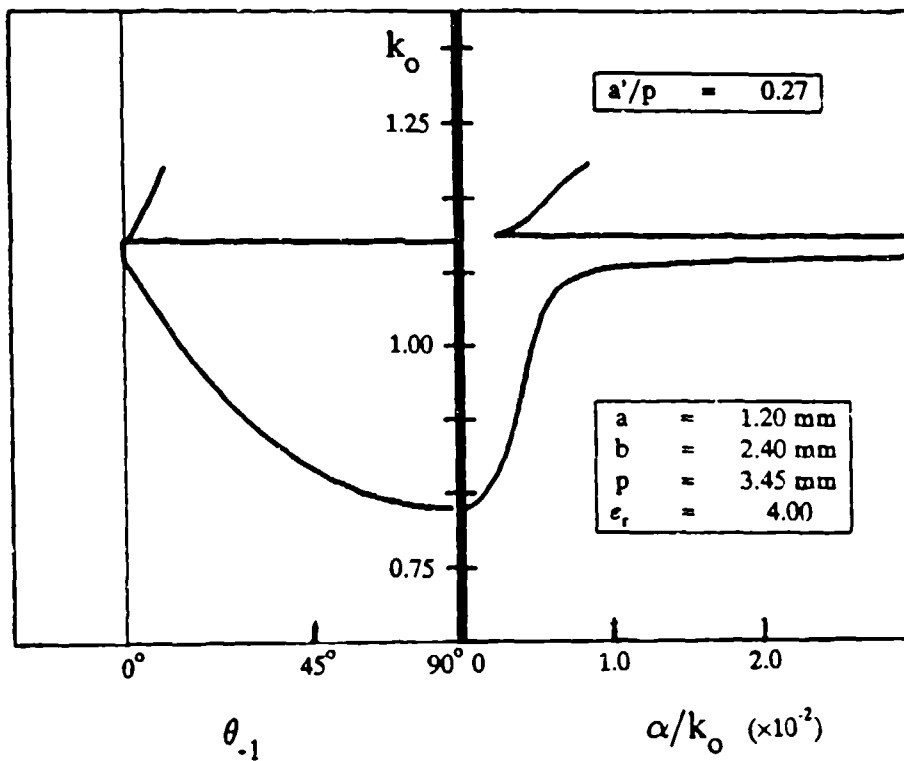


Fig. 11.11 On the vertical axis is the free-space wavenumber k_0 ; the right-hand abscissa axis represents the normalized leakage constant α/k_0 ; and the left-hand abscissa axis shows the elevation beam angle θ_{-1} in degrees. Angle θ_{-1} appears in polar coordinate form, so it is always positive; however, it is in the backward quadrant for lower values of k_0 and enters the forward quadrant after passing through broadside. The sharp peak in α/k_0 is due to the open "stop band" near broadside. This case corresponds to relative slit width $a'/p = 0.27$, and to zero cross-plane scan.

curve drops extremely sharply; we expect that it should go to zero, but the calculation steps were not fine enough to exhibit that behavior.

The other three figures in this set are Figs. 11.12, 11.13 and 11.14, for which $a'/p = 0.25, 0.22$ and 0.10 , respectively. The curves for θ_{-1} are hardly distinguishable from each other, but the ones for α/k_o change in systematic ways, as expected. The magnitude of α/k_o decreases as a'/p is reduced, consistent with Figs. 11.8 and 11.10, and the width and extent of the "stop band" spike become smaller as a'/p is reduced. The leakage rate for the value $a'/p = 0.10$ in Fig. 11.14 is so small that it was necessary to expand the abscissa scale by a factor of 50; the "stop band" region was not computed for this case.

Figures 11.7 through 11.14 therefore tell us how β_o/k_o and α/k_o behave as we change either the slit width or the frequency (actually k_o). Increasing the slit width changes the β_o/k_o value (and therefore the beam angle θ_{-1}) relatively little, but it produces a large change in the value of α/k_o , which in turn affects the beam width. As frequency, or k_o , is increased, the beam swings around as we expect from the discussion in Sec. B, and the leakage rate increases slowly over most of the scan range, but behaves wildly in the "stop band" region near broadside, which should therefore be avoided unless the beam is sufficiently wide.

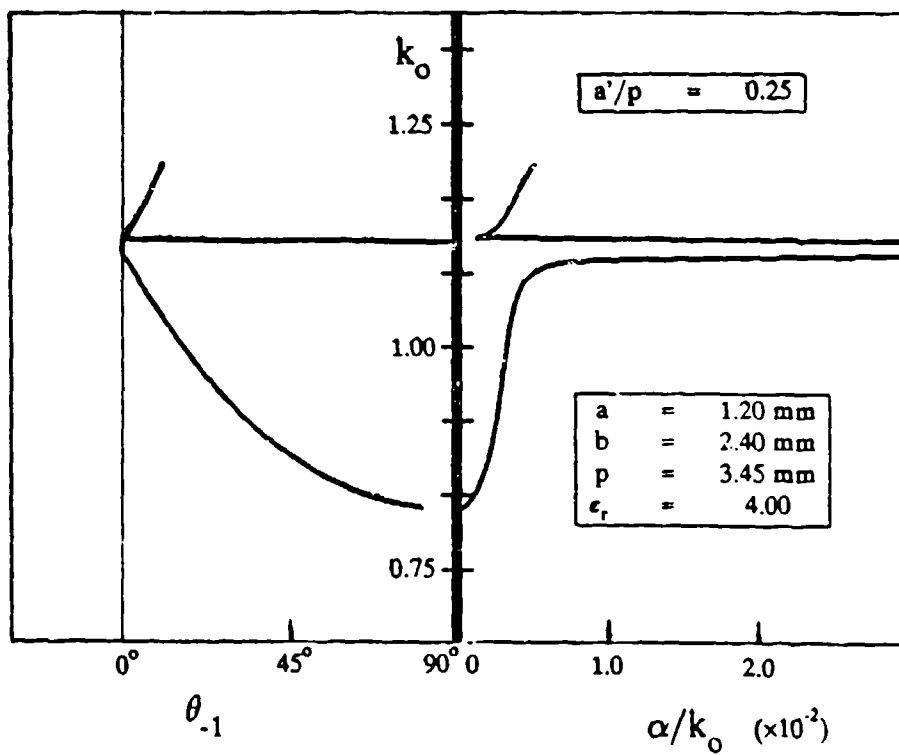


Fig. 11.12 Same as Fig. 11.11, but for $a'/p = 0.25$.

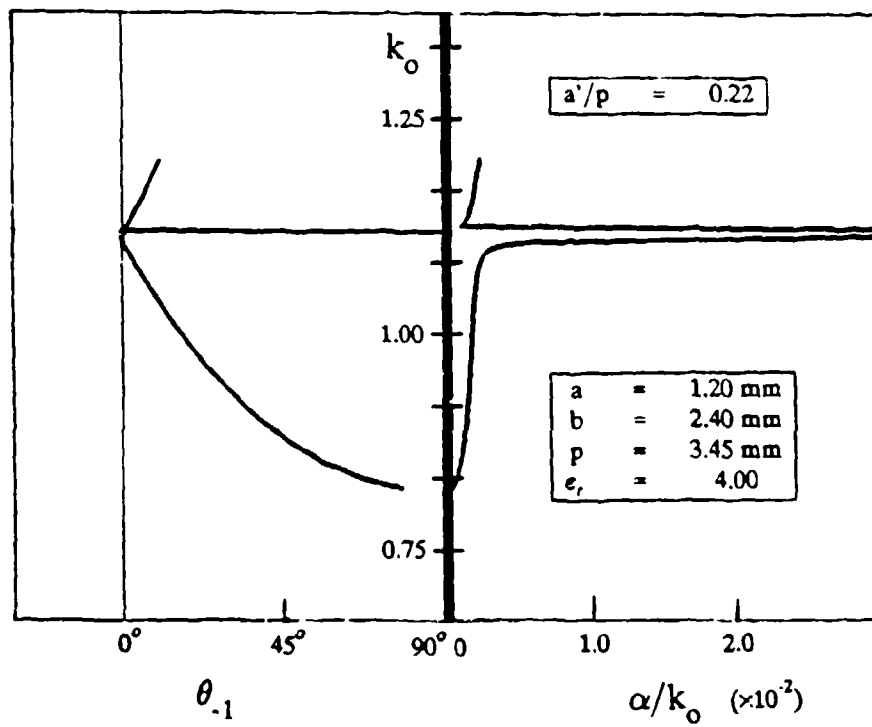


Fig. 11.13 Same as Fig. 11.11, but for $a'/p = 0.22$, a much narrower aperture.

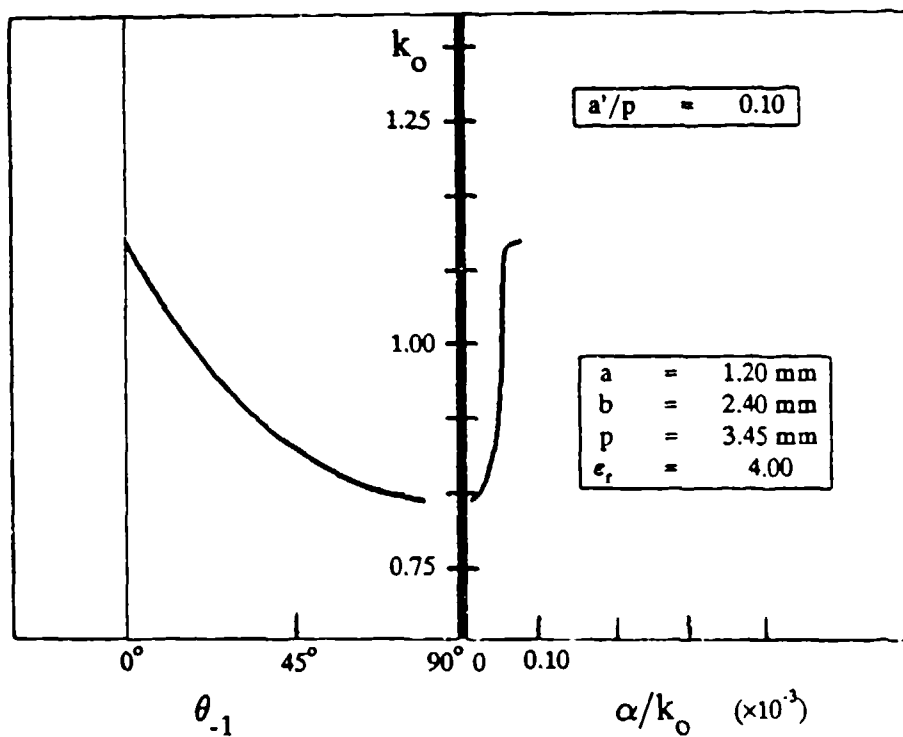


Fig. 11.14 Same as Fig. 11.11, but for $a'/p = 0.10$, a very tiny aperture electrically. The right-hand abscissa scale has been multiplied by 50 as compared with Fig. 11.11, and the "stop band" region was not calculated.

E. EFFECTS OF CROSS-PLANE SCANNING

As in the arrays described in Chaps. IV and X, scanning in the cross plane, and therefore in azimuth, is accomplished by inserting a phase shift between successive parallel line sources in the array. The phase shift introduces a wavenumber component in the x direction, which we have called $k_{xp,-1}$ because it occurs in the periodic waveguide and is due to the $n = -1$ space harmonic for the array of slits on the air-dielectric interface. With respect to the periodic array of line sources, it represents the $n = 0$ space harmonic, since that is the only one that is above cutoff in the vertical (y) direction.

The phase shift per unit cell is then $k_{xp,-1}a$, where a is the width of each unit cell; this statement is the same as the one in (10.92) or (10.68) of Chap. X. In Chap. X, the phase shift per unit cell was used as a measure of the cross-plane scan. In Chap. IV, it was θ_x , where $\sin \theta_x = k_{xop}/k_o$, as shown in (4.10), for example, and k_{xop} is the equivalent of $k_{xp,-1}$ here. We have not been consistent in this report with respect to what measure to employ for the cross-plane scan, and it is not clear which one is best. We have chosen the ratio $k_{xp,-1}/k_o$ as the measure in this chapter. The three measures are, therefore: θ_x , or $\sin^{-1}(k_{xop}/k_o)$, in Chap. IV, $k_{xop}a$ in Chap. X, and $k_{xp,-1}/k_o$ in this chapter. With respect to the measure employed now, we see that the scan range cannot exceed unity, a convenient maximum value.

As discussed in the other two chapters, the radiating open-end discontinuity between the periodic waveguide and the air-filled parallel-plate guide is no longer neglectable when $k_{xp,-1} \neq 0$, and it produces two principal effects: a *standing wave* between that discontinuity and the one representing the grating on the air-dielectric interface, and *possible coupling* to channel-guide leaky modes excited at the radiating open end. Two other concerns arise with respect to cross-plane scan: possible deviations from strict conical scan, and the possible presence of blind spots. The calculation results discussed below address all these questions.

First, we examine the behavior of β_o/k_o and α/k_o as a function of the *relative height* c/λ_o of the metal baffles, i.e., the air-filled parallel-plate region. In Figs. 11.15 and 11.16 we present the variations with c/λ_o of β_o/k_o and α/k_o , respectively, for a relatively large phase shift, corresponding to $k_{xp,-1}/k_o = 0.90$, and a value of $k_o = 1.099 \text{ mm}^{-1}$. We observe that the curve for β_o/k_o possesses a slight periodic variation as c/λ_o changes, but that its amplitude is very small and its average value is almost the same as that found for $k_{xp,-1} = 0$, in Fig. 11.9, for $a'/p = 0.25$, which is the

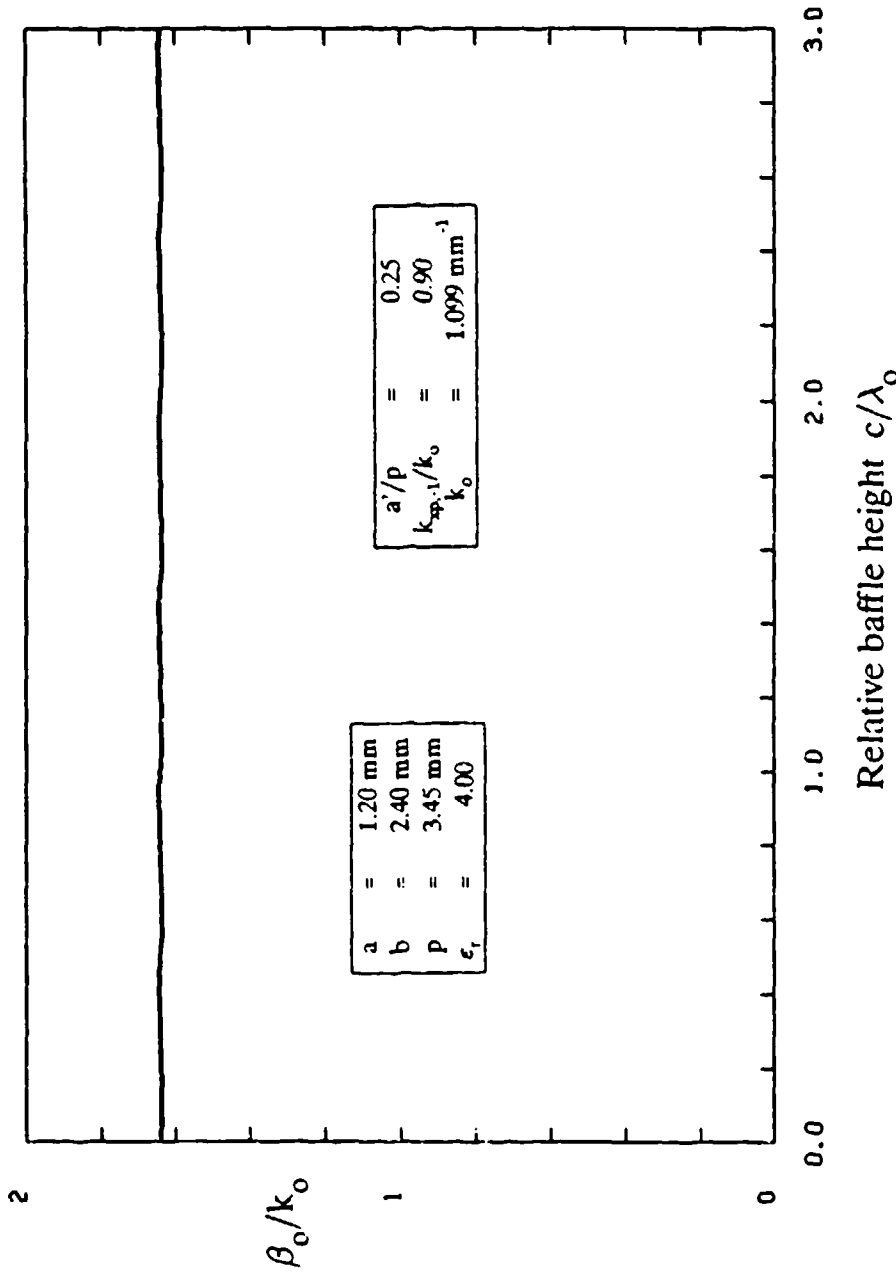


Fig. 11.15 The variation of β_o/k_o , the normalized phase constant of the basic $n = 0$ space harmonic, as a function of c/λ_o , where c is the height of the metal baffles of the array in the air region, for $k_{sp,1}/k_o = 0.90$, which corresponds to a large value of cross-plane scan.

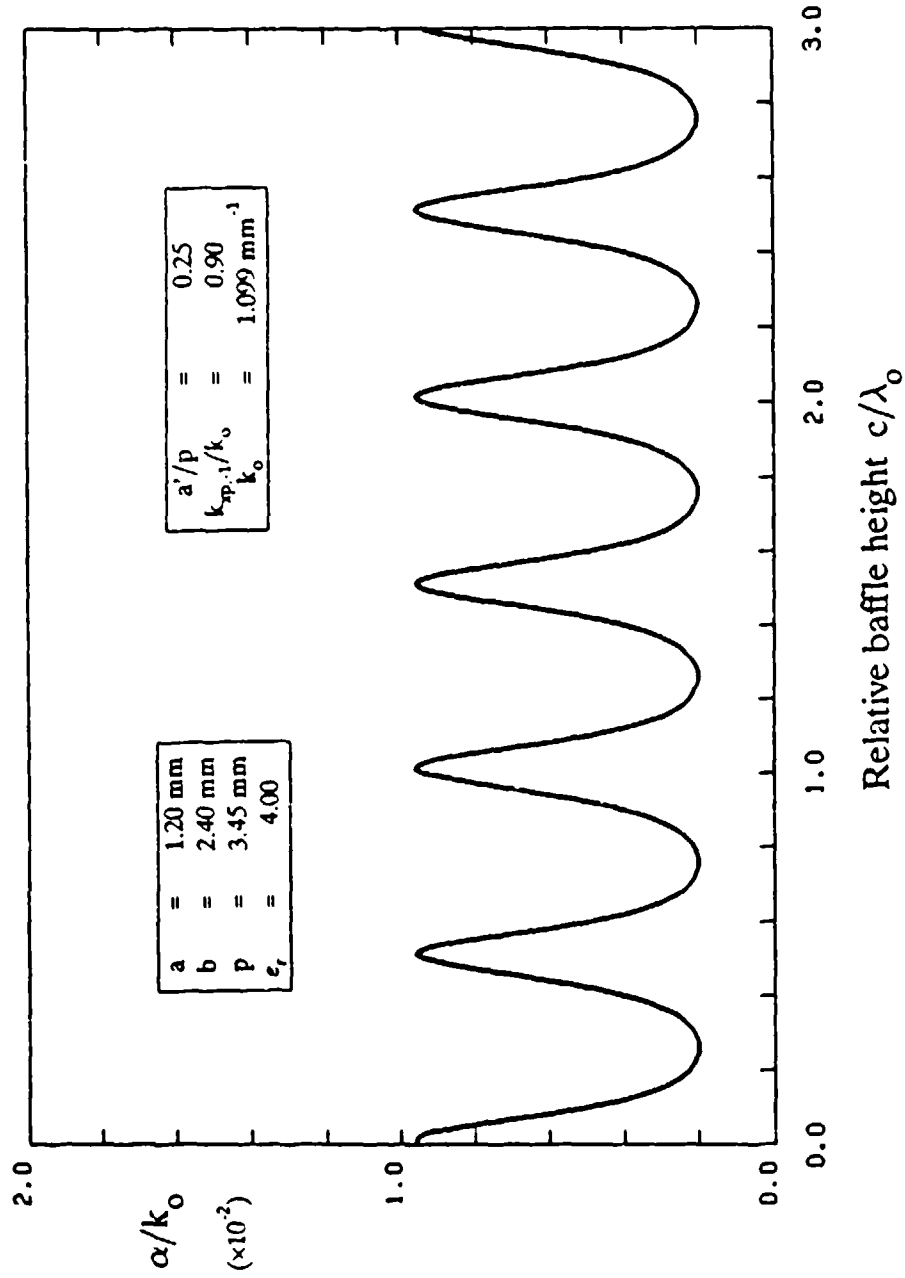


Fig. 11.16 The variation of α/k_0 , the normalized leakage constant, as a function of c/λ_0 . See caption for Fig. 11.15 for further information.

value used here. The curve for α/k_o in Fig. 11.16, however, shows a very large periodic variation with c/λ_o , where the maximum value is nearly five times the minimum value. The average value of the variation is seen to agree fairly well with the value for $a'/p = 0.25$ in Fig. 11.10, showing that the average value is approximately what one would find when the radiating discontinuity is replaced by metal walls continuing indefinitely.

It is interesting to note that no interactions with channel-guide leaky modes were found for this set of parameters. The beam width in elevation corresponding to the maximum value of α/k_o in Fig. 11.16 is only about 2.7° , so a larger value of a'/p may be necessary before these interactions occur.

The curves in Figs. 11.15 and 11.16 correspond to $k_o = 1.099 \text{ mm}^{-1}$ which, for the dimensions listed, would correspond to an angle in elevation equal to about -1° if $k_{xp,-1} = 0$. That result agrees with the discussion in Sec. D. Now, with $k_{xp,-1}/k_o = 0.90$, the beam position is quite different. We recall that the beam undergoes conical scan; when the elevation angle before cross scan is close to broadside, however, the azimuth angle rapidly approaches near to 90° . From (2.16) or (10.93), we know that if the elevation angle before cross scan is 1° the azimuth angle when the beam hits the ground will be 89° (or -1° and 91° , respectively). For an arbitrary value of $k_{xp,-1}/k_o$, we may compute the actual values of elevation angle θ_{-1} and azimuth angle ϕ_{-1} from (10.98) and (10.99), which are, in present notation,

$$\sin \theta_{-1} = \left[(k_{xp,-1}/k_o)^2 + (\beta_{-1}/k_o)^2 \right]^{1/2} \quad (11.43)$$

and

$$\sin \phi_{-1} = \frac{k_{xp,-1}/k_o}{\left[(k_{xp,-1}/k_o)^2 + (\beta_{-1}/k_o)^2 \right]^{1/2}} \quad (11.44)$$

where $k_{xp,-1}/k_o$ is imposed and β_{-1}/k_o is given by (11.4), with the values of β_o/k_o furnished by the various curves.

For the parameters in Fig. 11.15, we find from (11.43) and (11.44) that the elevation angle θ_{-1} and the azimuth angle ϕ_{-1} , corresponding to $k_{xp,-1}/k_o = 0.90$, are

$$\theta_{-1} = 64.2^\circ, \quad \phi_{-1} \approx 89^\circ$$

In the final sets of curves, our goals are to determine the *deviation from conical scan* and to see if there exists any evidence for or tendency towards *blind spots* during the cross-plane scan process. Towards these ends, we present numerical results for β_o/k_o and α/k_o as a function of the relative phase shift, measured by $k_{xp,-1}/k_o$, over the whole scan range, for several cases.

In Figs. 11.17 through 11.19, we have selected $a/p = 0.25$, and we present results for β_o/k_o for three quite different conical scan situations. For Fig. 11.17, the elevation angle before cross-plane scan is about -1° , as in Figs. 11.15 and 11.16. The conical scan here corresponds to the widest possible one, coming from almost broadside down to the ground in elevation, and ending with the beam at $\phi_{-1} = 91^\circ$. For Fig. 11.18, the value of $k_o = 0.9325 \text{ mm}^{-1}$, so that $\lambda_o = 6.738 \text{ mm}$; with $\beta_o/k_o = 1.455$, as obtained from the figure for $k_{xp,-1}/k_o = 0$, we find that the elevation angle before cross-plane scan is -29.9° , in the backward quadrant. When this beam reaches the ground, $\phi_{-1} = 119.9^\circ$. For the third scan situation, in Fig. 11.19, we have $k_o = 0.8492 \text{ mm}^{-1}$ and $\lambda_o = 7.399 \text{ mm}$, and from the figure we see that $\beta_o/k_o = 1.313$ when $k_{xp,-1}/k_o = 0$. The elevation angle θ_{-1} before cross-plane scan is therefore -56.3° , which is much closer to the ground, near backward endfire; the value of azimuth angle at the other end of the scan range is $\phi_{-1} = 146.3^\circ$.

Let us now look at the behavior of β_o/k_o in Figs. 11.17 through 11.19 over the remainder of the scan range. We see that the curves are almost flat; the one in Fig. 11.17 rises very slightly, the one in Fig. 11.19 drops very slightly, whereas the one in the middle range of scan, Fig. 11.18, seems completely flat. In all cases, the curves are so flat that we can assert that *any deviation from conical scan is very small indeed*.

We also note from these figures that the scan *range* changes as well from one to the other. The maximum value that $k_{xp,-1}/k_o$ can have, corresponding to the end of the scan range, when the beam reaches the ground, is given in Chap. X as (10.96); we repeat it here in present notation as

$$(k_{xp,-1}/k_o)_{\max} = \cos(\theta_{-1})_{\phi=0} = \cos(\sin^{-1} \beta_{-1}/k_o)_{\phi=0} \quad (11.45)$$

For Fig. 11.17, the original elevation angle was so near to broadside that the maximum value of $k_{xp,-1}/k_o$ is essentially unity. For Fig. 11.18, the value of $(\theta_{-1})_{\phi=0} = -29.9^\circ$, so that $k_{xp,-1}/k_o = 0.867$, in agreement with the curve in the figure. We found that the elevation angle before cross-plane scan was 56.3° for the parameters in Fig. 11.19, so that $(k_{xp,-1}/k_o)_{\max}$ is found from (11.45) to be 0.555, in exact agreement with the curve in Fig. 11.19.

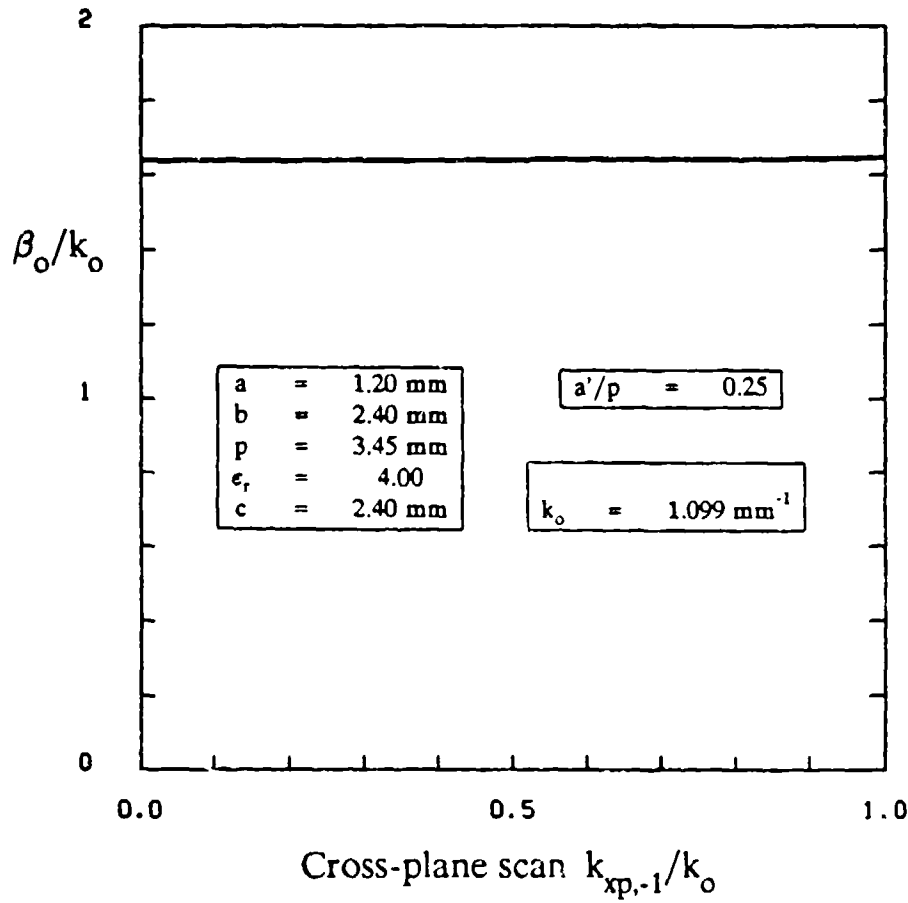


Fig. 11.17 Behavior of β_0/k_0 , the normalized phase constant of the basic $n = 0$ space harmonic, as a function of $k_{xp,-1}/k_0$, a measure of the amount of cross-plane scan, over the whole scan range. For this case, the relative slit width $a'/p = 0.25$, and the free-space wavenumber k_0 is 1.099 mm^{-1} , for which the beam is almost at broadside when the cross-plane scan is zero.

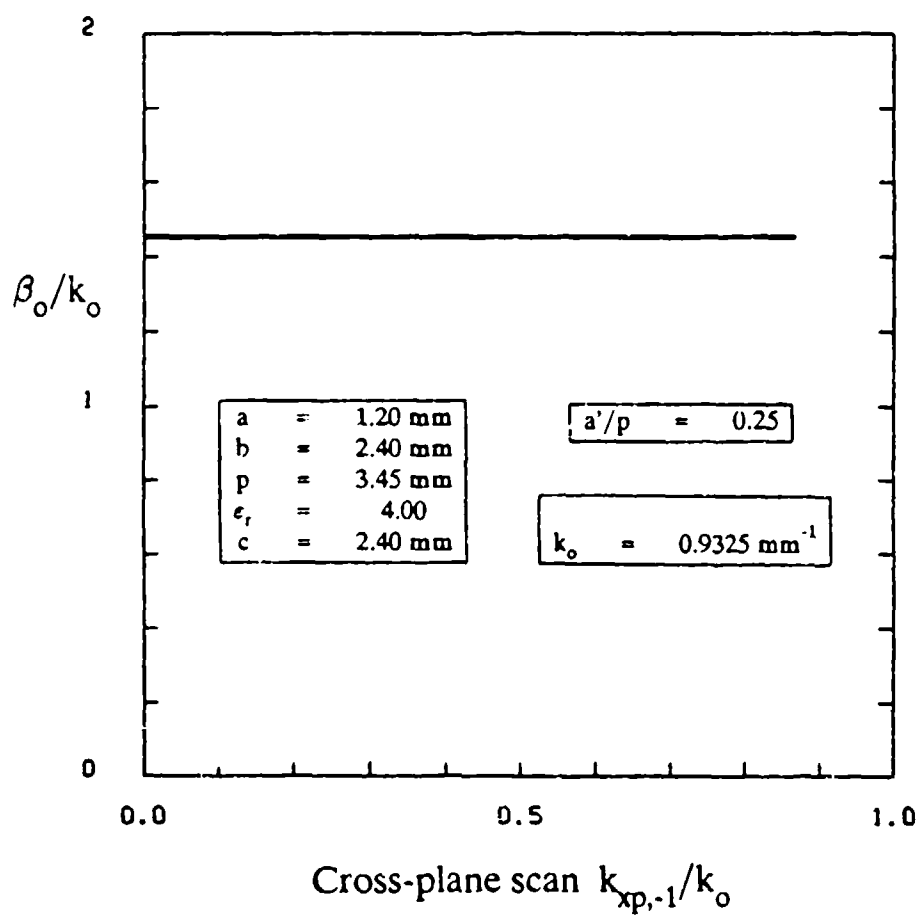


Fig. 11.18 Same as Fig. 11.17, but for $k_o = 0.9325 \text{ mm}^{-1}$, for which the beam is at -29.9° from broadside when the cross-plane scan is zero.

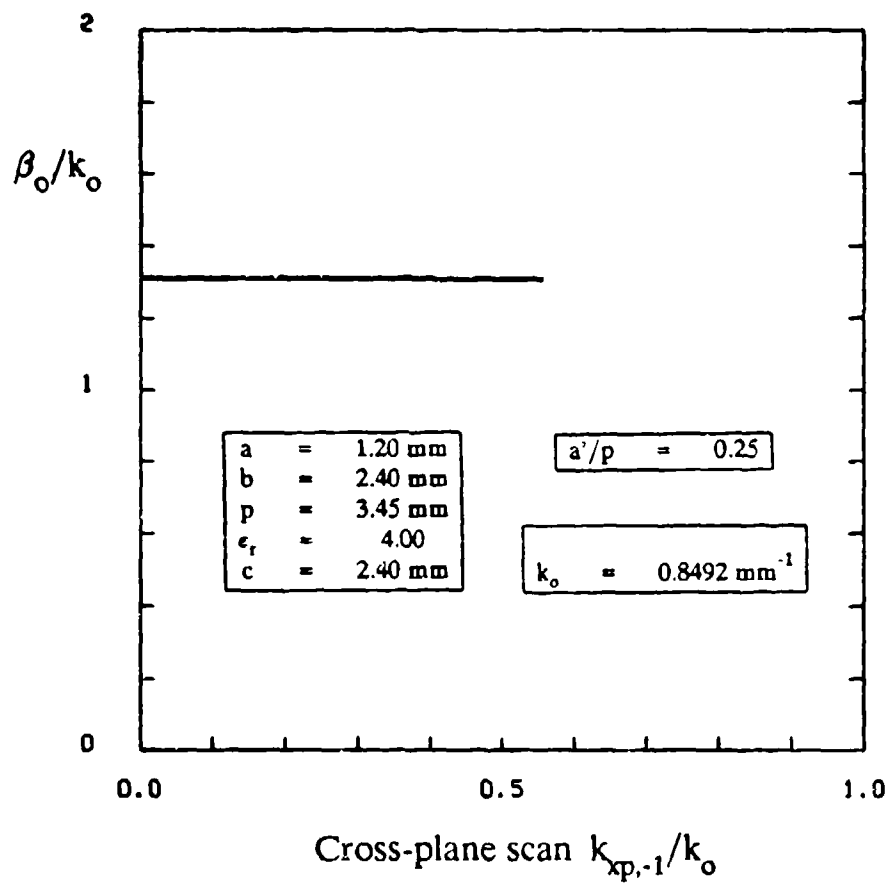


Fig. 11.19 Same as Fig. 11.17, but for $k_0 = 0.8492 \text{ mm}^{-1}$, for which the beam is at -56.3° from broadside when the cross-plane scan is zero.

The companion figures to Figs. 11.17 through 11.19, for α/k_o instead of β_o/k_o , are Figs. 11.20 through 11.22. The most important point to note about these curves is that they are relatively flat until near the end, where they drop to zero because the beam has reached the ground and all radiation ceases. There are no sharp dips anywhere, so that there is *no evidence of blind spots*. All three figures have the same ordinate scale, and we have seen in Figs. 11.11 through 11.14 that the value of α/k_o decreases as the value of k_o is reduced, so it is to be expected that the level of α/k_o becomes progressively smaller in these three figures.

Finally, we can obtain added information by referring to Fig. 11.16, which shows α/k_o vs. baffle height c/λ_o for $k_{xp,-1}/k_o = 0.90$. The value of c chosen for the calculations in Figs. 11.17 through 11.22 is 2.40 mm; in both Figs. 11.16 and 11.20 the value of λ_o is 5.716 mm, so that $c/\lambda_o = 0.420$ in Fig. 11.20. That value in Fig. 11.16 corresponds to a point approximately mid-way in the amplitude variation, and not much different from the value before cross-plane scan. As $k_{xp,-1}$ increases, we would therefore expect the value of α/k_o to remain relatively flat over the whole scan range, as we find in Fig. 11.20. If the value of c were chosen to correspond to the *bottom* of the periodic variations in Fig. 11.16, the curve in Fig. 11.20 would drop off more rapidly; if it corresponded to the *top* of the variations, the curve in Fig. 11.20 would peak up before dropping down to zero at the end of the scan range. Such behavior was obtained in Chaps. IV and X for the same reason. The curve of β_o/k_o in Fig. 11.17 would probably not be quite as flat if c were chosen to correspond to the top or the bottom of the periodic variations, but, again judging from our experience with the other arrays, the change would be expected to be small.

The last set of curves is shown in Figs. 11.23 to 11.28. They are similar to those in Figs. 11.17 through 11.22, except that a larger slit aperture was selected, with $a'/p = 0.26$ rather than 0.25, so that larger values of α/k_o are obtained. All of the behavior characteristics for α/k_o and β_o/k_o are similar to those for $a'/p = 0.25$.

Instead of choosing the largest elevation angle before cross-plane scan to be almost at broadside, however, a value slightly removed from it was taken, in Figs. 11.23 and 11.26. The value of $k_o = 1.058 \text{ mm}^{-1}$, so that $\lambda_o = 5.94 \text{ mm}$; the value of β_o/k_o from Fig. 11.23 is seen to be 1.60, so that $\beta_{-1}/k_o = 0.122$ and θ_{-1} at $\phi_{-1} = 0$ is -7.0° , which is still close to broadside but away from the "stop band" region. The maximum value of $k_{xp,-1}/k_o$ is now 0.99, as found from (11.45), so that essentially the complete scan range is achieved; this minor distinction is actually discernable in Figs. 11.23 and 11.26.

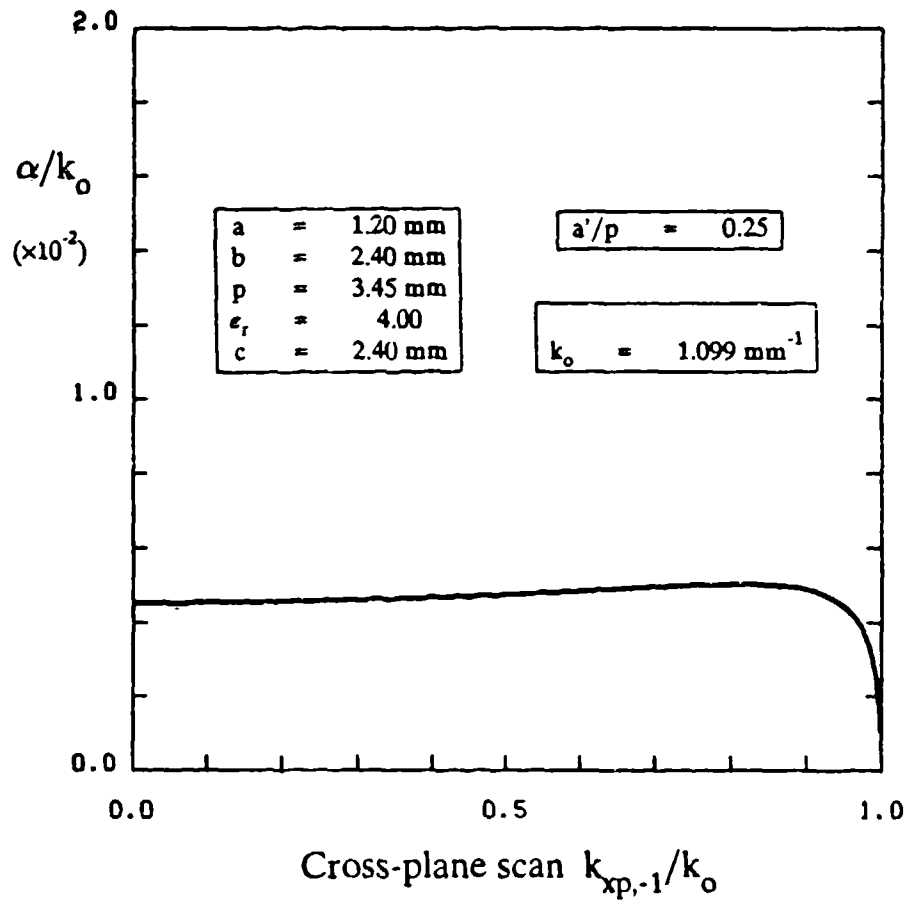


Fig. 11.20 Behavior of α/k_0 , the normalized leakage constant, as a function of $k_{xp,-1}/k_0$. See caption for Fig. 11.17 for further information.

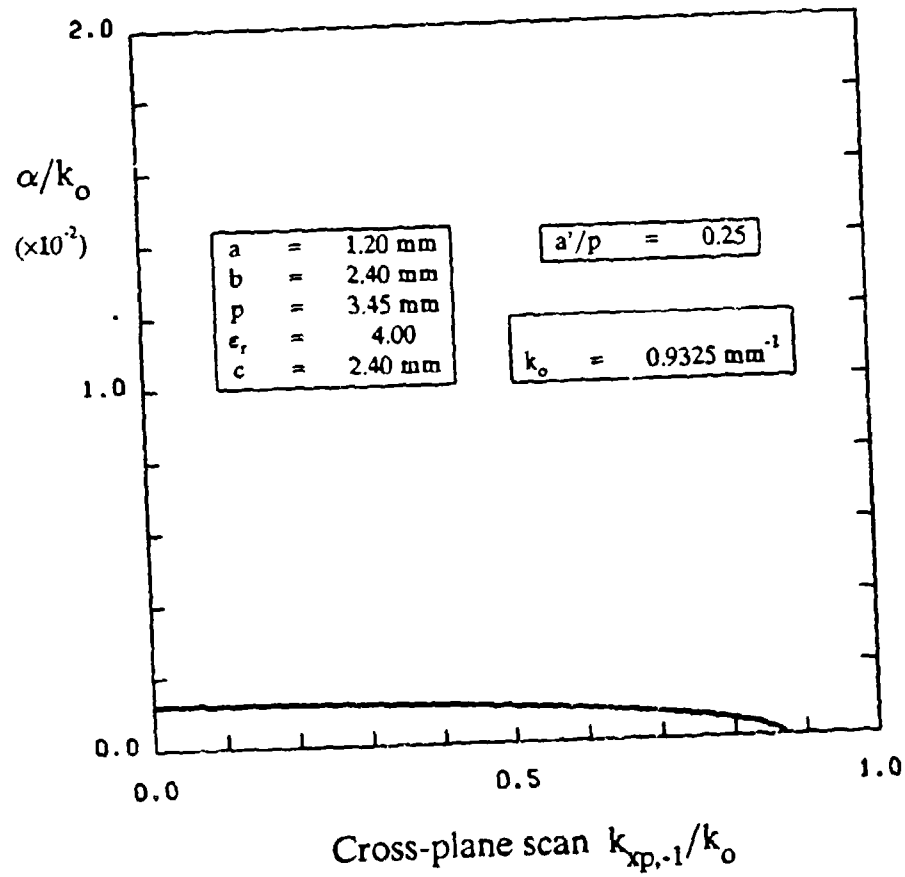


Fig. 11.21 Same as Fig. 11.20, but for $k_0 = 0.9325 \text{ mm}^{-1}$, for which the caption for Fig. 11.18 contains further information.

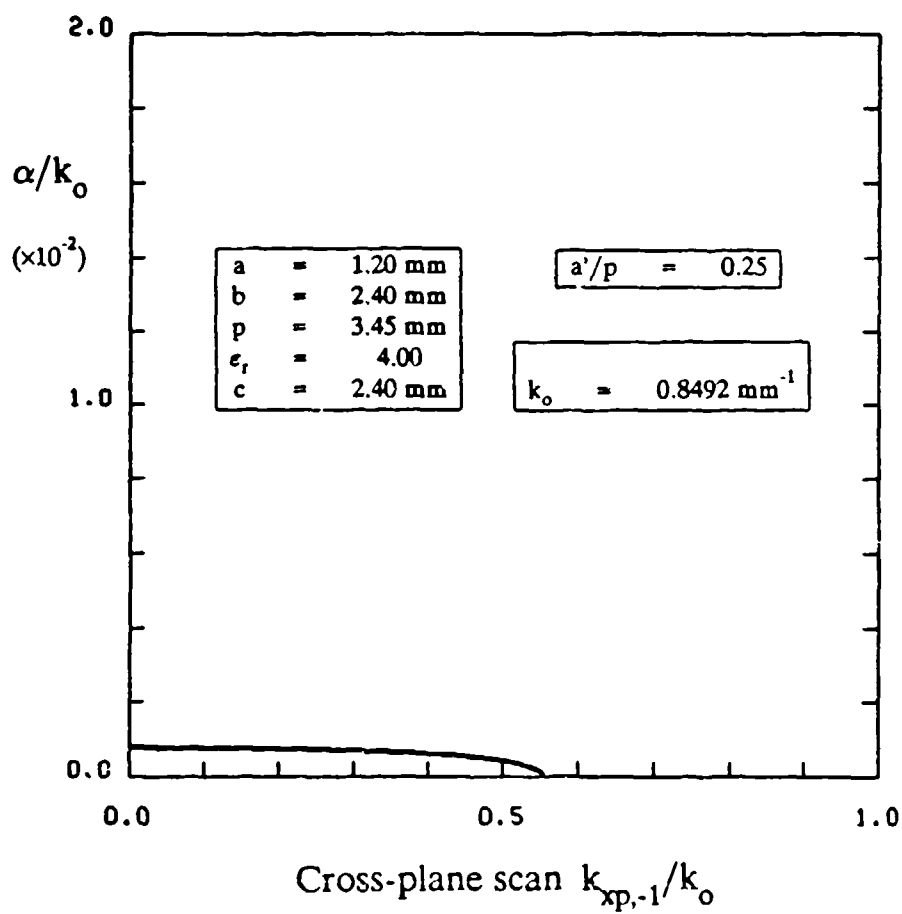


Fig. 11.22 Same as Fig. 11.20, but for $k_o = 0.8492 \text{ mm}^{-1}$, for which the caption for Fig. 11.19 contains further information.

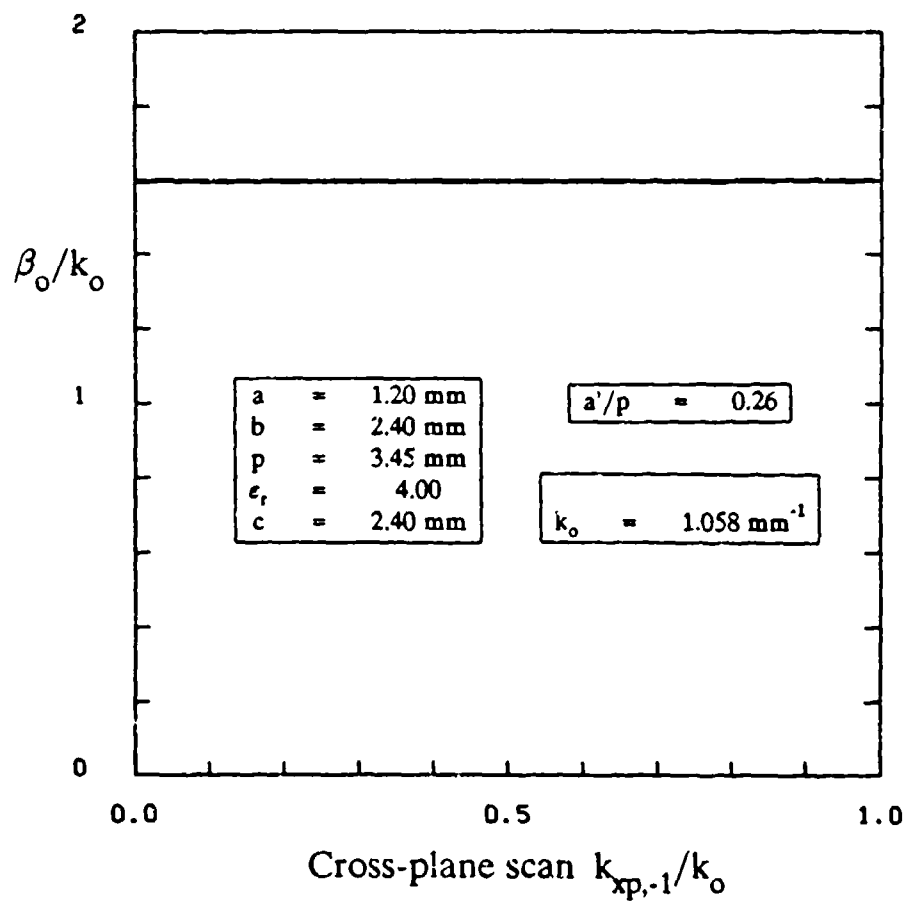


Fig. 11.23 Same as Fig. 11.17, but for $a'/p = 0.26$, and for $k_0 = 1.058 \text{ mm}^{-1}$, for which the beam is at -7.0° from broadside when the cross-plane scan is zero.

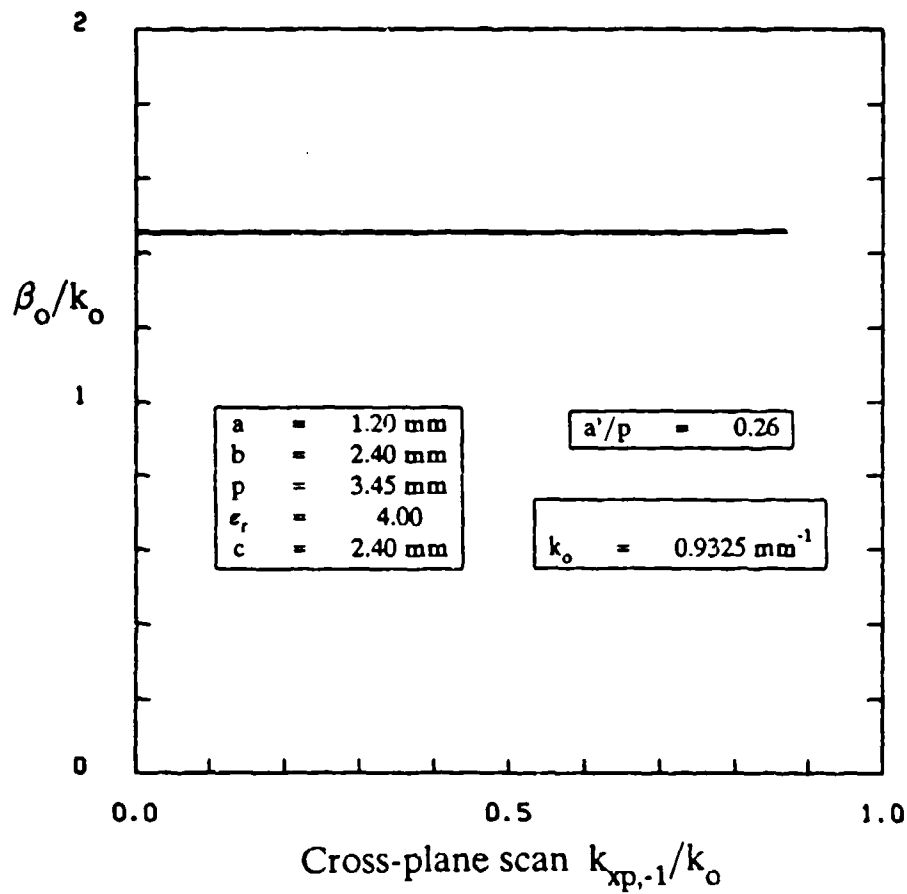


Fig. 11.24 Same as Fig. 11.23, but for $k_o = 0.9325 \text{ mm}^{-1}$, for which the caption in Fig. 11.18 contains further information.

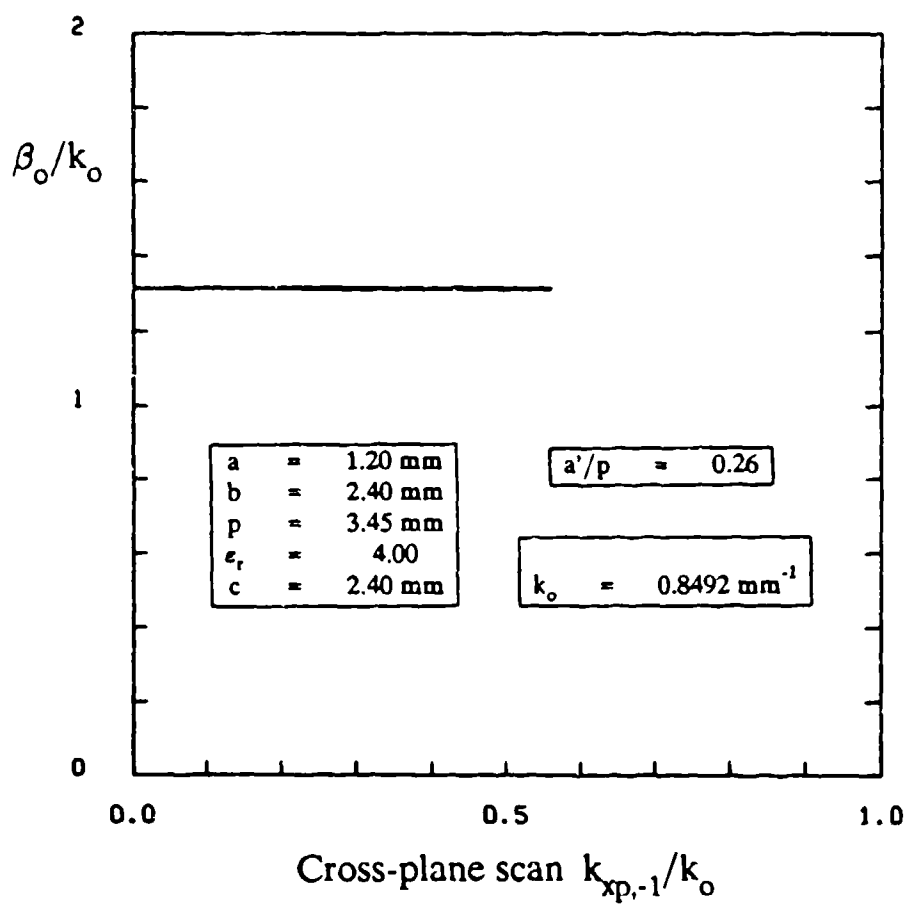


Fig. 11.25 Same as Fig. 11.23, but for $k_0 = 0.8492 \text{ mm}^{-1}$, for which the caption in Fig. 11.19 contains further information.

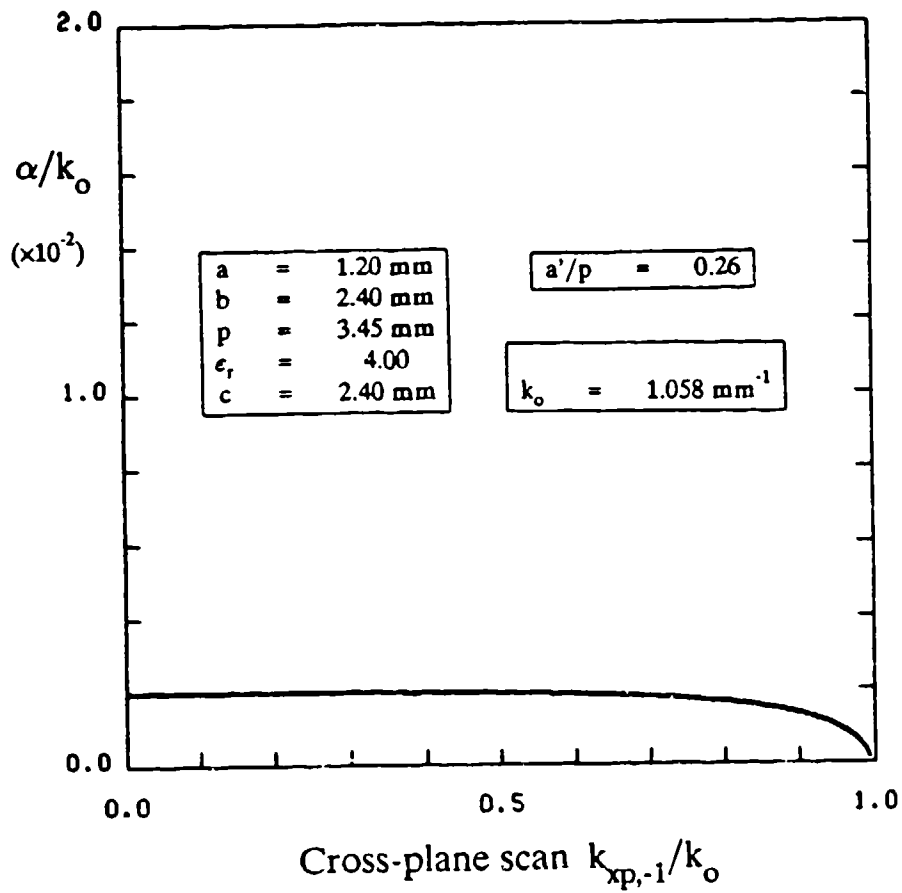


Fig. 11.26 Same as Fig. 11.20, but for $a'/p = 0.26$, and for $k_0 = 1.058 \text{ mm}^{-1}$, for which the caption in Fig. 11.23 contains further information.

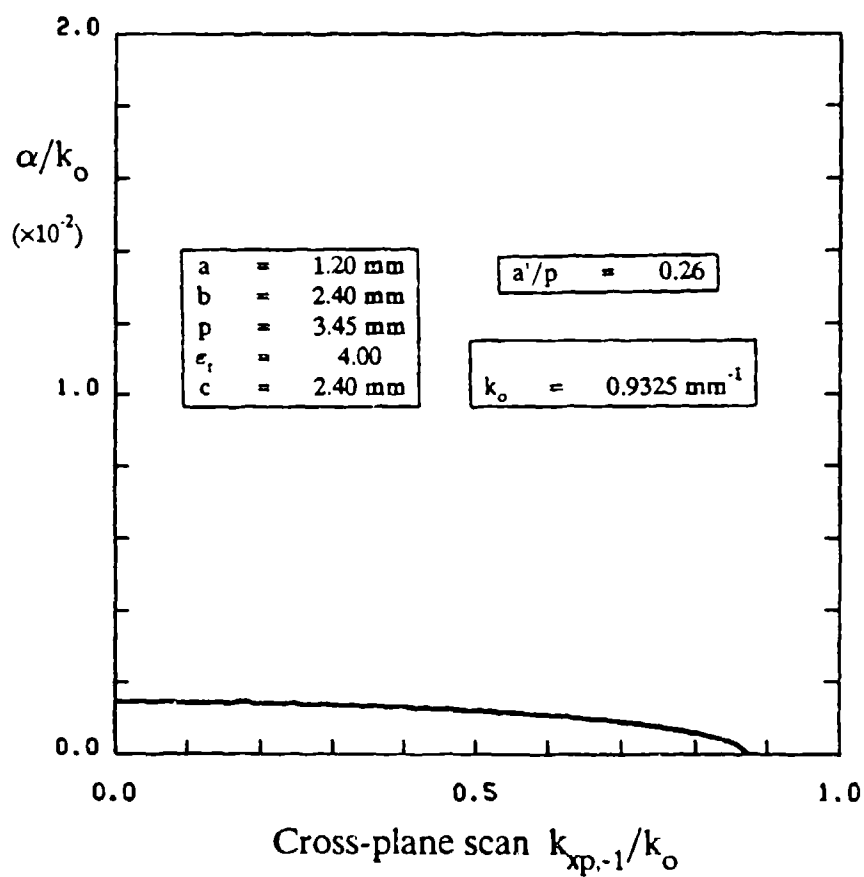


Fig. 11.27

Same as Fig. 11.26, but for $k_0 = 0.9325 \text{ mm}^{-1}$, for which the caption in Fig. 11.18 contains further information.

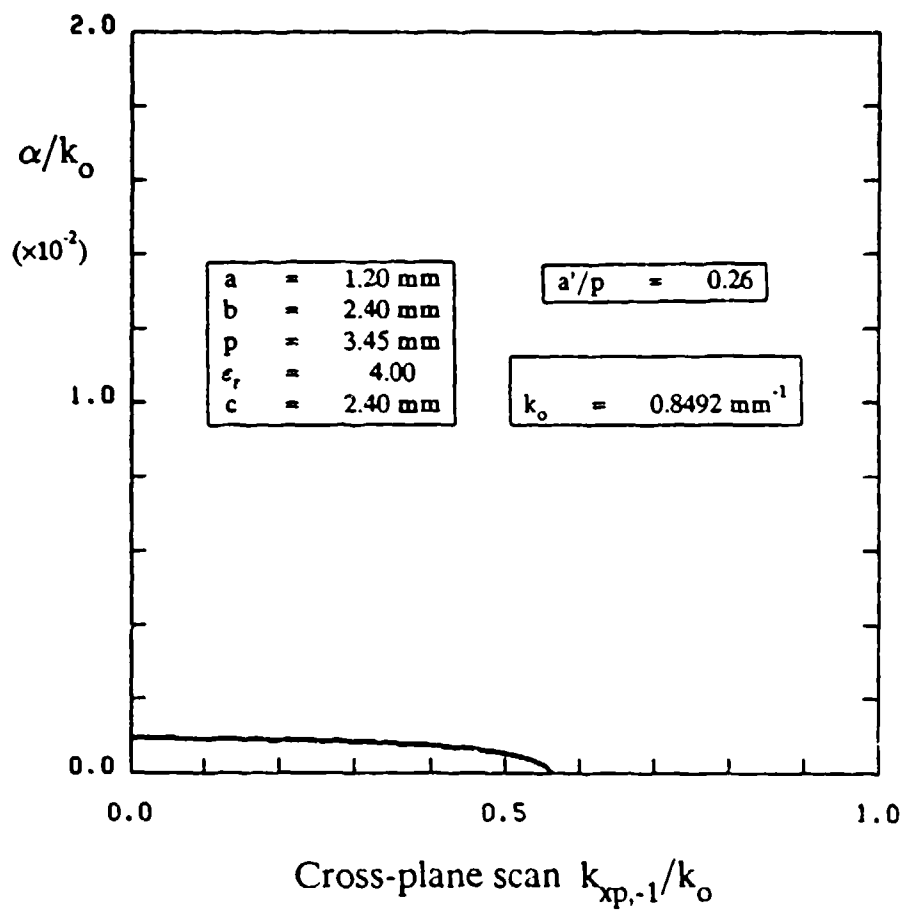


Fig. 11.28 Same as Fig. 11.26, but for $k_o = 0.8492 \text{ mm}^{-1}$, for which the caption in Fig. 11.19 contains further information.

We have not examined the effect on performance of changes in width a . The behavior of the array when the cross-plane scan is zero is unaffected by that dimension, but some practical considerations are required with respect to the phase-shift scanning aspects. Although this matter should be considered more carefully, some preliminary comments can be made now. First of all, the width a will be quite small unless some structural modifications are made. Let us assume that height b of the dielectric-filled region is $3\lambda_e/4$, which is $3\lambda_o/8$ when $\epsilon_r = 4.00$. Thus, width a will be $3\lambda_o/16$, which is rather small. The width can be increased by tapering, which introduces mechanical complexity. A small width would require only a small phase shift per element, but more elements, and therefore more phase shifters, would be needed for the same beam width in azimuth. An advantage to a narrower width is that the height c of the metal baffles can be made smaller, since the higher modes in the air-filled region would then decay more rapidly. It is clear that tradeoffs are involved that require further consideration.

The array treated in this chapter differs from the other two arrays, discussed in Chaps. IV and X, in that the leaky-wave line sources are periodically modulated here, as we pointed out at the beginning of the chapter. This distinction has permitted a larger and more versatile scan range, as desired, but otherwise the behavior during cross-plane scan is qualitatively similar to what was found for the other arrays.

XII. REFERENCES

523

XII. REFERENCES

1. Final Report on predecessor contract: RADC Contract No. F19628-81-K-0044, Principal Investigator, Arthur A. Oliner, July 31, 1984.
2. P. Lampariello and A.A. Oliner, "A New Leaky Wave Antenna for Millimeter Waves Using an Asymmetric Strip in Groove Guide, Part I: Theory," IEEE Trans. Antennas and Propagation, Vol. AP-33, pp. 1285-1294, December 1985.
3. P. Lampariello and A.A. Oliner, "A New Leaky Wave Antenna for Millimeter Waves Using an Asymmetric Strip in Groove Guide, Part II: Design Considerations," IEEE Trans. Antennas and Propagation, Vol. AP-33, pp. 1295-1303, December 1985.
4. A. Sanchez and A.A. Oliner, "A New Leaky Waveguide for Millimeter Waves Using Nonradiative Dielectric (NRD) Waveguide - Part I: Accurate Theory," IEEE Trans. Microwave Theory Tech., Vol. MTT-35, pp. 737-747, August 1987.
5. Q. Han, A.A. Oliner and A. Sanchez, "A New Leaky Waveguide for Millimeter Waves Using Nonradiative Dielectric (NRD) Waveguide - Part II: Comparison with Experiments," IEEE Trans. Microwave Theory Tech., Vol. MTT-35, pp. 748-752, August 1987.
6. S. Edelberg and A.A. Oliner, "Mutual Coupling Effects in Large Antenna Arrays, Part I: Slot Arrays," Trans. IRE on Antennas and Propagation, Vol. AP-8, pp. 286-297, May 1960.
7. A.A. Oliner and R.G. Malech, Chapter III, pp. 195-335, of "Array Theory and Practice," Vol. II of *Microwave Scanning Antennas*, ed. R.C. Hansen, Academic Press, New York, 1966.
8. N. Marcuvitz, *Waveguide Handbook*, Vol. 10 of the MIT Radiation Laboratory Series, McGraw-Hill Book Co., New York, 1951.
9. T. Yoneyama and S. Nishida, "Nonradiative Dielectric Waveguide for Millimeter-Wave Integrated Circuits," IEEE Trans. on Microwave Theory Tech., Vol. MTT-29, No. 11, pp. 1188-1192, November 1981.

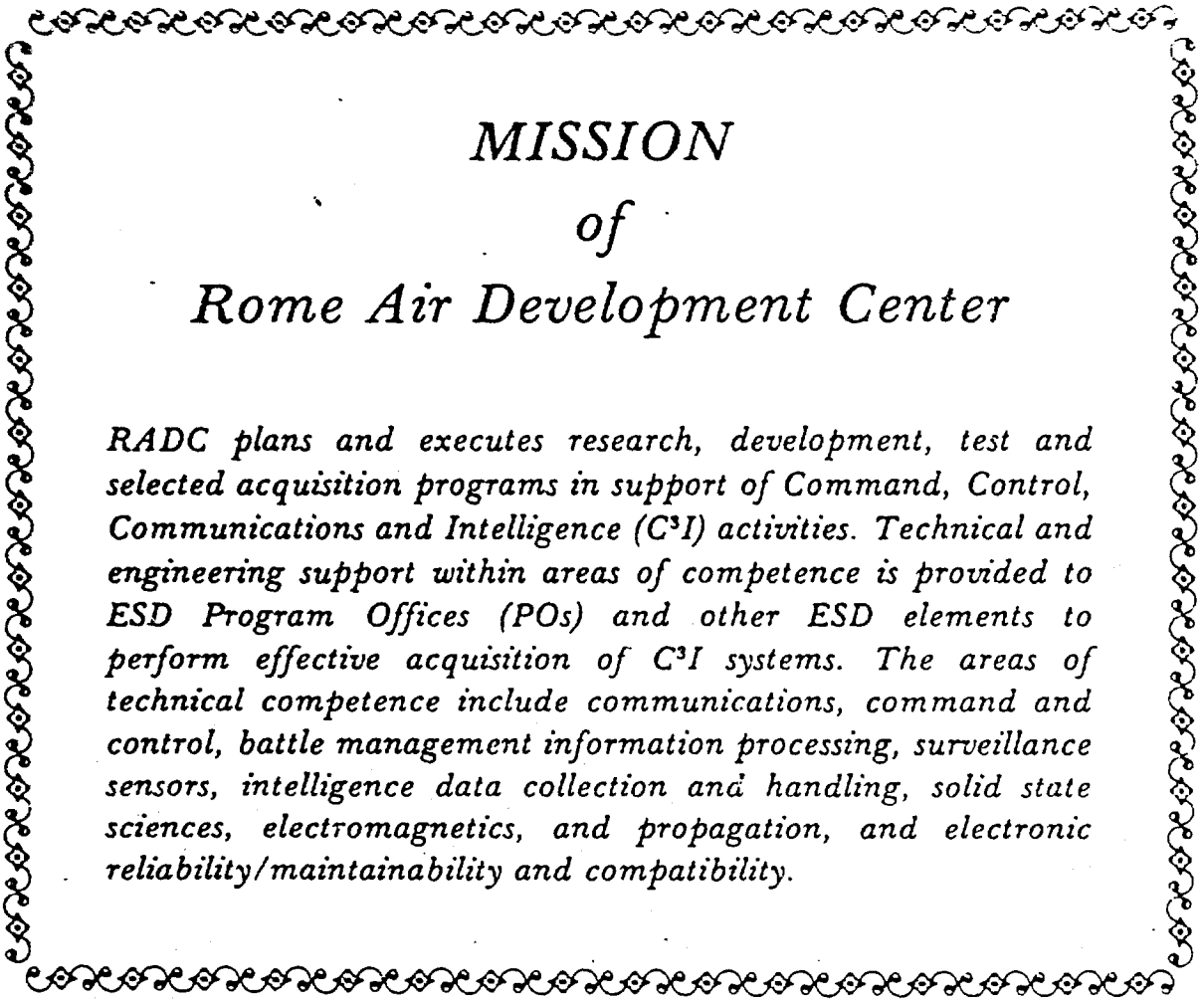
10. A.A. Oliner, S.T. Peng and K.M. Sheng, "Leakage from a Gap in NRD Guide," Digest 1985 IEEE International Microwave Symposium, pp. 619-622, St. Louis, MO, June 3-7, 1985.
11. H. Shigesawa, M. Tsuji and A.A. Oliner, "Effects of Air Gap and Finite Metal Plate Width on NRD Guide," Digest IEEE International Microwave Symposium, pp. 119-122, Baltimore, MD, June 2-4, 1986.
12. H. Shigesawa, M. Tsuji and A.A. Oliner, "Coupling Effects in an NRD Guide Leaky Wave Antenna," Digest National Radio Science Meeting, p. 27, Philadelphia, PA, June 9-13, 1986.
13. F. Schwering, private communication.
14. S.T. Peng and A.A. Oliner, "Guidance and Leakage Properties of a Class of Open Dielectric Waveguides, Part I: Mathematical Formulations," IEEE Trans. Microwave Theory Tech., Vol. MTT-29 (Special Issue on Open Guided Wave Structures), pp. 843-855, September 1981. Invited paper.
15. A.A. Oliner, S.T. Peng, T.I. Hsu and A. Sanchez, "Guidance and Leakage Properties of a Class of Open Dielectric Waveguides, Part II: New Physical Effects," IEEE Trans. Microwave Theory Tech., Vol. MTT-29 (Special Issue on Open Guided Wave Structures), pp. 855-869, September 1981. Invited paper.
16. A.A. Oliner and S.J. Xu, "A Novel Phased Array of Leaky-Wave NRD Guides," Digest National Radio Science Meeting, p. 139, Blacksburg, VA, June 15-19, 1987.
17. A.A. Oliner, "Equivalent Circuits for Slots in Rectangular Waveguide," Report R-234, Microwave Research Institute, Polytechnic Institute of Brooklyn, for the Air Force Cambridge Research Center, under Contract AF19(122)-3, August 1951. This comprehensive report also contained contributions by J. Blass, L.B. Felsen, H. Kurss and N. Marcuvitz.
18. A.A. Oliner and P. Lampariello, "The Dominant Mode Properties of Open Groove Guide: An Improved Solution," Trans. IEEE on Microwave Theory Tech., Vol. MTT-33, pp. 755-764, September 1985.

19. T. Nakahara and N. Kurauchi, "Transmission Modes in the Grooved Guide," J. Inst. of Electronics and Commun. Engrs. of Japan, Vol. 47, No. 7, pp. 43-51, July 1964.
20. A.A. Oliner and P. Lampariello, "A New Simple Leaky Wave Antenna for Millimeter Waves." Digest 1985 North American Radio Science Meeting, p. 57, Vancouver, Canada, June 17-21, 1985.
21. A.A. Oliner and P. Lampariello, "A Simple Leaky Wave Antenna that Permits Flexibility in Beam Width," Digest National Radio Science Meeting, p. 26, Philadelphia, PA, June 9-13, 1986.
22. P. Lampariello, F. Frezza, H. Shigesawa, M. Tsuji and A.A. Oliner, "Guidance and Leakage Properties of Offset Groove Guide," Digest IEEE International Microwave Symposium, pp. 731-734, Las Vegas, NV, June 9-11, 1987.
23. H. Shigesawa, M. Tsuji and A.A. Oliner, "Theoretical and Experimental Study of an Offset Groove Guide Leaky Wave Antenna," Digest IEEE International Symposium on Antennas and Propagation, pp. 628-632, Blacksburg, VA, June 15-19, 1987.
24. G.A. Deschamps, "Determination of Reflection Coefficients and Insertion Loss of a Waveguide Junction," Jour. Appl. Phys., Vol. 24, p. 1046, 1953.
25. H. Ermert, "Guided Modes and Radiation Characteristics of Covered Microstrip Lines," A.E.U., Band 30, pp. 65-70, February 1976.
26. H. Ermert, "Guiding and Radiation Characteristics of Planar Waveguides," IEE Microwave, Optics and Acoustics, Vol. 3, pp. 59-62, March 1979.
27. W. Menzel, "A New Travelling-Wave Antenna in Microstrip," A.E.U., Band 33, pp. 137-140, April 1979.
28. J. Boukamp and R.H. Jansen, "Spectral Domain Investigation of Surface Wave Excitation and Radiation by Microstrip Lines and Microstrip Disk Resonators," Proc. European Microwave Conference, Nurnberg, Germany, September 5-8, 1983.

29. A.A. Oliner and K.S. Lee, "The Nature of the Leakage from Higher Modes on Microstrip Line," Digest IEEE International Microwave Symposium, pp. 57-60, Baltimore, MD, June 2-4, 1986.
30. A.A. Oliner and K.S. Lee, "Microstrip Leaky Wave Strip Antennas," Digest IEEE International Symposium on Antennas and Propagation, pp. 443-446, Philadelphia, PA, June 9-13, 1986.
31. A.A. Oliner, "Leakage from Higher Modes on Microstrip Line with Application to Antennas," Proc. URSI International Symposium on Electromagnetic Theory, pp. 25-27, Budapest, Hungary, August 25-29, 1986.
32. A.A. Oliner, "Leakage from Higher Modes on Microstrip Line with Application to Antennas," Radio Science, Vol. 22, pp. 907-912, November 1987.
33. H.M. Aitschuler and L.O. Goldstone, "On Network Representations of Certain Obstacles in Waveguide Regions," IRE Trans. Microwave Theory Tech., Vol. MTT-7, pp. 213-221, April 1959.
34. D.C. Chang and E.F. Kuester, "Total and Partial Reflection from the End of a Parallel-Plate Waveguide with an Extended Dielectric Loading," Radio Science, Vol. 16, pp. 1-13, January-February 1981.
35. E.F. Kuester, R.T. Johnk and D.C. Chang, "The Thin-Substrate Approximation for Reflection from the End of a Slab-Loaded Parallel-Plate Waveguide with Application to Microstrip Patch Antennas," IEEE Trans. Antennas and Propagation, Vol. AP-30, pp. 910-917, September 1982.
36. L.O. Goldstone and A.A. Oliner, "Leaky-Wave Antennas I: Rectangular Waveguides," IRE Trans. Antennas and Propagation, Vol. AP-7, pp. 307-319, October 1959.
37. T. Tamir and A.A. Oliner, "Guided Complex Waves, Part I: Fields at an Interface," Proc. Inst. Elec. Eng., Vol. 110, pp. 310-324, February 1963.
38. T. Tamir and A.A. Oliner, "Guided Complex Waves, Part II: Relation to Radiation Patterns," Proc. Inst. Elec. Eng., Vol. 110, pp. 325-334, February, 1963.

39. A. Hessel and A.A. Oliner, "A New Theory of Wood's Anomalies on Optical Gratings," *Appl. Opt.*, Vol. 4, pp. 1275-1297, October 1965.
40. I. Palocz and A.A. Oliner, "Leaky Space Charge Waves I: Cerenkov Radiation," *Proc. IEEE*, Vol. 53, pp. 24-36, January 1965.
41. I. Palocz and A.A. Oliner, "Leaky Space Charge Waves II: Smith-Purcell Radiation," *Proc. IEEE*, Vol. 55, pp. 46-56, January 1967.
42. T. Tamir and A.A. Oliner, "The Influence of Complex Waves on the Radiation Field of a Slot-Excited Plasma Layer," *IRE Trans. Antennas and Propagation*, Vol. AP-10, pp. 55-65, January 1962.
43. A.A. Oliner and T. Tamir, "Radiation from Semi-Infinite Slot-Excited Plasma-Sheath Configurations," pp. 32-48, in *Electromagnetic Aspects of Hypersonic Flight*, Spartan Books, Baltimore, MD, 1964.
44. G.H. Knittel, A. Hessel, and A.A. Oliner, "Element Pattern Nulls in Phased Arrays and Their Relation to Guided Waves," *Proc. IEEE*, Vol. 56, pp. 1822-1836, November 1968.
45. T. Tamir and H.L. Bertoni, "Lateral Displacement of Optical Beams at Multilayered and Periodic Structures," *J. Opt. Soc. Am.*, Vol. 61, pp. 1397-1413, October 1971.
46. A.A. Oliner, "Equivalent Circuits for Small Symmetrical Longitudinal Apertures and Obstacles," *IRE Trans. on Microwave Theory Tech.*, Vol. MTT-8, pp. 72-80, January 1960.
47. M. Guglielmi and A.A. Oliner, "Multimode Network Descriptions of a Planar Periodic Metal Strip Grating at a Dielectric Interface," *Digest National Radio Science Meeting*, p. 166, Philadelphia, PA, June 9-13, 1986.
48. M. Guglielmi and A.A. Oliner, "Multimode Network Description of a Planar Periodic Metal Strip Grating at a Dielectric Interface, Part I: Network Formulations," accepted for publication by *IEEE Trans. on Microwave Theory and Techniques*.

49. M. Guglielmi and A.A. Oliner, "Multimode Network Description of a Planar Periodic Metal Strip Grating at a Dielectric Interface, Part II: Small-Aperture and Small-Obstacle Solutions," accepted for publication by IEEE Trans. on Microwave Theory and Techniques.



MISSION of Rome Air Development Center

RADC plans and executes research, development, test and selected acquisition programs in support of Command, Control, Communications and Intelligence (C³I) activities. Technical and engineering support within areas of competence is provided to ESD Program Offices (POs) and other ESD elements to perform effective acquisition of C³I systems. The areas of technical competence include communications, command and control, battle management information processing, surveillance sensors, intelligence data collection and handling, solid state sciences, electromagnetics, and propagation, and electronic reliability/maintainability and compatibility.